Study of Li-rich lamellar oxides as positive electrode materials for lithium-ion batteries

Hideyuki Koga

To cite this version:

Hideyuki Koga. Study of Li-rich lamellar oxides as positive electrode materials for lithium-ion batteries. Other. Université Sciences et Technologies - Bordeaux I, 2013. English. NNT : 2013BOR14751 . tel-00923812

HAL Id: tel-00923812
https://theses.hal.science/tel-00923812

Submitted on 5 Jan 2014

HAL is a multi-disciplinary open access archive for the deposit and dissemination of scientific research documents, whether they are published or not. The documents may come from teaching and research institutions in France or abroad, or from public or private research centers.

L'archive ouverte pluridisciplinaire **HAL**, est destinée au dépôt et à la diffusion de documents scientifiques de niveau recherche, publiés ou non, émanant des établissements d'enseignement et de recherche français ou étrangers, des laboratoires publics ou privés.

N d'ordre : 4751

THÈSE

PRÉSENTÉE A

L'UNIVERSITÉ BORDEAUX I

ÉCOLE DOCTORALE DES SCIENCES CHIMIQUES

Par **Hideyuki KOGA**

POUR OBTENIR LE GRADE DE

DOCTEUR

SPÉCIALITÉ : PHYSICO-CHIMIE DE LA MATIÈRE CONDENSÉE

Study of Li-rich lamellar oxides as positive electrode materials for lithium-ion batteries

---

Après avis de :

M **Philippe DENIARD**	Directeur de recherche	Rapporteur
Mme **Laure MONCONDUIT**	Directrice de recherche	Rapporteur

Devant la Commission d'examen formée de :

Mme **Stéphanie BELIN**	Ingénieur de Recherche	Examinatrice
Mme **Laurence CROGUENNEC**	Chargée de Recherche	Examinatrice
M **Claude DELMAS**	Directeur de Recherche	Examinateur
M **Mario MAGLIONE**	Directeur de Recherche	Président
M **Yoshio UKYO**	Toyota Central R&D Labs	Examinateur

- 2013 -

Université : Université Bordeaux 1
Laboratoire : Institut de Chimie de la Matière Condensée de Bordeaux

Résumé :

Les mécanismes mis en jeu lors du cyclage de batteries au Lithium Li//$Li_{1.20}Mn_{0.54}Co_{0.13}Ni_{0.13}O_2$ ont été étudiés avec l'objectif de déterminer l'origine des capacités très élevées délivrées par les oxydes lamellaires « $(1-x)LiMO_2.xLi_2MnO_3$ ». La caractérisation par diffraction des RX et des neutrons montre que la structure est maintenue et l'existence de fluctuations de composition qui peuvent être assimilées à l'existence de deux phases de compositions voisines. Les résultats des tests électrochimiques et les analyses menées au cours du cyclage en spectroscopie d'absorption des rayons X ont suggéré la participation de l'oxygène aux processus redox. Celle-ci a été confirmée par la préparation et la caractérisation de matériaux désintercalés et réintercalés chimiquement en lithium. Les analyses en microscopie électronique à transmission (HAADF-STEM) et en nanodiffraction, montrent qu'une densification associée à un dégagement d'oxygène a lieu à la périphérie des particules

Mots clés :

- Electrode positive pour batteries Li-ion
- Réaction électrochimique
- Processus redox
- Oxydes lamellaires riches en Lithium
- Mécanisme de charge et de décharge
– Modifications structurales

Abstract :

The charge and discharge mechanism of $Li_{1.20}Mn_{0.54}Co_{0.13}Ni_{0.13}O_2$ was studied using several characterization tools in order to determine the origin of the high capacity observed for the system $(1-x)LiMO_2.xLi_2MnO_3$ used as positive electrode for Li-ion batteries. The electrochemical results and *in operando* XAS analyses performed during the 1st cycle of Li//$Li_{1.20}Mn_{0.54}Co_{0.13}Ni_{0.13}O_2$ cells suggested the possible participation of oxygen anion to the redox processes. It was supported by the in-depth analysis of materials prepared by chemical Li deintercalation and reinsertion. The results of XRD, HAADF-STEM and nanodiffraction analyses, combined with electrochemical experiments performed in different conditions (rate, temperature …), revealed that different types of reactions occur in the particles during the 1st cycle. Within the bulk Ni, Co and O are involved in the redox processes, whereas Mn is not: oxygen ions are oxidized in charge and reduced during the next discharge reversibly. At the surface, the same oxidation processes occur during the first charge, but with the release of oxygen gas and a densification of the lattice. During the next discharge and subsequent cycles, the redox reaction occurring near the surface after the 1st charge involves thus Co, Ni and Mn.

Keywords :

- Positive electrode for Li-ion batteries
- Li-rich layered oxides
- Electrochemical reaction
- Charge and discharge mechanism
- Redox processes
- Structural changes

N d'ordre : 4751

THÈSE

PRÉSENTÉE A

L'UNIVERSITÉ BORDEAUX I

ÉCOLE DOCTORALE DES SCIENCES CHIMIQUES

Par **Hideyuki KOGA**

POUR OBTENIR LE GRADE DE

DOCTEUR

SPÉCIALITÉ : PHYSICO-CHIMIE DE LA MATIÈRE CONDENSÉE

Study of Li-rich lamellar oxides as positive electrode materials for lithium-ion batteries

---

Soutenue le : 30 janvier 2013

Après avis de :

M **Philippe DENIARD**	Directeur de recherche	Rapporteur
Mme **Laure MONCONDUIT**	Directrice de recherche	Rapporteur

Devant la Commission d'examen formée de :

Mme **Stéphanie BELIN**	Ingénieur de Recherche	Examinatrice
Mme **Laurence CROGUENNEC**	Chargée de Recherche	Examinatrice
M **Claude DELMAS**	Directeur de Recherche	Examinateur
M **Mario MAGLIONE**	Directeur de Recherche	Président
M **Yoshio UKYO**	Toyota Central R&D Labs	Examinateur

- 2013 -

Acknowledgements

I am deeply grateful to responsible persons for this research work, Dr. Claude Delmas and Dr. Laurence Croguennec. I received many supports from them about managements of the research work and scientific parts. I also would like to express my gratitude to Dr. François Weill and Dr. Michel Ménétrier. They gave many supports and advices for our research work.

I am heartily thankful to Dr. Laure Monconduit and Dr. Philippe Deniard for participating in my defense as rapporteurs. I would like to thank Dr. Mario Maglione to accept the chair of my defense. I also would like to thank Dr. Yoshio Ukyo to participate in my defense and gave the useful comments for our work.

This thesis would not have been possible unless any supports by many persons. I would like to thank Dr. Stéphanie Belin, beamline scientist in synchrotron Soleil, she helped for our XAS measurements and participated in my defense. I want to thank Dr. Cécile Genevois Mazellier, research engineer CNRS in Rouen, she performed HAADF-STEM and nano electron diffraction measurements for our work. I also want to thank Dr. Emmanuelle Suard, instrument scientist of ILL, she supported the neutron diffraction measurements. I want to thank Dr. Lydie Bourgeois for Raman measurements. I would like to thank Dr. Dominique Denux who carried out TGA measurements and volume density measurements. I want to thank Dr. Sonia Gomez for EELS measurements. I would like to thank Dr. Laetitia Etienne for ICP measurements. Deeply thank to Eric Lebraud for XRD measurements. I would like to thank Dr. Christine Labrugère for XPS measurements. I want to thank Dr. Olivier Nguyen for SQUID measurements. We could obtain very important results thanks to their supports.

Deeply thank to Mr. Philippe Dagault and Mrs. Cathy Denage for support our experiments.

I would like to express my gratitude to Mr. Philippe Mannessiez, Mr. Kais Douhil and Mrs. Elodie Guérin for their much supports for this work.

I would deeply thank to members of group 2, all people working in the common services and all the other members of the Labs

This work is in the framework of collaboration with ICMCB and Toyota Motor Europe. I express my gratitude to everybody involved in this project.

I would deeply thank to members in Toyota Motor Europe, Mr. Kazuaki Takada, Mr. Ichiro Sakata, Mr. Hisao Kato, Dr. Toshiya Saito and Mr. Hiroaki Takahashi. I also want to appreciate to members in Toyota Motor Corporation, Dr. Hideki Iba and Dr. Shinji Nakanishi. We could progress this project for their supports.

At last I wish to thank all those who helped me in France. I could not have completed this work without them.

Thank my parents and my family
30th, Jan, 2013
Hideyuki Koga

List of contents

General Introduction……..……………………………………...……... 1

1 – Layered oxides of general formula $LiMO_2$………………………………….…….. 3

1. 1 – $LiCoO_2$ and $LiNiO_2$……………………………………………………….…… 3

1. 2 – $LiNi_{1/3}Mn_{1/3}Co_{1/3}O_2$…………………………………………..…….. 5

2 – The spinel oxide $LiMn_2O_4$……..………………………………………..……. 5

3 – Li excess layered oxides……………………………………………..…… 6

3. 1 – Li_2MnO_3…………………………………………………………..… 7

3. 2 – Li excess layered oxides of general formula $Li_{1+x}M_{1-x}O_2$ (M = Mn, Ni, Co).. 9

3. 2. 1 – Pristine material……………………………………………………… 9

3. 2. 2 – Charge - discharge mechanism……………………………...………. 10

3. 2. 3 – Electrochemical properties…………………………………..……... 12

3. 2. 3. 1 - Irreversible capacity……………………………………..…….. 12

3. 2. 3. 2 - Rate performance and cyclability………………………........... 12

3. 2. 4 – Safety……………………………………………………..…..... 13

3. 3 – Li-rich layered oxides $Li_{1+x}M_{1-x}O_2$ (M = Cr, Ru, Pt, Sn …)
of original compositions……………………………………...…………….. 14

4 – References………………………………………………………………. 15

Chapter I – Summary of the thesis……………………………….…… 21

I. 1 – Overview of Li rich layered oxides for Li-ion batteries
(General introduction part)……………………………………..……..... 23

I. 2 - Results

I. 2. 1 – Properties of the pristine material (Chapter II)………..…………………...24

I. 2. 2 – Mechanism upon charge and discharge: structural changes observed
(Chapter III)…………………………….……………………………. 25

I. 2. 3 – Mechanism upon charge and discharge
: redox processes and structural changes……………………..………….... 28

I. 2. 3. 1 – Study of the redox processes with XAS measurement
carried out *in operando* (Chapter IV)………………………………... 28

I. 2. 3. 2 – In depth characterization of the material recovered
after chemical Li (de)intercalation (Chapter V)................................. 29

I. 2. 3. 3 – Study of the local structural changes using HAADF-STEM and nano electron diffraction (Chapter VI)……………………….....30

I. 3 – Summary of $Li_{1.20}Mn_{0.54}Co_{0.13}Ni_{0.13}O_2$………………………………………… 31

Chapter II – Characterization of $Li_{1.20}Mn_{0.54}Co_{0.13}Ni_{0.13}O_2$…………… 33

II. 1 – Introduction……………………………………………………………….. 35

II. 2 – Experimental……………………………………………………………….36

II. 3 - Results and discussion…………………………………………………...39

II. 3. 1 – Effect of the thermal treatment on the material's formation and degradation…………………………………………...……… 39

II. 3. 2 – Global analysis (phase, composition and homogeneity) of the materials prepared……………………………………………44

II. 3. 3 – Structure of the materials prepared……………………………………… 49

II. 3. 4 – Electrochemical tests in lithium cells……………………………… 60

II. 4 – Conclusion…………………………………………………………………62

II. 5 – References………………………………………………………………… 62

Chapter III – The charge and discharge mechanism of $Li_{1.20}Mn_{0.54}Co_{0.13}Ni_{0.13}O_2$ – Global structural change –…………….....…65

III. 1 – Introduction……………………………………………………………… 67

III. 2 – Experimental……………………………………………………………... 68

III. 3 – Results and discussion……………………………………………………69

III. 3. 1 – Composition, structure and microstructure of the powders prepared at different temperatures………………………………………………… 69

III. 3. 2 – Structural changes observed during the first cycle……………………… 72

III. 3. 3 – Effect of the powder particle size and cycling conditions on the phase separation……………………………………………... 79

III. 3. 4 - Discussion………………………………………………………………86

III. 4 – Conclusion……………………………………………………………….. 88

III. 5 – References……………………………………………………………….. 90

Chapter IV - The charge and discharge mechanism of $Li_{1.20}Mn_{0.54}Co_{0.13}Ni_{0.13}O_2$ – Redox reaction studied by XAFS –………. 93

IV. 1 – Introduction……………………………………………………………… 95

IV. 2 – Experimental……………………………………………………………... 95

IV. 3 – Results and discussion…………………………………………………………… 98
IV. 3. 1 – Electrochemical performance of the cell developed for *Operando* study using Synchrotoron radiation……………………………………………… 98
IV. 3. 2 – XANES study during the charge and discharge of Li//$Li_{1.20}Mn_{0.54}Co_{0.13}Ni_{0.13}O_2$ batteries…………………………………… 100
IV. 3. 2. 1 – Ni K-edge…………………………………………………………….. 100
IV. 3. 2. 2 – Co K-edge……………………………………………………………. 103
IV. 3. 2. 3 – Mn K-edge…………………………………………………………… 106
IV. 3. 3 – Analysis of the EXAFS spectra recorded *in operando* upon cycling….. 112
IV. 3. 4 – Discussion……………………………………………………………… 119
IV. 4 – Conclusion……………………………………………………………………….. 119
IV. 5 – References……………………………………………………………………... 121
IV. 6 – Appendix………………………………………………………………………. 123

Chapter V – The charge and discharge mechanism of $Li_{1.20}Mn_{0.54}Co_{0.13}Ni_{0.13}O_2$ – Study of materials prepared chemically – ………………………………………………………………………. 125
V. 1 – Introduction……………………………………………………………………. 127
V. 2 – Experimental………………………………………………………………….... 128
V. 3 – Results and discussion………………………………………………………… 131
V. 3. 1 – Comparison of the materials obtained from chemical and electrochemical reactions…………………………………………………………….. 131
V. 3. 2 – Characterization of the material recovered after chemical Li deintercalation and reinsertion………………………………………………………. 142
V. 3. 3 – Discussion……………………………………………………………... 148
V. 4 – Conclusion…………………………………………………………....... 148
V. 5 – References…………………………………………………………………… 150

Chapter VI – The charge and discharge mechanism of $Li_{1.20}Mn_{0.54}Co_{0.13}Ni_{0.13}O_2$ – Local structural change with HAADF-STEM –………………………151
VI. 1 – Introduction…………………………………………………………………… 153
VI. 2 – Experimental…………………………………………………………………... 153
VI. 3 – Results and discussion………………………………………………………… 155
VI. 3. 1 – Pristine material………………………………………………………… 155

VI. 3. 2 – Upon lithium deintercalation and reinsertion………………………….... 161
VI. 3. 2. 1 - Comparison of the materials obtained electrochemically after the 1st cycle, with or without the ‘‘plateau’’……………….... 161
VI. 3. 2. 2 – After chemical lithium deintercalation and reinsertion……….....   165
VI. 4 – Conclusion………………………………………………………………….. 167
VI. 5 – References………………………………………………………………….... 168

Conclusion………………………………………………….……………….. 169

List of figures……………………………………………………………… 175

List of tables…………………………………………………………...…... 187

Introduction générale

(4 pages en français)

Introduction générale

1 – Les oxydes lamellaires de formule générale $LiMO_2$

1. 1 - $LiCoO_2$ et $LiNiO_2$

Les oxydes lamellaires ont été largement étudiés comme matériaux d'électrodes positives pour batteries lithium-ion depuis les premiers résultats reportés par J. B. Goodenough en 1980 **[1]**. $LiCoO_2$, qui est synthétisé par voie solide en chauffant un mélange de Li_2CO_3 et de Co_3O_4 à 700-900°C sous air, est utilisé intensivement pour les applications de type batteries Lithium-ion pour les outils portables. $LiCoO_2$ présente une structure lamellaire consistant en l'empilement de couches de métaux de transition (faites d'octaèdres CoO_6 partageant des arêtes) et de couches de lithium (faites d'octaèdres LiO_6 partageant des arêtes), décrites dans le groupe d'espace *R-3m* comme montré sur les figures **Fig. 1** et **Fig. 2**. Les ions Li^+ peuvent être désintercalés et réintercalés dans Li_xCoO_2, respectivement au cours de la charge et de la décharge, avec une grande réversibilité jusqu'à x=0.5 et une capacité réversible de 140 mAh/g. Une série de transitions de phase réversibles a lieu lors du cyclage : la première est associée à une transition isolant – métal ($0.70 < x < 0.94$) **[2]**, la seconde à un ordre Lithium/Lacunes et à une distorsion monoclinique (x = ½) **[3-4]**, la troisième à la formation d'une succession de domaines de type O3 et O1 (le domaine de type O1 étant obtenu à partir du premier par un glissement de feuillets) ($x \leq 0.33$) et le quatrième à la formations de la phase O1 par glissement de feuillets (x = 0) **[5-6]**. Ici O3 et O1 indiquent les différents types de structures lamellaires : la lettre O indique que les ions alcalins occupent des sites octaédriques (P pour des prismes trigonaux et T pour des tétraèdres) et le chiffre donne le nombre de feuillets MO_2 nécessaires pour décrire la maille hexagonale. Lorsque le cyclage est réalisé dans une plus large fenêtre de potentiel telle que $x < 0.4$ dans Li_xCoO_2, la réversibilité diminue du fait de grandes modifications structurales (glissement de feuillets, variation de volume, etc.) **[7]**. Certains auteurs ont également mentionné la possibilité pour les métaux de transition Co de migrer du feuillet vers l'espace interfeuillet (formation d'une phase de type spinelle) et également une dissolution possible à haut potentiel **[8-9]**. Dans notre groupe à l'ICMCB, une surstoechiometrie en lithium a été mise en évidence pour $LiCoO_2$ selon la formule chimique $Li_{1+\delta}Co^{III}_{1-\delta}O_{2-\delta}$: les ions cobalt trivalent de configuration électronique de type spin intermédiaire sont présents dans des environnements MO_5 alors que les ions Li^+ sont présents en excès dans les sites des métaux de transition. Ces défauts ont été identifiés plus spécifiquement en utilisant la spectroscopie RMN MAS du ^7Li. En fonction de la stœchiométrie de "$LiCoO_2$" le diagramme de phase de Li_xCoO_2 est modifié, la présence de défauts empêche les deux premières transitions de phase mentionnées précédemment **[10]**. Les principaux inconvénients de $LiCoO_2$ pour être considéré pour les batteries développées pour les applications véhicules électriques et hybrides sont le prix élevé du Co et les problèmes de sécurité, i.e. l'instabilité thermique de Li_xCoO_2 à l'état chargé de la batterie. En effet, à haut potentiel la plupart des ions Co sont à l'état tétravalent, qui est un état d'oxydation instable au dessus de 200°C **[11-12]**. La décomposition thermique du matériau induit un dégagement d'oxygène qui réagit avec les solvants de l'électrolyte, en générant des dégagements de gaz et une augmentation de pression dans les batteries Lithium-ion. Par conséquent, de nouveaux matériaux d'électrode positive ont été étudiés pour les grosses batteries développées notamment pour le transport.

$LiNiO_2$ est décrit dans le même groupe d'espace que $LiCoO_2$ (*R-3m*) et délivre une plus grande capacité que $LiCoO_2$, probablement du fait de son plus faible potentiel et d'une plus faible variation de volume : un cyclage hautement réversible est possible jusqu'à x = 0.3 pour Li_xNiO_2 en comparaison de x = 0.4 pour Li_xCoO_2 **[13-14]**. Il est difficile de contrôler la stœchiométrie de $LiNiO_2$, un déficit en Lithium est en effet le plus souvent observé avec la formation de $Li_{1-z}Ni_{1+z}O_2$. Le déficit en lithium est compensé par la présence d'ions Ni^{2+} dans les feuillets et espaces interfeuillets tels que $[Li_{1-z}Ni^{2+}{}_z]_{Interfeuillet}[Ni^{2+}{}_zNi^{3+}{}_{1-z}]_{Feuillet}O_2$ **[15-16]**. Le matériau le plus déficitaire en lithium présente également de mauvaises propriétés de diffusion. Les ions Ni présents dans l'espace interfeuillet bloquent la diffusion du lithium, induisant ainsi une diminution des performances en puissance **[17]**. Le contrôle de la synthèse et de la structure du nickelate de lithium a donc fait l'objet de nombreuses études avant d'arriver à l'optimisation de la 2nde génération d'oxydes lamellaires comme électrodes positives de batteries Lithium-ion. Une substitution partielle au nickel a montré qu'elle permettait de contrôler le caractère lamellaire de la structure (et par conséquent la diffusion) et d'optimiser la cyclabilité et la stabilité thermique à l'état chargé **[17-21]**. La substitution du Co au Ni a permis de promouvoir la formation d'une structure strictement lamellaire du fait de la plus petite taille des ions Co^{3+} par rapport aux ions Ni^{3+} ($r_i(Co^{3+})$ = 0.545 Å vs. $r_i(Ni^{3+})$ = 0.56 Å), ceux-ci déstabilisent la présence des plus gros ions Ni^{2+} ($r_i(Ni^{2+})$ = 0.69 Å) dans les sites des métaux de transition **[22-25]**. La substitution de l'aluminium au nickel stabilise l'oxyde lamellaire à l'état chargé. La plus petite taille des ions Al^{3+} ($r_i(Al^{3+})$ = 0.535 Å) aide à stabiliser les ions Co^{4+} à haute température. Les ions Al^{3+} sont stables dans les sites tétraédriques, qui sont les sites intermédiaires occupés lors de la transition de la structure lamellaire vers la structure spinelle : ceci induit un ralentissement du processus de dégradation de l'oxyde lamellaire qui se traduit par une perte d'oxygène lors d'une augmentation de la température **[26-27]**. En accord avec ces résultats $LiNi_{1-y-z}Co_yAl_zO_2$ a été développé comme 2nde génération d'oxydes lamellaires pour matériaux d'électrode positive et utilisé dans de nombreuses applications comme le véhicule électrique hybride **[28-30]**.

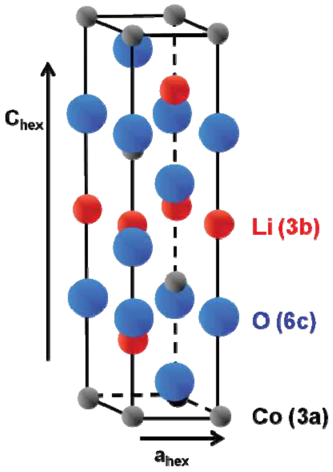

Fig. 1: Maille élémentaire de $LiCoO_2$.

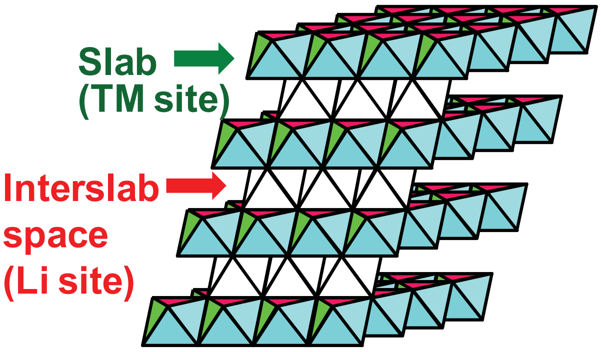

Fig. 2: Représentation de la structure de $LiCoO_2$.

1. 2 - $LiNi_{1/3}Mn_{1/3}Co_{1/3}O_2$

Plus récemment $LiNi_{1/3}Mn_{1/3}Co_{1/3}O_2$, qui contient moins de Co que $LiCoO_2$, a été proposé par Ohzuku comme un matériau très attractif à l'électrode positive, il présente spécifiquement une stabilité thermique significativement accrue à l'état chargé (plus grande sécurité) **[31]**. Sa structure est également décrite dans le groupe d'espace *R-3m* (comme α-$NaFeO_2$), mais au contraire de $LiCoO_2$ et $LiNi_{1-y-z}Co_yAl_zO_2$ un ordre cationique est observé entre les ions Ni, Mn et Co dans les feuillets menant à l'établissement d'une surstructure de type $\sqrt{3}\times\sqrt{3}$ comme montré sur la **Fig. 3** **[32]**. Dans $LiNi_{1/3}Mn_{1/3}Co_{1/3}O_2$ les ions Ni, Mn et Co ions sont présents respectivement sous la forme de Ni^{2+}, Mn^{4+} et Co^{3+}. Les ions Ni^{2+} et Co^{3+} sont oxydés aux degrés d'oxydation Ni^{4+} et Co^{4+} lors de la charge, ils sont ensuite réversiblement réduits lors de la décharge. Les ions Mn^{4+} ne participent pas aux réactions mais ils peuvent être à l'origine des propriétés très attractives de cet oxyde lamellaire. En effet, à l'état chargé une grande quantité des métaux de transition (Mn^{4+}) sont stables même à des températures élevées induisant une stabilisation de la structure à haute température (300°C vs. 230°C pour $LiNi_{1-y-z}Co_yAl_zO_2$) **[31, 33-34]**. Ensuite, comme les ions Mn ne participent pas aux processus redox les ions Mn^{3+} associés à une distorsion de type Jahn-Teller ne sont pas formés en cyclage. Dans le cas de ces oxydes lamellaires riches en manganèse, la dissolution du manganèse n'est pas significative au contraire des observations faites pour la phase spinelle $LiMn_2O_4$, pour laquelle une réaction de dismutation des ions Mn^{3+} en Mn^{4+} et Mn^{2+} est observée, ces derniers étant solubles dans l'électrolyte. Une capacité de décharge de 200 mAh/g a été obtenue pour les batteries Li// $LiNi_{1/3}Mn_{1/3}Co_{1/3}O_2$ quand elles sont chargées jusqu'à 4.6V vs. Li^+/Li, avec une bonne cyclabilité **[35-37]**.

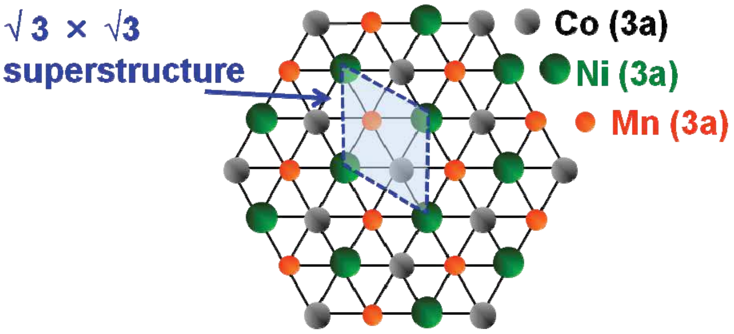

Fig. 3: Arrangement des ions métalliques dans les feuillets de $LiNi_{1/3}Mn_{1/3}Co_{1/3}O_2$.

2 – L'oxyde $LiMn_2O_4$ de structure spinelle

$LiMn_2O_4$ de structure spinelle a été largement étudié comme candidat à l'électrode positive de batteries Li-ion, il est très attractif du fait du faible cout du Mn bien plus faible que celui du Co et du Ni **[38]**. La structure de $LiMn_2O_4$ est décrite dans le groupe d'espace *Fd-3m*. Les ions Li^+ occupant les sites 8a, les ions Mn^{3+} et Mn^{4+} les sites 16d et les anions O^{2-} les sites 32e comme décrit sur la **Fig. 4**, avec les ions Mn en sites octaédriques et les ions Li en sites tétraédriques. Comme la diffusion des ions Li est tridimensionnelle avec des chemins de diffusion faits de sites tétraédriques 8a et de sites octaédriques 16c, ses performances à régime rapide sont excellentes. Les batteries Li//$LiMn_2O_4$ sont caractérisées par deux plateaux de décharge à 3V vs. Li^+/Li et à 4V vs. Li^+/Li, mais la réversibilité du plateau à 3V associée à une réaction biphasée entre $LiMn_2O_4$ et $Li_2Mn_2O_4$ est très limitée du fait d'une large variation de volume (6.4%) **[39]**. Par conséquent, seulement 1 mole de Li peut être utilisée efficacement en charge et en décharge dans $LiMn_2O_4$. Le problème le plus sérieux rencontré pour $LiMn_2O_4$ est la solubilité des ions Mn dans l'électrolyte lors du cyclage, tout spécialement à haute température **[40-41]**. La substitution d'autres métaux au Mn tels Mg, Al, Zr et Ti peut réduire la dissolution des ions Mn dans les solvants, mais ceci conduit néanmoins à une diminution de capacité **[42-45]**.

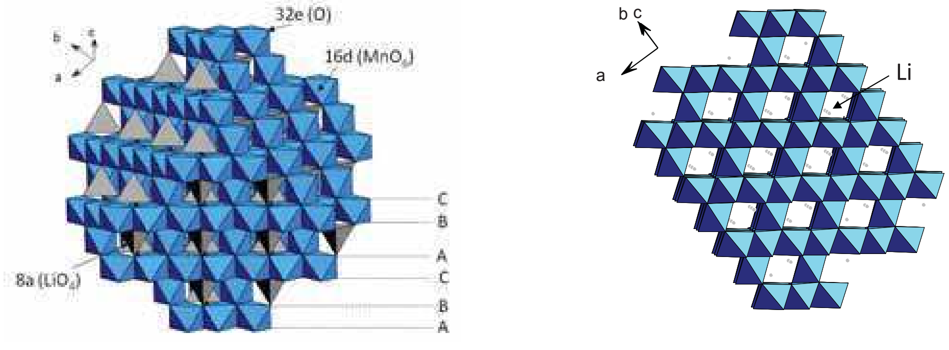

Fig. 4: Représentation de la structure de $LiMn_2O_4$.

General introduction

General introduction

1 - Layered oxides of general formula $LiMO_2$

1. 1 - $LiCoO_2$ and $LiNiO_2$

Layered oxides have been largely studied as positive electrode materials for Lithium-ion batteries since the first results reported by J. B. Goodenough in 1980 **[1]**. $LiCoO_2$, which is synthesized by solid state reactions heating a mixture of Li_2CO_3 and Co_3O_4 at 700-900°C in air, is intensively used for applications in Lithium-ion batteries for portable devices. $LiCoO_2$ has a layered structure made of transition metal layers (edge-sharing CoO_6 octahedra) and Li layers (edge-sharing LiO_6 octahedra), described in the R-3m space group as shown in **Fig. 1** and **Fig. 2**. Lithium ions can be deintercalated and reintercalated in Li_xCoO_2 during charge and discharge respectively, with a high reversibility up to x=0.5 and a reversible capacity of 140 mAh/g. A series of reversible phase transitions occurs upon cycling: the first associated to an insulator to metal transition ($0.70 < x < 0.94$) **[2]**, the second associated to a Lithium/Vacancy ordering and a monoclinic distortion ($x = ½$) **[3-4]**, the third associated to a staging between O3 and O1-type domains (the O1-type domain being obtained from the first through slab gliding) ($x \leq 0.33$) and the fourth associated to the formation of the O1 phase through slab gliding ($x = 0$) **[5-6]**. Here O3 and O1 indicate the different types of layered structures: the letter O indicates that the alkali ions occupy octahedral sites (P for trigonal prisms and T for tetrahedra) and the number gives the number of MO_2 slabs per hexagonal cell. When cycled at high voltage such as $x < 0.4$ in Li_xCoO_2, decreasing reversibility is observed due to larger structural modifications (slab gliding, volume change, etc.) **[7]**. Some authors have also mentioned possible Co migration (formation of spinel-type phase) and dissolution at high voltage **[8-9]**. In our group in ICMCB, overstoichiometry in lithium was also evidenced in $LiCoO_2$ with the formula $Li_{1+\delta}Co^{III}_{1-\delta}O_{2-\delta}$: trivalent cobalt ions in intermediate spin electronic configuration are present in MO_5 environment whereas lithium ions are present in excess in the transition metal sites. These defects were identified using especially ^7Li MAS NMR spectroscopy. Depending on the stoichiometry of "$LiCoO_2$" the Li_xCoO_2 phase diagram is modified, the presence of defects prevents the two first phase transitions mentioned just before **[10]**. The main drawbacks of $LiCoO_2$ to be considered for large batteries for electric vehicles and hybrid vehicles are the high price of Co and the safety concern, i.e. the thermal instability of Li_xCoO_2 in the charge state of the battery. Indeed at high potential most of the Co ions are at the Co^{4+} oxidation state, which is not stable above 200°C **[11-12]**. The thermal material decomposition induces a release of oxygen gas that reacts with the organic solvents of the electrolyte, generating further gas and pressure in the lithium-ion cells. Thus new positive electrodes materials have been studied for large batteries.

$LiNiO_2$ is described in the same space group as $LiCoO_2$ (R-3m) with a higher capacity than $LiCoO_2$, probably due to its lower voltage and smaller volume change: highly reversible cycling is possible up to x = 0.3 in Li_xNiO_2 in comparison with x = 0.4 in Li_xCoO_2 **[13-14]**. In fact, the ideal stoichiometry is difficult to control in $LiNiO_2$, because deficiency in lithium is often observed with the formation of $Li_{1-z}Ni_{1+z}O_2$. The deficiency in lithium is compensated by the presence of Ni^{2+} ions, in the slabs and in the interslab spaces such as $[Li_{1-z}Ni^{2+}_z]_{Interslab}[Ni^{2+}_zNi^{3+}_{1-z}]_{Slab}O_2$ **[15-16]**. The more deficient in lithium the material has, the more difficult the diffusion is. As Ni ions present in the interslab spaces block Li diffusion, it leads thus to a decreasing rate performance **[17]**. The control of the synthesis and structure of the lithium nickel oxide has thus been the goal of several studies before reaching the optimization of the 2nd generation of layered oxides as positive electrodes for Lithium-ion batteries. Partial substitution for nickel was shown to allow controlling the lamellar character of the structure (and thus diffusion) and optimizing cyclability and thermal stability in the charge state **[17-21]**. Co substitution for Ni was shown to promote ideal lamellar character as the smaller size of Co^{3+} ions versus Ni^{3+} ($r_i(Co^{3+})$ = 0.545 Å vs. $r_i(Ni^{3+})$ = 0.56 Å) destabilizes the presence of the larger Ni^{2+} ions ($r_i(Ni^{2+})$ = 0.69 Å) in the transition metal slabs **[22-25]**. Aluminum substitution for nickel was shown to stabilize the layered oxide in its charged state. The smaller size of the Al^{3+} ions ($r_i(Al^{3+})$ = 0.535 Å) helps to stabilize the Co^{4+} ions at higher temperature. Al^{3+} ions are stable in tetrahedral sites, the intermediate sites occupied during the phase transition from the layered structure to the spinel structure: that induces a slower degradation process of the layered oxide with oxygen loss upon increasing temperature **[26-27]**. According to these results $LiNi_{1-y-z}Co_yAl_zO_2$ was developed as the 2nd generation of layered oxides for positive electrodes and used in numerous applications like HEV **[28-30]**.

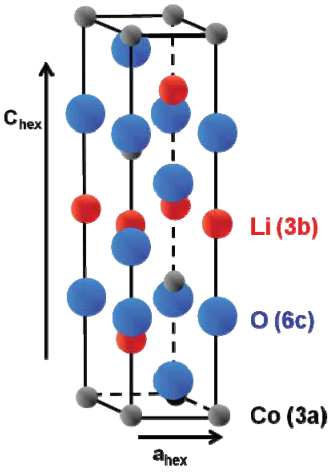

Fig. 1: Unit cell of $LiCoO_2$.

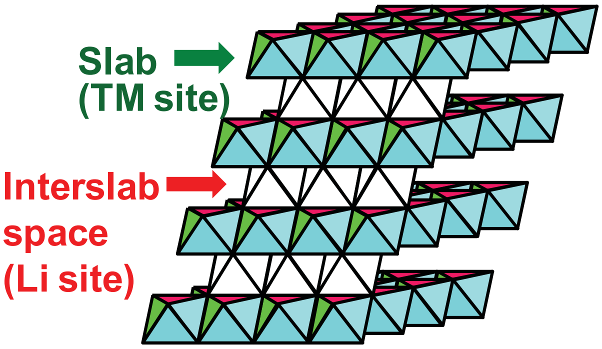

Fig. 2: Structural schematic view of $LiCoO_2$.

1. 2 - $LiNi_{1/3}Mn_{1/3}Co_{1/3}O_2$

More recently, $LiNi_{1/3}Mn_{1/3}Co_{1/3}O_2$ with smaller amount of Co than $LiCoO_2$ has been proposed for the first time by Ohzuku and coworkers as a very attractive candidate for new positive electrode, with especially a significantly improved thermal stability in the charge state (larger safety) **[31]**. Its structure is also described in the R-3m space group (as α-$NaFeO_2$), but on the contrary to $LiCoO_2$ and $LiNi_{1-y-z}Co_yAl_zO_2$ a cation ordering is observed between Ni, Mn and Co in the slabs leading to a $\sqrt{3}\times\sqrt{3}$ superstructure as shown in **Fig. 3** **[32]**. In $LiNi_{1/3}Mn_{1/3}Co_{1/3}O_2$ Ni, Mn and Co ions are present as Ni^{2+}, Mn^{4+} and Co^{3+} respectively. Ni^{2+} and Co^{3+} are oxidized up to Ni^{4+} and Co^{4+} in charge, they are reversibly reduced in discharge. Mn^{4+} does not participate to the reaction but they are at the origin of the very attractive properties of this layered oxide. Indeed, in the charge state a large amount of transition metal ions (Mn^{4+}) are stable even at high temperature inducing a stabilization at higher temperature (300°C vs. 230°C for $LiNi_{1-y-z}Co_yAl_zO_2$) **[31, 33-34]**. Then, as Mn does not participate to the redox processes Mn^{3+} with Jahn-Teller effect is not formed upon cycling. For these Mn-rich layered oxides manganese dissolution is not significant on the contrary to observations made for the Spinel $LiMn_2O_4$, for which Mn^{3+} dismutation is observed in Mn^{4+} and Mn^{2+}, that latter being soluble in the electrolyte. 200 mAh/g discharge capacity has been obtained for Li// $LiNi_{1/3}Mn_{1/3}Co_{1/3}O_2$ cells when charged up to 4.6V vs. Li^+/Li, with a good cyclability **[35-37]**.

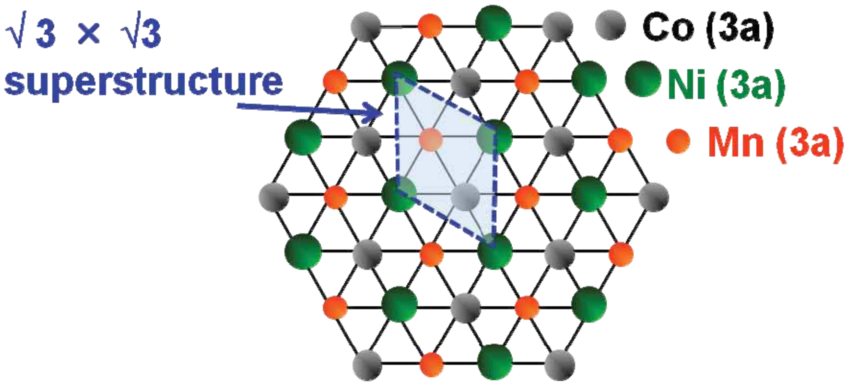

Fig. 3: Arrangement of metal ions in transition metal layers of $LiNi_{1/3}Mn_{1/3}Co_{1/3}O_2$.

2 – The spinel oxide $LiMn_2O_4$

$LiMn_2O_4$ with spinel structure has also been largely studied as a candidate at the positive electrode with the attractiveness that Mn is of lower cost than Co and Ni **[38]**. The structure of $LiMn_2O_4$ is described in the cubic Fd-3m space group. Li^+ ions occupy the 8a site, Mn^{3+} and Mn^{4+} the 16d site and O^{2-} the 32e site as shown in **Fig. 4**, with Mn ions in octahedral sites and Li ions in tetrahedral sites. As Li diffusion occurs in 3D paths build of 8a tetrahedral sites and

16c octahedral sites, its rate performance is excellent. Li//$LiMn_2O_4$ cells are characterized by two discharge plateaus at 3V vs. Li^+/Li and 4V vs. Li^+/Li, but the reversibility of the 3V plateau associated to the biphased reaction between $LiMn_2O_4$ and $Li_2Mn_2O_4$ is very limited because of large volume changes (6.4%) **[39]**. Thus only 1 mol Li in $LiMn_2O_4$ can be used for efficient charges and discharges. The most serious problem of $LiMn_2O_4$ is that Mn ions are dissolved into the electrolyte during the cycling, especially at high temperature **[40-41]**. The substitution of other metal ions to Mn such as Mg, Al, Zr and Ti can restrain the dissolution of Mn into solvents, but it still leads to decrease of capacity **[42-45]**.

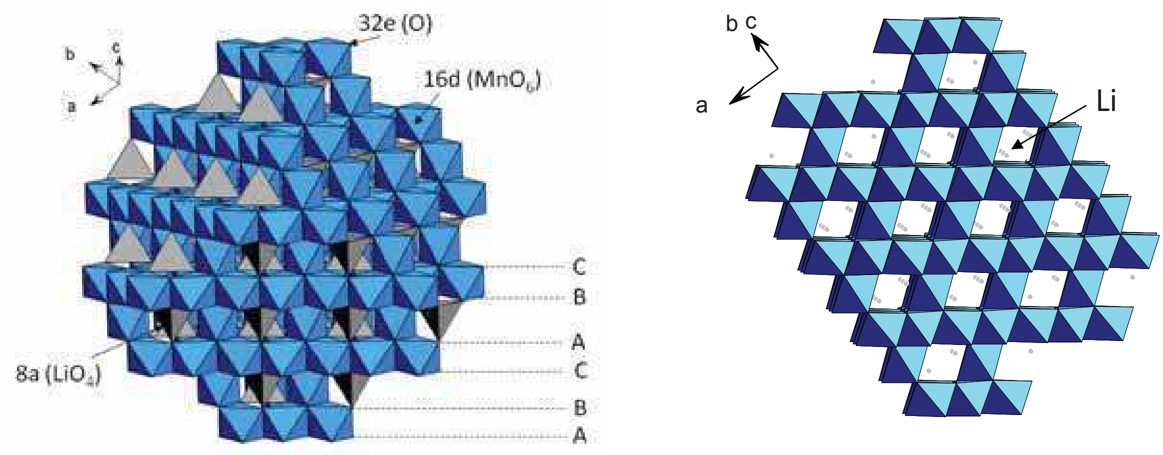

Fig. 4: Structural schematic views of $LiMn_2O_4$.

3 - Li excess layered oxides

In 2003, Dahn and coworkers have shown that lithium can be incorporated into the transition metal layers of $Li(Ni,Mn)O_2$-type phase, leading to a new family of layered oxides described with the general formula $Li(Li,Ni,Mn)O_2$ **[63]**. The same authors have also revealed that a long voltage “plateau” appears at 4.5V vs. Li^+/Li when Lithium cells using these Li-rich layered oxides at the positive electrode were overcharged. In the next discharge the cell capacity observed was shown to be very large (200-250 mAh/g) versus those observed for non-overlithiated layered oxides (just mentioned before). Following this discovery a strong interest was devoted to this series of compounds which was extended to $Li(Li,Ni,Co,Mn)O_2$-type phases. The analogy with the Li_2MnO_3 phase ($Li[Li_{1/3}Mn_{2/3}]O_2$) was also rapidly addressed.

The attractiveness of these Li-rich layered oxides for applications led to a considerable number of works to improve the material electrochemical properties and to understand the mechanism involved during the cycling of these materials. Indeed, surprisingly it was shown that lithium ions were possibly deintercalated at high voltage during the first charge despite all the transition metal ions were already oxidized at the tetravalent state. In the very first papers, it was assumed that lithium deintercalation occurs during the “plateau” simultaneously with oxygen gas evolution and formation of oxygen vacancies in the lattice **[57]**. In our group in ICMCB the densification mechanism was proposed to explain this behavior in the $Li_{1.12}Mn_{0.374}Ni_{0.374}Co_{0.132}O_2$ phase **[82]**.

In order to get more insight into the understanding of the mechanism involved in these overlithiated layered oxides a general study was carried out in relation with Toyota Motor Europe. Our studies were mainly focused on the $Li_{1.20}Mn_{0.54}Ni_{0.13}Co_{0.13}O_2$ phase which belongs to the $Li_2MnO_3.LiNi_{1/3}Mn_{1/3}Co_{1/3}O_2$ system with the 0.4 : 0.4 ratio, and which is on the contrary to that previously studied in our group rich in lithium and in manganese. The following points will be successively addressed in this manuscript:

- Synthesis, chemical and structural characterization
- Electrochemical behavior in different cycling conditions and for different samples
- In-depth characterization of materials obtained by chemical lithium deintercalation and reinsertion
- Structural modifications occurring upon cycling and studied by high resolution transmission electronic microscopy
- Redox processes followed in operando, during the two first cycles of the battery, by X-ray absorption spectroscopy

The combination of all the results obtained leads to a relevant model to explain the original behavior observed for these lithium and manganese-rich layered oxides.

In the following, a synthetic review of the most representative papers (from our point of view) published in the last few years is presented. It is organized by sub-classes of materials and also by properties being the most relevant for battery applications. Some papers were published during the last 3 years and are in agreement with our results.

3. 1 - Li_2MnO_3

The structure of Li_2MnO_3 is described in the monoclinic space group C2/m and can be also notated as $Li[Li_{1/3}Mn_{2/3}]O_2$ with 1/3 Li ions being located in the transition metal layers and surrounded by 6 Mn^{4+} ions as shown in **Fig. 5** and **6.** This cation ordering between Li and Mn leads to a $\sqrt{3}\times\sqrt{3}$ superstructure in the transition metal layers and, on the contrary to what was described for $LiNi_{1/3}Mn_{1/3}Co_{1/3}O_2$, to a correlation between the ordered slabs along the stacking axis **[46]**. This difference explains the change in the symmetry and space group from hexagonal R-3m to monoclinic C2/m. Slightly different Li_2MnO_3 materials can be obtained depending on the synthesis conditions. Various degrees of disorder, along the c-direction, in the stacking of the ordered $Li_{1/3}Mn_{2/3}$ sheets in Li_2MnO_3 are obtained with different synthesis temperatures and it is in fact difficult to obtain the material free of stacking faults **[47, 48]**. Li_2MnO_3 was also reported to contain small different domains of $LiMnO_2$ and $LiMn_2O_4$, either as intergrowths within the crystals of Li_2MnO_3 or as impurities **[49]**. Nevertheless, as shown by Baren et al. using high-angle annular dark-field imaging (HAADF) scanning transmission electron microscopy Li_2MnO_3 can also be obtained without any defect **[50]**.

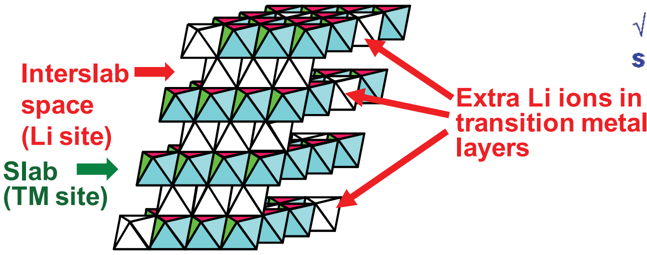
Interslab space (Li site)
Slab (TM site)
Extra Li ions in transition metal layers

Fig. 5: Structural schematic view of Li_2MnO_3.

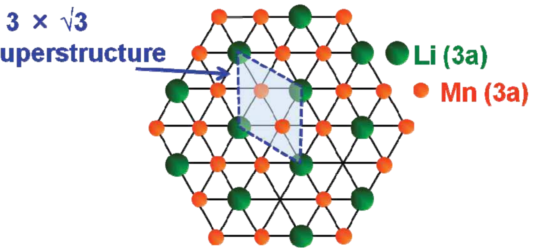

Fig. 6: Arrangement of metal ions in transition metal layers of Li_2MnO_3.

Li_2MnO_3 had been considered as electrochemically inactive **[51]**. But, it was shown more recently that acid treatments could make it active electrochemically **[52-54]**. The acid leaching of Li_2MnO_3 is accompanied with a Li^+/H^+ exchange **[55]**. γ-MnO_2 is formed as a final product when $[H^+] / [Li^+] = 1$ by acid treatment **[56]**. At high temperature (55°C) this exchange occurs in lithium cells exclusively upon charge through oxidation of the electrolyte: H^+ ions generated are exchanged with Li^+ ions to form $Li_{2-x}H_xMnO_3$. The presence of H^+ ions between the oxygen layers leads to changes in the stacking from O3 to P3, the latter being more stable for H^+ with the formation of dumbbell environments O - H - O. Then, the formation of this P3-type stacking through slab gliding promotes further Li removal with charge compensation through oxygen loss as if Li_2O was formed **[57]**. At room temperature Li removal is mainly compensated by oxygen loss.

Li_2MnO_3 with small particle size appears to be also active electrochemically **[58, 59]**. The charge-discharge capacity of Li_2MnO_3 gradually increases as its particle size decreases from 650 nm to 80 nm. Nevertheless, the first cycle efficiency is about 60-70 % regardless the size of particles. Composition and structural analyses of Li_2MnO_3 upon cycling indicated that Li ions are removed from both the Li and transition metal layers. Results from X-ray-Absorption Fine-Structure measurements suggest that the valence of Mn remains at 4^+ upon charge, but is reduced to 3^+ upon discharge. Lithium deintercalation is accompanied by oxygen loss, oxygen being the main gas detected **[59]**. Oxidation of the organic electrolyte also occurs with generation of protons that can be exchanged with lithium ions. At room temperature the first mechanism prevails, whilst at high temperature (55°C) the Li^+/H^+ exchange mechanism becomes more important **[60]**. A systematic first-principles calculation based on Density Functional Theory was carried out to discuss the redox processes involved in Li_2MnO_3 upon lithium deintercalation. The electronic structure of $Li_{2-x}MnO_3$ shows that manganese ions remain at the Mn^{4+} oxidation state and that the charge of deintercalated lithium ions is compensated by oxidation of oxygen **[61]**. The pinning of the manganese t_{2g} band at the top of the oxygen p band makes that latter available for oxidation and charge compensation for lithium deintercalation. During the charge, development of local spinel-like structure and disordering of Mn in Li_2MnO_3 are observed using Raman spectroscopy and XAS particularly at low lithium loadings (high potentials) **[62]**. Upon cycling, changes in the shape of the electrochemical curve with the formation of 3 and 4 V domains, suggesting transformation of Li_2MnO_3 to spinel structure. The formation of spinel phase is linked to Mn re-arrangement in the lattice and lowering of oxygen content **[62]**.

3. 2 - Li excess layered oxides of general formula $Li_{1+x}M_{1-x}O_2$ (M = Mn, Ni, Co)

3. 2. 1 - Pristine material

Lithium-rich layered oxides were reported by Dahn and coworkers to deliver high discharge capacity after a first charge over 4.5 V vs. Li^+/Li **[63]**. The most studied can be notated as $xLiMO_2$. yLi_2MnO_3 (M = Ni, Co, Mn, etc), nevertheless their formula is not restricted to this composition range. As expected for a solid solution XAFS measurements suggest that $(Li_{1/3}Mn_{2/3})$ is substituted for M in $LiMO_2$ **[64]**. Almost all the overlithiated materials are characterized by extra peaks between 20-30° ($2\theta_{Cu}$) in their XRD patterns, corresponding to cation ordering in transition metal layers **[63, 65]**. The common layered oxide structure is described in the space group R-3m. In these lithium and manganese rich layered oxide materials, the lithium ions present in excess in the transition metal layers are preferentially surrounded by Mn (as in Li_2MnO_3), leading to non random distribution of the cations that allows minimization of the strains within the lattice and local charge compensation **[66, 67]**. The presence of Co and Ni promotes the complexity of the cation distribution. Nevertheless, in these systems Ni, Co and Mn are most often present at the divalent, trivalent and tetravalent states respectively. Ni^{2+} is a large cation as Li^+ (0.69 Å and 0.72 Å respectively) whereas Co^{3+} and Mn^{4+} are small cations (0.545 Å and 0.53 Å respectively): Ni^{2+} and Li^+ (in excess in the slabs) are thus present in the α sites of the $\sqrt{3}\times\sqrt{3}$ superstructure and, Mn^{4+} and Co^{3+} occupy the β sites with α:β close to 1:2. Depending on the composition and on the large cations over small cations ratio homogeneity of these materials at the local scale can be more or less extended. Some researchers indicated that $xLi_2MnO_3.1\text{-}xLiMO_2$ can be nanocomposites build of domains with different structures (described either in the R-3m space group or in the C2/m space group) in **[68-71]**. On the other hand, Dahn reported that careful X-ray diffraction measurements of $Li[Ni_xLi_{(1/3-2x/3)}Mn_{(2/3-x/3)}]O_2$ and $Li[Cr_xLi_{(1-x)/3}Mn_{(2-2x)/3}]O_2$ samples suggested that these compounds are true solid solutions **[72]**. More recently Abraham and coworkers reported that $Li_{1.2}Mn_{0.4}Co_{0.4}O_2$ contains mostly Mn^{4+} in Li_2MnO_3 like atomic environments and Co^{3+} in $LiCoO_2$-like atomic environments, but intimately mixed over short length scale of 2-3 nm, resulting in homogeneous distribution (solid solution) over long range **[73, 74]**. However, depending on the composition, the cation ordering is not fully extended within the transition metal layers and thus along the c-axis. Then, even for extended ordering within the slabs, stacking faults can be observed along the c-axis **[65, 75]**.

3. 2. 2 – Charge - discharge mechanism

The first charge behavior is unique to Li-rich layered oxide. A long “plateau” appears after all transition metal ions reach the tetravalent state, then oxidation states of Mn, Ni, and Co do not change during the “plateau” **[76]**. Different models were considered by several groups so far to explain the charge and discharge mechanism involved in Li rich layered oxides.

First is the oxygen loss model: oxygen ions were removed as oxygen gas from the material on this high voltage “plateau” (~ 4.5 V vs. Li^+/Li) to compensate for lithium deintercalation. In this model, oxygen vacancies are formed within the lattice. Armstrong et al. measured oxygen gas generated from $Li[Ni_{0.20}Li_{0.20}Mn_{0.60}]O_2$ in the charge using gas chromatography **[77-78]**. However oxygen loss was not confirmed using weight loss measurement for $Li[Ni_{0.20}Li_{0.20}Mn_{0.60}]O_2$ by Y. -S. Hong, showing that controversial results (or interpretations) are reported in literature **[76]**.

Second is proton exchange model, the protons generated by electrolyte decomposition on the “plateau” during the first charge exchange with Li ions in the lithium-rich layered oxide **[57, 79]**. The amount of protons present in the material, as a result of the Li^+/H^+ exchange reaction during the 1st charge, was confirmed by Thermogravimetry Thermal Analysis coupled to Mass Spectrometry (TGA-MS) and was shown to increase with the cycling temperature. ^1H - Magic Angle spinning Nuclear Magnetic Resonance (MAS NMR) experiments were performed in our group in ICMCB to study electrodes of $Li_xNi_{0.374}Mn_{0.374}Co_{0.32}O_2$ obtained on the “plateau” during the 1st charge and it was clearly shown that proton exchange was systematically associated to the parasitic reaction of electrolyte degradation.

Third is densification model **[78, 80]**. The transition metal migration would occur from the outside to the inside of the particles on the "plateau", accompanied with oxygen loss at the surface. In this model, as the transition metal ions migrate filling the sites left vacant after Li deintercalation from the transition metal layers, the number of Li sites available is reduced after the 1st charge leading thus to a large irreversible capacity. A small expansion of c/a lattice ratio and a small increase in Li/Ni interlayer mixing were confirmed after the 1st cycle, indicating some cation migration in the structure **[81]**. Furthermore, very recently high-angle annular dark-field scanning transmission electron microscopy (HAADF-STEM) and selected-area electron diffraction (SAED) revealed a partial migration of the transition metal ions from the slabs to the interslab spaces during the 1st charge and discharge, leading to the formation of "Spinel derivative structure" **[82]**. The formation of this framework started from the beginning of the "plateau" during the 1st charge.

Forth model is oxygen participation in charge and discharge **[83]**. Experimental discharge capacity of 266 mAh/g is larger than 199 mAh/g, estimated from the oxidation of transition metal ions only during the 1st cycle and followed by XAS measurement. This result suggests that oxygen participates to the redox processes in charge and in discharge. However there is no clear evidence yet for this model.

Other charge and discharge models were also proposed. J. Kikkawa reported that oxygen ions in $Li_{1.2}Mn_{0.4}Fe_{0.4}O_2$ are removed from the material during the 1st charge to compensate for lithium deintercalation, then the extracted oxygen is partially reinserted into the material during the 1st discharge **[84]**. N. Yabuuchi reported that the overcapacity of $Li_{1.20}Co_{0.13}Ni_{0.13}Mn_{0.54}O_2$ could be partial explained by the surface reaction. Indeed the surface analysis confirms the formation of oxygen containing species such as lithium carbonate, which accumulate on the electrode surface during the discharge below 3.0 V vs. Li^+/Li **[85].** It is interesting to mention that Li insertion into the lithium-rich layered oxide $Li_{1.16}Ni_{0.40}Co_{0.06}M_{0.05}Mn_{0.33}O_2$ (M=Zr, Mg) can happen by the reduction of manganese or nickel cations (Li_2NiO_2) to divalent valence state, but below 1.5V vs. Li^+/Li **[70, 86]**

3. 2. 3 – Electrochemical properties (irreversible capacity, rate performance and cyclability)

3. 2. 3. 1 - Irreversible capacity

In the peculiar case of $LiNi_{1/2}Mn_{1/2}O_2$, which is not Li-rich but characterized by lithium in the transition metal layers due to a Li/M exchange of more than 8%, Grey and coworkers reported that lithium ions in the transition metal layers become unstable due to Li deintercalation from Li layers: Lithium ions nearby the vacancies in the Li layers move to the adjacent tetrahedral sites with no activation barrier. Higher potential is necessary to remove these lithium ions during the charge **[87]**. ^{6}Li MAS NMR spectra of materials recovered after the 1st cycle showed that only a reduced amount of Li ions could be intercalated back into the transition metal layers during the next discharge **[77]**, at least in the first few cycles **[66]**.

Transition metal migration in the 1st charge is also one possible cause for the large irreversible capacity observed for these Li-rich layered oxides $Li_{1+x}M_{1-x}O_2$, as in that case the number of available Li sites is reduced due to migration of transition metal ions to Li vacancies **[80, 81]**. The disappearance of XRD peaks corresponding to the cation ordering in the transition metal layers during the 1st cycle would also support the transition metal migration model **[77, 78]**. The surface modification with Al_2O_3, CeO_2, ZrO_2, SiO_2, ZnO_2, $AlPO_4$ and Li_3PO_4 reduces the irreversible capacity loss in the first cycle. These surface modifications would prevent oxygen loss from the lattice even during the 1st charge, resulting in less transition metal migration and less capacity loss **[88-90]**. Acid-treatment reduces the length of the “plateau” in the 1st charge associated to removal of Li and oxygen in the material, reducing the irreversible capacity of the initial charge and discharge cycle of the cells **[91, 92]**.

Some researchers reported on the mixtures of Li-rich layered oxides with other compounds, with the goal to intercalate reversibly in discharge the extra lithium ions that were deintercalated during the 1st charge: Lithium insertion hosts such as V_2O_5 **[93]**, $Li_4Mn_5O_{12}$ and LiV_3O_8 **[94]** were considered as co-positive electrode materials to reduce the large irreversible capacity observed at the end of the 1st cycle for Li-rich layered oxides. Mixtures of $Li_{1.20}Mn_{0.54}Co_{0.13}Ni_{0.13}O_2$ and V_2O_5 show excellent coulombic efficiency in the 1st cycle **[93]**.

3. 2. 3. 2 – Rate performance and cyclability

A rapid capacity fading is observed when these Li-rich layered oxides were charged above 4.5V vs. Li^+/Li at a constant current density of 20 mA/g; transmission electron microscopy (TEM) studies revealed the formation of micro-cracks at the crystal surface and the distortion of crystal periodicity. Pre-cycling treatment was shown to prevent the formation of defects and to significantly improve cycle performance: the batteries were successively charged and discharged with a gradual increase in the charge voltage limit (4.5 V vs Li^+/Li, 4.6 V etc.) **[95, 96]**. Formation of coatings with stable materials like Al_2O_3 **[97]**, $AlPO_4$, Al **[98]**, LiF **[99]**, Li_3PO_4 **[90]**, $LiCoPO_4$ **[100]**, etc. could improve the cycle performance by decreasing deterioration of the electrolyte at high voltage. The discharge capacity fading turned serious at higher Co contents, but it was significantly diminished with the decrease of Co content **[101]**. Koenig et al. reported that particles with internal gradients in transition metal composition were synthesized by coprecipitation to optimize the reversible capacity and cyclability, the material prepared with a core enriched in Ni for high capacity and a shell enriched in Mn for high stability showed excellent cyclability **[102]**.

The surface modification with $(NH_4)_2SO_4$ generates spinel defects near the surface and improves the rate performance due to higher electronic conductivity of spinel versus Li-rich layered oxide **[103]**. Nano-scaled $LiCoPO_4$ **[100]** and $LiNiPO_4$ **[104]** coating improve the rate capability. Carbon coating by thermal evaporation process also improves the rate performance and cyclability due to suppression of the SEI (Solid Electrolyte interface) formation **[105]**.

3. 2. 4 - Safety

Thermal stability of that type of materials was survey with differential scanning calorimetry (DSC) **[106]**. The thermal stability of Li-rich layered oxide materials is different depending on the synthesis methods, particle sizes, etc. The thermal decomposition process in presence of electrolyte occurs at about 205°C for the material recovered from the battery after $Li_{1.20}Mn_{0.54}Co_{0.13}Ni_{0.13}O_2$ was charged at 4.8V vs. Li^+/Li, occurring at lower temperature than when $LiCoO_2$ is charged at 4.3V. The reaction is highly exothermic (sharp peak associated to the heat flux). In fact the thermal stability of these materials after a deep charge would be lower or similar than that of normal layered oxides, despite the high concentration of stable Mn^{4+} ions. The coating with TiO_2, AlF_3, etc. is effective to delay the thermal decomposition **[107]**. The thermal stability of $Li_{1.2}Ni_{0.6}Co_{0.2}Mn_{0.2}O_{2+d}$ is almost the same as that of $LiCoO_2$ in a cell overcharged at 4.6V **[108]**.

3. 3 - Li-rich layered oxides $Li_{1+x}M_{1-x}O_2$ (M = Cr, Ru, Pt, Sn …) of original compositions

All the lithium ions present in $Li_{1.20}Mn_{0.40}Cr_{0.40}O_2$ with Mn^{4+} and Cr^{3+} could be deintercalated without oxygen participation as Cr is oxidized from Cr^{3+} to Cr^{6+}, as it was confirmed by XAS experiments. The irreversible capacity after the 1st cycle is still large and coulombic efficiency limited to 70%. These results show that small coulombic efficiency is not related to the oxygen loss process. Chromium ions have in fact to move reversibly between the regular octahedral sites from the R-3m-like lattice to interstitial tetrahedral sites during the charge and discharge processes **[109-111]**

Li_2RuO_3 **[112-114]**, Li_2PtO_3 **[115, 116]**, Li_2MoO_3 **[117]**, $Li_2Mn_{0.4}Ru_{0.6}O_3$ **[118]** and Li_2SnO_3 **[119]** have been reported as Li rich layered oxides. As Ru, Pt and Mo can be stable until high oxidation states such as +6, changes in the oxidation state of the transition metal ion can compensate for all Li ions deintercalated. In these cases, the "plateau" associated to oxidation of oxygen ions and/or oxygen loss is not observed during the 1st charge even if they have high coulombic efficiency in the 1st cycle as shown in **Fig. 7 [114]**.

Li_2NiO_3 synthesized under high pressure has similar structural properties as Li_2MnO_3 **[120, 121].** Its electrochemical performance are similar to those of Li_2MnO_3, the "plateau" with oxidation of oxygen ions appear in the 1st charge as shown in **Fig. 8**. The detail mechanism in charge and discharge of these materials is still not clear.

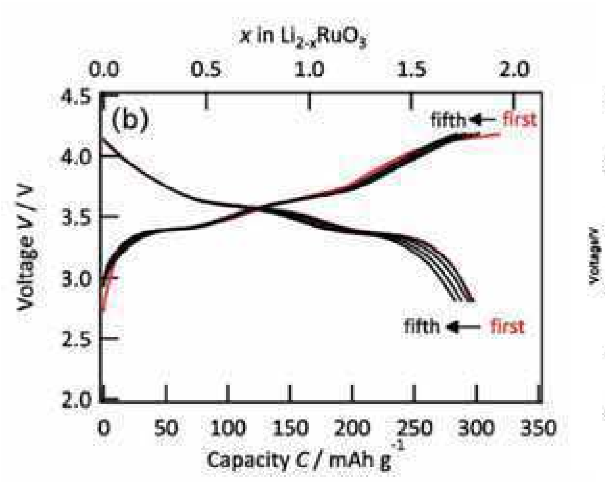

Fig. 7: Charge and discharge curves of Li_2RuO_3.

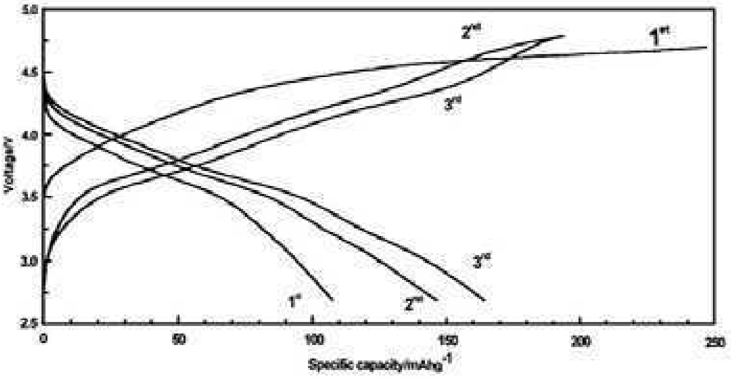

Fig. 8: Charge and discharge curves of Li_2NiO_3.

4 - References

[1] K. Mizushima, P. C. Jones, P. J. Wiseman and J. B.Goodenough, Mater. Res. Bull., 15 (1980) 783

[2] M. Ménétrier, I. Saadoune, S. Levasseur and C. Delmas, J. Mater. Chem., 9 (1999) 1135-1140

[3] J. N. Reimers and J. R. Dahn, J. Electrochem. Soc., 139 (1992) 2091

[4] T. Ohzuku and A. Ueda, J. Electrochem. Soc., 141 (1994) 2972

[5] X. Sun, X. Q. Yang, J. McBreen, Y. Gao, M.V. Yakovleva, X.K. Xing and M.L. Daroux, J. Power. Sources, 97-98 (2001) 274-276

[6] G. G. Amatucci, J. M. Tarascon, L. C. Klein, J. Electrochem. Soc., 143 (1996) 1114

[7] H. Wang, Y. -I. Jang, B. Huang, D. R. Sadoway, and Y.-M. Chiang, J. Electrochem. Soc., 146 (1999) 473-480

[8] Z. Wang, L. Liu, L. Chen, X. Huang, Solid State Ionics, 148 (2002) 335-342

[9] D. Aurbach, B. Markovsky, A. Rodkin, E. Levi, Y. S. Cohen, H. -J. Kim, M. Schmidt, Electrochimica Acta, 47 (2002) 4291-4306

[10] S. Levasseur, M. Ménétrier, Y. S. -Horn, L. Gautier, A. Audemer, G. Demazeau, A. Largeteau, and C. Delmas, Chem. Mater, 15 (2003) 348-354

[11] Y. Baba, S. Okada, J. Yamaki, Solid State Ionics 148 (2002) 311-316

[12] J. R. Dahn, E.W. Fuller, M. Obrovac, U. von Sacken, Solid State ionics 69 (1994) 265-270

[13] M. G. S. R. Thomas, W. I. F. David, J. B. Goodenough and P. Groves, Mater. Res. Bull., 20 (1985) 1137

[14] J. R. Dahn, U. Von Sacken, M. W. Juzkow, and H. Al-Janaby, J. Electrochem. Soc., 138 (1991) 2207

[15] A. Mendibourn, C. Delmas and P. Hagenmuller, Mater.Res.Bull., 19 (1984) 1383

[16] R. Kanno, H. Kubo, Y. Kawamoto, T. Kamiyama, F. Izumi, Y. Takeda, and M. Takano, J. Solid State Chem., 110 (1994) 216

[17] C. Pouillerie, L. Croguennec,; P. Biensan, P. Willmann; C. Delmas, J. Electrochem. Soc., 147 (2000) 2061 – 2069

[18] Y. Nishida, K. Nakane, T. Satoh, J. Power Sources 68 (1997) 561

[19] H. Arai, S. Okada, Y. Sakurai, J. Yamaki, J. Electrochem. Soc. 144 (1997) 3117

[20] S. H. Chang, S. Kang, S. Song, J. Yoon, J. Choy, Solid State Ionics, 86–88 (1996) 171.

[21] M. Guilmard, A. Rougier, M. Grune, L. Croguennec, C. Delmas, J. Power. Sources, 115 (2003) 305-314

[22] R. D. Shannon, Acta Crystallogr., Sect. A: Cryst. Phys., Diffr., Theor. Gen. Crystallogr. 32 (1976) 751

[23] C. Delmas, I. Saadoune, Solid State Ionics, 53–56 (1992) 370

[24] C. Delmas, I. Saadoune, A. Rougier, J. Power Sources 43–44 (1993) 595.

[25] A. Rougier, I. Saadoune, P. Gravereau, P. Willmann, C. Delmas, Solid State Ionics 90 (1996) 83.

[26] T. Ohzuku, A. Ueda, M. Kouguchi, J. Electrochem. Soc. 142 (1995) 4033

[27] T. Ohzuku, T. Yanagawa, M. Kouguchi, A. Ueda, J. Power Sources, 68 (1997) 131

[28] M. Guilmard ,C. Pouillerie, L. Croguennec, C. Delmas, Solid State Ionics, 160 (2003) 39

[29] C. J. Han, J. H. Yoon, W. I. Cho, H. Jang, J. Power Sources, 136 (2004) 132

[30] G. Hu, W. Liu, Z. Peng, K. Du, Y. Cao, J. Power. Sources, 198 (2012) 258-263

[31] N. Yabuuchi, T. Ohzuku, J. Power Sources 119–121 (2003) 171–174

[32] Y. Koyam, Y. Makimura, I. Tanaka, H. Adachi, and T. Ohzuku, J. Electrochem. Soc., 151 (2004) A1499

[33] I. Belharouak, Y. -K. Sun, J. Liu, K. Amine, J. Power Sources, 123 (2003) 247

[34] I. Belharouak, W. Lu, D. Vissers, K. Amine, Electrochem. Comm. 8 (2006) 329–355.

[35] N. Yabuuchi, Y. Makimura, T. Ohzuku, J. Electrochem. Soc. 154 (2007) A314

[36] K. M. Shaju, G.V. Subba Rao, B. V. R. Chowdari, Electrochim. Acta, 48 (2002) 145

[37] J. -M. Kim, H.-T. Chung, Electrochim. Acta, 49 (2004) 937

[38] M. M. Thackeray, P. J. Johnson, L. A. Picciotto, P. G. Bruce, J. B. Goodenough, Mater. Res. Bull. 19 (1984) 179

[39] T. Ohzuku, M. Kitagawa and T. Hirai, J. Electrochem. Soc., 137 (1990) 769

[40] D. Aurbach, M. D. Levi, K. Gamulski, B. Markovsky, G. Salitra, E. Levi, U. Heider, L. Heider, R. Oesten, J. Power Sources, 81 (1999) 472-479

[41] Y. Y. Xia, Y. H. Zhou, M. Yoshio, J. Electrochem. Soc., 144 (1997) 2593-2600

[42] R. J. Gummow, A. Dekock, M. M. Thackeray, Solid State Ionics, 69 (1994) 59-67

[43] K. –S. Lee, S. –T. Myung, H. J. Bang, S. Chung, Y. –K. Sun, Electrochimica Acta, 52 (2007) 5201-5206

[44] Y. J. Lee, S. H. Park, C. Eng, J. B. Parise, C. P. Grey, Chemistry of Materials, 14 (2002) 194-205

[45] L. Hernan, J. Morales, L. Sanchez, J. Santos, Solid State Ionics, 118 (1999) 179-185

[46] P. Strobel and B. L. Andron, J. Solid State Chem., 75 (1998) 90-98

[47] J. Breger, M. Jiang, N. Dupre, Y. S. Meng, Y. Shao-Horn, G. Ceder, C.P. Grey, J. Solid State Chem., 178 (2005) 2575-2585

[48] A. Boulineau, L. Croguennec, C. Delmas, F. Weill, Solid State Ionics, 180 (2010) 1652-1659

[49] S.-H. Park, Y. Sato, J. -K. Kim, Y. -S. Lee, Materials Chemistry and Physics, 102 (2007) 225-230

[50] J. Baren, C. H. Lei, J. G. Wen, S. -H. Kang, I. Petrov, and D.P. Abrahaham, Adv. Mater., 22 (2010) 1122–1127

[51] V. Massarotti, D. Capsoni, M. Bini, and G. Chiodelli, J. Solid State Chem., 131 (1997) 94-100

[52] C. S. Johnson, S. K. Korte, J. T. Vaughey, M. M. Thackeray, T. E. Bofinger, Y. Shao-Horn, S. A. Hackney, J. Power. Sources, 81-82 (1999) 491-495

[53] Y. Shao-Horn, Y. Ein-Eli, A. D. Robertson, W. F. Averill, S. A. Hackney, and W. F. Howard, Jr., J. Electrochem. Soc., 145 (1998) 16

[54] C. S. Johnson, J. Power Sources, 165 (2007) 559-565

[55] Y. Paik, C. P. Grey, C. S. Johnson, J. -S. Kim, and M. M. Thackeray, Chem. Mater. 14 (2002) 5109-5115

[56] W. Tang, H. Kanoh, X. Yang, and K. Ooi, Chem. Mater., 12, (2000) 3271

[57] A. D. Robertson and P. G. Bruce, Chem. Mater., 15 (2003) 1984-1992

[58] G. Jain, J. Yang, M. Balasubramanian, and J.J. Xu, Chem. Mater., 17 (2005) 3850-3860

[59] D. Y. W. Yu, K. Yanagida, Y. Kato, and H. Nakamura, J. Electrochem. Soc., 156 (2009) A417-A424

[60] A. R. Armstrong, A. D. Robertson, and P. G. Bruce, J. Power Sources, 146 (2005) 275

[61] Y. Koyama, I. Tanaka, M. Nagao, R. Kanno, J. Power. Sources, 189 (2009) 798-801

[62] D. Y. W. Yu and K. Yanagida, 158 (9) (2011) A1015-1022

[63] Z. Lu, L.Y. Beaulieu, R. A. Donaberger C. L. Thomas, and J. R. Dahn, J. Electrochem. Soc., 149 (2002) A778-791

[64] K. Nnumata, C. Sakai, S. Yamanaka, Solid State Ionics, 117 (1999) 257-263

[65] F. Weill, N. Tran, L. Croguennec, C. Delmas, J. Power Sources, 172 (2007) 893-900

[66] C. P. Grey and N. Dupre, Chem. Rev, 104 (2004) 4493-4512

[67] W-S Yoon, S. Iannopollo, C. P. Grey, D. Carlier, J. Gorman, J. Reed, and G. Ceder, Electrochemical and Solid-State letters, 7 (2004) A167-A171

[68] D. Kim, J. Gim, J. Lim, S. Park, J. Kim, Mater. Res. Bull., 45 (2010) 252-255

[69] K. A. Jarvis, Z. Deng, L.F. Allard, A. Manthiram, and P.J. Ferreira, Chem. Mater. 23 (2011) 3614-3621

[70] S. Sivaprakash, S. B. majumder, Solid State Ionics, 181 (2010) 730-739

[71] C. Pan, Y. J. Lee, B. Ammundsen, and C. P. Grey, Chem. Mater., 14 (2002) 2289-2299

[72] Z. Lu, Z. Chen, and J. R. Dahn, Chem. Mater., 15 (2003) 3214-3220

[73] J. Bareno, M. Balasubramanian, S. H. Kang, J. G. Wen, C.H. Lei, S. V. Pol, I. Petrov, and D. P. Abraham, Chem. Mater., 23 (2011) 2039-2050

[74] J.G. Wen,, J. Bareno, C.H. Lei, S.H. Kang, M. Balasubramanian, I. Petrov, D.P. Abraham, Solid State Ionics, 182 (2011) 98-107

[75] Y. S. Meng, G. Ceder, C. P. Grey, W. -S. Yoon, M. Jiang, J. Breger, and Y. Shao-Horn, Chem. Mater., 17 (2005) 2386-2394

[76] Y. -S. Hong, Y. J. Park, K.S. Ryu, S.H. Change and M. G. Kim, J. Mater. Chem., 14 (2004) 1424-1429

[77] M. Jiang, B. Key, Y.S. Meng, and C.P. Grey, Chem. Mater. 21 (2009) 2733-2745

[78] R. Armstrong, M. Holzapfel, P. Novak, C. S. Johnson, S. -H. Kang, M. M. Thackeray, P. G. Bruce, J. Am. Chem. Soc, 128 (2006) 8694

[79] A.D. Robertson and P.G. Bruce, 7(9) (2009) A294-A298

[80] N. Tran, L. Croguennec, M. Menetrier, F. Weil, P. Biensan, C. Jordy, and C. Delmas, Chem. Mater, 20 (2008) 4815-4825

[81] C. R. Fell, K. J. Carroll, M. Chi, and Y.S. Meng, J. Electrochem. Soc., 157 (11) (2010) A1202-A1211

[82] A. Ito, K. Shoda, Y. Sato, M. Hatano, H. Horie, Y. Ohsawa, 196 (2011) 4785-4790

[83] A. Ito, Y. Sato, T. sanada, M. Hatano, H. Horie, Y. Ohsawa, 196 (2011) 6828-6834

[84] J. Kikkawa, T. Akita, M. Tabuchi, K. Tatsumi and M. Kohyama, J. Electrochem. Soc., 158 (6) (2011) A760-768

[85] N. Yabuuchi, K. Yoshii, S.-T. Myung, I. Nakai, and S. Komaba, J. A. m. Chem. Soc., 133 (2011) 4404

[86] A. Pramanik, C. Ghanty, S.B. Majumder, Solid State Sciences 12 (2010) 1797-1802

[87] C. P. Grey, W.-S. Yoon, J. Reed, and G. Ceder, 7 (9) (2004) A290-A293

[88] Y. Wu, A. Manthiram, Solid State Ionics, 180 (2009) 50-56

[89] Y. Wu and A. Manthiram, Electrochem. Solid-State Lett., 9 (5) (2006) A221-224

[90] J. R. Croy, M. Balasubramanian, D. Kim, S. -H. Kan and M. M. Thackeray, Chem. Mater., 23 (2011) 5415−5424

[91] C. S. Johnson, J. -S. Kim, C. Lefief, N. Li, J. T. Vaughey, M. M. Thackeray, Electrochem. Commun., 6 (2004) 1085-1091

[92] J. -S. Kim, C. S. Johnson, J. T. Vaughey, M. M. Thackeray, J. Power Sources, 153 (2006) 258-264

[93] J. Gao, J. Kim, A. Manthiram, Electrochem. Commun., 11 (2009) 84-86

[94] J. Gao, A. Manthiram, J. Power Sources, 191 (2009) 644-647

[95] A. Ito, D. Li, Y. Ohsawa, Y. Sato, J. Power Sources, 183 (2008) 344-346

[96] A. Ito, D. Li, Y. Sato, M. Arao, M. Watanabe, M. Hatano, H. Horie, Y. Ohsawa, 195 (2010) 567-573

[97] Y. S. Jung, A. S. Cavanagh, Y. Yan, S. M. George and A. Manthiram, J. Electrochem. Soc., 158 (2011) A1298-A1302

[98] J. Liu, B. Reeja-Jayan, A. Manthiram, J. Phys. Chem. C, 114 (2010) 9528

[99] L. Croguennec, J. Bains, M. Menetrier, A. Flambard, E. Bekaert, C. Jordy, P. Biensan, and C. Delmas, J. Electrochem. Soc., 156 (5) (2009) A349-A355

[100] B. Liu, Q. Zhang, S. He, Y. Sato, J. Zheng, D. Li, 56 (2011) 6748-6751

[101] S. J. Jin, K. S. Park, M. H. Cho, C. H. Song, A. M. Stephan, K. S. Nahm, Solid State Ionics, 177 (2006) 105-112

[102] G. M. Koenig, Jr. I. Belharouak, H. Deng, Y. -K. Sun, and K. Amine, Chem. Mater., 23 (2011) 1954-1963

[103] D. Y. W. Yu, K. Yanagida and H. Nakamura, J. Electrochem. Soc., 157 11 (2010) A1177-1182

[104] S. -H. Kang and M. M. Thackeray, Electrochem. Commun., 11 (2009) 748-751

[105] J. Liu, Q. Wang, B. Reeja-Jayan, A. Manthiram, Electrochem. Commun., 12 (2010) 750-753

[106] Z. Lu, D. D. MacNeil and J. R. Dahn, Electrochem. Solid-State Lett., 4 (11) (2001) A191-A194

[107] H. Deng, I. Belharouak, C. S. Yoon, Y. -K. Sun, and K. Amine, J. Electrochem. Soc., 157 (10) (2010) A1035-A1039

[108] C. Gan, X. Hu, H. Zhan, Y. Zhou, Solid State Ionics, 176 (2005) 687-692

[109] J. McBreen and M. Balasubramanian, JOM, (2002) 25

[110] B. Ammundsen, J. Paulsen, I. Davidson, R. -S. Liu, C. -H. Shen, J. -M. Chen, L. -Y. Jang, and J. -F. Lee, J. Electrochem. Society, 149(4) (2002) A431-436

[111] M. Balasubramanian, J. McBreen, I. J. Davidson, P. S. Whitfield and I. Kargina, J.

Electrochem. Soc., 149 (2002) A176-A184

[112] A. M. Stux, K. E. Swider-Lyons, J. Power Sources, 165 (2007) 635-639

[113] H. Kobayashi, R. Kanno, Y. Kawamoto, M. Tabuchi, O. Nakamura, M. Takano, Solid State Ionics 82 (1995) 24-31

[114] Y. Zheng, S. Taminato, Y. Xu, K. Suzuki, K. Kim, M. Hirayama, R. Kanno, J. Power. Sources, 208 (2012) 447-451

[115] S. Okada, J. -I. Yamaki, K. Asakura, H. Ohtsuka, H. Arai, S.-I. Tobishima, Y. Sakurai, Electrochimica Acta, 45 (1999) 329-334

[116] K. Asakura, S. Okada, H. Arai, S.-I. Tobishima, Y. Sakurai, J. Power Sources, 81-82 (2009) 388-392

[117] H. Kobayashi, M. Tabuchi, M. Shikano, Y. Nishimura, H. Kageyama, T. Ishida, H. Nakamura, Y. Kurioka, R. Kanno, J. Power Sources, 81-82 (1999) 524-529

[118] D. Mori, H. Sakaebe, M. Shikano, H. Kojitani, K. Tatsumi, Y. Inagume, J. Power Sources, 196 (2011) 6934-6938

[119] M. Inagaki, S. Nakai and T. Ikeda, J. Nuclear Materials, 160 (1988) 224-228

[120] E. Shinova, E. Zhecheva, R. Stoyanova, G. D. Bromiley, J. Solid State Chem., 178 (2005) 1661-1669

[121] R. Stoyanova, E. Zhecheva, R. Alcantara, J. L. Tirado, G. Bromiley, F. Bromiley, T. Boffa Ballaran, Solid State Ionics, 161 (2003) 197-204

Chapter I

Summary of the thesis

Chapter I – Summary of the thesis

I. 1 - Overview of Li rich layered oxides for Li-ion batteries (General introduction part)

Lithium-ion batteries are used for portable devices since Sony Co. commercialized them in 1991. $LiCoO_2$ has been widely applied in lithium-ion batteries as a positive electrode. $LiCoO_2$ has layered structure composed of Li, transition metal and oxygen layers. Li-rich oxides also have layered structure and exhibit higher capacity than normal layered oxides as Li ions are located not only in Li layers but also in transition metal layers. $LiCoO_2$ cannot be deintercalated below x = 0.4 in Li_xCoO_2 as irreversible structural change occurs in these conditions, its capacity is limited to 160 mAh/g. On the other hand, after large Li deintercalation in $Li_{1+z}M_{1-z}O_2$, Li-rich layered oxides deliver higher capacity than other positive electrodes. Li-rich layered oxides have been largely studied since Dahn reported in 2002 that they deliver very attractive capacity after being charged over 4.5 V vs. Li^+/Li. The reports published from the beginning were concerned by the mechanism occurring during the first cycle, i.e. by the long voltage "plateau" during the first charge. They compared the electrochemical properties of materials with different chemical compositions $LiMO_2$-Li_2MnO_3 (M = Ni, Co and Mn). Recently many reports focus on the optimization for applications with for instance the use of coatings to improve the cycling properties. Thermal stability of Li-rich layered oxide would be safer than normal layered oxides due to the presence of stable Mn^{4+} in the charge state, but it is in fact strongly related to their chemical compositions. Rate performance is also improved with formation of coatings and controlling the morphology of particles. Transition metal ions migration in Li layers in the 1st charge would obstruct Li diffusion in Li layers, but there are no reports about this effect. Predictable Mn dissolution into solvents during the cycling has also not been reported so far.

The charge and discharge mechanism of Li-rich layered oxides is different from that of other layered oxides. A long "plateau" in the 1st charge would be associated to their large capacity, and several reports mentioned the possible mechanisms occurring during this "plateau". The followings are the main mechanisms considered during the plateau in the 1st charge.

[Oxygen loss reaction I]: Oxygen ions migration

Oxygen ions move from inside to the surface of the particle where they are oxidized as oxygen gas. Oxygen vacancies are distributed within the structure.

[Oxygen loss reaction II]: Transition metal migration

Oxygen ions from the surface are oxidized and oxygen evolution occurs, simultaneously transition metal ions migrate from outside to inside through vacancies formed by removal of Li ions in the transition metal layers. Densification of the lattice occurs.

An ion-exchange model was also proposed to explain the irreversible “plateau”: proton generated due to decomposition of electrolyte in charge would be exchanged with Li in the material; In fact this model would not be observed considering the results obtained by ^{1}H-MAS-NMR for materials recovered in charge. The two different oxygen loss mechanisms are still arguable. Considering the 1st model, oxygen ions with large ionic radius would diffuse with difficulty within the material, and even if it was possible, Ni^{4+} and Mn^{4+} are not stable in the MO_5 environments formed after that oxygen loss. Considering the 2nd model volume is shrunk due to transition metal migration and oxygen loss, with a decrease of the remaining Li sites. This decrease of available Li sites leads to capacity loss and can thus not explain the large capacity observed for these Li-rich layered oxides.

In this work, we have studied the charge and discharge mechanism occurring upon cycling in lithium batteries of $Li_{1.20}Mn_{0.54}Co_{0.13}Ni_{0.13}O_2$, which can be also written as 0.4 $LiNi_{1/3}Mn_{1/3}Co_{1/3}O_2$ - 0.4 Li_2MnO_3, with a high discharge experimental capacity over 270 mAh/g.

I. 2 - Results

I. 2.1 - Properties of the pristine material (Chapter II)

$Li_{1.20}Mn_{0.54}Co_{0.13}Ni_{0.13}O_2$ phases synthesized at 800, 900 and 1000°C were confirmed to have very similar compositions, structures (in the average and local scale) and electrochemical properties with several analyses such as ICP, magnetic measurement, XRD, neutron diffraction, electron diffraction, Raman and ^{7}Li MAS NMR. Neutron diffraction measurement was performed for $Li_{1.20}Mn_{0.54}Co_{0.13}Ni_{0.13}O_2$ synthesized at 1000°C to confirm the cation distribution. The Rietveld refinement of neutron diffraction data leads to the following distribution $(Li_{0.98}Ni^{II}_{0.02})(Li_{0.22}Mn^{IV}_{0.54}Ni^{II}_{0.11}Co^{III}_{0.13})O_2$. 0.02 mol Ni ions are distributed in the Li layers because of their ionic radius of 0.69 Å, similar to ionic radius of Li 0.72 Å. Electron diffraction analysis of $Li_{1.20}Mn_{0.54}Co_{0.13}Ni_{0.13}O_2$ synthesized at 1000°C was performed in order to get information on the cation ordering. Extra spots (with weak brightness) appear as dividing the distances between the main spots (with strong brightness) into three parts as shown in **Fig. I. 1a**. Their presence indicates the formation of a $\sqrt{3}a_{hex} \times \sqrt{3}a_{hex}$ superstructure and Li ions are ordered regularly in the transition metal layers as shown in **Fig. I. 1b**. The results of XRD and neutron diffraction analyses performed for $Li_{1.20}Mn_{0.54}Co_{0.13}Ni_{0.13}O_2$ suggested that the stacking of the ordered layers along the c axis would change every few atomic layers. As the results of several analyses with electron diffraction, neutron diffraction, Raman, magnetic measurement and HAADF-STEM, $Li_{1.20}Mn_{0.54}Co_{0.13}Ni_{0.13}O_2$ is shown to be a solid solution and not made of separated domains of Li_2MnO_3 and $LiNi_{1/3}Mn_{1/3}Co_{1/3}O_2$ as reported by other researchers. Ordering of the cations in the transition metal layers is strongly related to the chemical composition. Ideal ordering with $\sqrt{3}a_{hex} \times \sqrt{3}a_{hex}$ superstructure in the transition metal layers leads to two different sites for the cations, the larger sites are surrounded by six smaller sites with a ratio of 1:2 between the large and the small sites. Li_2MnO_3 is characterized by the ideal ratio of (Li^+; large cations)/(Mn^{4+}; small cations) =1/2, an extended ordering is thus observed in the transition metal layers with $\sqrt{3}a_{hex} \times \sqrt{3}a_{hex}$ superstructure and even along the c axis. $(Li_{0.98}Ni^{II}_{0.02})(Li_{0.22}Mn^{IV}_{0.54}Ni^{II}_{0.11}Co^{III}_{0.13})O_2$ is also characterized by the ratio (Li^+, Ni^{2+}; large cations) / (Co^{3+}, Mn^{4+}; small cations) equal to 1/2, and thus $Li_{1.20}Mn_{0.54}Co_{0.13}Ni_{0.13}O_2$ has a composition such as an extended cation ordering can be stabilized in the transition metal layers The presence of two different cations in each sub-site probably explain the limited ordering along the c-axis.

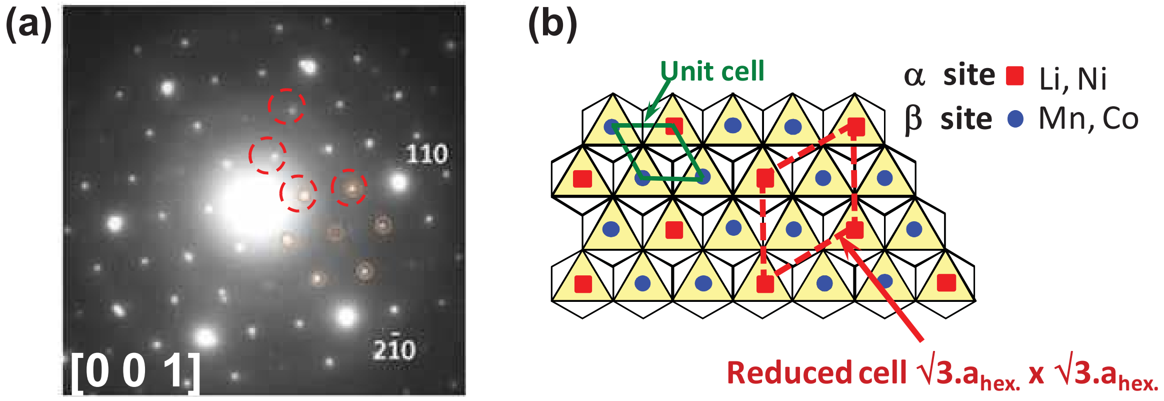

Fig. I. 1: (a) Electron diffraction pattern of $Li_{1.20}Mn_{0.54}Co_{0.13}Ni_{0.13}O_2$ and (b) representation of an ordered transition metal layer.

I. 2. 2 - Mechanism upon charge and discharge: structural changes observed (Chapter III)

The charge and discharge curves of $Li_{1.20}Mn_{0.54}Co_{0.13}Ni_{0.13}O_2$ synthesized at 800, 900 and 1000°C are shown in **Fig. I. 2**. 1.08 mol Li ions were deintercalated during the 1st charge from $Li_{1.20}Mn_{0.54}Co_{0.13}Ni_{0.13}O_2$ synthesized at 1000°C and 0.86 mol Li ions were reinserted during the next discharge. Supposing that oxygen loss occurred during the 1st charge according to the "oxygen loss reaction I" with oxygen ions migration and formation of oxygen vacancies, almost all MO_6 environments would be changed to MO_5 and it is known that Mn^{4+} and Ni^{4+} ions are not stable into MO_5 environments. Then, considering the "oxygen loss reaction II" mechanism, with transition metal migration and densification of the lattice, a decrease of the number of Li sites available is observed: only 0.78 mol Li can be inserted during the next discharge. The experimental value of 0.90 mol Li inserted can not be explained considering this model only. Here, the large capacity obtained could be explained from a theoretical point of view by a combination between the two models but as already mentioned the main cations present in the material in the charge state (Mn^{4+} and Ni^{4+}) are not stable in MO_5 environments. Thus we propose the oxygen participation to the redox process, with oxygen oxidation in charge and oxygen reduction in discharge.

XRD measurement was performed to study the material recovered during the 1st cycle and especially to determine the structural changes occurring during the 1st cycle. Lattice parameters change during the 1st cycle but no formation of spinel-like structure is observed as shown in **Fig. I. 3a-b**. The intensity of the extra-peaks corresponding to the cation ordering in the transition metal layers decreases during the 1st charge and is not recovered in the next discharge as also shown in **Fig. I. 3c**. It indicates at least that there is a partial loss of the ordering in the transition metal layers during the 1st cycle. Each XRD line splits into two lines during the 1st cycle, and this splitting is remained after the 1st cycle as indicated by arrows in **Fig. I. 3d**. As the pristine material before charge is a solid solution without any separation between domains of Li_2MnO_3 and $LiNi_{1/3}Mn_{1/3}Co_{1/3}O_2$, this result shows that a phase separation occurs during the 1st charge. $Li_{1.20}Mn_{0.54}Co_{0.13}Ni_{0.13}O_2$ was prepared with different particle sizes in order to study further this phase separation in details. It was shown that the ratio between "the two phases" formed during the first charge on the "plateau" evolves depending on the particle size and surface area: the amount of *phase 2* with smaller $c_{hex.}$ lattice parameter increases with a decrease of particle size and an increase of surface area. As a result, during the "plateau" in the 1st charge *phase 2* with smaller $c_{hex.}$ lattice parameter is probably formed at the surface of the particles whereas the main phase with larger $c_{hex.}$ lattice parameter (*phase 1*) would be observed within the bulk. *Phase 1* would be associated to a reversible participation of oxygen to the redox processes whereas *phase 2* would be associated to oxygen loss at the surface and densification of the host structure. **Fig. I. 4a** shows the cycling curves obtained for lithium cells with $Li_{1.20}Mn_{0.54}Co_{0.13}Ni_{0.13}O_2$ synthesized at 1000°C as positive electrode material: the 1st, 2nd, 10th, 50th and 100th charges and discharges. The shape of the charge and discharge curves evolves continuously during the cycles, as even more clearly highlighted by the differential curves *dQ/dV = f(V)* given in **Fig. I. 4b**. During the first cycles all the redox processes involved during lithium deintercalation and reintercalation occur above 3.2 V *vs.* Li^+/Li, with (after the 1st charge) two main potential ranges in charge and in discharge as pointed out by the two dotted lines *A* and *B*. Upon further cycling the redox processes involved partially shift to lower voltages as shown by line *C* (down to 2.75 V *vs.* Li^+/Li in discharge), with the disappearance of the intermediate potential process (line *B*) and maintenance of the higher potential one (line *A*). These results suggest a continuous structural modification of the material during the cycles, with in addition a continuous change in the redox couples involved in the lithium (de)intercalation reactions: manganese ions might participate more and more to the redox processes. As shown in **Fig. I. 5**, whatever the number of cycles the material recovered at the end of the discharge is a mixture of *"two phases"*. With an increasing number of cycles the heterogeneity of the material increases as revealed by the larger broadening of the X-ray diffraction lines. The amount of *phase 2* (smaller $c_{hex.}$) increases versus that of *phase 1* (larger $c_{hex.}$) upon cycling.

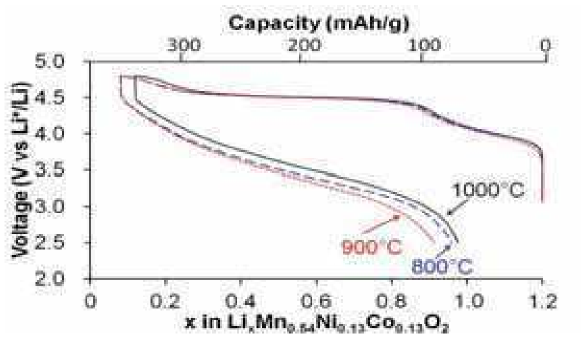

Fig. I. 2: The 1st cycle curves obtained at a rate of C/20 for different Li// $Li_xMn_{0.54}Co_{0.13}Ni_{0.13}O_2$ cells.

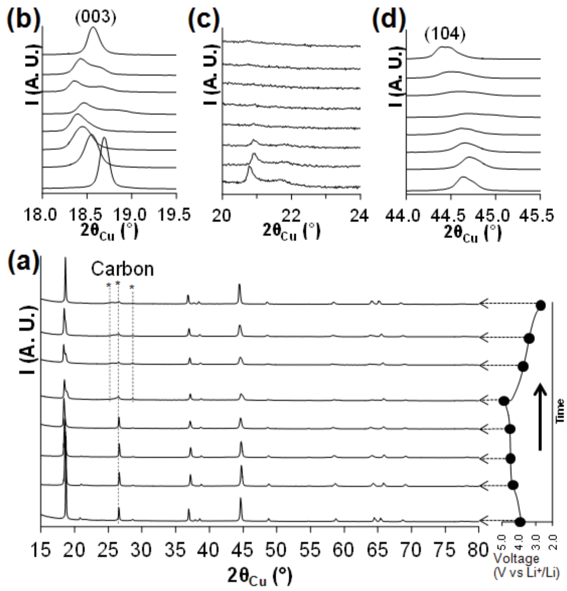

Fig. I. 3: (a) X-ray diffraction patterns of $Li_{1.20}Mn_{0.54}Co_{0.13}Ni_{0.13}O_2$ recovered during the 1st cycle at different states of charge and discharge. A typical electrochemical curve is given on the right part of the figure in order to indicate the lithium composition of the material studied. (b) Detailed XRD data in the 18 - 19.5° ($2\theta_{Cu}$) angular range, (c) in the 20-24° ($2\theta_{Cu}$) angular range, and (d) in the 44 - 45.5° ($2\theta_{Cu}$) angular range.

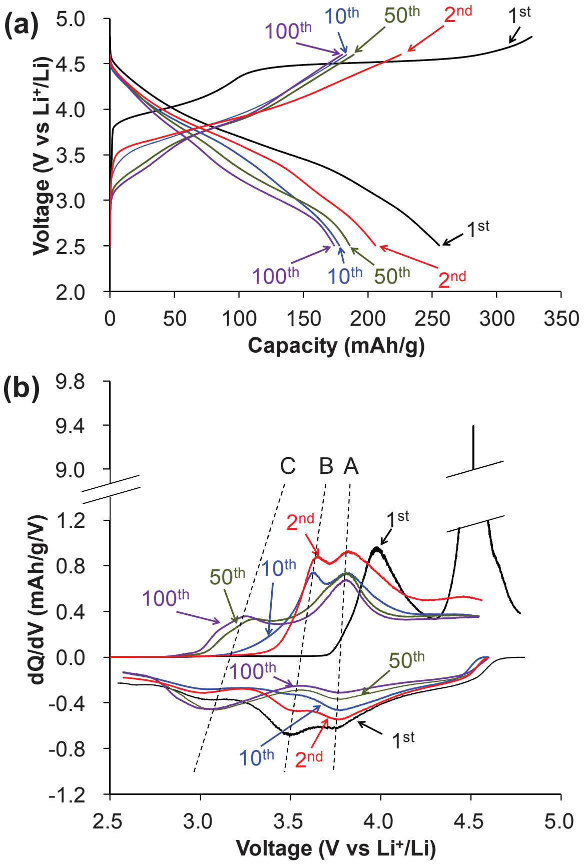

Fig. I. 4: (a) Comparison of the 1st, 2nd, 10th, 50th and 100th charge-discharge curves obtained for Li//$Li_{1.20}Mn_{0.54}Co_{0.13}Ni_{0.13}O_2$ cells with $Li_{1.20}Mn_{0.54}Co_{0.13}Ni_{0.13}O_2$ prepared at 1000°C. (b) Corresponding differential curves dQ/dV = f(V).

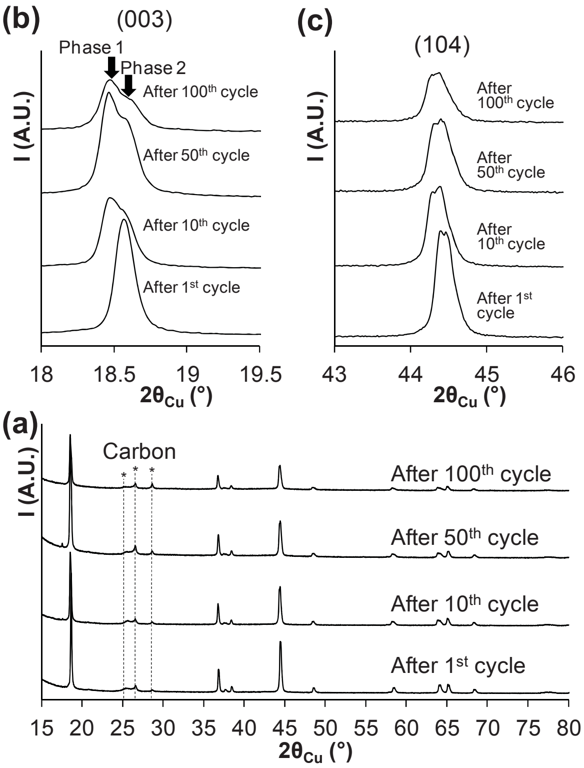

Fig. I. 5: X-ray diffraction patterns of $Li_{1.20}Mn_{0.54}Co_{0.13}Ni_{0.13}O_2$ synthesized at 1000°C and recovered from the batteries after the 1st, 10th, 50th and 100th cycle (a); detailed XRD data in the 18–19.5° ($2\theta_{Cu}$) range (b) and in the 43-46° ($2\theta_{Cu}$) range (c).

I. 2. 3 - Mechanism upon charge and discharge: redox processes and structural changes

I. 2. 3. 1 - Study of the redox processes with XAS measurement carried out *in operando* (Chapter IV)

The redox processes involved during the 1st cycle of Li//$Li_{1.20}Mn_{0.54}Co_{0.13}Ni_{0.13}O_2$ cells were studied with XAS measurements performed in operando. Changes in the oxidation state of Ni, Co and Mn were studied from the shift of XANES spectra and the determination of the M-O distances from EXAFS spectra recorded at the Ni, Co and Mn K-edges. The oxidation states of Ni, Co and Mn in $Li_{1.20}Mn_{0.54}Co_{0.13}Ni_{0.13}O_2$ were determined to be Ni^{2+}, Co^{3+} and Mn^{4+}. During the 1st charge before the "plateau", Ni^{2+} and Co^{3+} are oxidized to Ni^{4+} and Co^{4+} with the deintercalation of 0.39 mol Li. During the "plateau" in the 1st charge, oxidation states of Ni, Co and Mn do not change despite 0.64 mol Li are deintercalated. In the first discharge, Ni^{4+} and Co^{4+} are reduced to Ni^{2+} and Co^{3+} as expected with the insertion of 0.39 mol Li, and Mn ions were expected to be reduced whereas they are almost not participating to the redox processes during the first discharge, but also during the second cycle. As shown in **Fig. I. 6**. the M-O distance remains almost constant and smaller (or equal) to that observed in the pristine material, whereas with a reduction to Mn^{3+} an increase of the M-O distance would have been expected. Therefore, the redox reaction during the 1st cycle of $Li_{1.20}Mn_{0.54}Co_{0.13}Ni_{0.13}O_2$ could not be explained by only the oxygen loss model as it would imply directly during the first discharge a significant participation of Mn to the redox processes. As the oxidation state of Mn cannot be determined precisely using XAS, we decided to perform other analyses such as magnetic measurements and redox titrations to support the smaller participation of Mn to the redox processes than expected considering the oxygen loss models (either with formation of oxygen vacancies or with densification of the lattice).

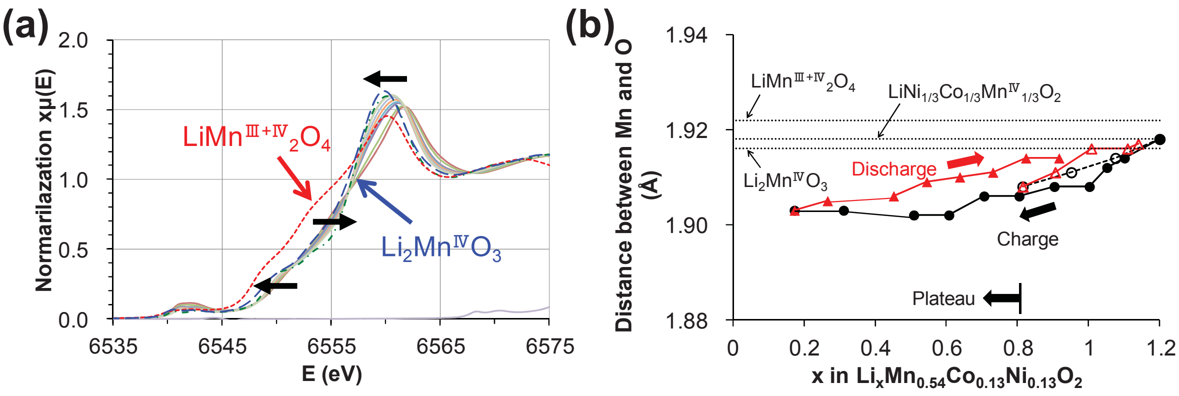

Fig. I. 6: (a) XANES spectra recorded at the Mn K-edge, in operando, during the 1st discharge of Li//$Li_{1.20}Mn_{0.54}Co_{0.13}Ni_{0.13}O_2$ cells, (b) the corresponding M-O distances determined from EXAFS spectra obtained at the Mn K-edge.

I. 2. 3. 2 – In depth characterization of the material recovered after chemical Li (de)intercalation (Chapter V)

The materials prepared from $Li_{1.20}Mn_{0.54}Co_{0.13}Ni_{0.13}O_2$ by chemical Li deintercalation with NO_2BF_4 and chemical Li reinsertion with LiI have rather similar chemical composition, oxidation state for each transition metal ion, structural properties and, as shown in **Fig. I. 7,** electrochemical performance than the material recovered after the 1st electrochemical cycle. The materials thus obtained are attractive to perform specific analyses such as density measurements and neutron diffraction as they do not contain any carbon and binder. The oxidation state of Mn and the amount of oxygen in the material prepared by chemical Li deintercalation and reinsertion were estimated combining redox titration by iodine, magnetic measurement, neutron diffraction and volume density measurement. The following chemical compositions were estimated from the results of these analyses for the material recovered after chemical Li deintercalation and reinsertion:

I. Redox titration with iodine combined with chemical analyses:

$Li_{1.03}\mathbf{Mn^{3.9+}}_{0.54}Co_{0.13}Ni_{0.13}\mathbf{O_{1.90}}$

II. Magnetic measurement combined with chemical analyses:

$Li_{1.03}\mathbf{Mn^{3.7+}}_{0.54}Co_{0.13}Ni_{0.13}\mathbf{O_{1.84}}$

III. Neutron diffraction: $Li_{1.03}\mathbf{Mn^{3.8+}}_{0.54}Co_{0.13}Ni_{0.13}\mathbf{O_{1.86}}$

Volume density was shown to be between that of $Li_{1.03}Mn^{3.0+}_{0.54}Co_{0.13}Ni_{0.13}O_{1.64}$ supposing complete oxygen loss and densification and that of $Li_{1.03}Mn^{4+}_{0.54}Co_{0.13}Ni_{0.13}O_{1.92}$ supposing no oxygen loss. All these results show that oxidation state of Mn ions is higher than that expected supposing one or the other of the oxygen loss models, in good agreement with the results obtained by XAS. We propose thus that these phenomena are intimately linked to oxygen participation to the redox processes.

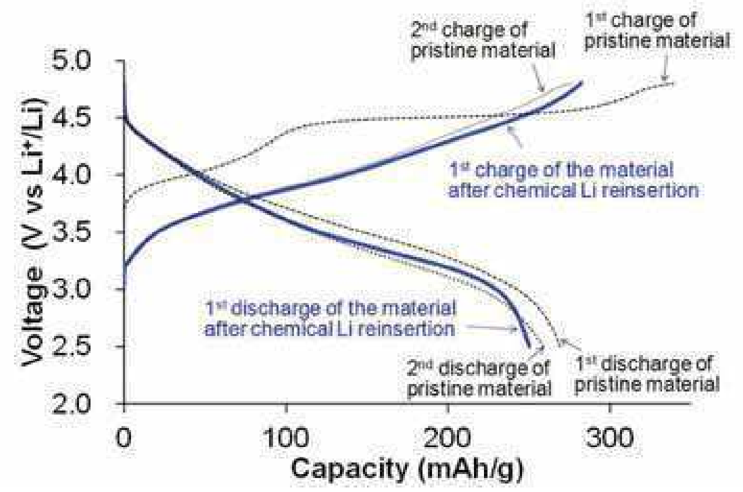

Fig. I. 7: Comparison of the charge and discharge curves obtained during the the 1st and 2nd cycles of lithium batteries using the pristine material $Li_{1.20}Mn_{0.54}Co_{0.13}Ni_{0.13}O_2$ as positive electrode (dotted black lines) with those obtained during the 1st cycle of lithium batteries using the material recovered after chemical Li deintercalation and reinsertion as positive electrode (continuous blue lines).

I. 2. 3. 3 – Study of the local structural changes using HAADF-STEM and nanodiffraction (Chapter VI)

HAADF-STEM and nano electron diffraction were performed to characterize the pristine material, the materials recovered from the batteries after the 1st cycle, with and without the "plateau", and the material prepared by chemical Li reinsertion after chemical Li deintercalation to observe local structural changes in the particles. HAADF-STEM images obtained for the pristine material clearly show that the alternance of two white dots and one dark dot. In Li_2MnO_3, in some crystallographic direction, there is alternance of two Mn and one Li atoms. In our materials the slab ordering results from the presence of 2/3 of small cations (0.54Mn + 0.13Co) and 1/3 large cations (0.20Li + 0.13Ni). Therefore, one can consider that the dark dots corresponding to columns of Li and Ni ions while the two bright dots corresponds to Mn and Co ions in the transition metal layers, as shown in **Fig. I. 8**. This ordering is in good agreement with the results of electron diffraction. Moreover, the stacking of the ordered slabs along the $c_{hex.}$ axis clearly changes every few layers as expected from the results of XRD and neutron diffraction reported in Chapter II. It indicates that transition metal layers are rotated of 60° within the *ab* plane along the $c_{hex.}$ axis every few layers without modification of the oxygen packing. In the cycled materials, the structure observed for the pristine material is still maintained in the bulk of the particle while spinel-type defects are observed at the surface of the particle as shown in **Fig. I. 9**. These spinel-type defects are the results of transition metal ions migration from the transition metal layers to the Li layers. In addition to these defects, at the surface of the particles we observed also migration of transition metals into the vacancies formed by Li deintercalation in the transition metal layers during the "plateau" in the 1st charge. These different structures in the bulk and near the surface can explain the different phases observed by ex-situ XRD measurement during the 1st cycle in Chapter III.

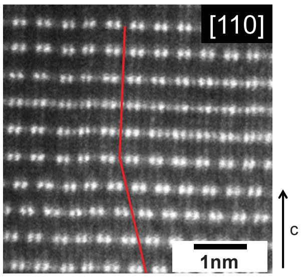

Fig. I. 8: STEM image of $Li_{1.20}Mn_{0.54}Co_{0.13}Ni_{0.13}O_2$.

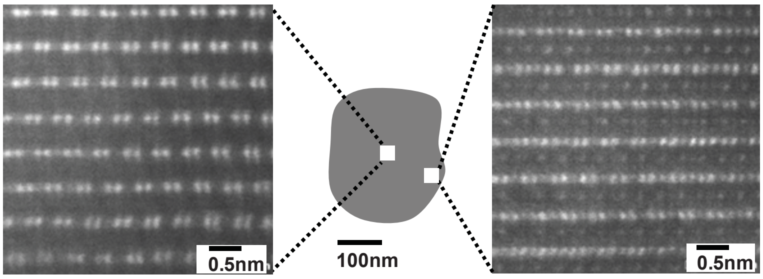

Fig. I. 9: HAADF-STEM images of the material obtained after chemical Li reinsertion in a material previously chemically deintercalated, in the bulk (left) and at the surface (right) of a particle.

I. 3 - Summary of $Li_{1.20}Mn_{0.54}Co_{0.13}Ni_{0.13}O_2$

Neutron diffraction was performed to characterize the structure of $Li_{1.20}Mn_{0.54}Co_{0.13}Ni_{0.13}O_2$ and especially to determine the cation distribution between the slabs and the interslab spaces. 0.02 mol Ni ions were shown to be present in the Li layers, as the cation distribution was determined to be $(Li_{0.98}Ni^{II}_{0.02})(Li_{0.22}Mn^{IV}_{0.54}Ni^{II}_{0.11}Co^{III}_{0.13})O_2$.

$Li_{1.20}Mn_{0.54}Co_{0.13}Ni_{0.13}O_2$ exhibits $\sqrt{3}a_{hex} \times\sqrt{3}a_{hex}$ superstructure in the transition metal layers in good agreement with a ratio of ½ for (large cations; Li^+, Ni^{2+})/(small cations; Co^{3+}, Mn^{4+}). The transition metal layers are rotated of 60° every few layers along the $c_{hex.}$ axis as shown by electron diffraction and HADDF-STEM. $Li_{1.20}Mn_{0.54}Co_{0.13}Ni_{0.13}O_2$ was confirmed combining several characterization tools to be a solid solution without separated domains between Li_2MnO_3 and $LiNi_{1/3}Mn_{1/3}Co_{1/3}O_2$.

During the 1st charge before the “plateau”, Ni^{2+} and Co^{3+} are oxidized to Ni^{4+} and Co^{4+}, whereas Mn^{4+} is not oxidized. During the “plateau”, Ni^{4+}, Co^{4+} and Mn^{4+} are not oxidized. Then in discharge, Ni and Co are reduced to Ni^{2+} and Co^{3+}, whereas Mn participates less than expected (considering oxygen loss) to the redox processes. Oxygen ions present at the surface of the crystallites are oxidized and then released as oxygen gas during the “plateau” inducing the densification due to migration of transition metal ions from the surface to the bulk. The densification being more difficult in the bulk than at the surface, there is also a same tendency of oxygen oxidation in the bulk. Oxygen ions in the bulk are thus oxidized but remain in the bulk without oxygen loss. In fact there is no really two phases but a continuous modification. These two different reactions during the “plateau” in the 1st cycle promote the formation of a composition distribution that we can describe schematically as two different phases: *phase 1* with a larger $c_{hex.}$ lattice parameter in the bulk where oxygen ions are oxidized without oxygen loss and *phase 2* with smaller $c_{hex.}$ lattice parameter in the outer part of particles with oxygen loss and densification of the lattice. *Phase 2* would gradually increase versus *Phase 1* upon cycling but XRD analysis of the material recovered after 100 cycles has shown that it was still a mixture of two phases.

We thus propose that oxygen participates to the redox processes, within the bulk without oxygen loss but with oxygen oxidation and at the surface with oxygen loss and densification of the host structure. In fact, according to the electronic structure of these Li and Mn-rich materials the *d* levels of Mn would be at the top of the *p* levels of oxygen making that upon oxidation electrons are removed from the anion levels.

Chapter II

Characterization of $Li_{1.20}Mn_{0.54}Co_{0.13}Ni_{0.13}O_2$

$Li_{1.20}Mn_{0.54}Co_{0.13}$ $Ni_{0.13}$ O_2 with different particle sizes as attractive positive electrode materials for lithium-ion batteries: insights into their structure

H. Koga, L. Croguennec, P. Mannessiez, M. Ménétrier, F. Weill, L. Bourgeois, M. Duttine, E. Suard, and C. Delmas,

J. Phys. Chem., 116(2012)13497-13506

Chapter II – Characterization of $Li_{1.20}Mn_{0.54}Co_{0.13}Ni_{0.13}O_2$

II. 1 - Introduction

Rechargeable lithium-ion batteries are the most promising systems for portable energy storage. The layered oxide $LiCoO_2$ is mainly used as positive electrode material for high capacity batteries developed for mobile devices; nevertheless, due to the high cost and possibly limited availability of Co, as well as safety issues, it cannot be considered in large scale batteries for automotive applications. $LiNi_{1/3}Mn_{1/3}Co_{1/3}O_2$ with less Co has been shown to be an attractive alternative to $LiCoO_2$ with excellent thermal stability in the charged state, despite a slightly smaller capacity when cycled in the same voltage window **[1]**. More recently, a lot of research groups focused their interest on systems such as $Li[Ni_xLi_{(1/3-2x/3)}Mn_{(2/3-x/3)}]O_2$ and $(1\text{-}x)LiMO_2.xLi_2MnO_3$ (M = Ni, Co, Mn) due a significant increase in their reversible capacity with a large capacity retention at high voltage as compared to other layered oxides **[2-3]**. Li_2MnO_3 is one of the end members for both systems: it was previously announced to be electrochemically inactive **[4-5]**, but formation of small particles was shown to promote fast transport properties and a reversible capacity over 200 mAh/g **[6-9]**. The $(1\text{-}x)LiMO_2.xLi_2MnO_3$ system (M = Ni, Co, Mn) can deliver a unique large capacity up to over 250 mAh/g after a first charge above 4.5V vs. Li^+/Li **[10]**. This system is characterized by the presence of Li^+ ions in the transition metal site and also, as shown by the $\sqrt{3}a_{hex} \times \sqrt{3}a_{hex}$ superstructure, by a tendency to cation ordering in these slabs in order to minimize the structural strains and to optimize the charge distribution **[11-13]**. Note that the extent of this ordering in the slabs and along the c-axis is highly dependent on the composition **[14]**. Controversies still remain about the structure of these materials: Is there formation of a complete solid solution between $LiMO_2$ (M = Ni, Co, Mn) and Li_2MnO_3 or of local domains of both types **[15-16]**.

Our group has focused its interest on $Li_{1.20}Mn_{0.54}Co_{0.13}Ni_{0.13}O_2$ (that can also be written as $0.4LiNi_{1/3}Mn_{1/3}Co_{1/3}O_2.0.4Li_2MnO_3$) because of its high capacity. The aim of this chapter is to get more insight in the structural description of this very attractive material, from the long range to the local scale. Its composition and structure are characterized combining chemical interest to investigate if differences in the local structure of the pristine materials are at the origin of these differences observed upon cycling. Note that first electrochemical results are also given in this chapter.

II. 2 - Experimental

Various samples of "$Li_{1.20}Mn_{0.54}Co_{0.13}Ni_{0.13}O_2$" were obtained by a sol-gel method from an aqueous solution of $Li(CH_3COO).H_2O$ (99 % Aldrich), $Mn(CH_3COO)_2.4H_2O$ (99 % Aldrich), $Co(CH_3COO)_2.4H_2O$ (99 % Fluka), $Ni(CH_3COO)_2.4H_2O$ (99 % Aldrich) and Glycolic acid (99 % Fluka) as chelating agent. This mixture was prepared with the 1.20 / 0.54 / 0.13 / 0.13 / 0.2 molar ratio and its PH value was adjusted to 2.0 through the addition of HNO_3 (68 % Prolabo). The gel thus obtained after complete water evaporation at 80°C was dried at 120°C for 10 h in air. A first thermal treatment of the gel was performed at 500°C during 5 h in air, and an intermediate grinding of the powder was then carried out before a final thermal treatment at high temperature during 5 h in air: the high temperature thermal treatment was performed at 800°C, 900°C or 1000°C. Note that the temperature of the thermal pre-treatment was chosen according to results given by TGA-DTA analyses (see further) and defined as 500°C for the full decomposition of the acetate precursors.

TGA-DTA analyses were performed using an SDT Q600 V3.8 Build 51 equipment to get more insight into the synthesis reaction. Two types of experiments were performed: either the gel obtained after complete water evaporation and drying at 120°C during 10 h was heated from 25°C to 1200°C under oxygen at 200°C / hour, or the powder obtained after the thermal pre-treatment at 500°C during 5 h in air was heated also in air first at a very high rate (800°C / hour) up to 800°C and then at 100°C / hour up to 1200°C.

An X-ray diffraction (XRD) study was also carried out *in situ* during the thermal treatment of the powder recovered just after the thermal pre-treatment at 500°C, in order to follow the material's formation and degradation. This study was performed under air using a PANalytical X'Pert Pro diffractometer equipped with an X'Celerator detector (real time multiple strip detector) and Co Kα radiation, in the 15 – 80° ($2\theta_{Co}$) range with steps of 0.017° ($2\theta_{Co}$) at a constant counting time of 1s. The heating and cooling rates were 4°C/min. and 10°C/min. respectively, and patterns were recorded during temperature steps at 25°C, 500°C, then every 50°C up to 800°C (6 patterns), every 20°C up to 1000°C (10 patterns), every 1 h up to 10 h at 1000°C (10 patterns), upon cooling every 100°C down to 500°C (5 patterns) and finally at 25°C.

Acquisition of XRD patterns for structural determination was achieved using a Siemens D5000 diffractometer equipped with a detector using energy discrimination and Cu Kα radiation, in the 10 – 80 ° ($2\theta_{Cu}$) angular range with steps of 0.02° ($2\theta_{Cu}$) at a constant counting time of 15s. The refinement of the XRD data by the Le Bail and Rietveld methods were performed using the Fullprof software **[17]**. The background was defined through a linear interpolation between a set of background points whereas the profile was described taking into account a pseudo-Voigt function. Whatever the structural model considered, a first refinement was always performed by the Le Bail method (only the cell parameters and profile parameters were refined) before the refinement of the structural parameters by the Rietveld method (atomic positions, site occupancies and atomic displacement parameters).

Chemical analyses were performed using inductively coupled plasma spectrometry after complete dissolution of the powders into an acidic solution; this allows determining the Li, Ni, Mn and Co contents and thus the Li/M ratio. Redox titrations were also carried out in order to determine the transition metal average oxidation state. The samples were hydrothermally dissolved at 40 °C overnight in a PTFE container in an aqueous solution of HCl and KI, then the solution obtained was titrated with $Na_2S_2O_3$ (0.01 M) for oxidized iodine produced upon reduction of all transition metals to the divalent state in solution. These redox titrations were carried out at least twice and a good reproducibility of the results was obtained. Combination of chemical analyses and redox titrations allowed us proposing a chemical formula such as $Li_{1+x}M_{1-x}O_2$ for these materials considering a stoichiometric layered oxide (i.e. without any oxygen or cation vacancies in the lattice).

Magnetic measurements were performed under a magnetic field of 500 Oe as a function of temperature (between 4 and 300K) using a Super-conducting Quantum Interference Device (SQUID) (quantum design MPMS-5S).

Raman scattering measurements were performed with a Horiba Jobin Yvon Labram HR-800 micro-spectrometer. Spectra were recorded using the 514.5 nm excitation wavelength of an Ar^+ laser, with a power adjusted to ca. 100 µW in order to avoid any degradation of the sample. No specific sample preparation was needed.

^{7}Li MAS NMR spectra were recorded using a Bruker Avance III spectrometer at 39 MHz in a 2.35 T magnet, with a standard Bruker 2.5 mm probehead spinning at 30 kHz. A synchronized Hahn echo sequence was used with a 1.2 µs 90° pulse, a 33.33 µs (one rotor period) interpulse delay and a 2 s recycle delay.

The electron diffraction study was carried out using a JEOL 2000FX microscope, equipped with a double tilt specimen stage, at an accelerating voltage of 200 kV. Prior to the observation, a suspension was obtained by grinding the material in hexane, a droplet of this suspension being deposited on a formvar carbon film supported on a copper grid. Electron diffraction experiments were carried out on many crystallites and very reproducible results were observed. The particles studied were chosen as isolated as possible.

Neutron diffraction was performed using the D2B beam line at ILL (Institut Laue-Langevin) in Grenoble (France). The diffraction pattern was collected in transmission mode at room temperature with a wavelength of 1.593610 Å in the [0-160]° angular range using an 0.05°

(2θ) step with an accumulation time of 10 hours. The sample was contained in an 8 mm diameter vanadium tube. Due to the geometry of the neutron diffractometer, it was necessary to correct the absorption in order to take into account a decrease of the experimental diffracted intensity compared to the expected one, through the μR factor (R the radius of the vanadium cylinder and μ the linear absorption factor). μR was found to be equal to 1.03.

The electrochemical properties of the prepared materials were tested using CR2325 coin cells with lithium metal as a counter electrode at 25 °C. The positive electrodes consisted of a mixture of 80 wt.% of active materials, 10 wt.% of carbon black / graphite (1:1) and 10 wt.% of polyvinylidene difluoride (PVdF) binder in solution in NMP cast on an aluminum foil. The electrodes were pressed at 40 MPa after drying at 80 °C overnight. The cells were assembled in an argon filled glove box with the electrolyte 1M $LiPF_6$ dissolved in a mixture of propylene carbonate (PC), ethylene carbonate (EC), and dimethyl carbonate (DMC) 1:1:3 by volume. The electrochemical measurements were conducted at a C/20 constant current (C corresponding to the theoretical exchange of one electron in 1 h) between 2.5-4.8 V vs. Li^+/Li.

II. 3 - Results and discussion

II. 3. 1 - Effect of the thermal treatment on the material's formation and degradation

Fig. II. 1a gives, for two different gels (obtained in similar conditions, *i.e.* recovered as described in detail in the experimental part after their drying in air at 120°C for 10 h), the changes in the weight and heat flow as a function of temperature. First, it can be observed that a very good reproducibility is obtained. A 62% weight loss occurs below 500°C, it is associated to the decomposition of acetates and nitrates: note that this experimental value is in rather good agreement with the one expected theoretically which is 68.9%. The small discrepancy can probably be attributed to a partial evaporation of HNO_3 during the drying at 120°C for 10 h. Above 500°C the weight loss is very small. This first TGA-DTA experiment allowed setting the synthesis conditions and especially choosing the temperature of the thermal pre-treatment (500°C) required to achieve a full decomposition of the precursors. **Fig. II. 1b** shows additional results obtained from the thermal treatment of the sample pre-treated at 500°C for 5 h. A small weight loss (< 2%) occurs at high temperature, it is associated to an endothermic reaction which could be due to Li_2O loss occurring above 800°C. The amount of Li_2O thus lost from 800°C to 1200°C was estimated to be 0.057 mol. for 1 mol. of "$Li_{1.20}Mn_{0.54}Co_{0.13}Ni_{0.13}O_2$". This second experiment highlights the instability of the layered oxide versus lithium and oxygen loss at high temperature and implies that attention has to be paid to the real stoichiometry of the materials formed depending on the synthesis conditions. The temperature parameter will be carefully considered in the following with thermal treatments performed at 800°C, 900°C or 1000°C.

In order to get further insight in the material's formation and degradation at high temperature, an *in situ* XRD study was performed during the thermal treatment of the material obtained after the thermal pre-treatment at 500°C. **Fig. II. 2a** shows the XRD patterns collected in the angular range 15° – 80° ($2\theta_{Co}$) upon heating and cooling in the temperature range [25°C - 1000°C], selected enlargements are given in **Fig. II. 2b-e** in order to highlight the main changes observed. In addition, **Fig. II. 3** gathers selected XRD patterns for easier comparison. The main diffraction lines observed at 25°C, except for the extra broad and small intensity peaks observed between 23 and 28° ($2\theta_{Co}$), can be indexed based on an α-$NaFeO_2$-type structure described using a hexagonal unit cell (space group *R-3m*). Between 500°C and 800°C, even if almost no change in composition is observed as deduced from TGA-DTA experiments, significant changes occur in the XRD patterns. First, all the main diffraction lines sharpen upon heating up to 800°C, in good agreement with an increase of the powder crystallinity, but also with an increased ordering of the cations between the slab and the interslab space (as shown by the increasing intensity ratio between the *(003)* and *(104)* lines). Then, between 800°C and ~ 940°C, the lamellar phase is modified with slight changes in composition (see **Fig. II. 1b**) and with significant changes in the relative intensity of the extra lines observed in the 23 and 28° ($2\theta_{Co}$) angular range and their global sharpening (**Fig. II. 2c**); as discussed in more details in the following, these changes support an extension of the cation ordering within the slabs and of the ordering of their stacking along the c-axis **[18]**. Additional peaks appear at 940°C and reveal the formation of a spinel-type phase (indexed in the *Fd-3m* space group); their intensities and positions change with temperature, supporting an increase in the quantity of the spinel-type phase upon heating but also changes in its composition. **Fig. II. 2b-e** highlights this phase transformation occurring upon increasing temperature from the layered structure to the spinel one: above 940°C, the lamellar phase tends to disappear to the profit of the spinel-type phase whereas it is recovered upon cooling under air (only partially in these conditions actually, since a mixture of phases is still observed after cooling down to 25°C). These results strengthen the fact that attention has to be paid to the nature of the material formed: depending on the synthesis conditions, a single lamellar phase or a mixture between lamellar and spinel-type phases can be formed.

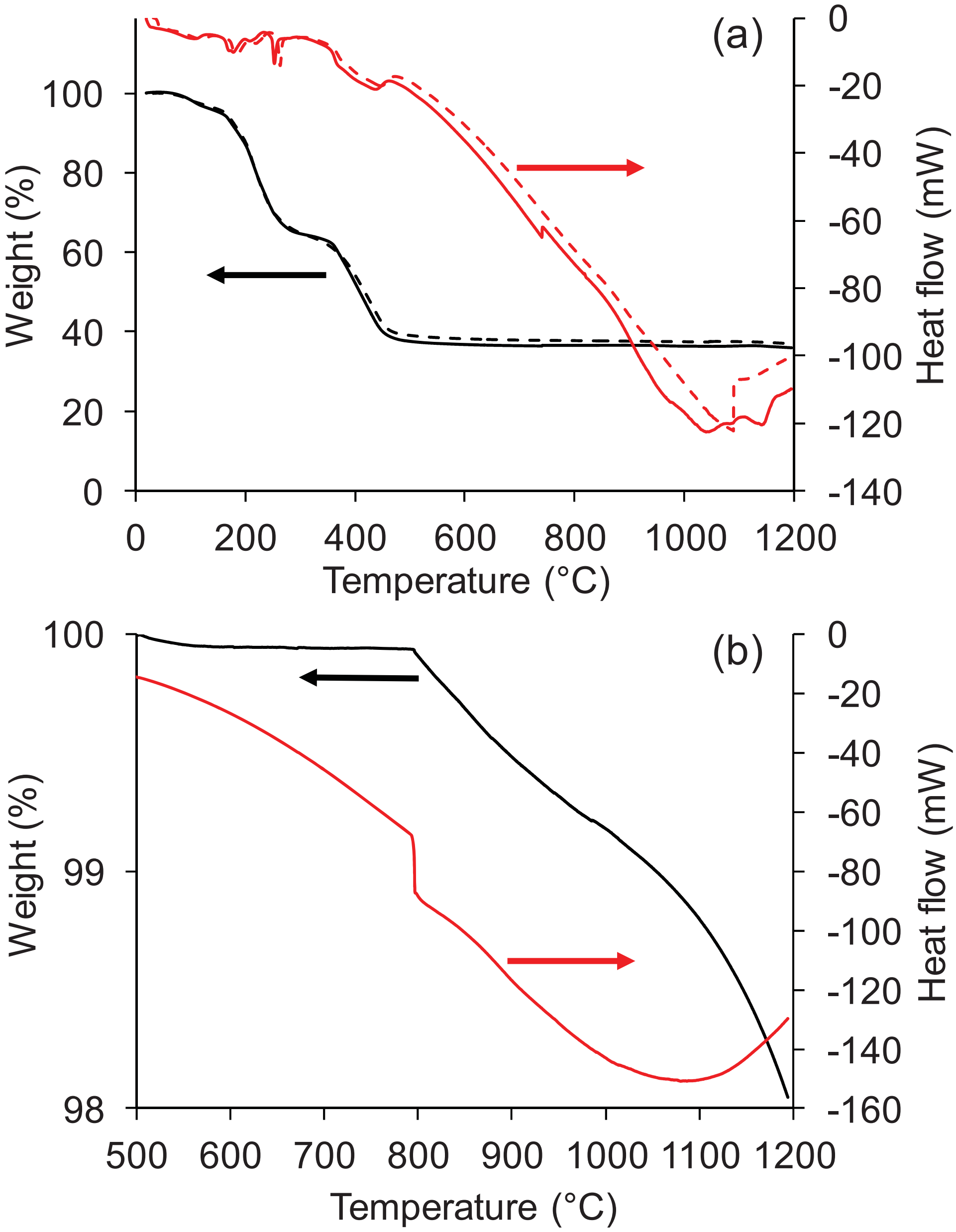

Fig. II. 1: TG-DTA curves obtained for “$Li_{1.20}Mn_{0.54}Co_{0.13}Ni_{0.13}O_2$”: (a) Comparison of the results obtained for 2 samples thermal-treated at 120°C for 10 h in air before the TGA-DTA experiment (temperature range 25 - 1200°C, heating rate 200 °C/h) and (b) “$Li_{1.20}Mn_{0.54}Co_{0.13}Ni_{0.13}O_2$” thermal-treated at 500°C for 5 h in air before the TGA-DTA experiment (the preheating to 800°C was done at 800°C/h and then the heating rate was 100°C/h in the temperature range 800 - 1200°C).

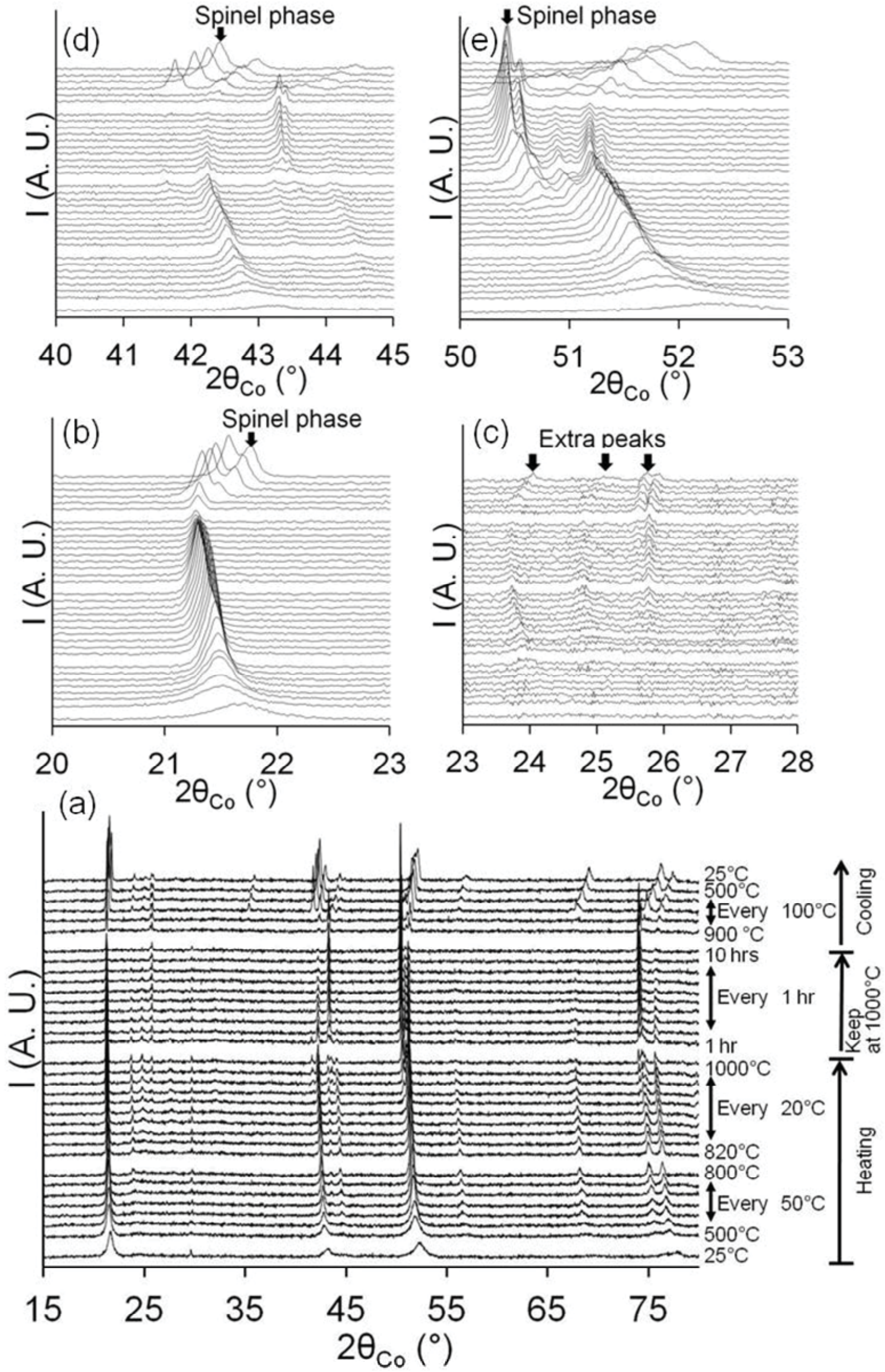

Fig. II. 2: In-situ XRD patterns obtained during the heat treatment between 25°C and 1000°C of the sample thermal-treated at 500°C for 5 h before the measurement. Heating conditions: Heating rate 4°C /min, temperature maintained at 1000° C for 10 h, cooling rate 10°C /min. (a) in the 15 – 80°, (b) 20 – 23°, (c) 23 – 28°, (d) 40 – 45°, (e) 50 – 53° 2θ angular ranges. Refer to the experimental part for more details on the *in situ* XRD experiment during the thermal treatment.

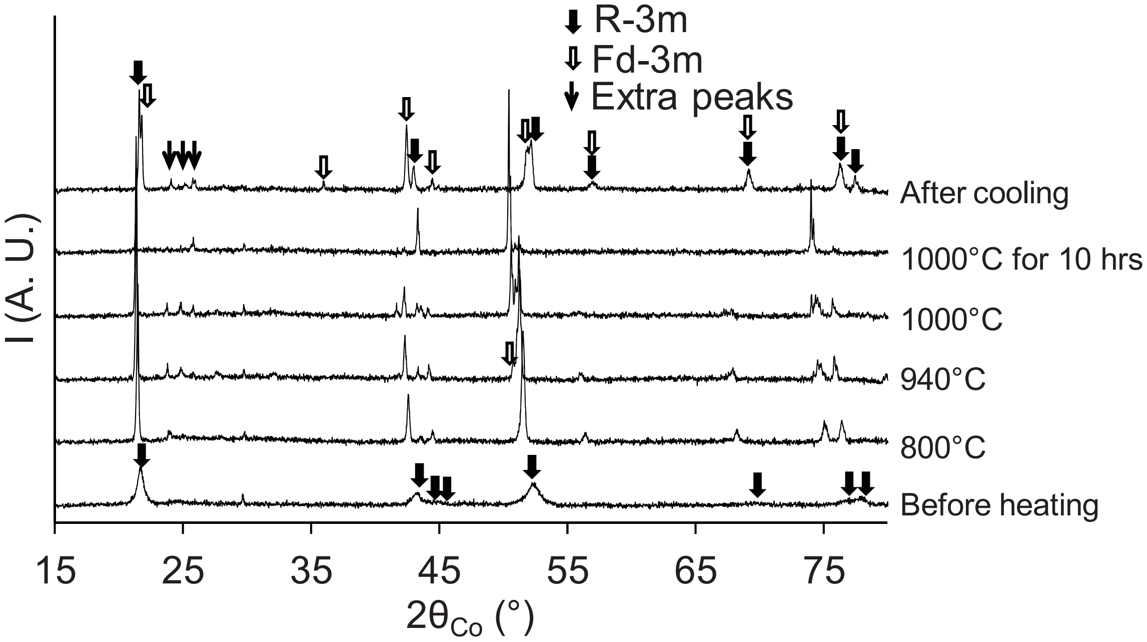

Temperature (°C)	*a*$_{cub.}$ *(Å)*
940	*8.363(5)*
1000	*8.380(2)*
1000 for 10 h	*8.4133(8)*
At room temperature, after cooling	*8.165(2)*

Fig. II. 3. XRD patterns of the pristine material thermal-treated at 500°C for 5 h before the measurement, upon a continuous thermal treatment at 800°C, 940°C and 1000°C (heating rate 4°C /min), after 10 h at 1000°C and finally after cooling. The $a_{cub.}$ cell parameter of the spinel-type phase (*Fd-3m*) formed upon heating is given for information for each XRD. Its decrease suggests an increasing average oxidation state for the transition metal ions.

II. 3. 2 - Global analysis (phase, composition and homogeneity) of the materials prepared

The XRD patterns of the materials “$Li_{1.20}Mn_{0.54}Co_{0.13}Ni_{0.13}O_2$” synthesized at 800°C, 900°C and 1000°C are compared in **Fig. II. 4**. All the peaks, except for the extra-peaks observed between 20 and 30° ($2\theta_{Cu}$), can be indexed based on a hexagonal cell (α-$NaFeO_2$-type structure described in the space group *R-3m*). The peaks observed between 20 and 30° ($2\theta_{Co}$) can be indexed considering a $\sqrt{3}.a_{hex.} \times \sqrt{3}.b_{hex.}$ superstructure in the *ab* transition metal planes due to an ordering between the Li, Mn, Co and Ni ions by analogy to the Li_2MnO_3 structure (described in the *C2/m* space group) **[13-14]**. Note that their width shows that the ordering is not fully extended within the layers nor along the c-axis despite a theoretical composition of the slabs such that the ratio between the large (Li^+ and Ni^{2+}) and the small (Mn^{4+} and Co^{3+}) cations is 1:2 **[13]**. However, the higher the synthesis temperature is, the sharper the diffraction lines are; for instance, the full width at half maximum of the *(003)* line decreases from ~0.19° at 800°C to ~0.12° at 1000°C.

Li, Ni, Mn and Co contents in the materials were determined using inductively coupled plasma spectrometry after the complete dissolution of the powder into an acidic solution. For the three materials the stoichiometry in lithium and transition metal ions was shown to be in agreement with that expected from the nominal composition, *i.e.* $Li_{1.20}Mn_{0.54}Co_{0.13}Ni_{0.13}O_2$ assuming the stoichiometry $Li(Li_xM_{1-x})O_2$, as reported in **Table II. 1**. The transition metal ions average oxidation states determined by iodometric titration are also given for information in **Table II. 1** and were found to be in good agreement, taking into account the accuracy of the analysis, with the values expected from these formulae.

Magnetic measurements were performed in a 500 Oe magnetic field as a function of temperature (between 4 and 300K) to determine the Curie constants (per mol. of transition metal ions) for these three materials and to check their adequacy with the proposed chemical formulae. The thermal evolution of the H/M ratio (H the magnetic field at 500 Oe and M the magnetization) is reported in **Fig. II. 5** for the three materials obtained at 800°C, 900°C and 1000°C: it is characteristic of a Curie-Weiss type behaviour above 150K. As reported in **Table II. 1**, the experimental Curie constants were found to be in good agreement with those expected considering the chemical formulae deduced from the chemical analyses and assuming a $Li(Li_xM_{1-x})O_2$ stoichiometry. These magnetic measurements fully support the presence of manganese, cobalt and nickel in these materials in a tetravalent state for manganese (d^3: $t_{2g}^3e_g^0$), a diamagnetic low spin trivalent state for cobalt (d^6: t_{2g}^6) and a divalent state for nickel (d^8: $t_{2g}^6e_g^2$).

Raman scattering and ^7Li MAS NMR spectroscopy allow investigating the local structure of these materials. Raman spectra of the materials synthesized at 800°C, 900°C and 1000°C are compared in **Fig. II. 6**, whereas the corresponding NMR spectra are compared in **Fig. II. 7**. These spectra are very similar whatever the synthesis temperature and thus reveal very close local environments for these three samples. A very small sharpening of the Raman bands is observed upon increasing temperature, as highlighted by the comparison of the spectra recorded for the 800°C and 1000°C samples and especially by the better-resolved signals at low wavenumbers. As for XRD this broadening obtained for the lower temperatures may be related to smaller particle sizes and higher disorder. A small band shift to lower wavenumbers is also observed upon increasing temperature, it is in good agreement with the small increase of the cell parameters that will be discussed in the following (see **Table II. 2**). The main isotropic signals of the NMR spectra are indicated by arrows, based on their analysis at different spinning speeds (not shown). The spectra show only very slightly different relative ratios of these contributions, revealing very similar Li environments in terms of distribution of cations at the local scale, which confirms the similarity of the samples. Note that in such compounds, a large number of contributions are expected, each corresponding to a Li^+ ion with a given environment in terms of transition metal ions whose single electrons exert a Fermi contact – type interaction on the Li nucleus. Assigning all these contributions is a rather delicate task, and beyond the scope of the present paper. However, in good agreement with the composition of the sample and a significant Li/M overlithiation ratio some of them are typical, such as Li present in the transition metal layer at 1525 (Li_2MnO_3 type environment) and 1420 ppm, overlapping with spinning sidebands of the main contributions that can be assigned mostly to Li in the Li sites **[19]**. The NMR spectra of all three samples also reveal a sharp but very minor peak close to 0 ppm, which corresponds to Li in a diamagnetic impurity not detected by any other technique. Considering the handling of the powders in air, it can be expected that it corresponds to traces of Li_2CO_3. The Li_2CO_3 characteristic bands and especially the intense signal at about 1090 cm^{-1} (spectral range measured but not shown in **Fig. II. 6**) were not detected in Raman spectroscopy due to a very small quantity, probably mainly present at the surface of the particles. It is likely that the amount and/or the size of the coherence domains in this impurity also prevent its detection by the diffraction methods.

To summarize, whatever the synthesis temperature these three materials are similar and close to the target composition $Li_{1.20}Mn_{0.54}Co_{0.13}Ni_{0.13}O_2$ with manganese in tetravalent state, nickel in divalent state and cobalt in low spin trivalent state.

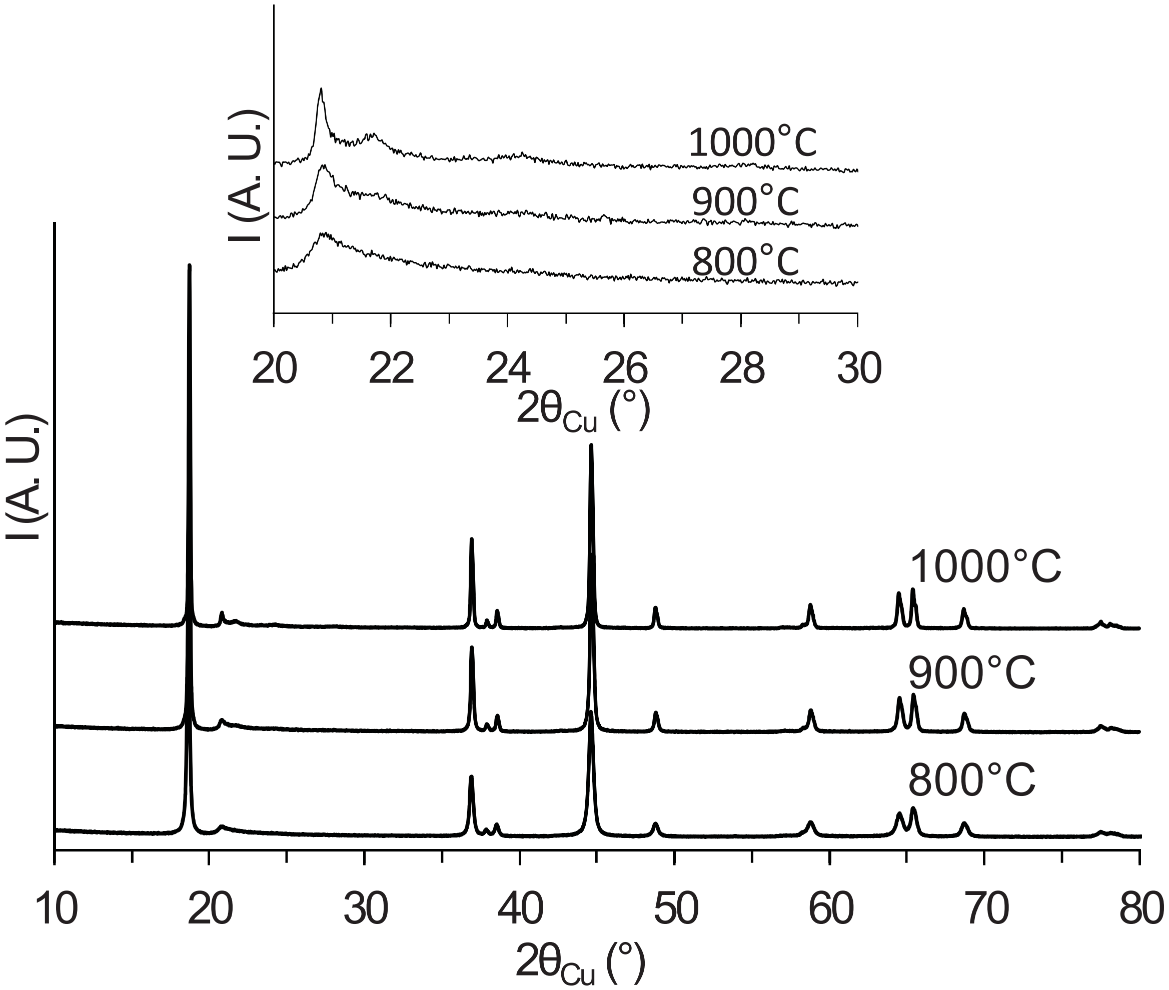

Fig. II. 4: X-ray diffraction patterns of "$Li_{1.20}Mn_{0.54}Co_{0.13}Ni_{0.13}O_2$" synthesized at 800°C, 900°C and 1000°C in the 10 – 80° ($2\theta_{Cu}$) range; an enlargement of the XRD patterns is given in the 20 – 30° 2θ angular range.

Table II. 1: Chemical composition, average oxidation state of transition metal ions and Curie constant determined for the three samples “$Li_{1.20}Mn_{0.54}Co_{0.13}Ni_{0.13}O_2$” synthesized at 800°C, 900°C and 1000°C.

Synthesis temperature (°C)	Chemical composition / mol				Average oxidation state of transition metal ions		Curie constant	
	Li	Mn	Co	Ni	Theoretical	Experimental	Theoretical	Experimental
800	1.20	0.54	0.13	0.13	3.5	3.4	1.43	1.29
900	1.20	0.54	0.13	0.13	3.5	3.4	1.43	1.37
1000	1.16	0.56	0.14	0.14	3.4	3.5	1.42	1.28

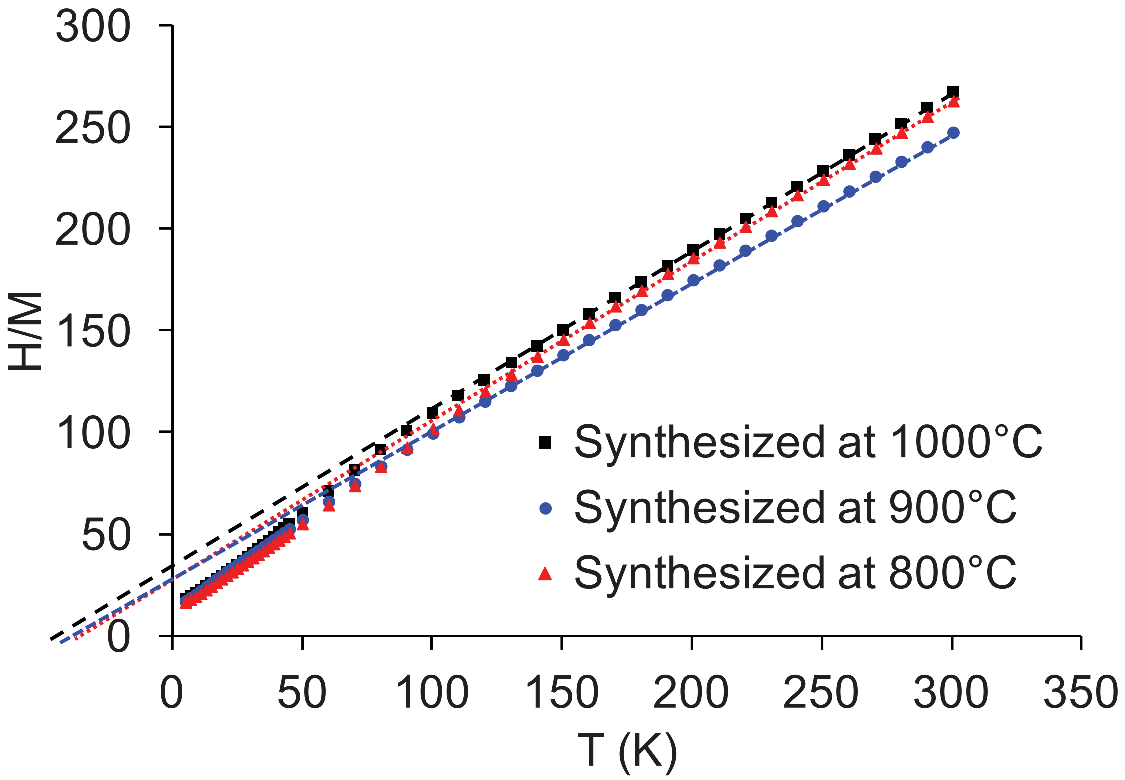

Fig. II. 5: Thermal evolution of the H / M ratio of “$Li_{1.20}Mn_{0.54}Co_{0.13}Ni_{0.13}O_2$” synthesized at 800°C, 900°C and 1000°C. H : the applied field (H = 500 Oe) and M : the measured magnetization. A Curie-Weiss type behavior is observed above 150K.

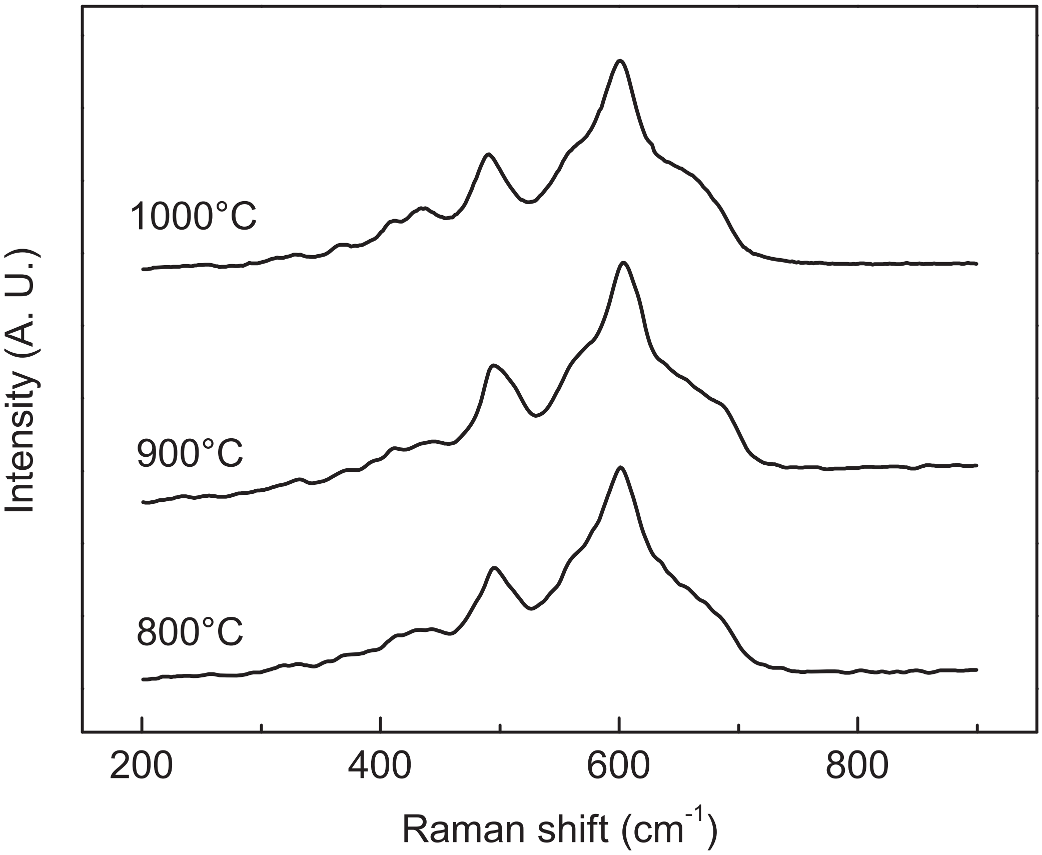

Fig. II. 6: Raman spectra of the materials synthesized at 800°C, 900°C and 1000°C.

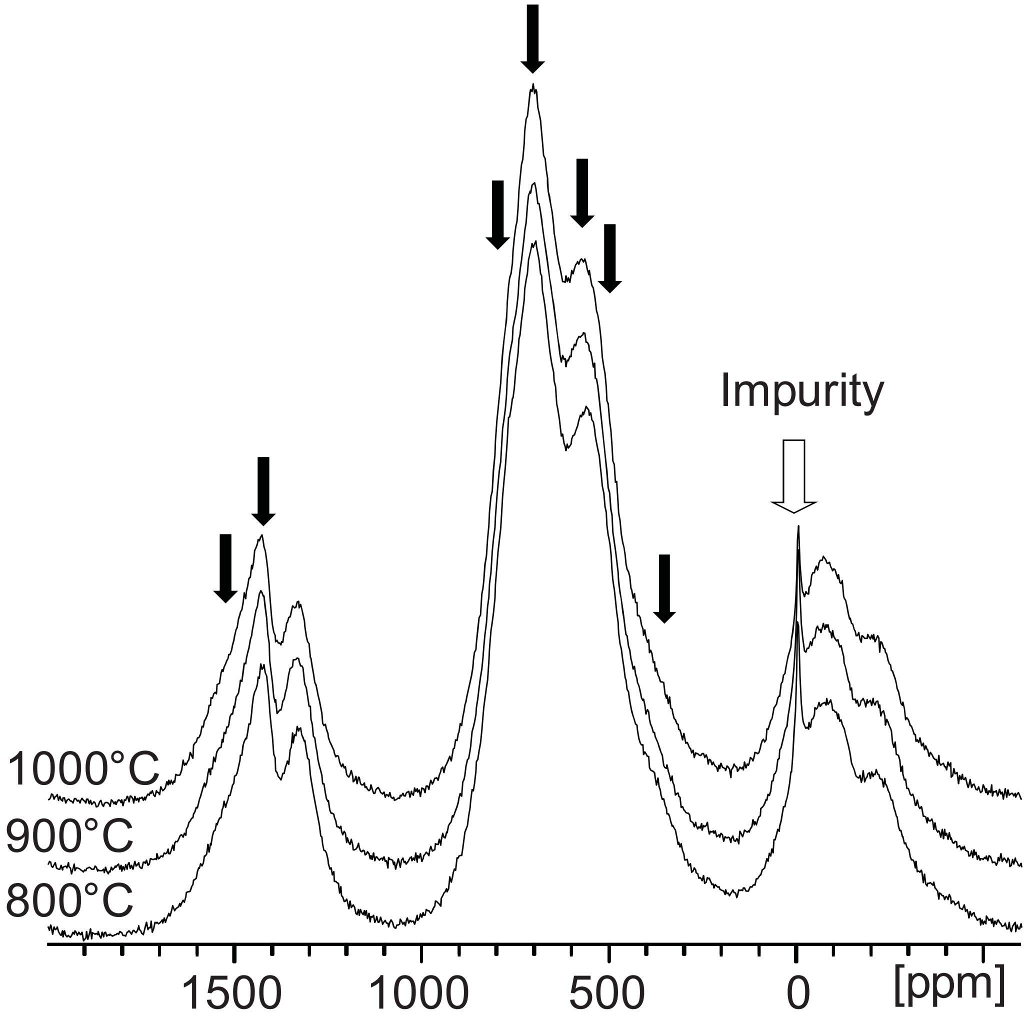

Fig. II. 7: ^{7}Li MAS NMR spectra for the three “$Li_{1.20}Mn_{0.54}Co_{0.13}Ni_{0.13}O_2$” compounds (Synchronized Hahn echo, 39 MHz, spinning 30 kHz). The main isotropic contributions are shown by arrows, the other signals being spinning sidebands.

II. 3. 3 - Structure of the materials prepared

A unit cell described in the *R-3m* space group (used for most of the $LiMO_2$ layered oxides) was chosen to analyze the XRD data recorded for the three samples by the Rietveld method, not taking into account the extra peaks between 20 – 30°($2\theta_{Cu}$) associated to a cation ordering between Li, Mn, Co and Ni in the transition metal layers by analogy to Li_2MnO_3. The refinements were conducted considering the exchange between some Ni ions from the slab and Li ions from the interslab space: $(Li_{1-z}Ni_z)_{3b}(Li_{x+z}Mn_{1-x-2y}Ni_{y-z}Co_y)_{3b}(O_2)_{6c}$. The cation exchanged with Li is expected to be Ni because the ionic radius of Ni^{2+} ($r(Ni^{2+}) = 0.69$Å) is similar to that of Li^+ ($r(Li^+) = 0.72$ Å) in contrast with the other cations ($r(Co^{3+}) = 0.54$ Å, $r(Mn^{4+}) = 0.53$ Å) **[20]**. The result of these refinements is shown for the 1000°C sample in **Fig. II. 8** and the main structural parameters are compared for the three samples in **Table II. 2**. The cell parameters were found similar whatever the synthesis temperature. The Li/Ni exchange between the lithium site and the transition metal site is smaller than 0.02 for the three samples, which are thus very close to ideal 2D materials. Note that the hysteresis loops versus magnetic field obtained at 5K for these three samples are nearly inexistent (with a very small magnetization at zero field) and thus support the presence of a negligible amount of Ni^{2+} ions in the interslab space, inducing only few magnetic interactions between the slab and the interslab space as shown in **Fig. II. 9**.

Electron diffraction analyses of the material obtained at 1000°C were performed in order to get more insight into the extent of the cation ordering in the transition metal layers, but also in order to detect the possible presence of spinel-type defects in this material obtained at high temperature **[21]**. **Fig. II. 10** shows typical electron diffraction patterns. In all of them, the fundamental reflections, i.e. the most intense ones can be indexed based on the hexagonal cell described in the *R-3m* space group. Additional spots also appear in **Fig. II. 10a**. Their presence indicates the formation of a $\sqrt{3}a_{hex} \times \sqrt{3}a_{hex}$ superstructure in the transition metal layer **[14]**. The superstructure reflections appearing in the [001] zone axis correspond to diffusion lines parallel to the c* axis (**Fig. II. 10b**). Along these diffusion lines a series of elongated spots are observed (as highlighted by the red arrows). The electron diffraction pattern observed along the [1-10] zone axis cannot be considered as being the sum of those typical of Li_2MnO_3 and $LiNi_{1/3}Mn_{1/3}Co_{1/3}O_2$-type materials, showing thus that this material cannot be described as separated domains of Li_2MnO_3 **[14]** and $LiNi_{1/3}Mn_{1/3}Co_{1/3}O_2$ **[22]**. These patterns are to some extent very similar to those recently reported by Jarvis *et al.* (see **Fig. 9c** in **[15]**), with more pronounced diffusion parallel to the c* axis in our case. They are typical of ordered transition metal layers stacked along the c-axis with changes in their orientation every few atomic layers due to crystal rotations, *i.e.* of changes in the relative positions of the two sites (associated to the large (Li^+,Ni^{2+}) and small (Mn^{4+},Co^{3+}) cations) versus each other along the c-axis (see **Fig. 9** in **[15])**. These observations explain why it is not possible to actually describe the structure of the material using a 3D space group (such as *C2/m* as for Li_2MnO_3). Note in addition that no extra spots associated to spinel-type defects were observed and that the sample was found highly homogeneous with a large number of crystallites studied and reproducible results obtained.

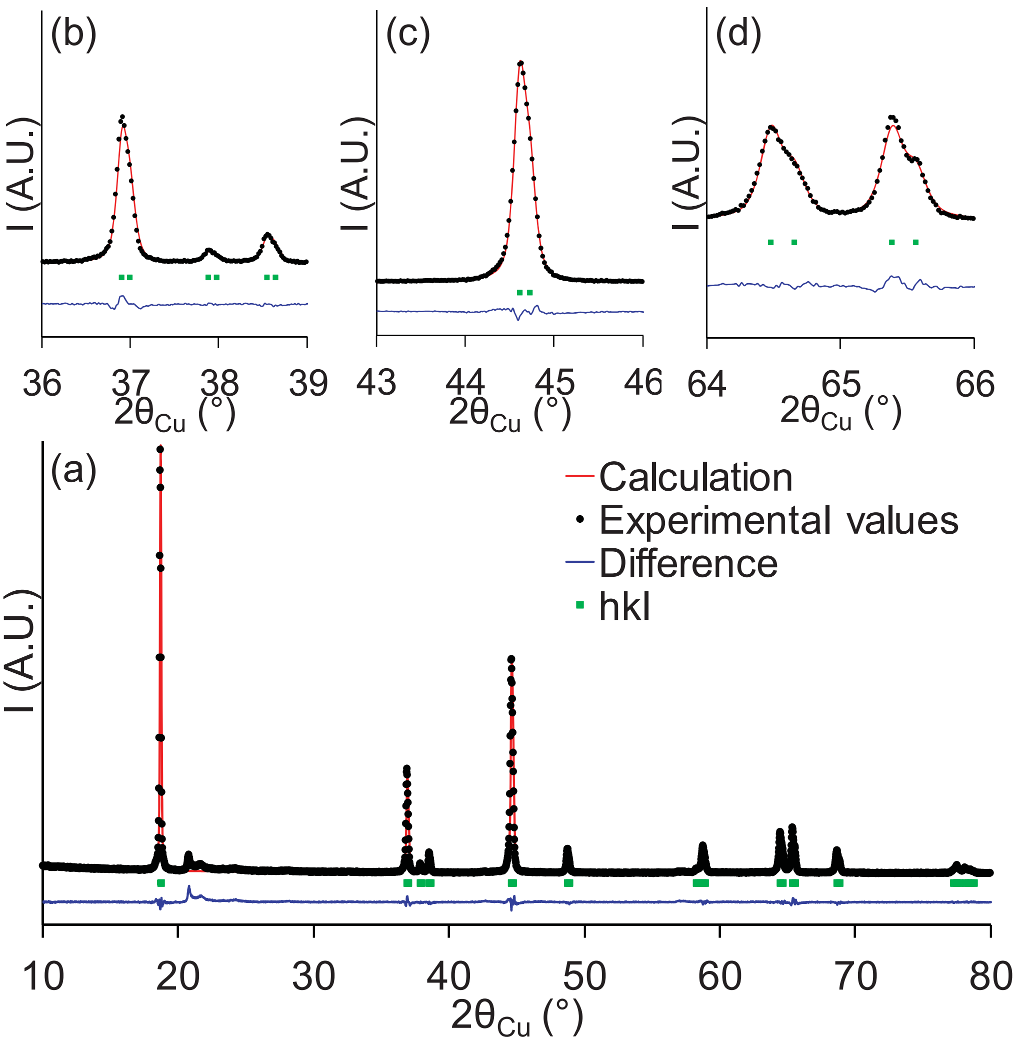

Fig. II. 8: Comparison for the 1000°C "$Li_{1.20}Mn_{0.54}Co_{0.13}Ni_{0.13}O_2$" sample between the experimental XRD pattern and that calculated by the Rietveld method: in the 10 – 80° (2θ$_{Cu}$) range (a), in the 36 – 39° (b), in the 43 - 46° (c) and in the 64 - 66° (d). These enlargements are given in order to highlight the good agreement between the two patterns and thus the good minimization of the difference.

Table II. 2: Structural parameters obtained from the refinement by the Rietveld method of the X-ray diffraction data recorded for "$Li_{1.20}Mn_{0.54}Co_{0.13}Ni_{0.13}O_2$" synthesized at 800°C, 900°C and 1000°C.

Heating temperature (°C)	Cell parameters			Ni in 3b site (mol)	Reliability factors	
	a (Å)	c (Å)	V (Å^3)		R_{wp} (%)	R_{Bragg} (%)
800	2.8511(2)	14.235(2)	100.21 (2)	0.011(2)	6.3	4.8
900	2.8511(2)	14.234(2)	100.20 (2)	0.020(2)	7.1	3.6
1000	2.8522(2)	14.238(2)	100.30 (2)	0.020(2)	8.1	2.7

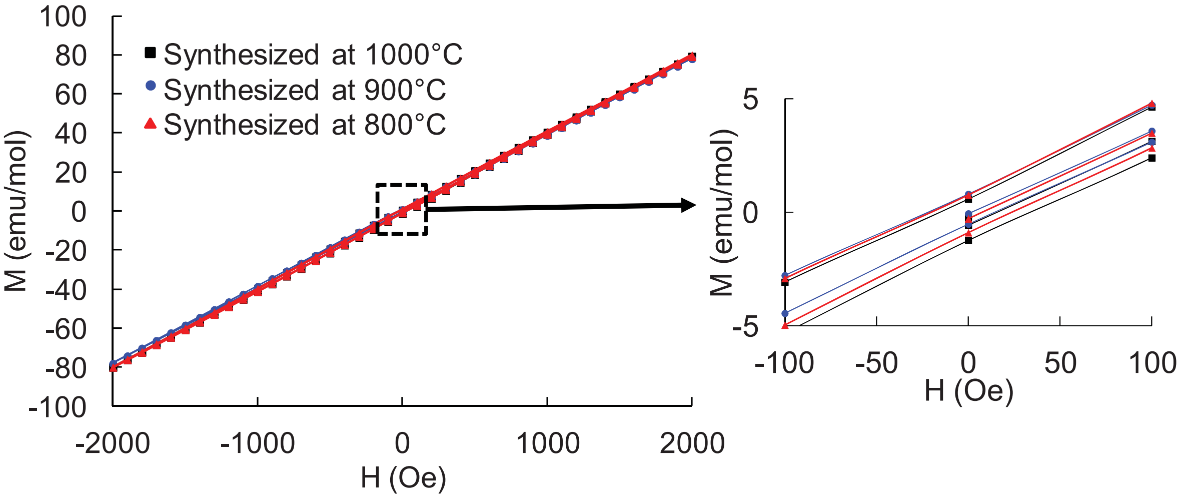

Fig. II. 9: Hysteresis loops (magnetization *vs.* magnetic field at 5K) obtained for "$Li_{1.20}Mn_{0.54}Co_{0.13}Ni_{0.13}O_2$" synthesized at 800°C, 900°C and 1000°C.

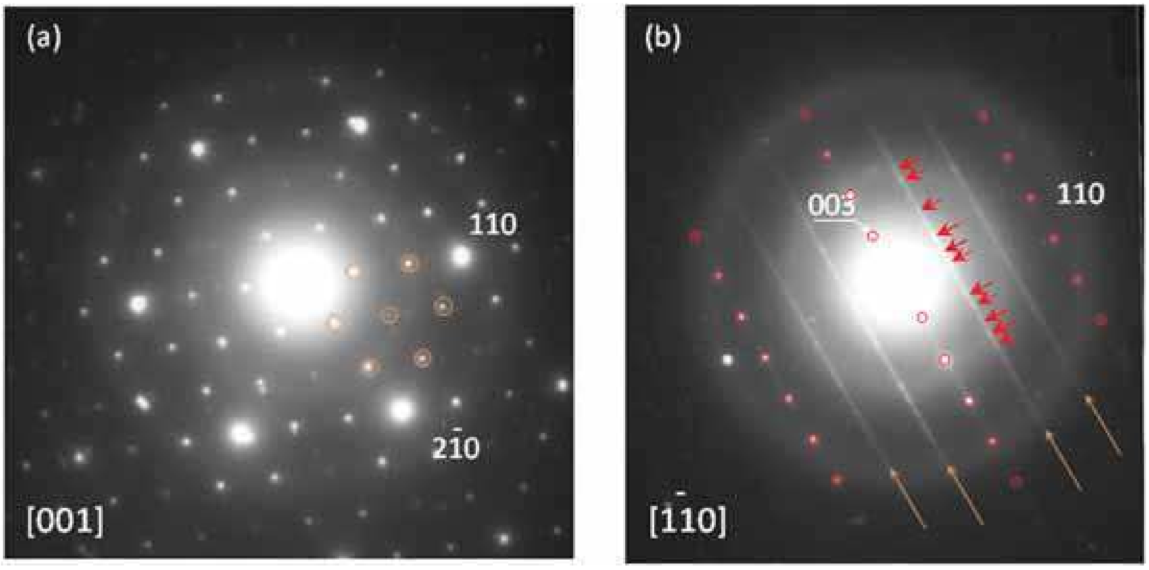

Fig. II. 10: Electron diffraction patterns of $Li_{1.20}Mn_{0.54}Co_{0.13}Ni_{0.13}O_2$: (a) [001] and (b) [1-10]. The circled reflections correspond to the cationic ordering in the transition metal layers. The diffusion lines pointed by the arrows indicate it is only a 2D ordering. The red arrows indicate elongated spots observed along the diffusion lines.

In order to confirm the cation distribution, the nature of the transition metal ions present in the lithium site, but also the stoichiometry in oxygen in these materials, neutron diffraction experiments were performed as the difference in Fermi length (sign and magnitude) allows discriminating between atoms with very close numbers of electrons (b(Mn) = -0.37 10^{-12} cm, b(Co) = 0.25 10^{-12} cm and b(Ni) = 1.03 10^{-12} cm) and to detect the light atoms such as Li (b(Li) = -0.19 10^{-12} cm, for natural abundance isotopic ratio). A procedure similar to that described previously for the refinement of the XRD data was followed, except that in this case two structural models were compared: $(Li_{1-z}M_z)_{3b}(Li_{x+z}M_{1-x-z})_{3b}(O_2)_{6c}$ (M = Ni, Mn, Co) described in the *R-3m* space group and $\{[Li_{1/3-z/3}M_{z/3}]_{2c}[Li_{2/3-2z/3}M_{2z/3}]_{4h}\}\{[Li_{x+z}M_{1/3-x-z}]_{2b}[M_{2/3}]_{4g}\}\{O_2\}_{4i,8j}$ (M = Ni, Mn, Co) described in the *C2/m* space group in order for this latter to take into account the cation ordering in the slabs and thus along the c-axis. This description implies also two sites (*2c* and *4h*) for the lithium ions and an ordering in the interslab space. A comparison of these refinements is given in **Fig. II. 11** for the material obtained at 1000°C. Whatever the structural hypothesis the main lines (that can be indexed in the unit cell commonly used to describe the α-$NaFeO_2$-type materials) are well fitted. Note that the extra lines observed in the 38-48 and 105-120 (2θ) ranges are in neutron diffraction those associated to the cation ordering between Li, Ni, Mn and Co in the slabs. As shown in **Fig. II. 11a** for the α-$NaFeO_2$–type structural model (*R-3m* space group) the extra lines associated to the cation ordering in the TM slabs cannot be taken into account by this unit cell, whereas for the Li_2MnO_3-type structural model (*C2/m* space group) as highlighted by arrows in **Fig. II. 11b** the experimental profile of some extra lines is not well taken into account. This mismatching supports again the fact that none of the two unit cells is able to fully describe the structure of these materials since on the one hand, considering the *R-3m* unit cell, a tendency to additional cation ordering exists in the slabs and on the other hand, considering the *C2/m* unit cell, the coherent length associated to this cation ordering is limited. Note that similar reliability factors were obtained for the two structural models ($Rwp = 11.6\%$ and $R_{Bragg} \sim 7.8\%$). These refinements confirm (i) that the exchange between the slab and the interslab space occurs for Ni and Li, and not for (Mn or Co) and Li, (ii) that ~1% Ni ions are present in the interslab space, and (iii) that the (Li + M)/O ratio is equal to 1 (the corresponding structural parameters obtained are given as additional information in **Table II. 3** and **Table II. 4**). The site occupancies for the *C2/m* hypothesis, according to the stoichiometry (composition) of the sample and considering the Li_2MnO_3-type structural description, are indeed based on the assumption that in the slabs the large Ni and extra Li ions occupy the 2b site whereas the small Mn and Co ions occupy the 4g site. However, the refinement yields, 0.14 mol Mn ions in the 2b site and thus exchanged with Li ions. It is therefore likely, in good agreement with results already obtained in our group for Li_2MnO_3 **[18]** and with the electron diffraction data just discussed, that this unexpected result (*i.e.* the presence of a small amount of small cations in a large site) simply corresponds to a mathematical artifact resulting from the refinement of diffraction data recorded for a sample showing no long range ordering along the c-axis with a unit cell considering such ordering.

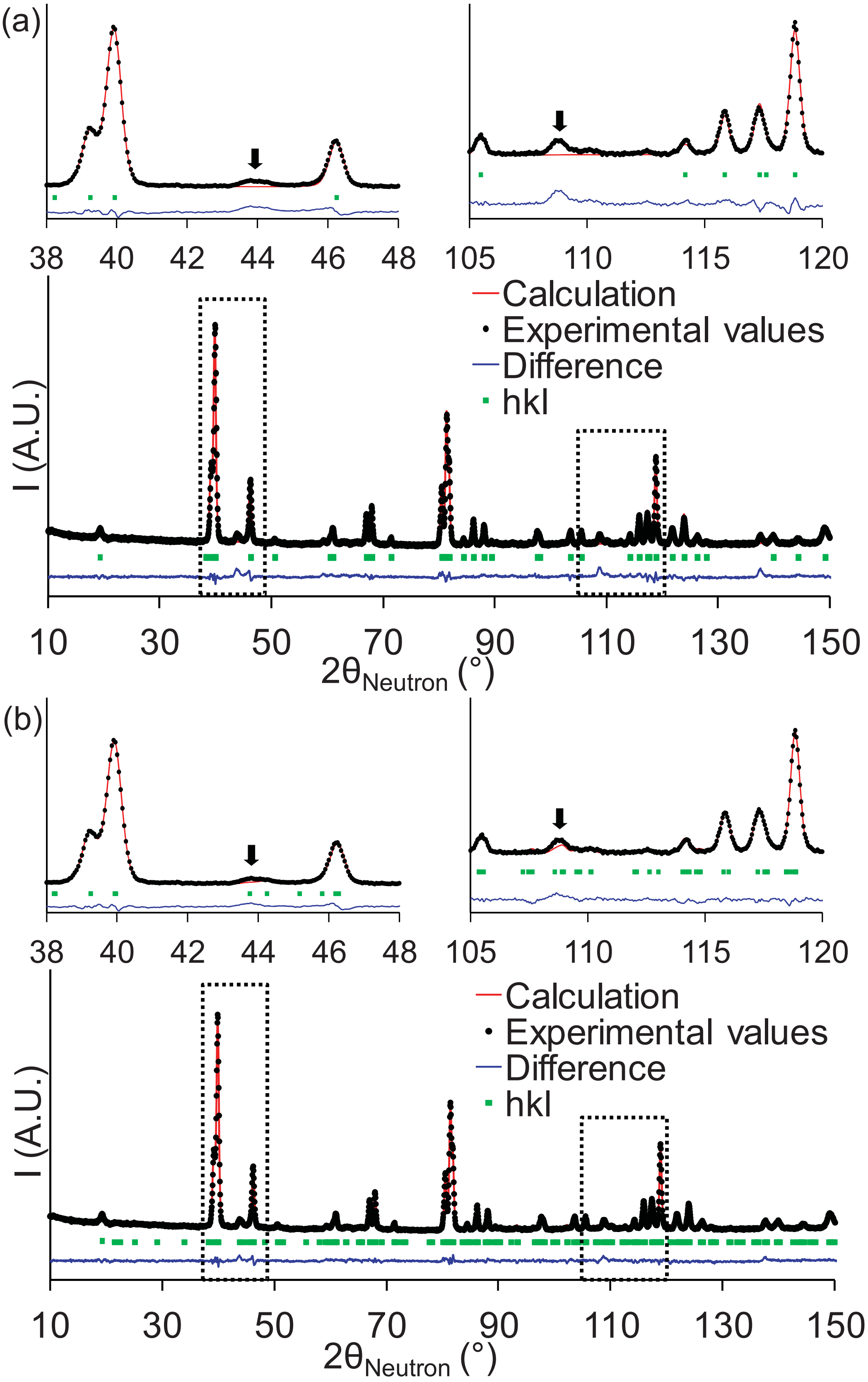

Fig. II. 11: Comparison of the experimental and calculated neutron diffraction data for the material “$Li_{1.20}Mn_{0.54}Co_{0.13}Ni_{0.13}O_2$” synthesized at 1000°C, the calculated patterns being obtained considering a description of the unit cell either in the *R-3m* space group (a) or in the *C2/m* space group (b).

Table II. 3: Structural parameters obtained from the refinement by the Rietveld method of the neutron diffraction data recorded for the pristine material “$Li_{1.20}Mn_{0.54}Co_{0.13}Ni_{0.13}O_2$” synthesized at 1000°C considering a unit cell described in the *R-3m* space group.

Pristine material : $Li_{1.20}Mn_{0.54}Co_{0.13}Ni_{0.13}O_2$
Space group: R3m
a = 2.8517(1) Å c = 14.237(9) Å R_{wp} = 11.6 %, R_{Bragg} = 7.9 %

Atom	Site	Wyckoff positions			Occupancy	Biso (Å^2)
Li(1)	3b	0	0	½	0.986(1)	0.9(3)
Ni(2)	3b	0	0	½	0.014(1)	0.9(3)
Li(2)	3a	0	0	0	0.214(1)	0.7(5)
Ni(2)	3a	0	0	0	0.116(1)	0.7(5)
Mn(1)	3a	0	0	0	0.540	0.7(5)
Co(1)	3a	0	0	0	0.130	0.7(5)
O(1)	6c	0	0	0.2589(2)	1.000	0.8(5)

Table II. 4: Structural parameters obtained from the refinement by the Rietveld method of the neutron diffraction data recorded for the pristine material “$Li_{1.20}Mn_{0.54}Co_{0.13}Ni_{0.13}O_2$” synthesized at 1000°C considering a unit cell described in the *C2/m* space group.

Pristine material : $Li_{1.20}Mn_{0.54}Co_{0.13}Ni_{0.13}O_2$
Space group: C2/m
a = 4.940(6) Å, b = 8.553(1) Å, c = 5.0268(4) Å, β = 109.25(2) °
R_{wp} = 11.6%, R_{Bragg} = 7.67 %

Atom	Site	Wyckoff positions			Occupancy	Biso (Å^2)
Li(2)	2c	0	0	½	0.984	0.9(1)
Ni(2)	2c	0	0	½	0.016	0.9(1)
Li(3)	4h	0	0.658(9)	½	0.987	0.8(1)
Ni(3)	4h	0	0.658(9)	½	0.013	0.8(1)
Li(1)	2b	0	½	0	0.194(2)	2.0(3)
Ni(1)	2b	0	½	0	0.354(1)	2.0(3)
Mn(1)	2b	0	½	0	0.452(7)	2.0(3)
Mn(2)	4g	0	0.170(6)	0	0.584(7)	1.1(2)
Co(1)	4g	0	0.170(6)	0	0.194	1.1(2)
Li(4)	4g	0	0.170(6)	0	0.222(7)	1.1(2)
O(1)	4i	0.222(3)	0	0.224 (3)	1.000	0.5(4)
O(2)	8j	0.250(2)	0.324(2)	0.223 (2)	1.000	0.6(2)

From these structural results, it appears interesting to discuss further the results obtained from Raman scattering, which is a sensitive probe for the local symmetry and may thus discriminate between the two proposed space groups. Theoretically, for ideal $LiMO_2$ layered oxides (M = Co and/or Ni) whose structure is described in the *R-3m* (D_{3d}^5) space group, only 2 Raman-active modes ($A_{1g} \oplus E_g$) are expected. For Li_2MnO_3 (or $Li(Li_{1/3}Mn_{2/3})O_2$) whose structure is described in the *C2/m* (C_{2h}^3) space group, the number of predicted active modes is significantly higher with 15 Raman-active modes ($7A_g \oplus 8B_g$). Note that from a general point of view, additional bands, wavenumber shifts and/or broadenings may be observed for a non ideal material characterized for instance by non-stoichiometry, substitutions or exchanges. The Raman spectrum of the 1000°C "$Li_{1.20}Mn_{0.54}Co_{0.13}Ni_{0.13}O_2$" sample is compared to that of $LiCoO_2$ (*R-3m*), $LiNi_{1/3}Mn_{1/3}Co_{1/3}O_2$ (described in the *R-3m* space group but showing a cation ordering in the slab **[22]**) and Li_2MnO_3 (*C2/m*) in **Fig. II. 12**. Firstly the Raman spectrum of "$Li_{1.20}Mn_{0.54}Co_{0.13}Ni_{0.13}O_2$" is clearly not a simple combination of those of Li_2MnO_3 and $LiNi_{1/3}Mn_{1/3}Co_{1/3}O_2$, supporting thus again that this material is not made of domains of these two compositions and structures. The difference between $LiCoO_2$ and $LiNi_{1/3}Mn_{1/3}Co_{1/3}O_2$, both described in the *R-3m* space group, is associated to the ordering between Ni and (Co,Mn) in the cation layers. As for Li_2MnO_3, numerous bands are observed for "$Li_{1.20}Mn_{0.54}Co_{0.13}Ni_{0.13}O_2$", with broader bands shifted to lower wavenumbers for the latter, as well as an additional band at ~660 cm^{-1}. These results are consistent with those suggested by diffraction and support the presence of environments with similar local symmetry as in Li_2MnO_3. The shift of the bands is probably due to an increase in the cell parameters for "$Li_{1.20}Mn_{0.54}Co_{0.13}Ni_{0.13}O_2$" with a unit cell volume of 100.3 $Å^3$ vs. 99.7 $Å^3$ for Li_2MnO_3 (for this latter V/2 is given for comparison, V being the cell volume). The additional band at ~660 cm^{-1}, which is probably due to the presence of a shorter Mn-O and/or Co-O bond, was observed for other Li-Mn-O compounds as reported for instance for "HT-$Li_{0.52}MnO_{2.1}$" (*$I4_1/amd$*) **[23]** and more recently for $(1-x)Li_2MnO_3.xLi_4Mn_5O_{12}$ composites (*Fd-3m*) **[24]**. As all these unit cells describe similar oxygen triangular lattices with only differences in the distribution of the transition metal ions, it is not surprising to find very close Raman spectra due to similar local environments for compounds being intermediate between layered and spinel structures. Mn-O bonds are in average longer in "$Li_{1.20}Mn_{0.54}Co_{0.13}Ni_{0.13}O_2$" than in Li_2MnO_3, nevertheless note that one is significantly shorter (1.898 Å versus distances over 1.911 Å in Li_2MnO_3). In addition, all the Co-O bonds are significantly shorter in "$Li_{1.20}Mn_{0.54}Co_{0.13}Ni_{0.13}O_2$" than in $LiNi_{1/3}Mn_{1/3}Co_{1/3}O_2$ and $LiCoO_2$ (smaller than 1.942 Å versus distances of 1.962 Å in $LiNi_{1/3}Mn_{1/3}Co_{1/3}O_2$ and over 2.005 Å in $LiCoO_2$). This extra band at ~660 cm^{-1} could thus be tentatively attributed to a drastic shortening of some M-O bonds with respect to those observed in ideal Li_2MnO_3 (*C2/m*) and $LiCoO_2$ (*R-3m*) layered oxides, as well as in $LiNi_{1/3}Mn_{1/3}Co_{1/3}O_2$.

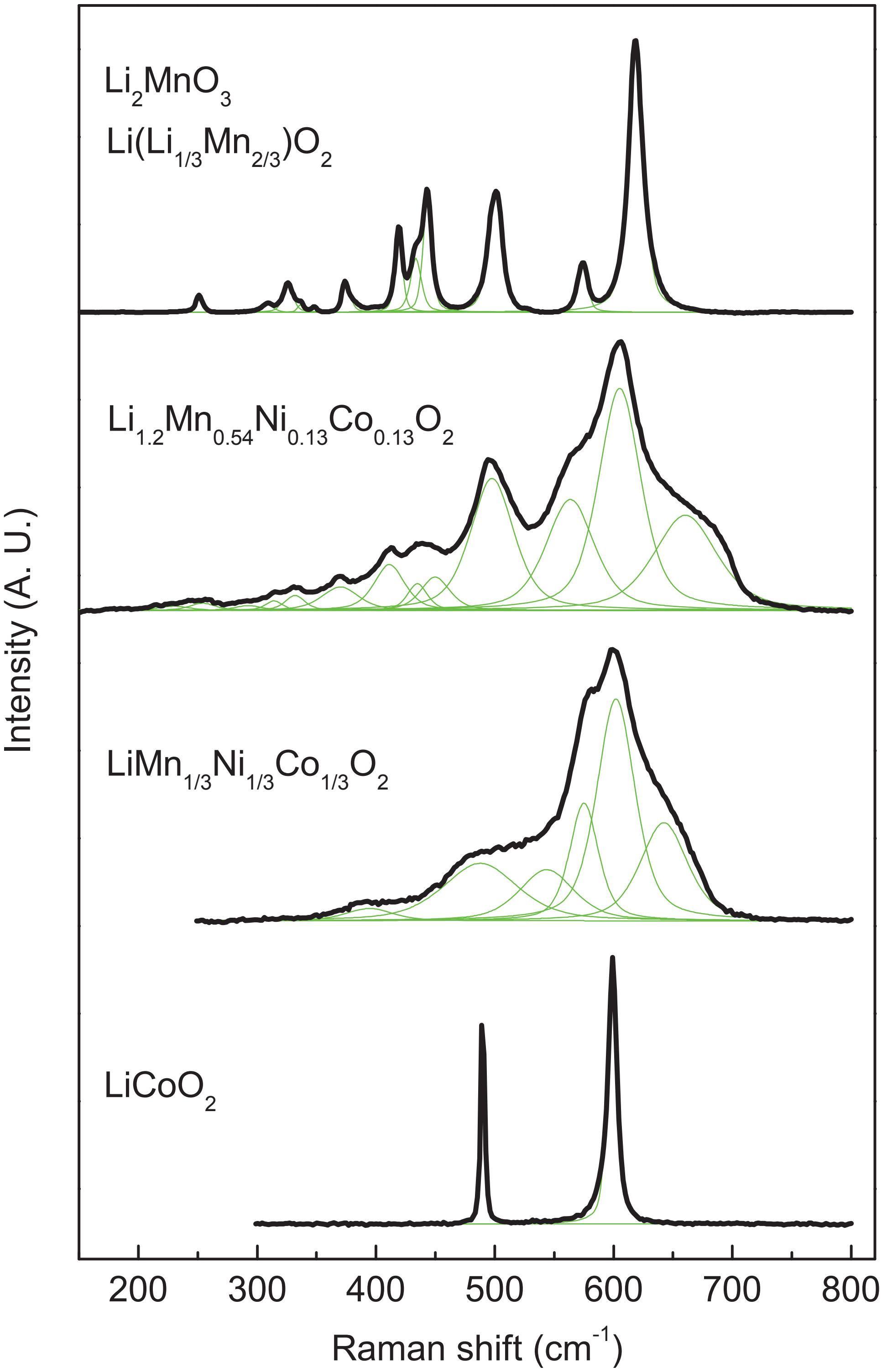

Fig. II. 12: Raman spectrum of "$Li_{1.20}Mn_{0.54}Co_{0.13}Ni_{0.13}O_2$" obtained at 1000°C and its comparison with those of Li_2MnO_3, $LiNi_{1/3}Mn_{1/3}Co_{1/3}O_2$ and $LiCoO_2$. The spectra were fitted using pseudo-Voigt bands (here in green) in order to allow their easier comparison.

To summarize, these three materials show similar structures with an almost ideal 2D lamellar stacking and very close cation distribution between the slab and the interslab space but also within the slabs. The control of the composition has a huge impact on the structure and especially on the extent of the cation ordering (within the slabs and of course also along the c-axis). Some of us studied a few years ago the $Li_{1+x}(Ni_{0.425}Mn_{0.425}Co_{0.15})_{1-x}O_2$ materials; in that case the cation ordering within the slabs exists but not fully extended as the (large cations)/(small cations) ratio is significantly different from ½: no correlation exists along the c-axis and the diffraction patterns were thus refined considering the unit cell described in the *R-3m* space group **[13]**. For Li_2MnO_3, in the slabs the Li/Mn ratio is ½ with an extended cation ordering in the slabs but also along the c-axis since Li fully occupies one site (*2b*) of the slabs and Mn occupies the other (*4g*): the unit cell is thus described in the *C2/m* space group **[14]**. The case of the "$Li_{1.20}Mn_{0.54}Co_{0.13}Ni_{0.13}O_2$" materials is intermediate: the (large cations)/(small cations) ratio being equal to ½, an extended cation ordering exists in the slabs but with only short coherent lengths along the c-axis since each of these two sites of the slabs is statistically occupied by two cations different in charge and in electronic configuration. Raman scattering especially highlights that the local environment in these Li and Mn rich materials is very close to that observed in Li_2MnO_3, whereas electron diffraction reveals also ordering along the c-axis limited to a few atomic layers. Finally the material "$Li_{1.20}Mn_{0.54}Co_{0.13}Ni_{0.13}O_2$" is shown to be a solid solution and not made of separated domains of Li_2MnO_3 and $LiNi_{1/3}Mn_{1/3}Co_{1/3}O_2$.

II. 3. 4 - Electrochemical tests in lithium cells

The cycling tests were performed in coin cells with the "$Li_{1.20}Mn_{0.54}Co_{0.13}Ni_{0.13}O_2$" samples synthesized at 800°C, 900°C or 1000°C. The three electrochemical curves are very similar as shown in **Fig. II. 13**. Upon charge, in a first step the potential changes continuously as a function of the lithium composition, then an irreversible plateau is observed at 4.5V *vs.* Li^+/Li and finally a continuous change in potential is again observed. During the following discharge and cycles, the potential changes continuously over the whole lithium composition range. Large irreversible capacities are observed at the end of the 1st cycle (larger than 15% of the first charge capacity), with also a continuous change in the shape of the charge-discharge cycle and a decrease of the average potential upon cycling. As shown in **Fig. II. 13d**, the reversible capacity obtained in (non optimized) laboratory lithium cells is around 225 mAh/g after 10 cycles for these materials. The effect of the synthesis temperature is not obvious on the cycling performance since the differences observed here remain of the order of the reproducibility of the experiments. According to the composition of the samples and to the oxidation states of the transition metal cations (divalent nickel, trivalent cobalt and tetravalent manganese mainly) in the pristine materials, the first part of the charge (up to $Li_{\sim 0.8}Mn_{0.54}Co_{0.13}Ni_{0.13}O_2$) is expected to be associated to the oxidation of Ni and Co to the tetravalent state, and the "plateau" to a deintercalation of Li that could be compensated for by oxygen loss based on previous reports **[25-28]**. Finally, the discharge is expected to be associated to the reduction of Co, Ni and Mn to the trivalent, divalent and partially trivalent state respectively **[28-30]**. Experiments are currently in progress in order to get more insight in these redox processes and the structural reorganization occurring upon cycling (and especially during the first cycle); these results are discussed in detail in next chapters.

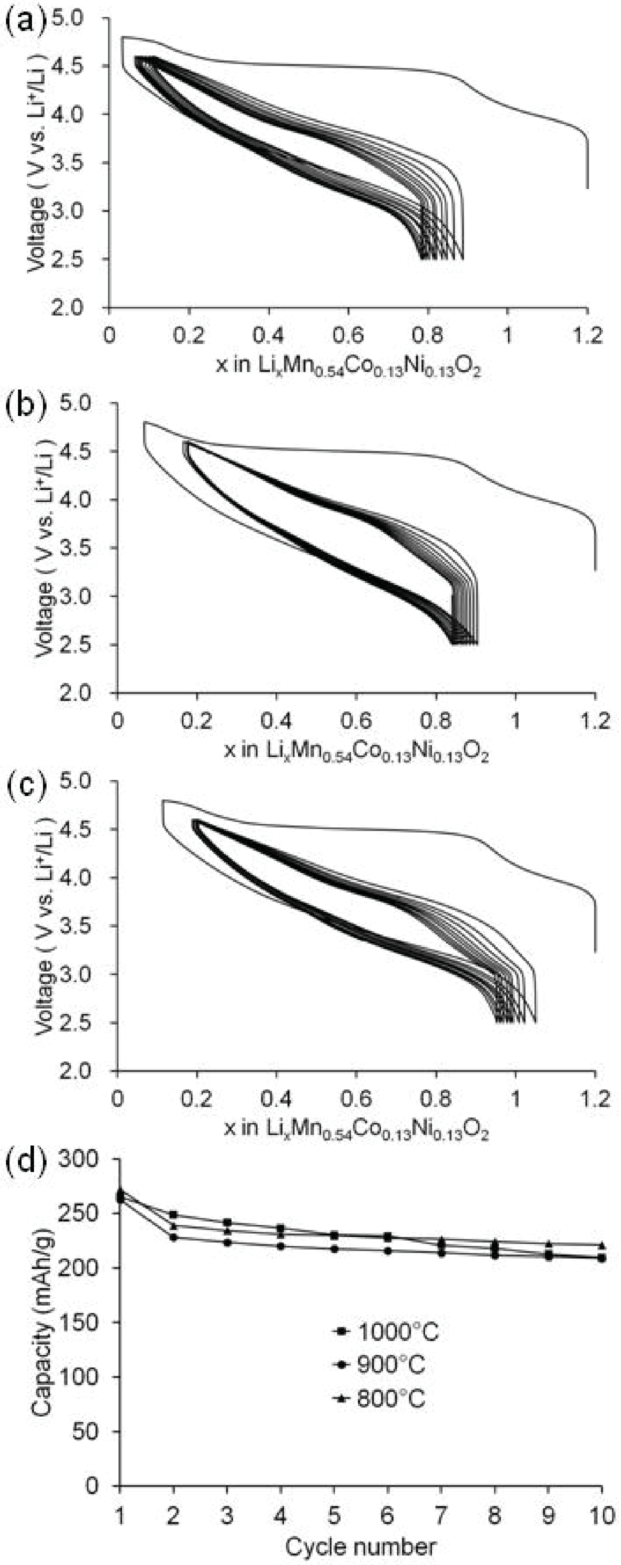

Fig. II. 13: The 1st to 10th cycling curves obtained for different Li//Li$_x$Mn$_{0.54}$Co$_{0.13}$Ni$_{0.13}$O$_2$ cells, "Li$_{1.20}$Mn$_{0.54}$Co$_{0.13}$Ni$_{0.13}$O$_2$" being synthesized at 1000°C, 900°C and 800°C (a-c). Changes in reversible capacity observed for the different Li//Li$_x$Mn$_{0.54}$Co$_{0.13}$Ni$_{0.13}$O$_2$ cells (d). Voltage range is 2.5 – 4.8 V vs. Li$^+$/Li in the 1st cycle and 2.5 – 4.6V vs. Li$^+$/Li in the 1st cycle after the 2nd cycle.

II. 4 - Conclusions

Despite synthesis temperatures ranging between 800 and 1000°C different "$Li_{1.20}Mn_{0.54}Co_{0.13}Ni_{0.13}O_2$" materials show very similar compositions, structures and electrochemical properties. NMR and Raman spectroscopies show that the three compounds are very similar in their local structures, while neutron and electron diffraction allowed getting more insights into their average structure. Their global structure is in fact very close to an ideal 2D stacking, with a stoichiometry in oxygen such as (Li+M)/O = 1, less than 0.02 Ni^{2+} ions in the Li site and an extended cation ordering in the slabs between (Li^+, Ni^{2+}) ions in one site and (Mn^{4+}, Co^{3+}) ions in the other site in accord with the stoichiometry 1:2. "$Li_{1.20}Mn_{0.54}Co_{0.13}Ni_{0.13}O_2$" is clearly not made of separate domains of Li_2MnO_3 and $LiNi_{1/3}Mn_{1/3}Co_{1/3}O_2$, but is a solid solution. The electrochemical tests have revealed an overcapacity during the first charge, as well as a high discharge capacity over 220 mAh/g after 10 cycles. Characterization of the structural changes and redox processes occurring upon cycling is discussed in next chapters: this study takes especially into account the impact of the particles size on the nature of the materials formed upon cycling.

II. 5 - References

(1) Ohzuku, T.; Makimura, Y. *Chem. Lett.* **2001**, *7*, 642-643.

(2) Lu, Z.; Dahn, J. R. *Electrochem. Solid State lett.* **2001**, 4(11), A191-A194.

(3) Park, Y. J.; Hong, Y. S.; Wu, X.; Ryu, K. S.; Chang, S. H. *J. Power Sources* **2004**, *129*, 288-295.

(4) Shao-Horn, Y.; Ein-Eli, Y.; Robertson, A. D.; Averill, W. F.; Hachney, S. A.; Howard Jr. W. F. *J. Electrochem. Soc.* **1998**, *145*, 16-23.

(5) Johnson, C. S.; Korte, S. D.; Vaughey, J.T.; Thacheray, M. M.; Bofinger, T. E.; Shao-Horn, Y.; Hachney, S. A. *J. Power Sources* **1999**, *81/82*, 491-495.

(6) Johnson, C. S.; Kim, J.-S.; Lefief, C.; Li, N.; Vaughey, J. T.; Thackeray, M. M. *Electrochem. Commun.* **2004**, *6*, 1085-1091.

(7) Kang, S.-H.; Johnson, C. S.; Vaughey, J. T.; Amine, K.; Thackeray, M. M. *J. Electrochem. Soc.* **2006**, 153, A1186-A1192.

(8) Park, S.-H.; Sato, Y.; Kim, J.-K.; Lee, Y.-S. *Materials Chemistry and Physics* **2007**, *102*, 225-230.

(9) Yu, D.Y.W.; Yanagida, K.; Kato, Y.; Nakamura, H. *J. Electrochem. Soc.* **2009**, *156*, A417-A424.

(10) Wu, Y.; Manthiram, A. *Electrochem. Solid-State Lett.* **2006**, *9*, A221-A224.

(11) Meng, Y. S.; Ceder, G.; Grey, C. P.; Yoon, W. S.; Shao-Horn, Y. *Electrochem. Solid State Lett.* **2004**, *7*, A155-A158.

(12) Yabuuchi, N.; Koyama, Y.; Nakayama, N.; Ohzuku, T. *J. Electrochem.Soc.* **2004**, *151*, A1545-A1551.

(13) Weill, F.; Tran, N.; Croguennec, L.; Delmas, C. *J. Power Sources* **2007**, *172*, 893-900.

(14) Boulineau, A.; Croguennec, L. ; Delmas, C. ; Weill, F. *Chem. Mater.* **2009**, *21*, 4216-4222.

(15) Jarvis, K. A.; Deng, Z.; Allard, L. F.; Manthiram, A.; Ferreira, P. J. *Chem. Mater.* **2011**, *23* (16), 3614–3621.

(16) Bareno, J.; Balasubramanian, M.; Kang, S. H.; Wen, J. G.; Lei, C. H.; Pol, S. V.; Petrov, I.; Abraham, D. P. *Chem. Mater.* **2011**, *23*, 2039-2050.

(17) Rodriguez-Carvajal, J. Laboratoire Léon Brillouin. http://www-llb.cea.fr/fullweb/powder.htm (2004)

(18) Boulineau, A.; Croguennec, L.; Delmas, C.; Weill, F. *Solid State Ionics* **2010**, *180*, 1652-1659.

(19) Jiang, M.; Key, B.; Meng, Y. S.; Grey, C. P. *Chem. Mater.* **2009**, *21*, 2733-2745.

(20) Tran, N.; Croguennec, L.; Labrugère, C.; Jordy, C.;Biensan, P.; Delmas, C. *J. Electrochem. Soc.* **2006**, *153*, A261-A269.

(21) Boulineau, A.; Croguennec, L.; Delmas, C.; Weill, F. *Dalton Transactions* **2012**, *41*, 1574-1581.

(22) Koyama, Y.; Yabuuchi, N.; Tanaka, I.; Adachi, H.; Ozhuku, T. *J. Electrochem. Soc.* **2005**, *152*, A1434-1440.

(23) Julien, C. M.; Massot, M. *Mater. Science and Engineering B* **2003**, *100*, 69-78.

(24) Yu, D.Y.W.; Yanagida, K. *J. Electrochem. Soc.* **2011**, *158*, A1015-A1022.

(25) Lu, Z.; Beaulieu, L. Y.; Donaberger, R. A.; Thomas, C. L.; Dahn, J. R. *J. Electrochem. Soc.* **2002**, *149*, A778-A785.

(26) Armstrong, A. R.; Holzapfel, M.; Novàk, P.; Johnson, C. S.; Kang, S-H.; Thackeray, M. M.; Bruce, P. G. *J. Am. Chem. Soc.* **2006***, 128*, 8694-8698.

(27) Tran, N.; Croguennec, L.; Ménétrier, M.; Weill, F.; Biensan, Ph.: Jordy, C.; Delmas, C. *Chem. Mater*. **2008**, *20*, 4815-4825.

(28) Yabuuchi, N.; Yoshii, K.; Myung, S. T.; Nakai, I.; Komaba, S. *J. Am. Chem. Soc.* **2011**, *133*, 4404-4419.

(29) Hong, Y. S.; Park, Y. J.; Ryu, K. S.; Chang, S. H.; Kim, M. G. *J. Mater. Chem.* **2004**, *14*, 1424-1429.

(30) Ito, A.; Sato, Y.; Sanada, T.; Hatano, M.; Horie, H.; Ohsawa, Y.*J. Power Sources* 2011, *196*, 6828-6834.

Chapter III

The charge and discharge mechanism of $Li_{1.20}Mn_{0.54}Co_{0.13}Ni_{0.13}O_2$

- Global structural change -

Different oxygen redox participation for bulk and surface: a possible global explanation for the cycling mechanism of $Li_{1.20}Mn_{0.54}Co_{0.13}Ni_{0.13}O_2$

H. Koga, L. Croguennec, M. Ménétrier, P. Mannessiez,

F. Weill and C. Delmas, J. Power Sources, 2013 (accepted)

Chapter III – The charge and discharge mechanism of $Li_{1.20}Mn_{0.54}Co_{0.13}Ni_{0.13}O_2$ – Global structural change -

III. 1 - Introduction

Lithium-ion batteries have been used already for quite a while to power portable devices such as cellular phones and notebooks, but they are now expected to store and deliver enough energy and power to answer the requirements for transportation and especially those for hybrid and electric vehicles. The most commonly used lithium-ion batteries remain those with the layered oxide $LiCoO_2$ and the carbon graphite at the positive and negative electrodes, respectively. Due to the high cost and possibly low resource of Co, a very intense research effort is currently under progress in order to propose alternatives to $LiCoO_2$ at the positive electrode **[1]**. $LiNi_{1-y-z}Co_yAl_zO_2$ is currently used in batteries developed for hybrid electric vehicles and for military and space applications. $LiFe^{II}PO_4$, made of cheap and abundant constituents and with a redox voltage around 3.45V vs. Li^+/Li, is presently the most praised electrode material for the next generation of Li-ion batteries to power electric vehicles as it remains chemically and thermally highly stable over the entire potential window **[2-3]**. Nevertheless, its weakness remains its low energy density compared to the layered oxide materials. More recently prospective research was performed on other polyanionic materials such as silicates **[2]**, di-phosphates **[4]**, borates **[5]**, fluorophosphates **[6-9]** and fluorosulphates **[10-13]**, in order in all cases to try to gain in energy density.

In parallel to the research on polyanionic materials, the lithium-rich layered oxides belonging to the $(1-x)LiMO_2.xLi_2MnO_3$ system (M = Ni, Co, Mn) are considered as very attractive materials as they deliver larger capacity with lower cost than $LiCoO_2$ **[14-16]**. These overlithiated materials (Li/M > 1) revealed a long *plateau* observed only during the first charge of the battery, which is uncommon in classical layered oxides $Li_{1-x}M_{1+x}O_2$ ($x \geq 0$ and M = Ni, Co mainly) **[17]**. This unusual mechanism is expected to be at the origin of the large capacity observed for these overlithiated materials. The mechanisms involved during the charge-discharge of this type of materials have been addressed recently **[17-21]** but deeper structural characterizations are still required in order to understand the structure of the materials formed upon cycling and the origin of these very attractive capacities. This paper focuses on $Li_{1.20}Mn_{0.54}Co_{0.13}Ni_{0.13}O_2$ also possibly written as $0.4\,LiNi_{1/3}Mn_{1/3}Co_{1/3}O_2$ - $0.4\,Li_2MnO_3$ with high capacity. The composition and structure of different $Li_{1.20}Mn_{0.54}Co_{0.13}Ni_{0.13}O_2$ materials, obtained by the sol-gel method followed by a thermal treatment at 800°C, 900°C or 1000°C, were analyzed in detail. As we reported in a previous paper **[22]**, they are very similar whatever the synthesis temperature, with a cation ordering in the transition metal layers and a quasi-ideal layered structure. We also showed that these materials are clearly not made of separate domains of Li_2MnO_3 and $LiNi_{1/3}Mn_{1/3}Co_{1/3}O_2$, but that they are solid solutions with ordered domains limited to a few layers along the c-axis. In the present paper, we report on the structural changes observed using X-ray diffraction for $Li_{1.20}Mn_{0.54}Co_{0.13}Ni_{0.13}O_2$ upon cycling, depending on the particle size of the active material and on the cycling conditions (number of cycles, cycling rate and temperature).

III. 2 - Experimental

Three materials of composition $Li_{1.20}Mn_{0.54}Co_{0.13}Ni_{0.13}O_2$ were prepared at temperatures of 800°C, 900°C or 1000°C using the sol-gel method, as described in detail in reference **[22]**. They were characterized by X-ray diffraction (XRD) using a Siemens D5000 diffractometer equipped with a detector using energy discrimination and Cu Kα radiation, in the 10 – 80 ° ($2\theta_{Cu}$) range, with steps of 0.02 ° ($2\theta_{Cu}$) and a constant counting time of 15s. The profile matching and Rietveld refinement of the XRD patterns were performed using the Fullprof software **[23]**. The morphology of the powders was observed by scanning electron microscopy (SEM) using a Hitachi S4500 field emission microscope with an accelerating voltage of 5.0 kV. The materials were coated with a thin layer of platinum in order to prevent any charge accumulation on their surface. Surface area measurements were carried out by the Brunauer, Emmet and Teller (B.E.T) method with a Quantachrome Autosorb-1 device after the sample was dried overnight under vacuum at 300 °C.

The electrochemical properties of the prepared materials were tested using CR2325 coin cells with lithium metal as negative electrode. The positive electrodes consisted of 80 wt% of active material, 10 wt% of a carbon black / graphite (1:1) mixture and 10 wt% of polyvinylidene difluoride (PVdF) binder and were cast from N-methylpyrrolidone (NMP) based slurry on an aluminum foil. They were then pressed at 40 MPa after drying at 80°C during overnight. The cells were assembled in an argon filled glove box with the electrolyte 1M $LiPF_6$ dissolved in a mixture of propylene carbonate (PC), ethylene carbonate (EC), and dimethylcarbonate (DMC) 1:1:3 by volume. The electrochemical measurements were performed between 2.5 and 4.8 V *vs.* Li^+/Li, the cycling rate being defined so that 1 C rate corresponds to a theoretical exchange of one electron in 1 h. *Ex situ* X-ray diffraction was performed on lithium deintercalated materials recovered from batteries at different states of charge and discharge. Before their analysis they were washed with DMC in large excess, dried at room temperature under vacuum and prepared in a specific sample-holder to prevent any contact with ambient atmosphere and thus avoid their evolution.

III. 3 - Results and discussion

III. 3. 1 - Composition, structure and microstructure of the powders prepared at different temperatures

As detailed in reference **[22]**, the XRD patterns obtained for the three $Li_{1.20}Mn_{0.54}Co_{0.13}Ni_{0.13}O_2$ materials prepared at 800°C, 900°C or 1000°C are compared in **Fig. III. 1a**. All the main peaks, except for the extra broad and small intensity peaks observed between 20 and 30° ($2\theta_{Cu}$) (enlarged in **Fig. III. 1b**) can be indexed based on a hexagonal cell described in the space group *R-3m* (α-$NaFeO_2$-type structure). The cell parameters $a_{hex.}$ and $c_{hex.}$ were determined to be ~ 2.851 Å and ~ 14.235 Å, respectively. As expected, the crystallinity of the powders increases with temperature, as shown by the sharpening of the X-ray diffraction lines from 0.19° to 0.12° for $FWHM_{(003)}$ and from 0.29° to 0.19 for $FWHM_{(104)}$ when the synthesis temperature increases from 800°C to 1000°C. The extra lines observed in the [20 - 30°] angular range can be indexed considering a $\sqrt{3}.a_{hex.}$ x $\sqrt{3}.a_{hex.}$ superstructure in the transition metal planes and reveal the presence of an ordering between the large (Li^+, Ni^{II}) cations on one site and the small (Mn^{IV}, Co^{III}) cations on the other site, by analogy to the Li_2MnO_3 structure (described in the *C2/m* space group). As shown by the width and relative intensity of these extra lines, and as supported by electron diffraction data **[22]**, the ordering in the transition metal layers is rather extended whereas the correlation between the ordered slabs is restricted along the c-axis. Despite a significant difference in their crystallinity, these three materials were shown to be very similar in structure, with *(i)* a quasi ideal 2D structure (the Li^+/Ni^{II} exchange between the slab and the interslab space is indeed limited to less than 0.02) and *(ii)* a very similar local ordering of cations as revealed by ^7Li MAS NMR, Raman and electron diffraction data **[22]**.

Fig. III. 2 gives a comparison of the SEM micrographs obtained for the three materials. The primary particle size increases with the heating temperature from 50 nm to 500 nm in diameter. The higher the synthesis temperature, the sharper are the edges of the primary particles, suggesting a better crystallization. The specific surface area of these powders decreases with an increase of the thermal-treatment temperature and is equal to 9.9 m^2/g, 4.3 m^2/g and 3.6 m^2/g for the compounds obtained at 800°C, 900°C and 1000°C, respectively.

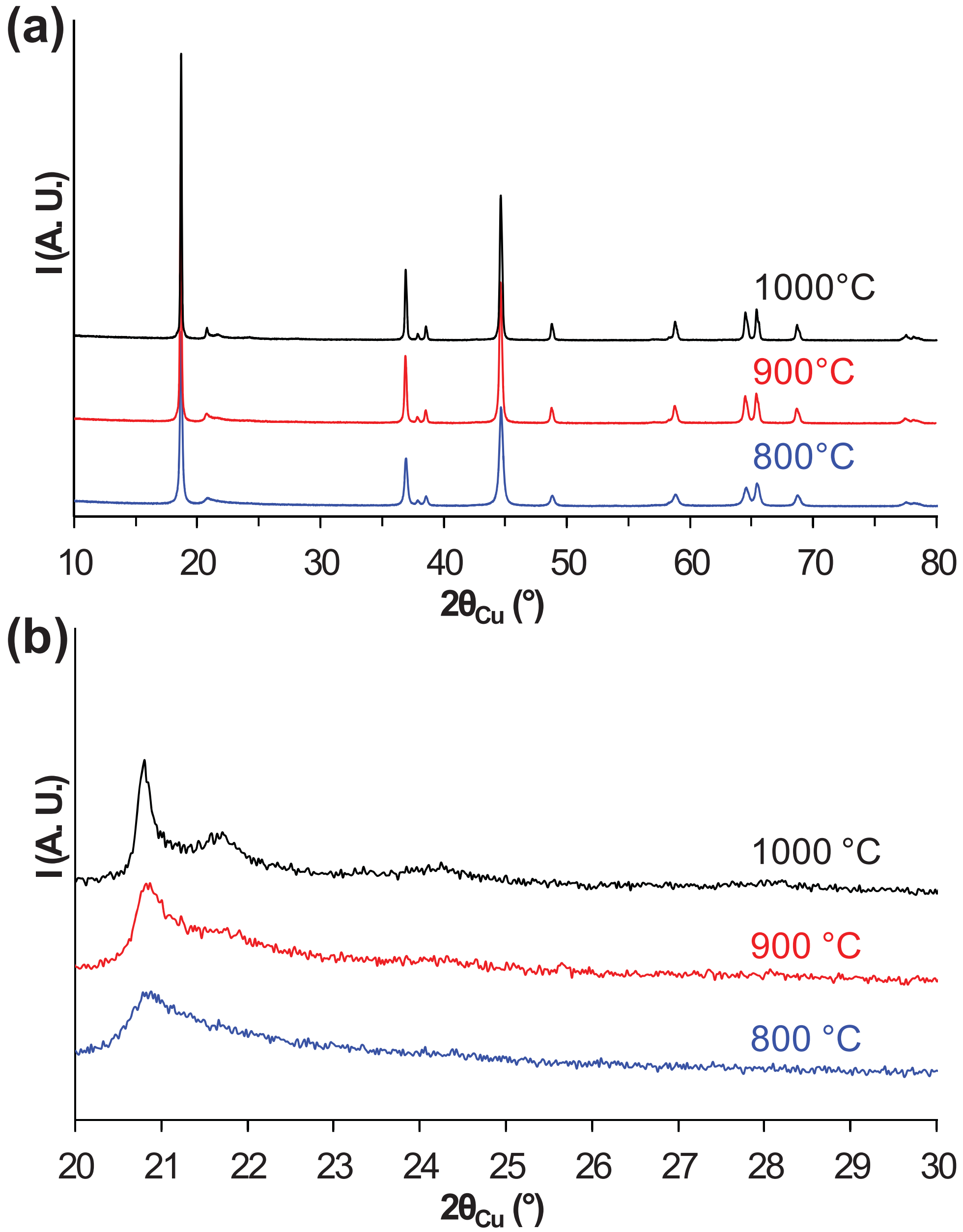

Fig. III. 1: *(a)* X-ray diffraction patterns of $Li_{1.20}Mn_{0.54}Co_{0.13}Ni_{0.13}O_2$ synthesized at 800°C, 900°C and 1000°C in the 10 – 80° ($2\theta_{Cu}$) range. *(b)* Detailed XRD data in the 20 – 30° angular range.

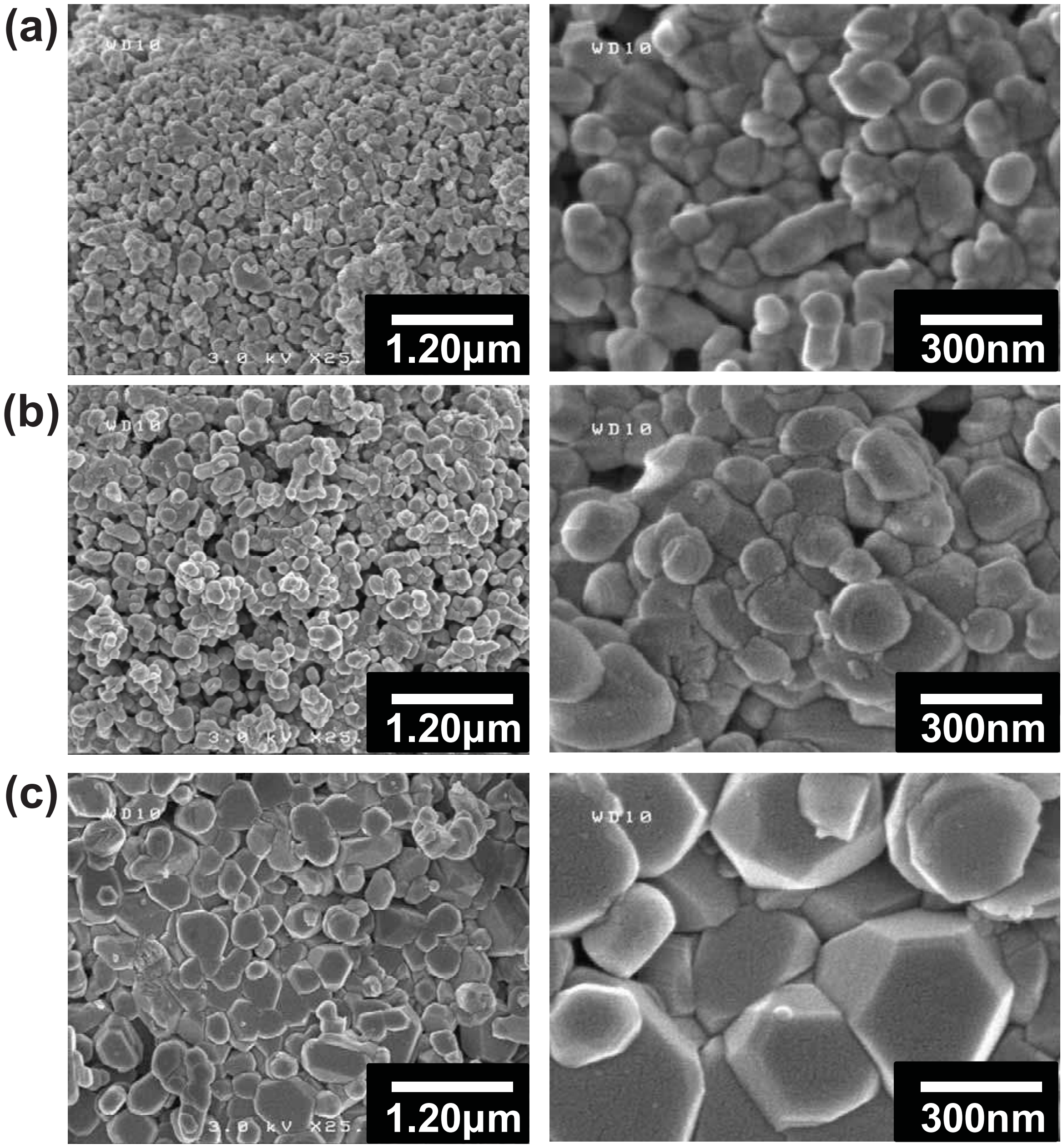
(a)
WD10
3.0 kV X25
1.20µm
WD10
300nm
(b)
WD10
3.0 kV X25
1.20µm
WD10
300nm
(c)
WD10
3.0 kV X25
1.20µm
WD10
300nm

Fig. III. 2: SEM images of $Li_{1.20}Mn_{0.54}Co_{0.13}Ni_{0.13}O_2$ synthesized at *(a)* 800°C, *(b)* 900°C and *(c)* 1000°C.

III. 3. 2 - Structural changes observed during the first cycle

The 1st cycle curves obtained for the lithium cells prepared with the three compounds as positive electrode materials and cycled at the C/20 rate in the 2.5 – 4.8 V *vs.* Li^+/Li potential window are compared in **Fig. III. 3**. The three curves are very similar, as expected from the very similar composition and structure of the powders. Upon charge the potential evolves, in a first step, continuously with lithium composition, then a voltage *plateau* is observed around 4.5V *vs.* Li^+/Li and, finally, a continuous evolution of the potential is again observed during the discharge over the whole lithium composition range. Large irreversible capacities are observed at the first cycle (more than 15% of the first charge capacity), with a first discharge capacity around 270 mAh/g (**Fig. III. 3**). This reversible capacity is around 230 mAh/g during the first 10 cycles **[22]** and decreases gradually down to 200 mAh/g at the 100th cycle. The effect of the synthesis temperature of $Li_{1.20}Mn_{0.54}Co_{0.13}Ni_{0.13}O_2$ is not obvious on the cycling performance since the differences observed here remain of the order of the reproducibility of the experiments.

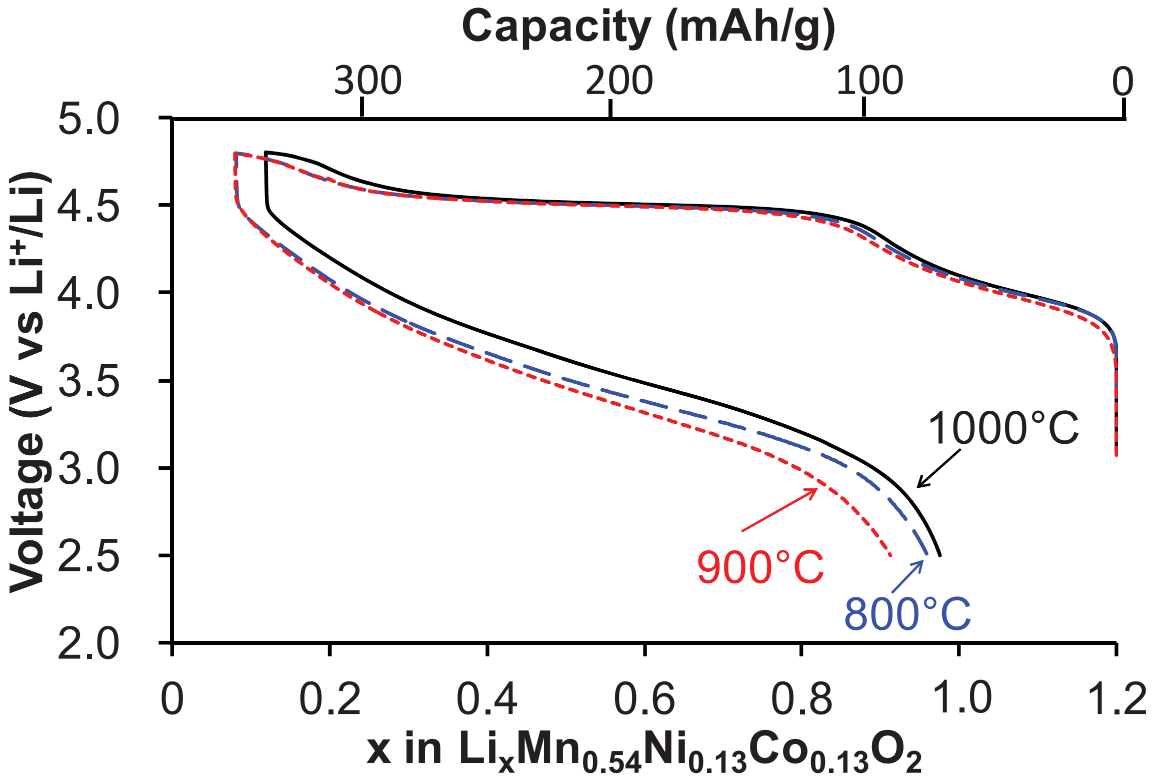

Fig. III. 3: The 1st cycle curves obtained at a rate of C/20 for different $Li//Li_xMn_{0.54}Co_{0.13}Ni_{0.13}O_2$ cells, $Li_{1.20}Mn_{0.54}Co_{0.13}Ni_{0.13}O_2$ being synthesized at 800°C, 900°C and 1000°C.

XRD analysis was carried out *ex situ* for $Li_{1.20}Mn_{0.54}Co_{0.13}Ni_{0.13}O_2$ prepared at 1000°C for different lithium compositions during the first charge and the following discharge of the battery. Eight XRD patterns are compared in **Fig. III. 4**, for key lithium compositions: 1.20 (pristine material), 0.88 (beginning of the *plateau*), 0.63, 0.37 (during the *plateau*) and 0.12 (end of the *plateau*) and then, 0.43, 0.69 and 0.98 at different discharge states. These results reveal first a fast broadening of the diffraction lines upon lithium deintercalation, as especially highlighted for the *(003)* line in **Fig. III. 4b** by the enlargement of the [18 - 19.5° ($2\theta_{Cu}$)] angular range. Then, from the beginning of the *plateau* two sets of diffraction lines that can be fully indexed in the *R-3m* space group are observed; they are maintained - with changes in the cell parameters - all along the *plateau* in charge and during the next discharge. At the end of the first discharge, as especially shown in **Fig. III. 4d** with the observation of the *(104)* line, two sets of diffraction lines are still present. In addition, the enlargement given in the [20 - 24° ($2\theta_{Cu}$)] angular range in **Fig. III. 4c** reveals the irreversible broadening and decrease in intensity of the extra lines associated to the superstructure due to the cation ordering in the slabs.

Changes in the lattice parameters with lithium composition (x in $Li_xMn_{0.54}Co_{0.13}Ni_{0.13}O_2$) are given in **Fig. III. 5** (in blue upon charge and in red upon discharge) and **Table III. 1**. An example of refinement is given in **Fig. III. 6** (by the Le Bail method for the material $Li_{1.20}Mn_{0.54}Co_{0.13}Ni_{0.13}O_2$ (1000°C) recovered after one cycle at C/20 rate at room temperature). From the beginning of the *plateau* in the first charge, all the XRD patterns were analyzed considering the presence of two lamellar oxide phases. The $a_{hex.}$ cell parameter decreases at the beginning of the first charge and maintains around 2.834 Å for the two phases formed during the *plateau*. During the discharge the $a_{hex.}$ cell parameter continuously increases in parallel for the two phases (**Fig. III. 5a**). As shown in **Fig. III. 5b** the $c_{hex.}$ cell parameter increases at the beginning of the first charge and then decreases for the two phases on the *plateau* so that they can be best separated at the end of the charge. During the following discharge the two phases remain, their $c_{hex.}$ cell parameters first increase and then decrease upon lithium intercalation. The value of $a_{hex.}$ is highly correlated to the average oxidation state of the transition metal ions since it corresponds to the metal – metal distance in the MO_2 slab. A decrease of $a_{hex.}$ is thus associated to a decrease of the transition metal ionic radius and therefore to its oxidation and, conversely, an increase associated to its reduction. The absence of change in $a_{hex.}$ suggests no change in the oxidation state of the transition metal ions on the *plateau* despite lithium deintercalation **[19]**, whereas the continuous increase of the $a_{hex.}$ cell parameter during the discharge suggests (contrary to what is observed during the preceding charge) a continuous reduction of the transition metal ions. $c_{hex.}$ first expands upon lithium deintercalation due to increasing electrostatic repulsions between the oxygen layers forming the interslab space since the deintercalated lithium ions do not play their screening role anymore. Upon further lithium deintercalation the Metal – Oxygen bond becomes more and more covalent leading to less charged oxygen ions and thus to a shrinkage of c_{hex}. Even if the global evolution of $c_{hex.}$ is expected for classical $Li_{1-x}M_{1+x}O_2$ layered oxides ($x \geq 0$) **[24]**, the uncommon evolution of $a_{hex.}$ as a function of the lithium content in $Li_xMn_{0.54}Co_{0.13}Ni_{0.13}O_2$ and the formation of two phases after the *plateau* highlight the occurrence of a complex lithium deintercalation mechanism in this overlithiated manganese-rich layered oxide during the first charge.

Biphased domains are often observed for classical layered oxides at the end of the 1st charge when total removal of Li ions from the structure requires for instance stabilization of another oxygen packing: an O1-type structure (with an *AB* oxygen packing as in CdI_2) is for instance formed for NiO_2 through a two-phase domain involving NiO_2 and $Li_{1/4}NiO_2$ **[24]**. In the case of $Li_{1.20}Mn_{0.54}Co_{0.13}Ni_{0.13}O_2$, the phase observed at the beginning of the *plateau* transforms into a mixture of two new phases, without any change in the oxygen packing, instead of progressively disappearing to the benefit of a new phase. Furthermore, the two phases formed evolve in parallel on the *plateau* with further lithium deintercalation. We have observed as shown in **Fig. III. 4** that a global broadening of the lines occurs during the first charge and is maintained during the next discharge, suggesting an increasing disorder in the material with a decrease of the coherent domains size. From X-ray diffraction experiments only, we cannot describe in depth the organization of these domains formed upon cycling. The XRD patterns were calculated taking into account the presence of *two phases*, but in fact each of them is most probably an average description of a distribution of phases with very close composition and cation distributions. It is also essential to mention that the appearance of this two-phase mixture cannot be associated to a heterogeneity that would be already present in the pristine material, indeed combining diffraction (X-rays, neutrons and electrons), NMR and Raman spectroscopies the homogeneity of $Li_{1.20}Mn_{0.54}Co_{0.13}Ni_{0.13}O_2$ was confirmed from longer to more local scales **[22]**. Finally, the $c_{hex.}/a_{hex.}$ ratio determined for the phases formed upon cycling remains always larger than 5 and is thus significantly different from 4.90 which is expected for a long range spinel-type structure. Nevertheless, it does not prevent the formation at the local scale of domains with transition metal ions in the interslab spaces, usually improperly called spinel phase in literature.

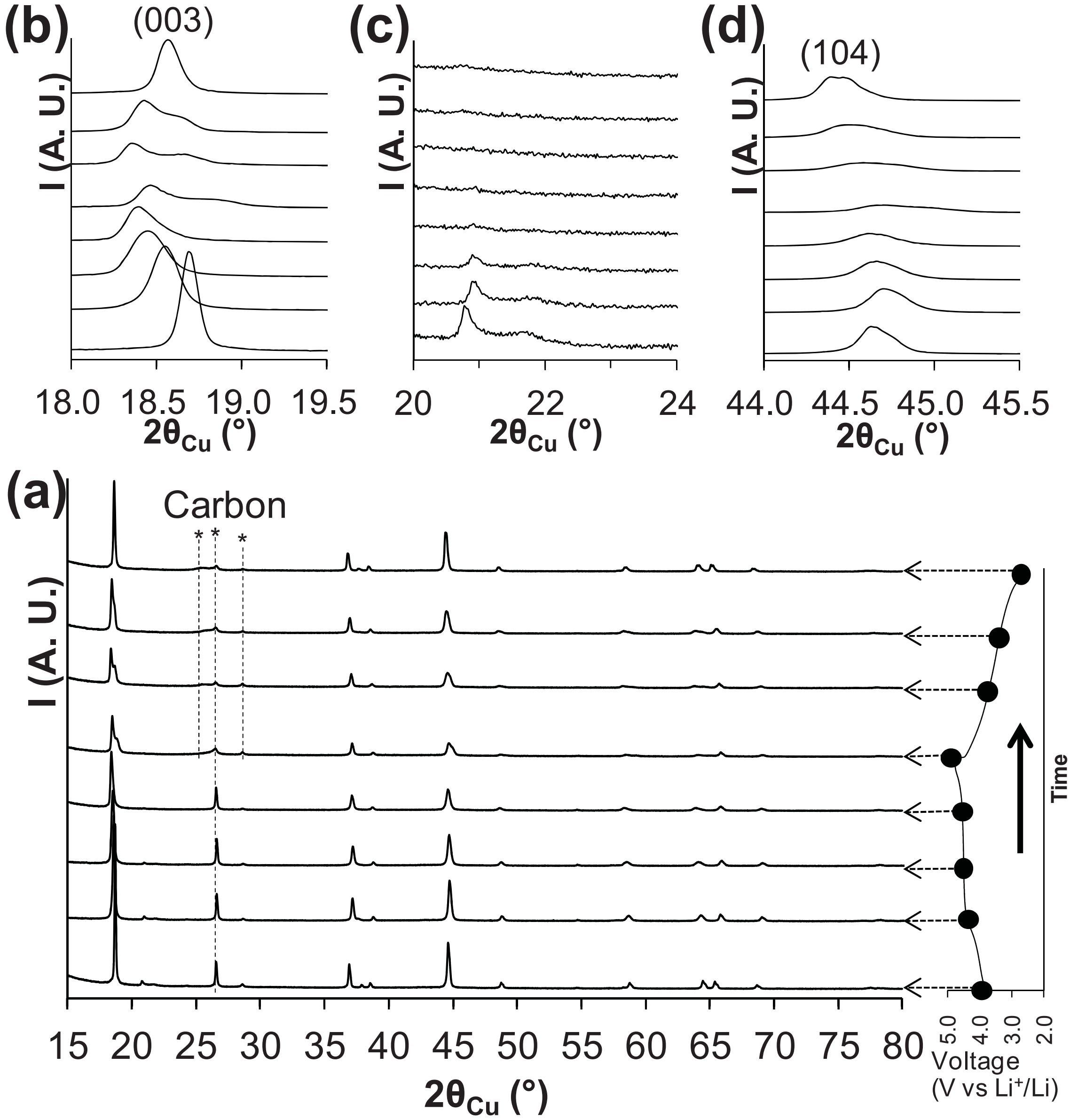

Fig. III. 4: *(a)* X-ray diffraction patterns of $Li_{1.20}Mn_{0.54}Co_{0.13}Ni_{0.13}O_2$ recovered during the 1st cycle at different states of charge and discharge of the lithium battery. A typical electrochemical curve is given on the right part of the figure in order to indicate the lithium composition of the material studied. *(b)* Detailed XRD data in the 18 - 19.5° ($2\theta_{Cu}$) angular range, *(c)* in the 20 - 24° ($2\theta_{Cu}$) angular range, and *(d)* in the 44 - 45.5° ($2\theta_{Cu}$) angular range.

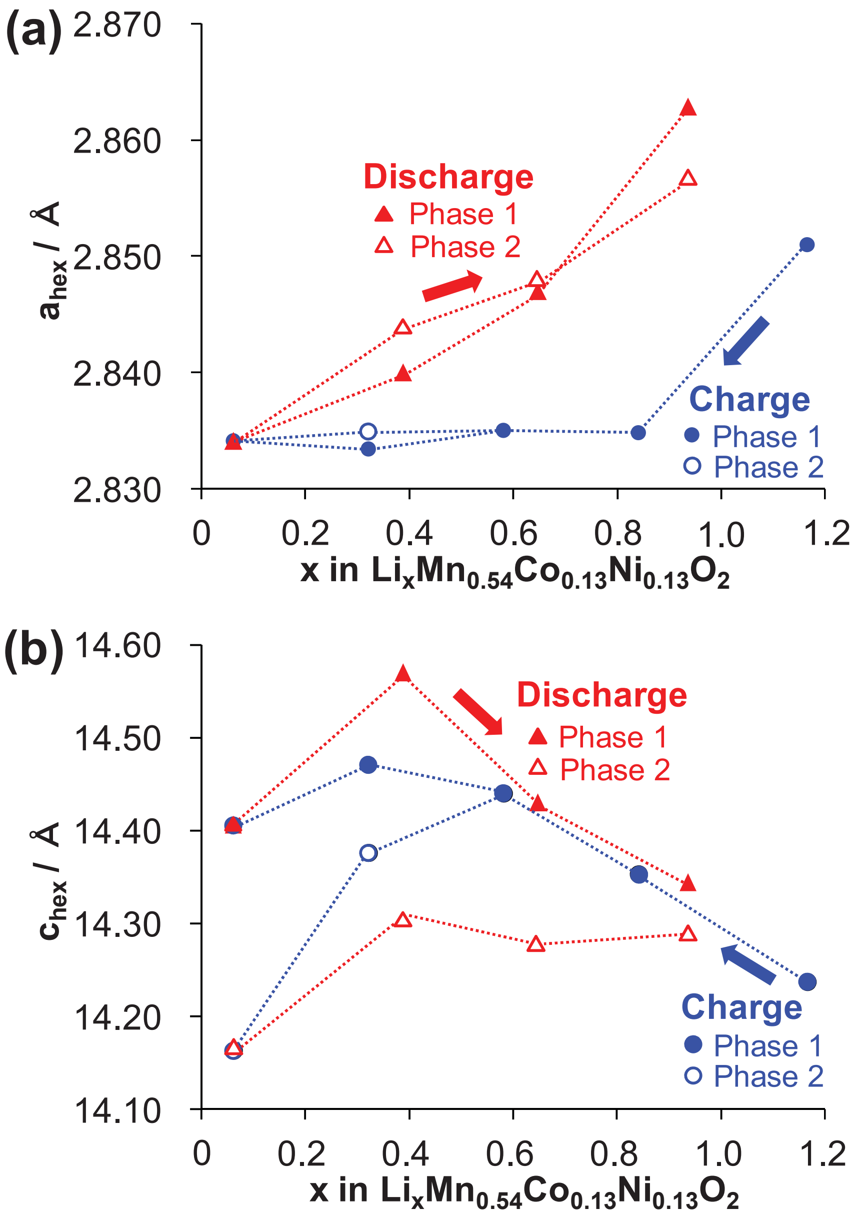

Fig. III. 5: Changes in lattice parameters, a_{hex} *(a)* and c_{hex} *(b),* versus lithium composition (x in $Li_xMn_{0.54}Co_{0.13}Ni_{0.13}O_2$) during the 1st charge and discharge. Due to the presence of these two phases in the material formed upon cycling, x defines the average composition in lithium for the mixture but not that of each phase.

Table III. 1: Changes in lattice parameters during the 1st charge and discharge.

	x ($Li_xMn_{0.54}Co_{0.13}Ni_{0.13}O_2$)	Phase 1		Phase 2	
		$a_{hex.}$	$c_{hex.}$	$a_{hex.}$	$c_{hex.}$
Charge	1.16	2.851(2)	14.237(3)	-	-
	0.84	2.8348(2)	14.353(3)	-	-
	0.58	2.835(2)	14.44(2)	-	-
	0.32	2.8334(3)	14.472(2)	2.8349(4)	14.376(4)
	0.07	2.8341(3)	14.406(3)	2.8342(2)	14.163(1)
Discharge	0.39	2.84(2)	14.57(2)	2.844(2)	14.31(1)
	0.65	2.847(2)	14.43(2)	2.848(1)	14.28(1)
	0.94	2.8629(2)	14.344(2)	2.8568(7)	14.29(3)

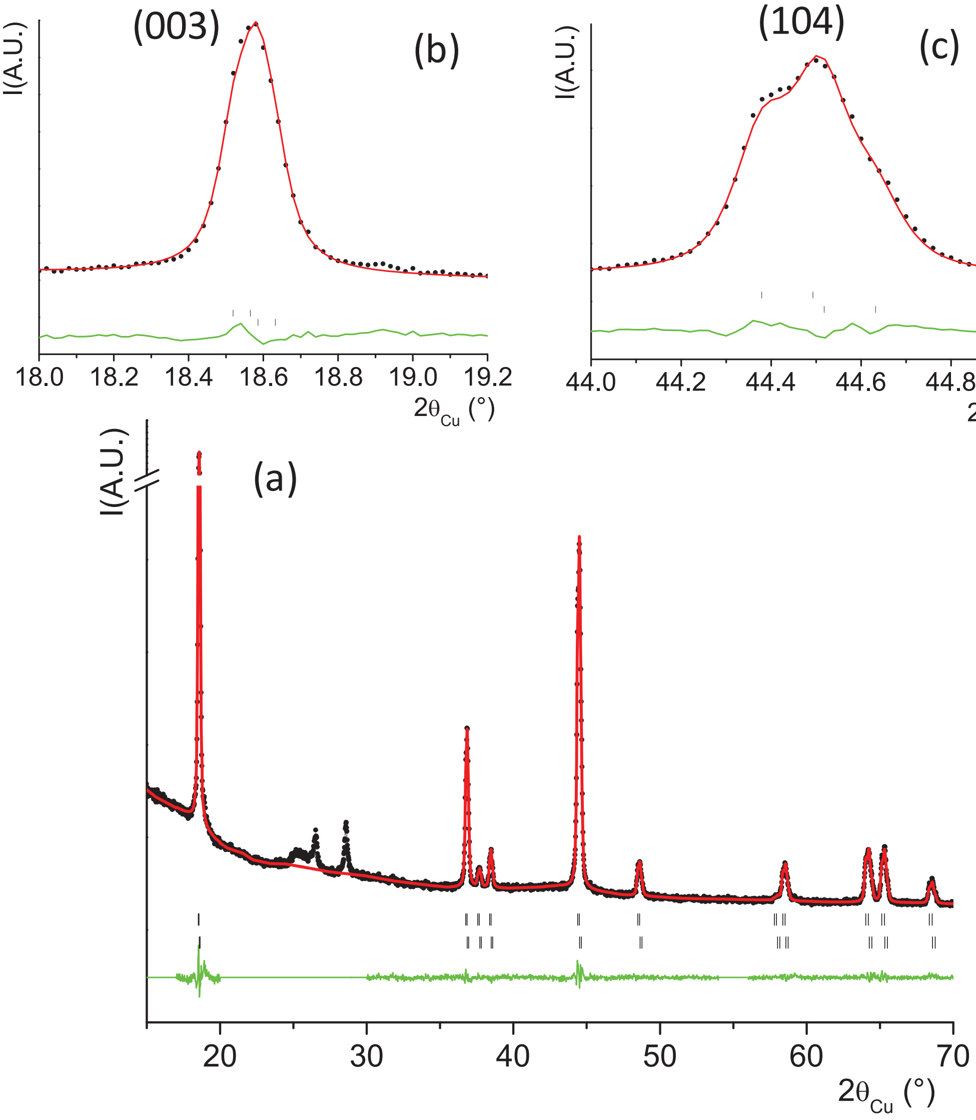

Fig. III. 6: *(a)* Results of the refinement by the Le Bail method of the X-ray diffraction pattern obtained for $Li_{1.20}Mn_{0.54}Co_{0.13}Ni_{0.13}O_2$ recovered from the battery after a 1st cycle at C/20 rate and at room temperature; detailed XRD data in the 18 – 19.2° ($2\theta_{Cu}$) range *(b)* and in the 44 - 45° ($2\theta_{Cu}$) range *(c)*.

III. 3. 3 - Effect of the powder particle size and cycling conditions on the phase separation

Similar analyses were performed for the $Li_{1.20}Mn_{0.54}Co_{0.13}Ni_{0.13}O_2$ material synthesized at 800°C and 900°C, and the results are compared to those obtained for the sample synthesized at 1000°C in **Fig. III. 7**. We chose here to restrict the XRD patterns to the *(003)* lines angular range in order to highlight changes in the phase diagram. Whatever the synthesis temperature of $Li_{1.20}Mn_{0.54}Co_{0.13}Ni_{0.13}O_2$, phase separation occurs from the beginning of the *plateau*; furthermore the amount of phase 2 (smaller $c_{hex.}$) versus phase 1 (larger $c_{hex.}$) increases when the particle size decreases and thus when the specific surface area increases.

Fig. III. 8a shows the cycling curves obtained for lithium cells with $Li_{1.20}Mn_{0.54}Co_{0.13}Ni_{0.13}O_2$ synthesized at 1000°C as positive electrode material: the 1st, 2nd, 10th, 50th and 100th charges and discharges obtained at C/20 rate and at room temperature are compared. The reversible discharge capacity was shown to reach ~ 200 mAh/g at the 100th cycle. The shape of the charge and discharge curves evolves continuously during the first fifty cycles, as even more clearly highlighted by the differential curves $dQ/dV = f(V)$ given in **Fig. III. 8b**. Then almost no changes are observed during the next fifty cycles. During the first cycles all the redox processes involved during lithium deintercalation and reintercalation occur above 3.2 V *vs.* Li^+/Li, with (after the 1st charge) two main potential ranges in charge and in discharge as pointed out by the two dotted lines *A* and *B*. Upon further cycling the redox processes involved partially shift to lower voltages as shown by line *C* (down to 2.75 V *vs.* Li^+/Li in discharge), with the disappearance of the intermediate potential process (line *B*) and maintenance of the higher potential one (line *A*). These results suggest a continuous structural modification of the material during the first fifty cycles, with in addition a change in the redox couples involved in the lithium (de)intercalation reactions: manganese ions might therefore participate to the redox processes. Indeed, it is interesting to recall that for *layered* O3-$LiMn^{III}O_2$ (monoclinic **[25-26]**), lithium deintercalation from the *layered* structure occurs during the 1st charge at 3.6 – 3.7 V vs. Li^+/Li with the oxidation of Mn^{3+} to Mn^{4+}. Then, upon cycling *layered* Li_xMnO_2 material transforms into spinel type structure with redox processes in two potential ranges, one around 3.0 V and another around 4.0 V vs. Li^+/Li. In the case of $Li_{1.20}Mn_{0.54}Co_{0.13}Ni_{0.13}O_2$ the redox process *B* (that disappears) could thus be associated to the Mn^{4+}/Mn^{3+} redox couple in the layered stacking, and the redox process *C* observed after tens of cycles could be associated to the Mn^{4+}/Mn^{3+} redox couple in the domains with transition metal ions in the interslab spaces. As shown in **Fig. III. 9** (and especially in **Fig. III. 9c**), whatever the number of cycles the material recovered at the end of the discharge is a mixture of *two phases*. With an increasing number of cycles the heterogeneity of the material increases as revealed by the larger broadening of the X-ray diffraction lines. Furthermore, the amount of *phase 2* (smaller $c_{hex.}$) increases versus that of *phase 1* (larger $c_{hex.}$) upon cycling. However despite the number of cycles no formation of long range spinel-type structure is observed: the ratio $c_{hex.}/a_{hex.}$ remains around 5.

The impact of a smaller charge rate (C/100; *i.e.* in conditions closer to the equilibrium) and of higher cycling temperature (55°C) on the homogeneity of the material formed upon cycling was checked versus classical conditions (charge at C/20 rate and at 25°C). The corresponding cycling curves are given in **Fig. III. 10** and the X-ray diffraction data recorded at the end of these first cycles in **Fig. III. 11**. Although almost no difference is observed between the three charges (except a slight decrease in potential for lower rate and higher temperature), an obvious difference in shape and in reversible capacity exists between the three discharges. The XRD patterns reveal the formation of still heterogeneous samples, with an increasing amount of *phase 2* (smaller $c_{hex.}$) versus *phase 1* (larger $c_{hex.}$).

Altogether it appears that whatever the cycling conditions (cycling rate, number of cycles, cycling temperature) and powder particle size, the materials formed upon cycling from the beginning of the *plateau* are and remain heterogeneous. This shows that, whatever the conditions, the materials are far from equilibrium.

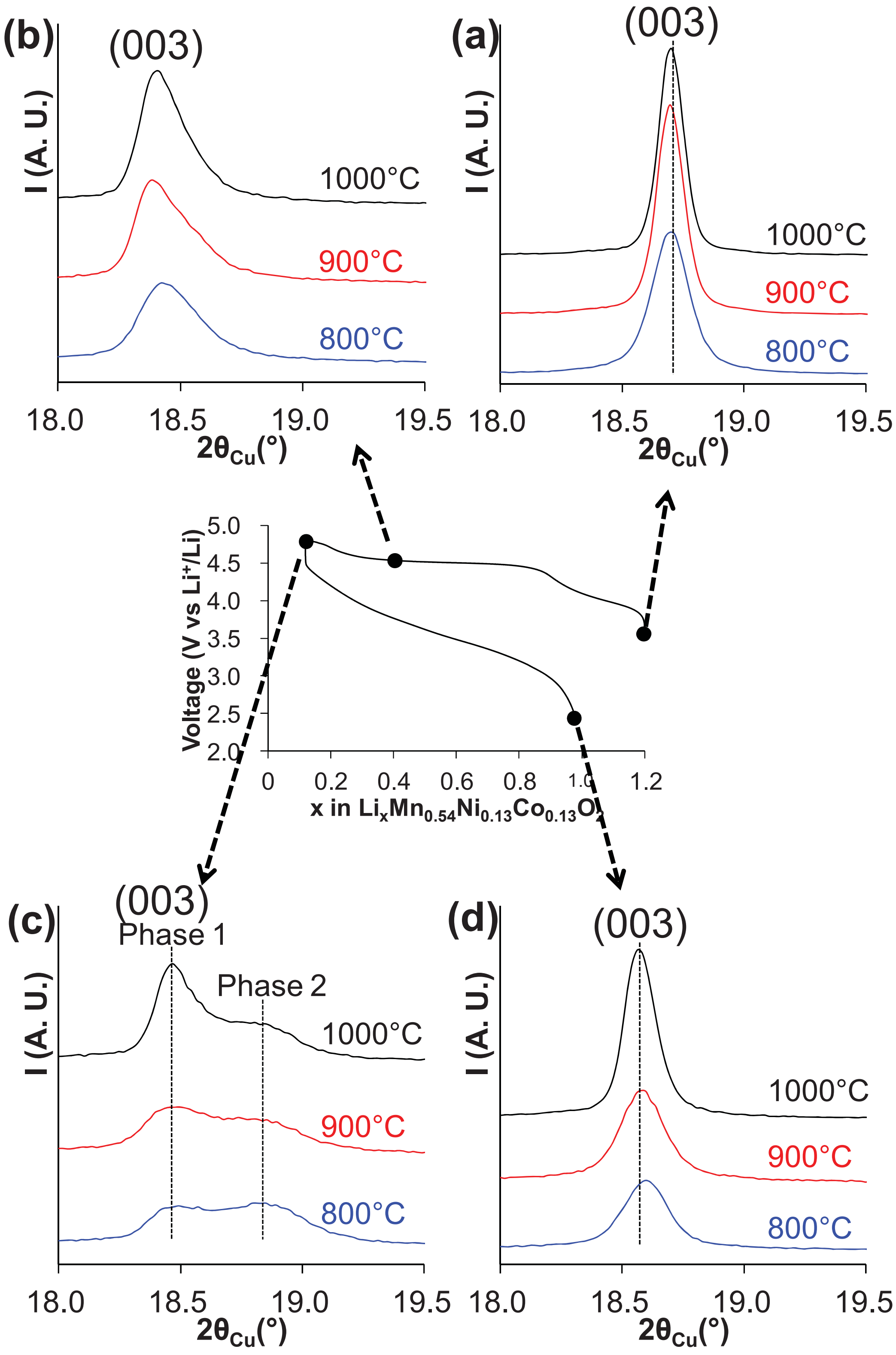

Fig. III. 7: Changes in the X-ray diffraction patterns of $Li_xMn_{0.54}Co_{0.13}Ni_{0.13}O_2$ synthesized at 800°C, 900°C and 1000°C and recovered from the batteries at different states of charge and discharge during the 1st cycle: *(a)* in the initial state, *(b)* on the *plateau*, *(c)* at the end of the *plateau* and *(d)* at the end of the 1st cycle. The angular range is limited to 18 – 19.5° ($2\theta_{Cu}$) in order to focus especially on the *(003)* diffraction lines.

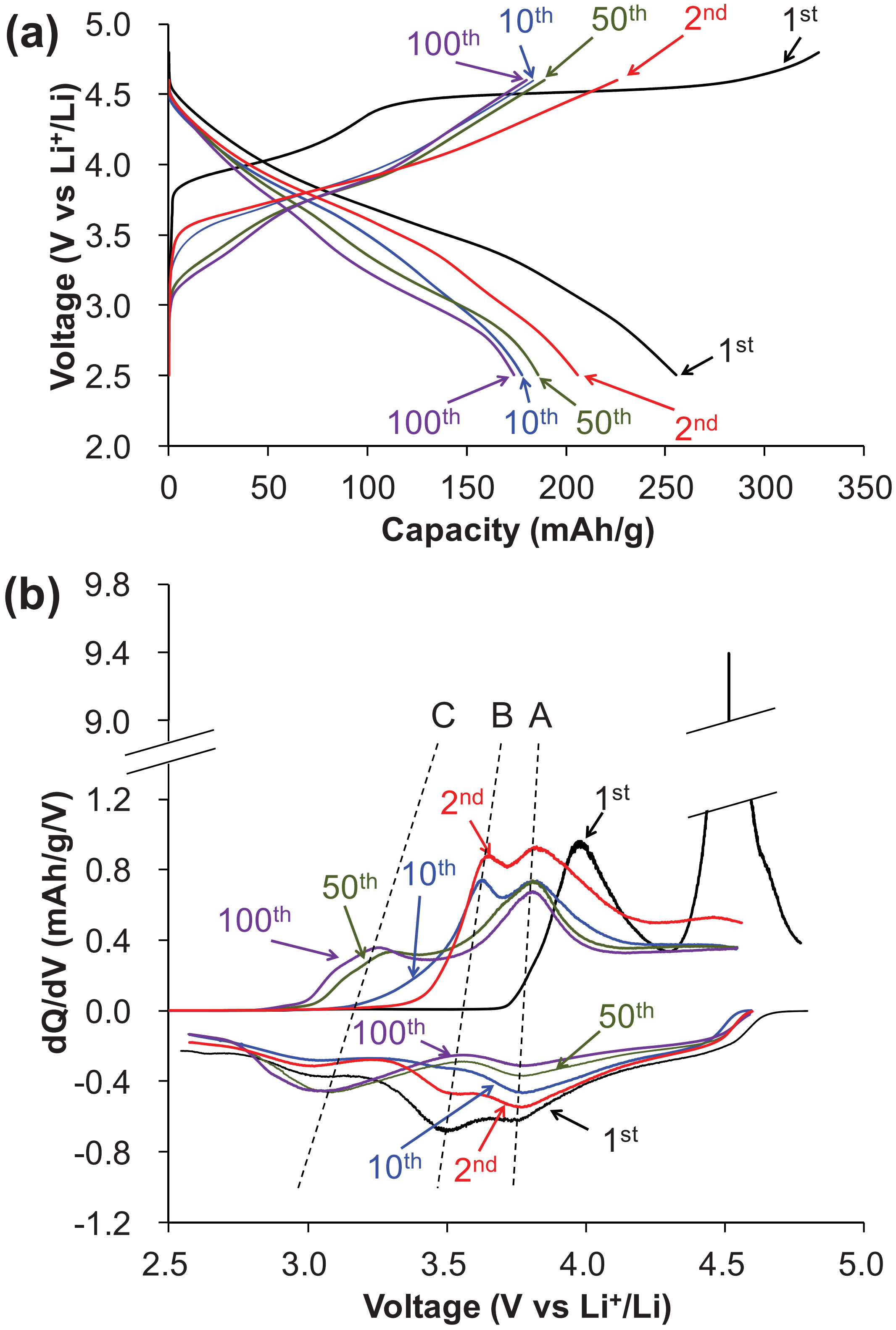

Fig. III. 8: *(a)* Comparison of the 1st, 2nd, 10th, 50th and 100th charge-discharge curves obtained for Li // $Li_{1.20}Mn_{0.54}Co_{0.13}Ni_{0.13}O_2$ cells with $Li_{1.20}Mn_{0.54}Co_{0.13}Ni_{0.13}O_2$ prepared at 1000°C. *(b)* Corresponding differential curves dQ/dV = f(V).

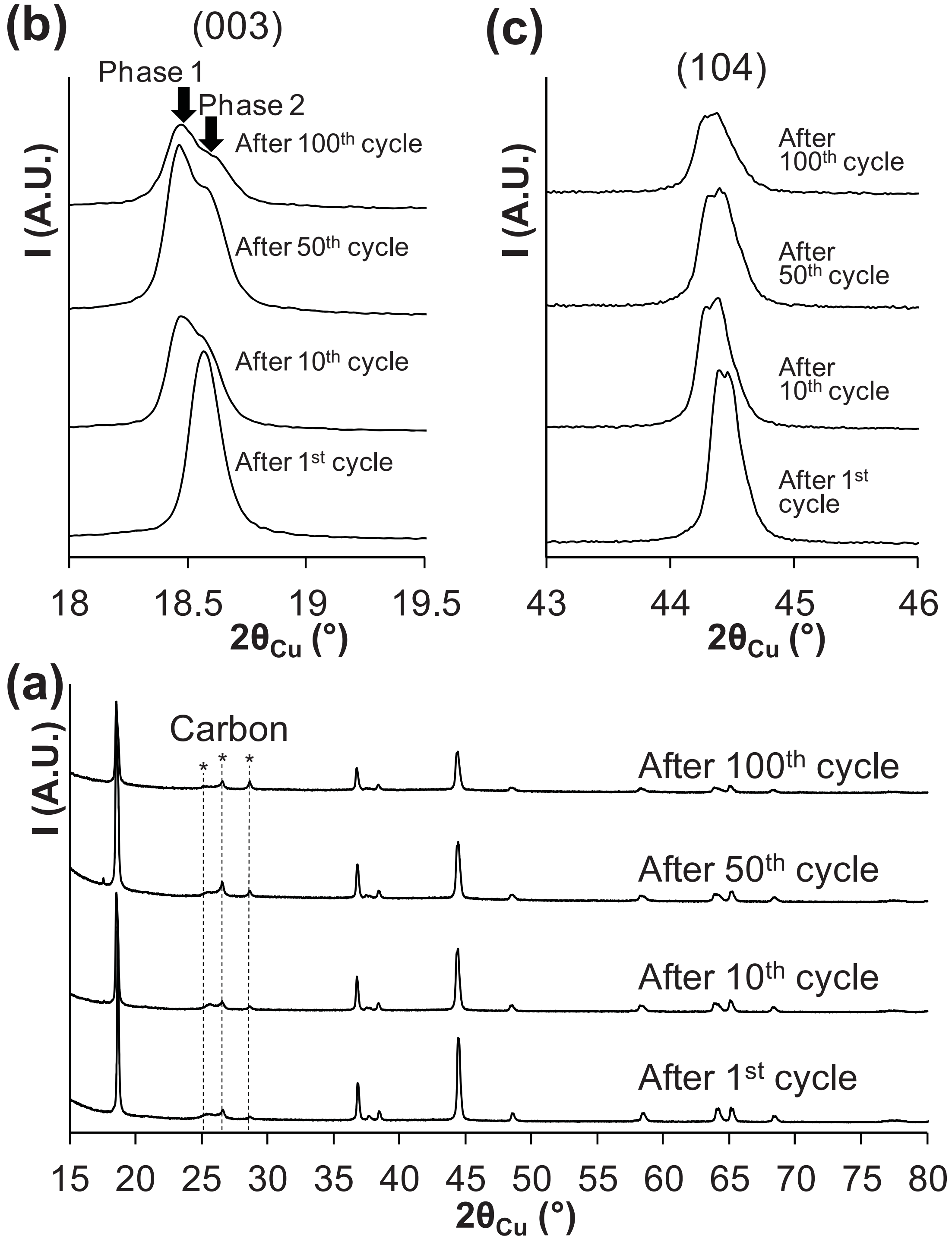

Fig. III: 9. X-ray diffraction patterns of $Li_{1.20}Mn_{0.54}Co_{0.13}Ni_{0.13}O_2$ synthesized at 1000°C and recovered from the batteries after the 1st, 10th, 50th and 100th cycle *(a)*; detailed XRD data in the 18 – 19.5° ($2\theta_{Cu}$) range *(b)* and in the 43 - 46° ($2\theta_{Cu}$) range *(c)*.

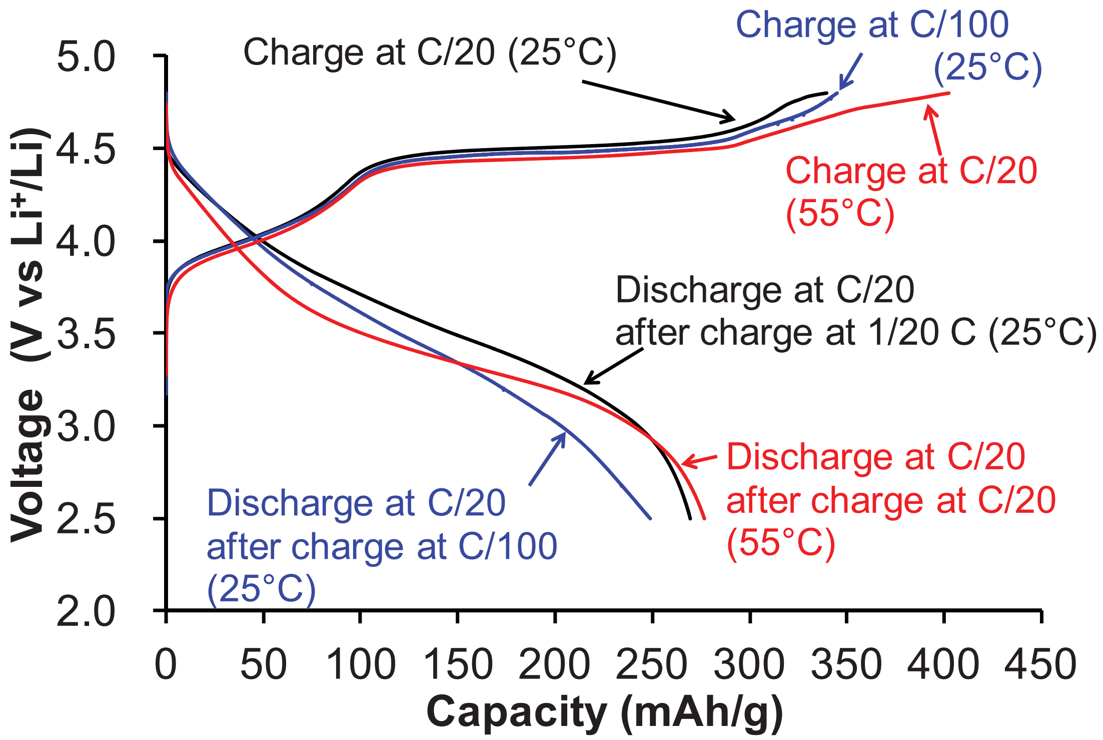

Fig. III. 10: Comparison of the first charge and discharge curves obtained for Li // $Li_{1.20}Mn_{0.54}Co_{0.13}Ni_{0.13}O_2$ cells in different conditions of cycling: charge with cycling rates of C/20 or C/100, discharge with cycling rate of C/20, cycling temperature of 25°C or 55°C.

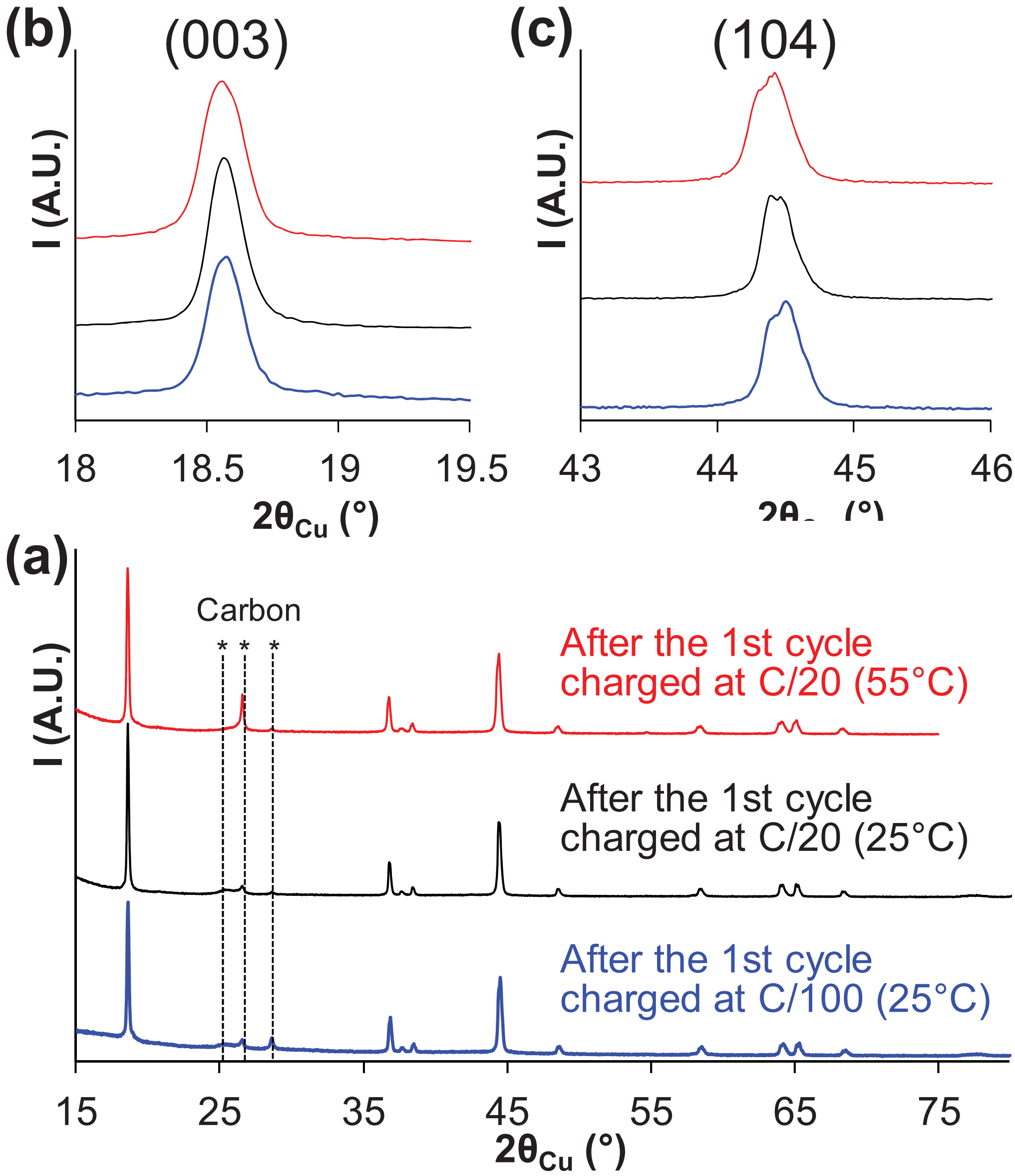

Fig. III. 11: Comparison of the X-ray diffraction patterns obtained for the material $Li_{1.20}Mn_{0.54}Co_{0.13}Ni_{0.13}O_2$ recovered from lithium cells charged in different conditions. All the discharges were performed at a C/20 rate.

]]>

III. 3. 4 - Discussion

According to the composition of the samples and to the oxidation states of the transition metal cations ($Li_{1.20}Mn^{\mathbf{IV}}_{0.54}Co^{\mathbf{III}}_{0.13}Ni^{\mathbf{II}}_{0.13}O_2$) in the pristine materials, the first part of the charge is expected to be associated to the oxidation of Ni and Co to the tetravalent state (up to $Li_{0.81}Mn^{\mathbf{IV}}_{0.54}Co^{\mathbf{IV}}_{0.13}Ni^{\mathbf{IV}}_{0.13}O_2$), and the *plateau* to a deintercalation of Li that was proposed by Lu *et al.* to be compensated for by oxygen loss **[17]**. As already reported, oxygen evolution is a unique property of these Li excess manganese-rich materials but the mechanism involved is still not clear. As we already discussed in reference **[19]** for $Li_{1+x}(Ni_{0.425}Mn_{0.425}Co_{0.15})_{1-x}O_2$, two models can theoretically be considered to account for the oxygen evolution, even if only the second is expected from solid state chemist's considerations:

- 1st model: Oxygen is lost at the surface and oxygen ions diffuse within the bulk (from inside to outside); oxygen vacancies are thus formed and distributed within the material. Considering this model (**Reaction I**), lithium vacancies would remain in the slabs and could be theoretically filled by lithium ions during the next discharge with the involvement of the Mn^{4+}/Mn^{3+} redox couple.

Reaction I

$(Li_{0.98}Ni^{II}_{0.02})(Li_{0.22}Mn^{IV}_{0.54}Ni^{II}_{0.11}Co^{III}_{0.13})O_2 \rightarrow$

$(\boldsymbol{\square}_{\mathbf{0.98}}Ni^{III}_{0.02})(\boldsymbol{\square}_{\mathbf{0.22}}Mn^{IV}_{0.54}Ni^{IV}_{0.11}Co^{IV}_{0.13})(\mathbf{O}_{\mathbf{1.58}}\boldsymbol{\square}_{\mathbf{0.42}}) + 1.20\ Li^+ + 1.20\ e^- + 0.21\ O_2$

This formula is proposed for the fully deintercalated composition considering lithium deintercalation with the formation of oxygen vacancies and, as already shown for $Li_{1-z}Ni_{1+z}O_2$ **[27]**, that the nickel ions present in the interslab spaces are oxidized up to the trivalent state only.

- 2nd model: Oxygen loss occurs at the surface with migration of the transition metal ions from the surface to the bulk. Indeed, due to the oxygen loss the transition metal ions present at the surface are expected to be unstable as MO_5 environments and would thus migrate from the surface to the bulk in the sites left vacant by the lithium ions already deintercalated in the slabs. This mechanism (**Reaction II**) would induce a shrinkage of the host structure, but also a decrease in the number of Li sites that can be occupied during the following discharge (0.78 versus 1.20 initially).

Reaction II

$(Li_{0.98}Ni^{II}_{0.02})(Li_{0.22}Mn^{IV}_{0.54}Ni^{II}_{0.11}Co^{III}_{0.13})O_2 \rightarrow$

$\mathbf{0.79}\ (\boldsymbol{\square}_{\mathbf{0.975}}Ni^{III}_{0.025})(\boldsymbol{\square}_{\mathbf{0.02}}Mn^{IV}_{0.68}Ni^{IV}_{0.14}Co^{IV}_{0.16})(\mathbf{O_2}) + 1.20\ Li^+ + 1.20\ e^- + 0.21\ O_2$

This formula proposed for the fully deintercalacted composition is obtained considering, in comparison to that proposed for the first model, a full densification of the oxygen lattice (here

O_2 versus $O_{1.58}\square_{0.42}$ with more than 20% of oxygen vacancies for the former) and thus a shrinkage of the host structure (here *0.79 mol of* MO_2 versus *1 mol of* $M_{0.80}(O_{1.58}\square_{0.42})$ for the former).

In good agreement with our previous conclusions for $Li_{1+x}(Ni_{0.425}Mn_{0.425}Co_{0.15})_{1-x}O_2$ **[19]**, we can conclude that the 1st model cannot explain the mechanism involved in our $Li_{1.20}Mn_{0.54}Co_{0.13}Ni_{0.13}O_2$ compound. Indeed, according to **reaction I**, ~ 1/6 oxygen ions are estimated to be lost from the structure of $Li_{1.20}Mn_{0.54}Co_{0.13}Ni_{0.13}O_2$ after a first full charge based on the Faradays and redox processes of the transition metal ions. Almost all MO_6 environments would thus be changed to MO_5, and it is known that Mn^{4+} and Ni^{4+} ions are not stable into MO_5 environments.

Therefore, considering the 2nd model, densification occurs inducing a decrease in the number of possible Li sites per transition metal ion. In that case, the discharge capacity (with participation of manganese in addition to nickel and cobalt to the redox processes) could be estimated to ~ 230 mAh/g after the 1st cycle (*i.e.* exchange of maximum 0.78 Li^+ ions) whereas it is in fact larger than 270 mAh/g (*i.e.* more than 0.90 Li^+ ions exchanged). The 2nd model involving densification, only by itself, can thus not account for the total number of electrons exchanged during the first discharge even if it remains the most realistic from solid state chemists' considerations.

The large capacity obtained could be explained from a theoretical point of view by a combination between the two models but as already mentioned the main cations present in the material in the charge state (Mn^{4+} and Ni^{4+}) are not stable in MO_5 environments which restricts the extent of the first mechanism which therefore cannot account for the experimentally obtained capacity. This discrepancy between the experimental and the expected reversible discharge capacities thus strongly suggests that oxygen participation to the redox processes, without oxygen loss but with oxygen oxidation, has to be considered as proposed by Koyama, Goodenough and Ito in particular **[21, 28-29]**. The pinning of the manganese t_{2g} band at the top of the oxygen p band makes that latter available for oxidation and charge compensation for Lithium deintercalation. This assumption is also supported by XAS results obtained by different authors **[20-21, 30]**: manganese participation to the redox processes occurs, as suggested also by our experimental electrochemical data given in **Fig. III. 8**, but is not sufficient to explain the number of electrons exchanged in the first discharge.

Our XRD analysis has shown the formation of *two phases* upon cycling, with larger amount of *phase 2* for smaller particles and for cycling conditions closer to equilibrium. At the present stage, considering only XRD data, it is of course difficult to describe the microstructure of these materials but we can reasonably make the hypothesis that *phase 2* would be formed preferentially at the particles' surface and *phase 1* remains in the bulk. As the densification mechanism involves transition metal diffusion in the solid and oxygen loss at the surface, *phase 2* would then most probably be the densified phase obtained after loss of the oxidized oxygen ions formed at the surface during the first charge **[19]**. Only the transition metal ions would participate to the redox processes involved during further cycling of *Phase 2* ($Ni^{4+}/Ni^{3+}/Ni^{2+}$, Co^{4+}/Co^{3+} and Mn^{4+}/Mn^{3+}). *Phase 1* would be rather similar in structure to the pristine material, with also the involvement of three redox couples, but in that case two cationic redox couples only ($Ni^{4+}/Ni^{3+}/Ni^{2+}$ and Co^{4+}/Co^{3+}) and one anionic redox couple ($O^{2-\delta}/O^{2-}$).

Our experimental results combined with those reported by other authors in literature **[20-21, 30-31]** lead us to propose this mechanism: **oxygen loss at the surface** with densification of the host structure and reversible **oxygen oxidation within the bulk** without oxygen loss and without major modification of the structure. Experiments are mentioned in next chapters in order to characterize these materials recovered after cycling, which are clearly heterogeneous and *composites,* and to check these hypotheses: aberration corrected scanning transmission electron microscopy and nano beam electron diffraction experiments to get more insights into the local structure of these materials (distribution between the *two phases* and evolution upon cycling), but also *in situ* XAS to follow changes in the redox processes upon cycling.

III. 4 - Conclusions

X-ray diffraction analyses reveal that irreversible structural reorganization occurs upon cycling of the lithium and manganese-rich layered oxide $Li_{1.20}Mn_{0.54}Co_{0.13}Ni_{0.13}O_2$ in lithium cells. A mixture of *two phases* is formed on the high voltage *plateau* and is then preserved upon long range cycling, showing that the reactions involved are out of equilibrium. The impact of the particles' size and cycling conditions (cycling rate, temperature and number of cycles) on the distribution between the *two phases* shows that the surface and the bulk react differently. As it was already proposed, oxygen participates to the reactions involved upon cycling of $Li_{1.20}Mn_{0.54}Co_{0.13}Ni_{0.13}O_2$. This occurs for one phase, rather present in the bulk, through (reversible) oxygen oxidation and, for the other phase, rather present at the surface, through oxidation of oxygen anion with departure of O_2. The origin of these *two phases* would come from the difference in stability for oxidized oxygen ions between the surface and the bulk of the material.

It appears that the *plateau* observed in the first charge is correlated to the "extra" capacity obtained during the subsequent cycling of lithium and manganese-rich layered oxides. In our model, this *plateau* is due to the surface reaction of the material with oxygen oxidation and loss, which induces a reconstruction (densification) of the outer part of the crystallites. However, a reversible oxygen oxidation also occurs in the bulk of the material during this first charge, but this is not detected on the voltage since the contact with the electrolyte is via the surface where this densification reaction occurs. Once this irreversible reaction has been completed on the first charge, the *plateau* is no longer observed during the following charges and, the voltage traduces the complex (reversible) combined redox reactions of the transition metals and of oxygen. These surface reaction and reconstruction appear necessary but not sufficient to activate the reversible oxygen oxidation/reduction reaction in lithium-rich layered oxide materials. Indeed, our group previously observed densification only for $Li_{1+x}(Ni_{0.425}Mn_{0.425}Co_{0.15})_{1-x}O_2$ ($x \leq 0.12$) **[19]**, whereas we report here combination of densification at the surface with reversible oxygen oxidation/reduction in the bulk for $Li_{1.20}Mn_{0.54}Co_{0.13}Ni_{0.13}O_2$. Changes in the electronic structure during the first charge is essential, with as discussed by Koyama and Goodenough a huge impact of manganese (and thus of the manganese content in the material formula) **[28-29]**.

This mechanism could also explain the effect of a coating on the extent of "oxygen vacancy elimination" as discussed by the group of Manthiram by the comparison of $Li_{1.20}Mn_{0.54}Co_{0.13}Ni_{0.13}O_2$ either coated with a homogeneous layer of Al_2O_3 or bare **[32]**. Less "oxygen vacancy elimination" or in other words less densification was reported for the Al_2O_3 coated compound. The formation of a coating indeed decreases the *free* specific surface area of the active material (*i.e.* that in contact with the electrolyte); it might thus allow to increase the fraction of oxygen ions stabilized in their oxidized state and thus lead to a decrease of the amount of oxygen ions lost from the structure. It is however important to mention that, even with this coating, the *plateau* observed in the first charge occurs, and the irreversible reaction due to oxygen elimination is decreased, but not suppressed, in agreement with our assumption that this is required to activate the reversible oxygen oxidation/reduction in the bulk of the material.

III. 5 - References

[1] Mizushima, K.; Jones, P. C.; Wiseman, P. J. and Goodenough, J. B., *Mater. Res. Bull.*, **1980**, 15, 783

[2] Ellis, B. L.; Lee, K. T. ; Nazar, L. F. ; *Chem. Mater.,* **2010**, 22, 691

[3] Maccario M., Croguennec L., Le Cras F. and Delmas C., *J Power Sources*, **2008**, 183, 411

[4] Nishimura, S.; Nakamura, M.; Natsui, R.; Yamada, A.; *J. American Chem. Soc.*, **2010**, 132, 13596.

[5] Yamada, A.; Iwane, N.; Harada, Y.; Nishimura, S.-i.; Koyama, Y.;Tanaka, I. *Adv. Mater*, **2010**, 22, 3583.

[6] Marx, N.; Croguennec, L.; Carlier, D.; Wattiaux, A.; Le Cras, F.; Suard, E.; Delmas, C. *Dalton Trans.* **2010**, 39(21), 5108.

[7] Recham, N.; Chotard, J. N.; Dupont, L.; Delacourt, C.; Walker, W.; Armand, M.; Tarascon, J. M.; *Nature Materials,* **2010**, 9, 68.

[8] Ramesh, T. N.; Lee, K. T.; Ellis, B. L.; Nazar, L. F.; *Electrochem. Solid-State Letters,* **2010**, 13(4), A43.

[9] Ateba Mba, J.M.; Masquelier, C.; Suard, E.; Croguennec, L., *Chem. Mater.*, **2012**, *24*, **1223.**

[10] Reddy, M. A.; Pralong, V.; Caignaert, V.; Varadaraju, U. V.; Raveau, B. *Electrochem. Comm.,* **2009**, 11, 1807.

[11] Barpanda, P. ; Ati, M. ; Melot, B. C. ; Rousse, G. ; Chotard, J-N. ; Doublet, M-L. ; Sougrati, M. T. ; Corr, S. A. ; Jumas, J.-C.; Tarascon, J.-M;. *Nature Materials*, **2011**, 10, 772.

[12] Liu L.; Zhang, B.; Huang, X.-J., *Progress in Natural Science: Materials International*, **2011**, 21, 211.

[13] Tripathi, R.; Popov, G.; Ellis, B.L.; Huq, A.; Nazar, L. F.; *Energy & Environmental Science,* **2012**, 5, 6238.

[14] Lu, Z.; Dahn, J. R., *Electrochemical and solid state letters,* **2001**, 4, A191.

[15] Park, Y. J.; Hong, Y. S.; Wu, X.; Ryu, K. S.; Chang, S. H., *J. Power Sources*, **2004**, 129, 288.

[16] Wu, Y.; Manthiram, A., *Electrochem. Solid-State Lett.* **9** (2006) A221.

[17] Lu, Z.; Beaulieu, L. Y.; Donaberger, R. A.; Thomas, C. L.; Dahn, J.R., *J. Electrochem. Soc.*, **2002**, 149, A778.

[18] Armstrong, A.R.; Holzapfel, M.; Novàk, P.; Johnson, C.S.; Kang, S-H.; Thackeray, M.M.; Bruce, P.G., *J. Am.Chem. Soc.*, **2006**, 128, 8694.

[19] Tran, N.; Croguennec, L.; Ménétrier, M.; Weill, F.; Biensan, Ph.; Jordy, C.; Delmas, C., *Chem. Mater*., **2008**, 20, 4815.

[20] Yabuuchi, N.; Yoshii, K.; Myung, S.T.; Nakai, I.; Komaba, S., *J. Am. Chem. Soc.* **2011**, 133, 4404.

[21] Ito, A.; Sato, Y.; Sanada, T.; Hatano, M.; Horie, H. ; Ohsawa, Y., *J. Power Sources* **2011**, 196, 6828.

[22] Koga, H. ; Croguennec, L. ; Mannessiez, Ph. ; Ménétrier, M.; Weill, F.; Bourgeois, L. ; Duttine, M. ; Suard, E. ; Delmas, C., *J. Phys. Chem. C* **2012**, 116(25), 13497.

[23] Rodriguez-Carvajal, J. Laboratoire Léon Brillouin.
http://www-llb.cea.fr/fullweb/powder.htm (2004)

[24] Croguennec, L.; Pouillerie, C.; Delmas, C.; *J. Mater. Chem.*, **2001**, 11, 131.

[25] Capitaine, F.; Gravereau, P.; Delmas, C., *Solid State lonics*, **1996**, 89, 197.

[26] Armstrong, A. R.; Bruce, P. G.; *Nature,* **1996**, 381, 499.

[27] Pérès, J.P.; Delmas, C.; Rougier, A.; Broussely, M.; Perton, F.; Biensan, Ph. ; Willmann, P., *J. Phys. Chem. Solids,* **1996**, 57, 1057.

[28] Koyama, Y.; Tanaka, I.; Nagao, M.; Kanno, R., *J. Power Sources*, **2009**, 189, 798.

[29] Goodenough, J.B.; Kim, Y.; *Chem. Mater.*, **2010**, 22, 587.

[30] Hong, Y.S.; Park, Y.J.; Ryu, K.S.; Chang, S.H.; Kim, M.G., *J. Mater. Chem.*, **2004**, 14, 1424.

[31] Kikkawa, J.; Akita, T.; Tabuchi, M.; Tatsumi, K.; Kohyama, M., *J. Electrochem. Soc.*, **2011**, 158, A760.

[32] Liu, J.; Reeja-Jayan,B.; Manthiram, A.; *J. Phys. Chem. C,* **2010**, *114,* 9528.

Chapter IV

The charge and discharge mechanism of $Li_{1.20}Mn_{0.54}Co_{0.13}Ni_{0.13}O_2$

- Redox reaction studied by XAFS -

H. Koga, S. Belin, L. Croguennec, P. Mannessiez, M. Ménétrier,
F. Weill and C. Delmas

To be published

Chapter IV – The charge and discharge mechanism of $Li_{1.20}Mn_{0.54}Co_{0.13}Ni_{0.13}O_2$
- Redox reaction studied by XAFS-

IV. 1 - Introduction

Lithium-ion batteries have been used for portable devices for two decades, and they are favorite candidates as power sources for future vehicles such as hybrid, plug-in hybrid and electric vehicles. $LiCoO_2$ has been widely used in lithium-ion batteries as positive electrode **[1]**, however it is difficult to maintain $LiCoO_2$ in the batteries developed for vehicles due to high price and rare resource of Co. Recently, polyanionic materials represented by $LiFePO_4$ were proposed as new positive electrodes for lithium-ion batteries for transport applications. $LiFePO_4$ was found to be very attractive because iron as well as phosphate are abundant and thus low price raw materials, furthermore it shows a very high thermal stability in the charge state of the battery with (for optimized material) very good reversibility even at high rates. Nevertheless they have disadvantages as compared to $LiCoO_2$, low electronic and ionic conductivities, low energy density, etc **[2-3]**. The system $(1\text{-}x)LiMO_2.xLi_2MnO_3$ (M = Ni, Co, Mn) was reported as one of those delivering the larger capacity as compared to other layered oxides **[4-6]**. Indeed, the charge and discharge mechanism was found to be different, with an irreversible "plateau" around 4.5 V vs. Li^+/Li during the 1st charge. It was thought to be at the origin of the overcapacity observed for that kind of systems rich in Li and in Mn. During the "plateau", Dahn and coworkers mentioned that oxygen ions were oxidized and then that oxygen was lost from the structure **[4, 7-9]**, but the detailed mechanism is in fact still not clear.

XAS measurements were performed here in order to get more insight into changes occurring in $Li_{1.20}Mn_{0.54}Co_{0.13}Ni_{0.13}O_2$ to the oxidation state of each transition metal ion but also to their local environment during the charge and discharge. XAS measurement was performed *in operando* with an *in-situ* cell developed to prevent any evolution of the materials during their characterization but also to be closer to the materials really observed in the functioning of the battery **[10]**. This study was done in close collaboration with Stéphanie Belin from Soleil.

IV. 2 - Experimental

$Li_{1.20}Mn_{0.54}Co_{0.13}Ni_{0.13}O_2$ was prepared using the sol-gel method, as described in details in reference **[11]**. The positive electrodes for *ex-situ* XAS measurement consisted of 75 wt% of active material, 20 wt% of a carbon black / graphite (1:1) mixture and 5 wt% of polytetrafluoroethylene (PTFE). They were cut into ϕ14 mm with 11 mg/cm^2 of active material, and pressed at 40 MPa on an Al foil. Coin cells were assembled in an argon filled glove box with Li metal as the counter electrode and the electrolyte of 1M $LiPF_6$ dissolved in a mixture of propylene carbonate (PC), ethylene carbonate (EC), and dimethylcarbonate (DMC) 1:1:3 by volume. After cycling positive electrodes were recovered from coin cells at different states of charge and discharge in order to compare their XAS spectra to those obtained *Operando* during the cycling of the batteries (as described just after). Preliminary to these *ex-situ* experiments, the electrodes were rinsed in an excess of DMC in order to remove the residual salt ($LiPF_6$) of the electrolyte and then dried under vacuum. The positive electrodes for *Operando* XAS measurement were prepared with same processes as ex-situ XAS measurement before being pressed, and they were pressed at 40 MPa on an Al foil of 0.024 mm thickness. The cell for *Operando* XAS experiments was prepared in an argon filled glove box with the same counter electrode and electrolyte as those used for classical batteries, the specificity of the electrochemical cell developed for these kinds of experiments in transmission is the presence of two beryllium windows that allow X-rays passing through the overall stacking **[10]**. The electrochemical measurements were performed between 2.5 and 4.8 V *vs.* Li^+/Li at C/10 cycling rate, the cycling rate being defined such as the C rate corresponds to a theoretical exchange of one electron in 1 h during charge. *Operando* X-ray absorption spectroscopic investigations have been carried out to elucidate the changes of the electronic transitions and local structure of the three transition elements for the $Li_{1.20}Mn_{0.54}Co_{0.13}Ni_{0.13}O_2$ electrode during the first charge and discharge processes. We have taken advantage of the Quick-XAS monochromator **[12]** on SAMBA beamline (Synchrotoron SOLEIL), to record the three K-edges by edge-jumping between the two energy ranges [Mn, Co] and [Co, Ni] every three minutes during the functioning of the battery (**Fig. IV. 1**).

Operando XAS were carried out at SAMBA beamline of the French synchrotron radiation facility SOLEIL. The storage ring was operated in multibunch top-up at 2.75 GeV with a 400 mA current. The incident beam from the bending magnet was collimated by a first cylindrically bendable silicon Pd coated mirror, then was monochromatized using the channel-cut Si(111) QuickExafs monochromator **[12]** and the harmonic rejection was done thanks to two mirrors tilted at 6 mrad. The beam size 7 mm x 0.6 mm (horizontal x vertical) and the position on the sample were kept constant during the acquisition except when we move the cell to check the homogeneity of the electrode at the end of relaxation on one or two chosen samples. The spectra were collected at the three K-edges (Mn, Co and Ni) in transmission mode utilizing gas ionization chambers as detectors. As we have three detectors in series we can measure during all the experiments a Co metal foil which can be used as reference to calibrate the energy. The Co K edge was then recorded twice allowing us to follow continuously the running experiment and could also be used as a standard for energy calibration. X-ray Absorption Near Edge Structure (XANES) and Extended X-ray Absorption Fine Structure (EXAFS) data were performed with Athena and Artemis software package **[13].** Measurement was done at 1 Hz with an amplitude of 3.9° around the Bragg angle.

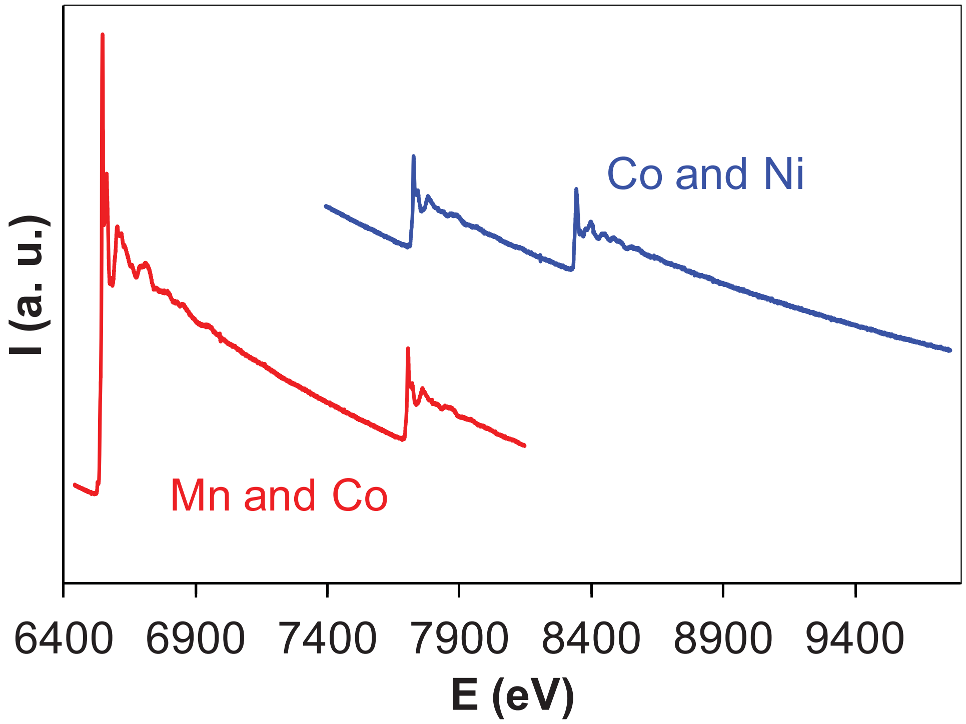

Fig. IV. 1: Energy range accessible by edge jumping with the Si(111) Quick-XAS monochromator.

IV. 3 - Results and discussion

IV. 3. 1 - Electrochemical performance of the cell developed for *Operando* study using Synchrotron radiation

XAS measurements with the cell developed for *Operando* study of processes occurring in batteries during their charge and discharge have the advantage that unstable state of a positive electrode at high voltage can be measured without any evolution. The electrochemical curves obtained for a Li//$Li_{1.20}Mn_{0.54}Co_{0.13}Ni_{0.13}O_2$ battery using either a coin cell or the cell developed for these *Operando* Synchrotron studies are compared in **Fig. IV. 2** to check for the good reproducibility between these experiments. The charge and discharge curves obtained for the *in-situ* cell appear in fact very similar to those obtained classically for a coin cell, showing that this set-up can be used to get more insights into the redox and structural changes occurring in $Li_{1.20}Mn_{0.54}Co_{0.13}Ni_{0.13}O_2$ upon cycling. To check the homogeneity of the electrochemical reaction within the electrode, XAS measurements were performed at different places of the electrode at the end of the relaxation process at the end of discharge for instance. The spectra obtained were found to be identical, showing thus that at C/10 rate the electrochemical reaction occurs homogeneously within the electrode in this cell running during the *Operando* XAS study.

Operando XAS measurements were performed during the 1st and 2nd cycles to get more insights into the irreversible reaction occurring during the 1st cycle. In addition, the first cycle was performed in different potential windows, the charge was either stopped just before the “plateau” observed at high voltage around 4.5 V vs. Li^+/Li or at 4.8 V (*i.e.* after the “plateau”).

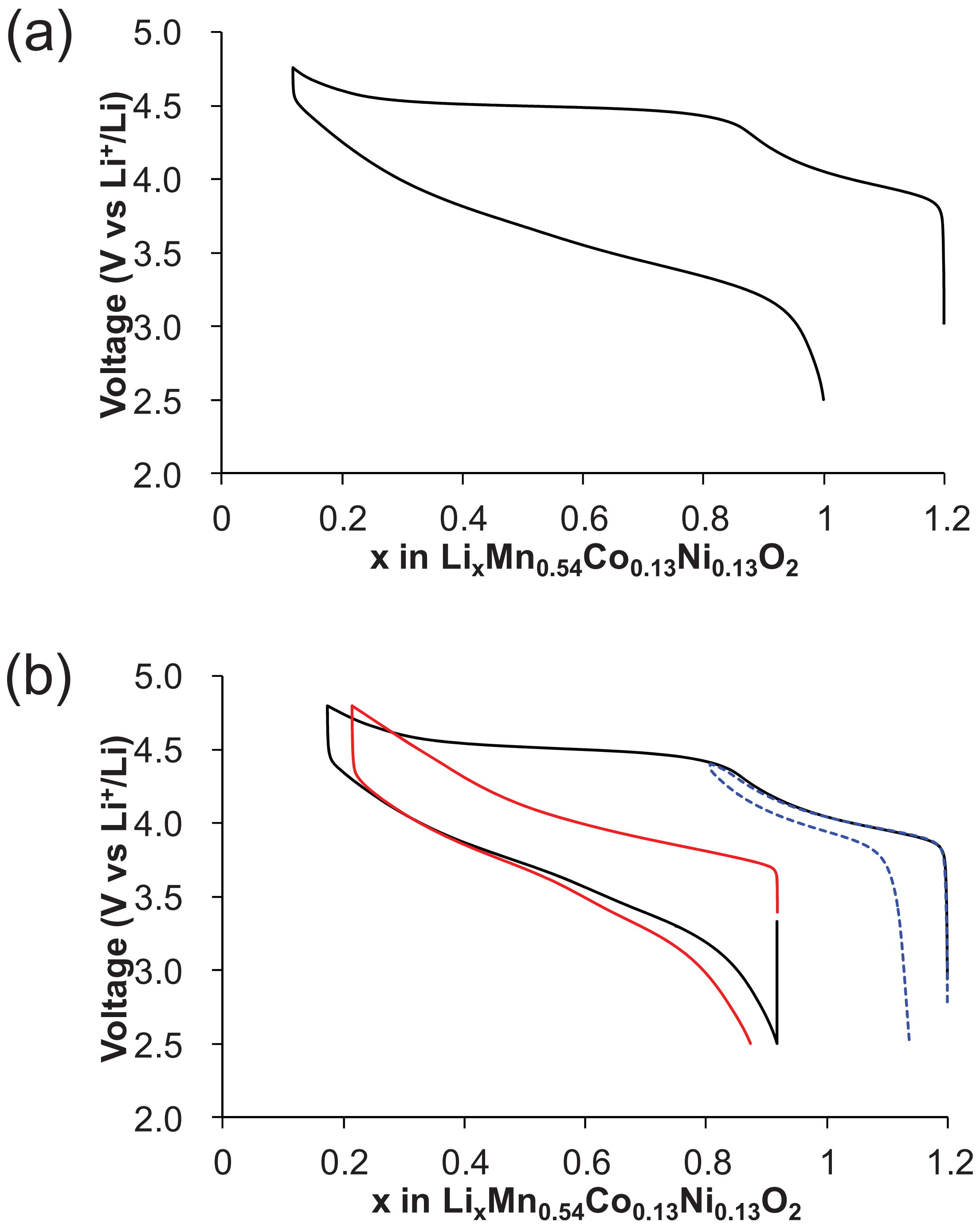

Fig. IV. 2: Charge and discharge curves obtained for Li//$Li_{1.20}Mn_{0.54}Co_{0.13}Ni_{0.13}O_2$ lithium cells: *(a)* 1st cycle obtained using a coin cell and *(b)* 1st cycle obtained with (in black) or without (in blue) the "plateau" during the 1st charge, as well as 2nd cycle (in red), these three last cycles being obtained using the cell developed for *Operando* Synchrotron studies [10].

IV. 3. 2 - XANES study during the charge and discharge of Li//$Li_{1.20}Mn_{0.54}Co_{0.13}Ni_{0.13}O_2$ batteries

XANES spectra obtained at the Ni, Co and Mn K-edges during the 1st cycle with the “plateau”, the 1st cycle without the “plateau” and the 2nd cycle (with the “plateau”) are shown in **Fig. IV. 3, Fig. IV. 4, Fig. IV. 5, Fig. IV. 6, Fig. IV. 7 and Fig. IV. 8**. Representative XANES spectra are given for each transition metal K-edge for various compositions as indicated by arrows during the charge and discharge. XANES spectra were recorded in 500 ms (2 spectra at 1 Hz) and the spectra reported in this manuscript are in fact the sum of 100 similar spectra.

IV. 3. 2. 1 - Ni K-edge

XANES spectra obtained at the Ni K-edge for $LiNi^{II}_{1/3}Co_{1/3}Mn_{1/3}O_2$ and $LiNi^{III}_{0.80}Co_{0.15}Al_{0.05}O_2$ are given in **Fig. IV. 3** and **Fig. IV. 4** as references for the different oxidation states of Ni in a layered oxide structure. Oxidation state of Ni in the pristine material could be determined as Ni^{2+} as its spectrum was found to be similar to that of $LiNi^{II}_{1/3}Co_{1/3}Mn_{1/3}O_2$ (**Fig. IV. 3a**). During the charge before the “plateau”, XANES spectra recorded at the Ni K-edge clearly shift continuously to higher energies, even higher than that observed for the spectrum of $LiNi^{III}_{0.80}Co_{0.15}Al_{0.05}O_2$ as highlighted by the arrow reported in **Fig. IV. 3a**. This shift of the Ni K-edge and the comparison with results already reported for Li_xNiO_2 indicate that Ni^{2+} ions are oxidized to the Ni^{4+} oxidation state during the charge before the “plateau” **[14-17]**. When the lithium cell is immediately discharged, before the “plateau”, XANES spectra recorded at the Ni K-edge shift reversibly to lower energy at the same position as that observed for the pristine material (**Fig. IV. 4a**). It shows that Ni ions are reduced back to the Ni^{2+} oxidation state during the discharge. During the charge during the “plateau”, XANES spectra recorded at the Ni K-edge do not shift, only a very small change in their shape is observed as pointed out by the arrows given in **Fig. IV. 3b**. Ni ions are as expected not oxidized further, but local structural changes probably occur. During the discharge after the “plateau”, XANES spectra obtained at the Ni K-edge shift continuously to lower energies until the position observed initially for the pristine material (**Fig. IV. 3c**). It reveals that Ni ions are reduced back to the Ni^{2+} oxidation state during the discharge. During the 2nd cycle performed after a 1st cycle in the potential window 2.5 - 4.8 V vs. Li^+/Li XANES spectra recorded at the Ni K-edge show, as commonly observed for other layered oxides, the oxidation of Ni ions to the Ni^{4+} oxidation state during the charge and their reversible reduction to the Ni^{2+} oxidation state during the discharge (**Fig. IV. 4b-c**).

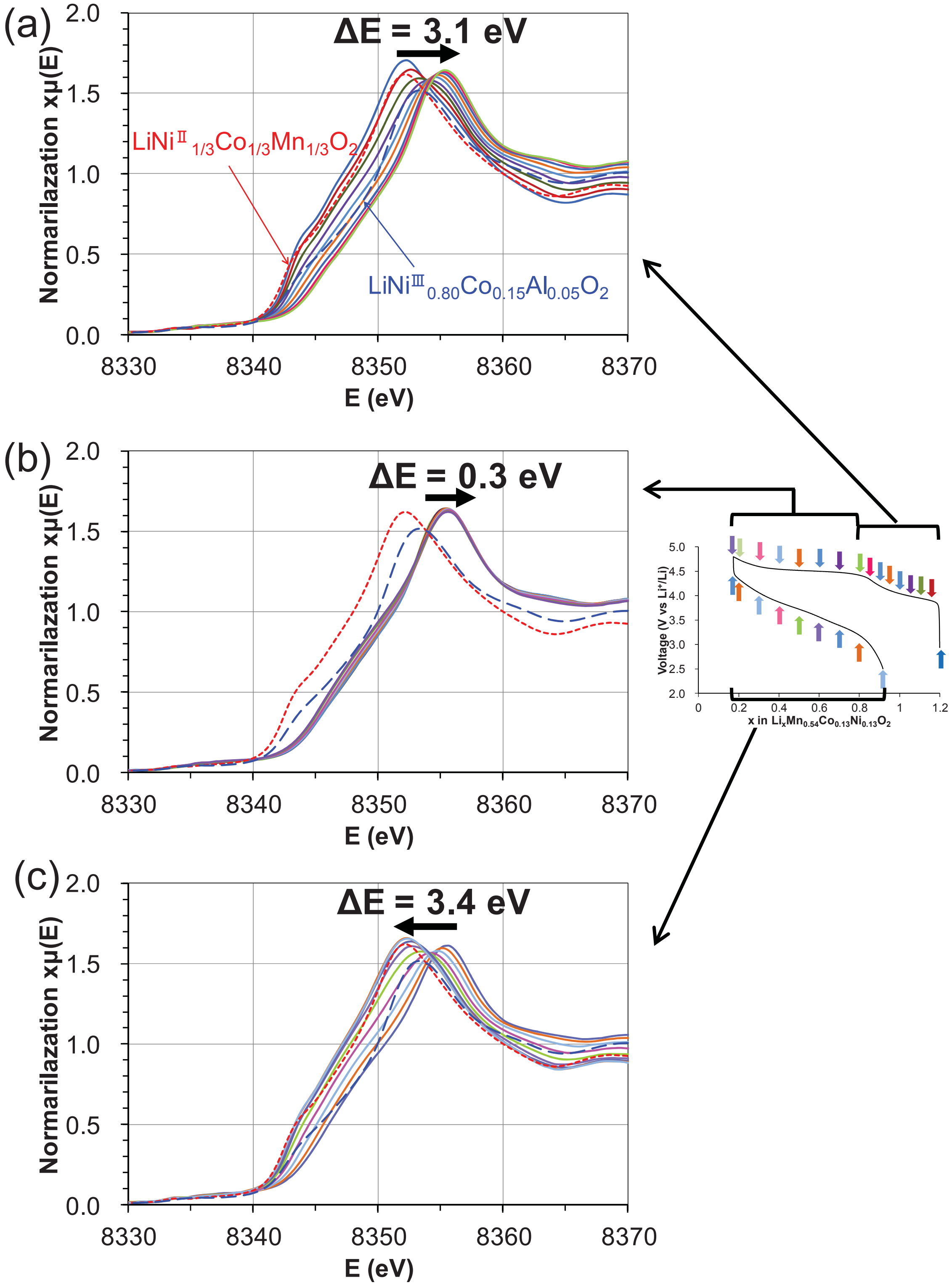

Fig. IV. 3: Normalized XANES spectra at the Ni K-edge for $Li_{1.20}Mn_{0.54}Co_{0.13}Ni_{0.13}O_2$ during the 1st charge before the "plateau" (a), the 1st charge during the "plateau" up to 4.8 V vs. Li^+/Li (b) and the 1st discharge after the "plateau" (c).

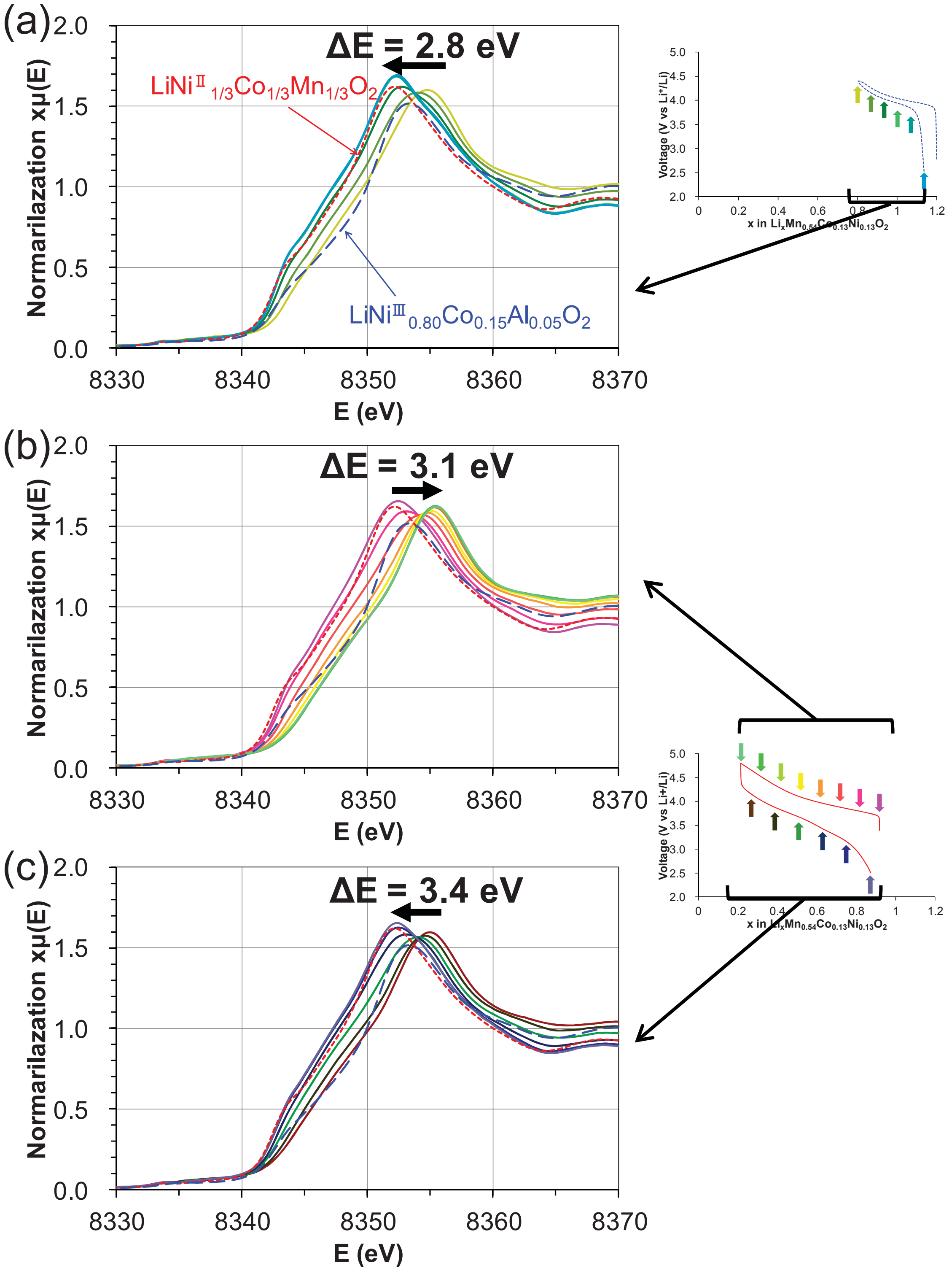

Fig. IV. 4: Normalized XANES spectra at the Ni K-edge for $Li_{1.20}Mn_{0.54}Co_{0.13}Ni_{0.13}O_2$ during the 1st discharge before the “plateau” (a), the 2nd charge after a 1st cycle in the potential window 2.5 - 4.8 V (b) and the 2nd discharge after a 1st cycle in the potential window 2.5 - 4.8 V (c).

IV. 3. 2. 2 - Co K-edge

$LiNi_{1/3}Co^{III}_{1/3}Mn_{1/3}O_2$ and $Co^{II,III}_3O_4$ were measured as references for different oxidation states for Co ions. XANES spectrum recorded at the Co K-edge for the pristine material is found to be close to that observed for the layered oxide $LiNi_{1/3}Co^{III}_{1/3}Mn_{1/3}O_2$ as shown in **Fig. IV. 5a**, revealing thus that the oxidation state of Co ions in the pristine material is Co^{3+}. During the charge before the “plateau”, the half-height energy of XANES spectra does not shift significantly as shown in **Fig. IV. 5a**. However, their shapes change continuously and especially, the position of the maximum of absorption shifts to higher energies ($\Delta E \sim 5$ eV). As reported for $LiNi_{1/3}Co_{1/3}Mn_{1/3}O_2$ in references **[17-18]**, despite small modifications only it reveals that Co^{3+} ions are oxidized to Co^{4+} during the 1st charge before the “plateau”. Then, during the discharge directly before the “plateau” XANES spectra recorded at the Co K-edge change continuously and reversibly back to one similar to that of the pristine material, showing thus that Co ions are reduced to the Co^{3+} oxidation state (**Fig. IV. 6a**). During the “plateau”, almost no modifications are observed in the XANES spectra recorded at the Co K-edge (**Fig. IV. 5b**), showing as expected that Co ions are not oxidized further during the “plateau”. As shown in **Fig. IV. 5c**, during the 1st discharge after the “plateau” XANES spectra obtained at the Co K-edge shift to lower energies as Co ions are reduced to Co^{3+} as in the pristine material. During the 2nd cycle performed after a 1st cycle in the potential window 2.5 - 4.8 V vs. Li^+/Li XANES spectra continuously shift to higher energies during the charge and to lower energies during the discharge as shown in **Fig. IV. 6b-c**, in good agreement with the reversible oxidation and reduction of Co ions as commonly observed in layered oxides.

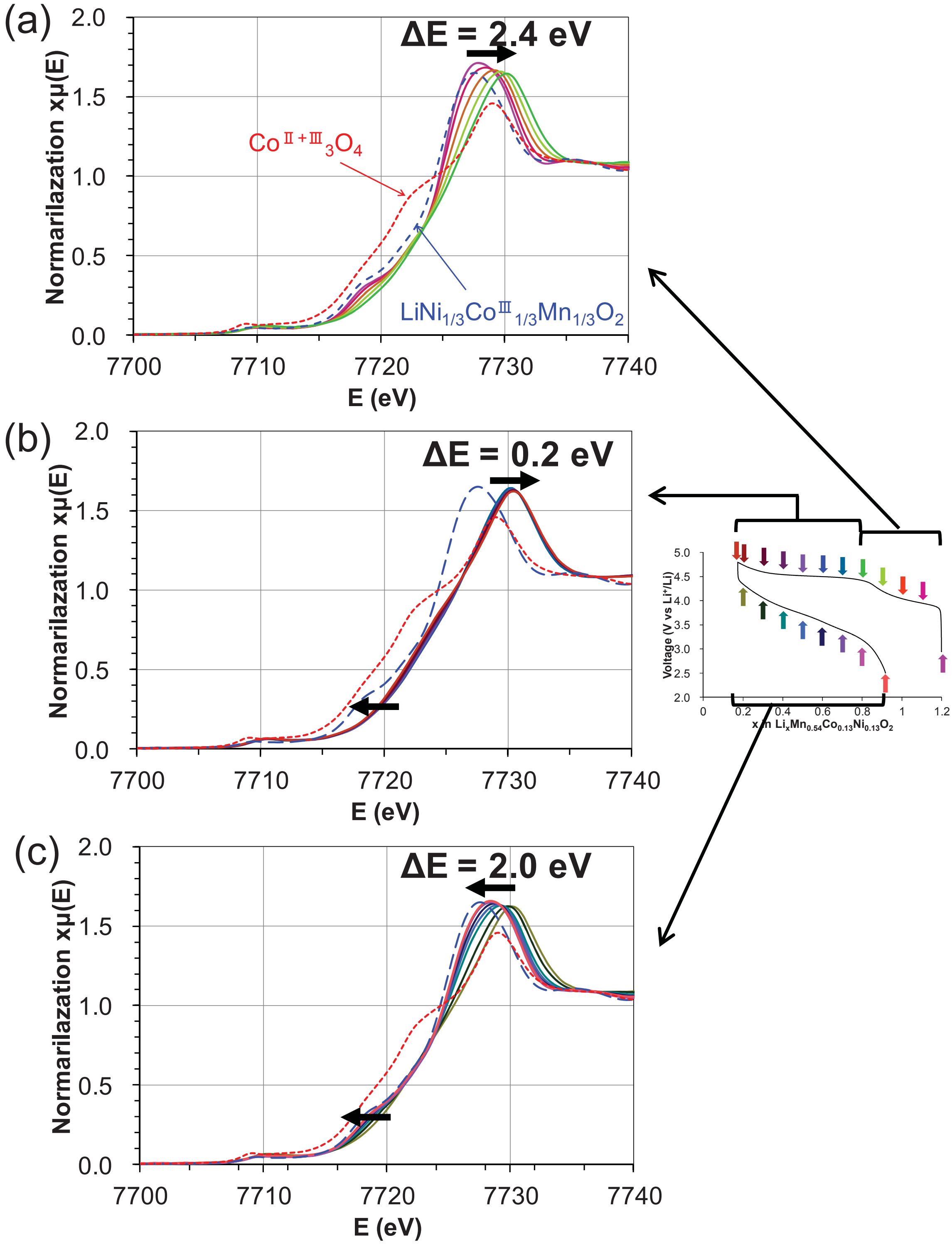

Fig. IV. 5: Normalized XANES spectra at the Co K-edge for $Li_{1.20}Mn_{0.54}Co_{0.13}Ni_{0.13}O_2$ during the 1st charge before the "plateau" (a), the 1st charge during the "plateau" up to 4.8 V vs. Li^+/Li (b) and the 1st discharge after the "plateau" (c).

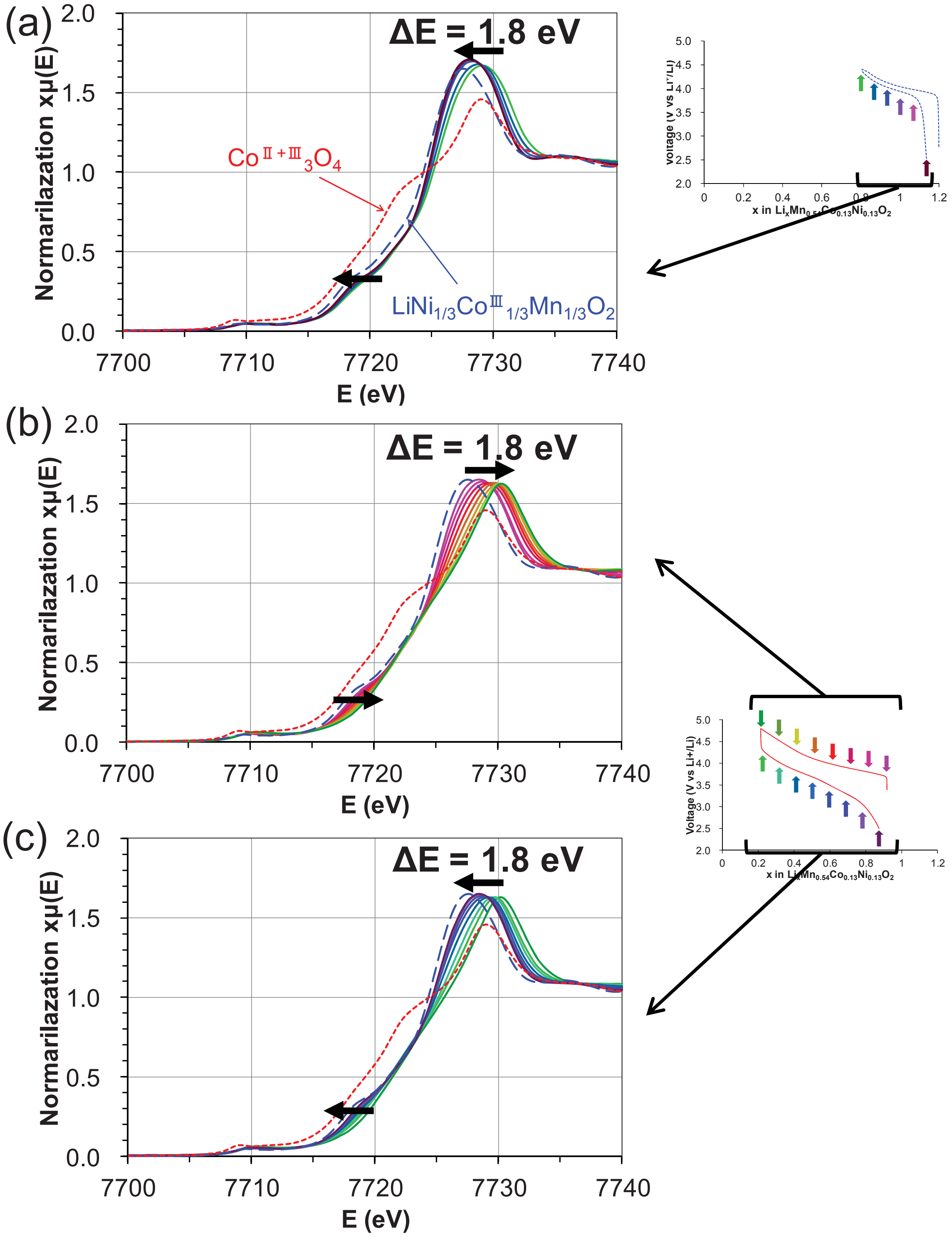

Fig. IV. 6: Normalized XANES spectra at the Co K-edge for $Li_{1.20}Mn_{0.54}Co_{0.13}Ni_{0.13}O_2$ during the 1st discharge before the "plateau" (a), the 2nd charge after a 1st cycle in the potential window 2.5 - 4.8 V (b) and the 2nd discharge after a 1st cycle in the potential window 2.5 - 4.8 V (c).

V. 3. 2. 3 - Mn K-edge

$LiNi_{1/3}Co_{1/3}Mn^{IV}{}_{1/3}O_2$, $LiMn^{III,IV}{}_2O_4$ and $Li_2Mn^{IV}O_3$ were measured as references for the different oxidation states of Mn ions, the comparison of their XANES spectra with that of the pristine material in **Fig. IV. 7a** supports the presence of Mn^{4+} in $Li_{1.20}Mn_{0.54}Co_{0.13}Ni_{0.13}O_2$ as in $Li_2Mn^{IV}O_3$. Whatever the state of charge or of discharge XANES spectra recorded at the Mn K-edge do not change significantly; the maximum of the absorption edge is shifted of 1-2 eV only suggesting that Mn ions do not participate to the redox processes. It is interesting to mention that XANES spectra of Mn K-edge were reported to shift significantly for other Mn-rich materials as function of changes in Mn oxidation state **[19-20]**, in addition significant changes were also observed in the shape of their edge. Note also that depending on the charge state of the battery a small shift of less than 3 eV was also observed at the Mn K-edge for $LiNi_{1/3}Co_{1/3}Mn^{IV}{}_{1/3}O_2$ despite no participation of the Mn to the redox processes **[18]**. These small changes are expected since oxidation of Ni to the Ni^{4+} oxidation state induces an increase in the covalency of the Ni-O bonds and thus modification in the distribution of the electrons between Mn and O. Pre-edge of Mn K-edge XANES spectra was shown to be very sensitive to changes in the oxidation state of Mn ions **[21]**, the peak of the pre-edge at lower energy corresponds to the transitions from 1s to $3d_{eg}$ states and that at higher energy to the transitions from 1s to $3d_{t2g}$ states. Nevertheless, in our experiments pre-edges of XANES spectra recorded at the Mn K-edge during the 1st cycle do not shift continuously as shown in **Fig. IV. 9**. However, intensity of pre-edge changes during charge and discharge. As intensity of pre-edge increases with distortion of octahedral sites **[22]**, these results revealed that the distortion increases during the first charge and decreases during the next discharge, but without recovering that of pristine material. Here we can also conclude that Mn ions could not be oxidized over Mn^{x+} (x>4). In case of Mn oxidation over Mn^{x+} (x>4), significant change of intensity should be observed for pre-edge due to migration from octahedral site to tetrahedral site for its stabilization **[23]**.

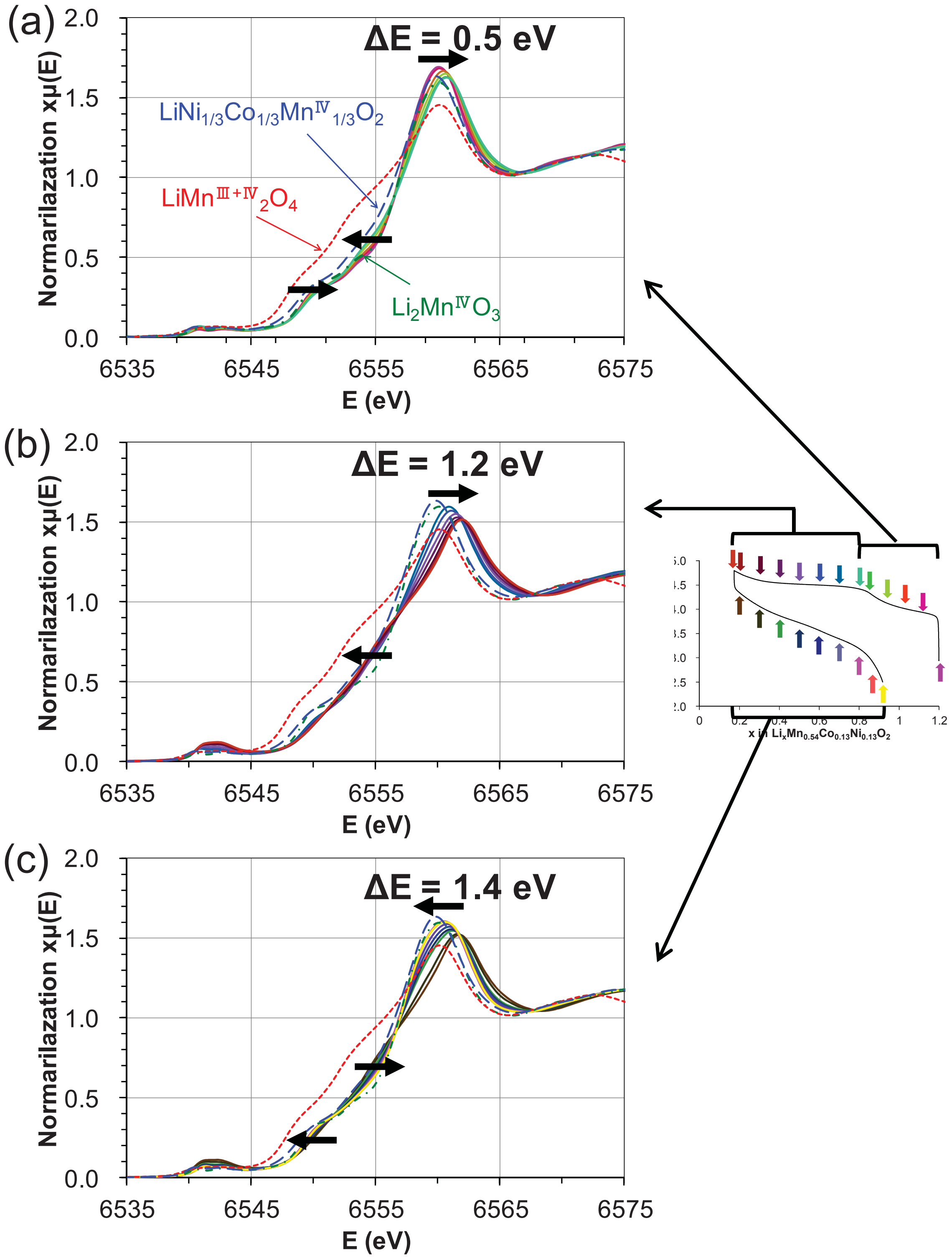

Fig. IV. 7: Normalized XANES spectra at the Mn K-edge for $Li_{1.20}Mn_{0.54}Co_{0.13}Ni_{0.13}O_2$ during the 1st charge before the “plateau” (a), the 1st charge during the “plateau” up to 4.8 V vs. Li^+/Li (b) and the 1st discharge after the “plateau” (c).

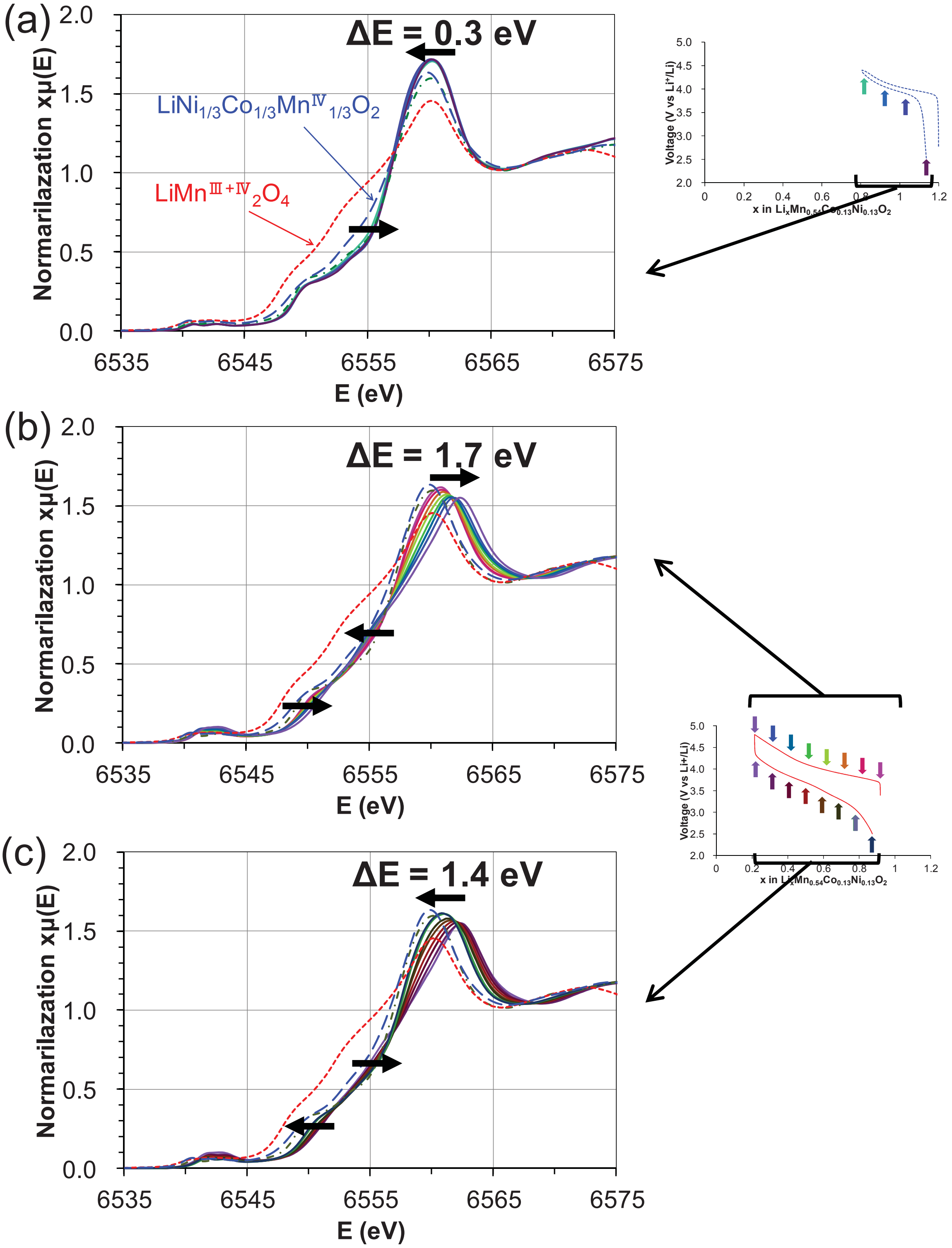

Fig. IV. 8: Normalized XANES spectra at the Mn K-edge for $Li_{1.20}Mn_{0.54}Co_{0.13}Ni_{0.13}O_2$ during the 1st discharge before the “plateau” (a), the 2nd charge after a 1st cycle in the potential window 2.5 - 4.8 V (b) and the 2nd discharge after a 1st cycle in the potential window 2.5 - 4.8 V (c).

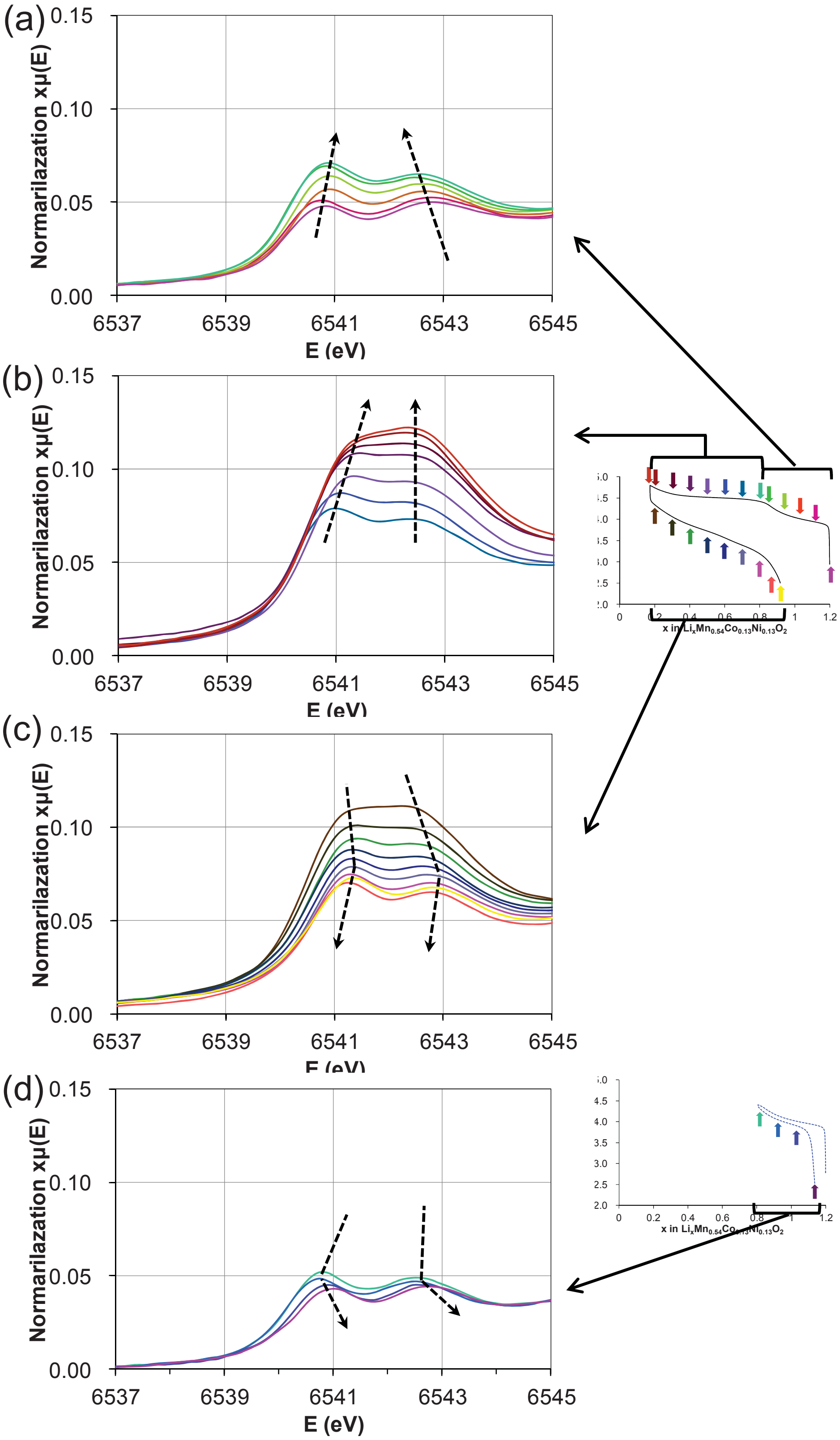

Fig. IV. 9: Pre-edge of normalized XANES spectra at the Mn K-edge of $Li_{1.20}Mn_{0.54}Co_{0.13}Ni_{0.13}O_2$ during the 1st charge before the "plateau" (a), the 1st charge up to 4.8 V vs. Li^+/Li (b), the 1st discharge after the "plateau" (c), and the 1st discharge before the "plateau" (d).

XANES spectra recorded at the Ni, Co and Mn K-edges and obtained for the pristine material and the material after the 1st cycle are compared in **Fig. IV. 10**. No difference between XANES spectra obtained *ex-situ* or *in operando* is observed, whatever the metal K-edge obtained. The reproducibility between *in operando* and ex-situ experiments is not surprising as the studies were performed *in operando* at C/10, which is a rather low rate. Ni spectra recorded for the pristine material and the material obtained after the 1st cycle with the "plateau" are very similar in position and in shape, whereas the Co and Mn spectra are different in shape. This difference between Ni and (Co, Mn) is expected from the cation ordering observed in the slabs. Ni is surrounded by oxygens as first neighbors and then by Co and Mn as second neighbors. Its local environment appears thus not to change significantly between the beginning and the end of the 1st cycle. On the contrary, Mn and Co are surrounded by oxygens as first neighbors and by (**2Li**, 1Ni, 3(Co, Mn)) as second neighbors, the difference in the Co and Mn spectra between the beginning and the end of the first cycle shows thus that an irreversible modification occurs at the local scale which could be attributed to irreversible lithium deintercalation from the slabs.

The comparison of these XANES spectra at the Ni, Co and Mn K-edges with those obtained after the 10th cycle is also given in **Fig. IV. 10**. All these spectra are found very similar to those obtained for the material after the 1st cycle, showing thus that the oxidation state and environment of each transition metal ion does not evolve significantly between the 1st and the 10th cycles. Irreversible "plateau" is observed only in the first charge, the charge and discharge curves continuously change upon cycling **[24]**. But from our XANES spectra, this change is not mainly caused by changes in the redox processes. In order to get more insights into changes in the local structure the EXAFS spectra were analyzed in details in the following at the Ni, Co and Mn K-edges.

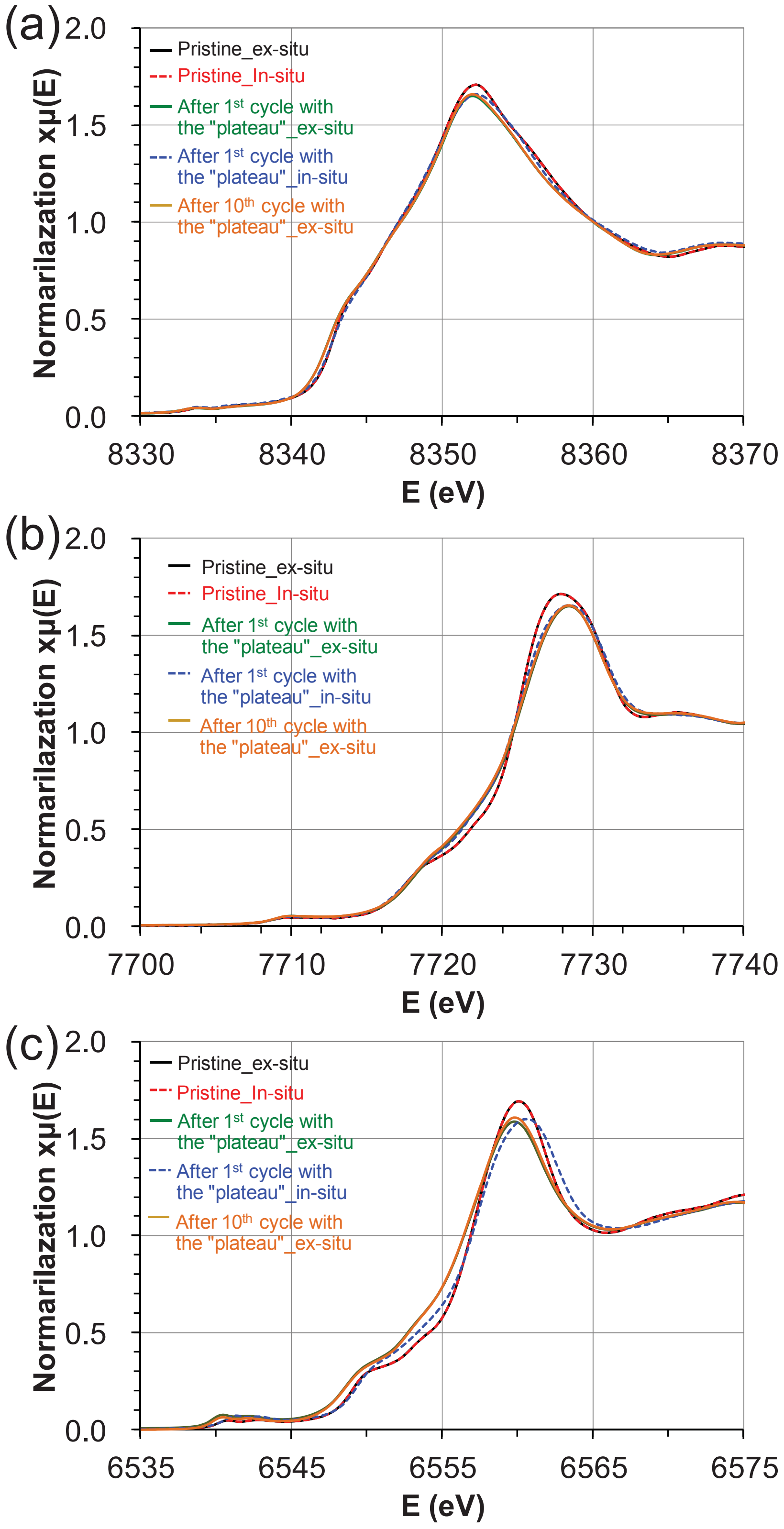

Fig. IV. 10: Normalized XANES spectra of $Li_{1.20}Mn_{0.54}Co_{0.13}Ni_{0.13}O_2$ at the Ni K-edge (a), Co K-edge (b) and Mn K-edge (c) for the pristine material, the pristine material within the cell developed for Operando studies, the material recovered *ex-situ* after the 1st cycle of a Lithium cell, the material after the 1st cycle within the *in operando* cell and the material recovered *ex-situ* from a Lithium cell after 10 cycles.

V. 3. 3 - Analysis of the EXAFS spectra recorded *in operando* upon cycling

The distance between metal-oxygen and metal-metal could be estimated from EXAFS spectra to follow changes in the oxidation state of each transition metal and in their local structure during the charge and discharge.

Fitting of EXAFS data was performed using Artemis software. Better fitting results could be obtained considering the description of the structure in the *C2/m* space group, *i.e.* cation local orderings as in Li_2MnO_3: Ni ions are surrounded by 6 transition metals whereas Co and Mn ions are surrounded by 4 transition metals and 2 Li^+ ions. For comparison, the description of the structure considering the *R-3m* space group as for $LiNiO_2$ would lead to all transition metal ions surrounded by 6 transition metal ions. This result is another confirmation of the cation local ordering, with different environments depending on the nature (size) of the transition metals ions, and is in good agreement with the results previously obtained by electron diffraction, ^{7}Li MAS NMR and Raman spectroscopy **[11]**.

k^3-weighted Fourier transforms of EXAFS spectra recorded at the Ni, Co and Mn K-edges are compared in **Fig. IV. 11** for the pristine material, the material obtained in charge just before the “plateau”, the material obtained after a charge before the “plateau” and then a first discharge, the material obtained after a full charge up to 4.8 V vs. Li^+/Li and finally the material after the 1st cycle. Changes in the intensity and position, especially for the first peak which is related to the M-O distance, are observed during the 1st cycle. These changes are reported by some authors to be caused by oxygen loss during the 1st charge of Li-rich layered oxides **[21]**. However similar changes in intensity were observed by other authors in normal (non overlithiated) layered oxides **[15-17]** and in materials with other structures **[19]**. Furthermore, according to our results, the intensity of the first peak in EXAFS data decreases as compared with that of the pristine material already when charged up before the “plateau”, *i.e*. at a step at which oxygen loss was not expected to have occurred. In our opinion the change in the peak intensity is thus not directly linked to oxygen loss (to a decrease in the number of oxygen neighbors) but most probably to a larger disorder (distribution of distances, or larger Debye Waller factor). We have also considered possible changes in the number of oxygen neighbors around each transition metal ion, but reliable results could not be obtained due to a strong correlation between the Debye-Waller factors and the number of oxygen neighbors, but also to non continuous and significant changes from 6.

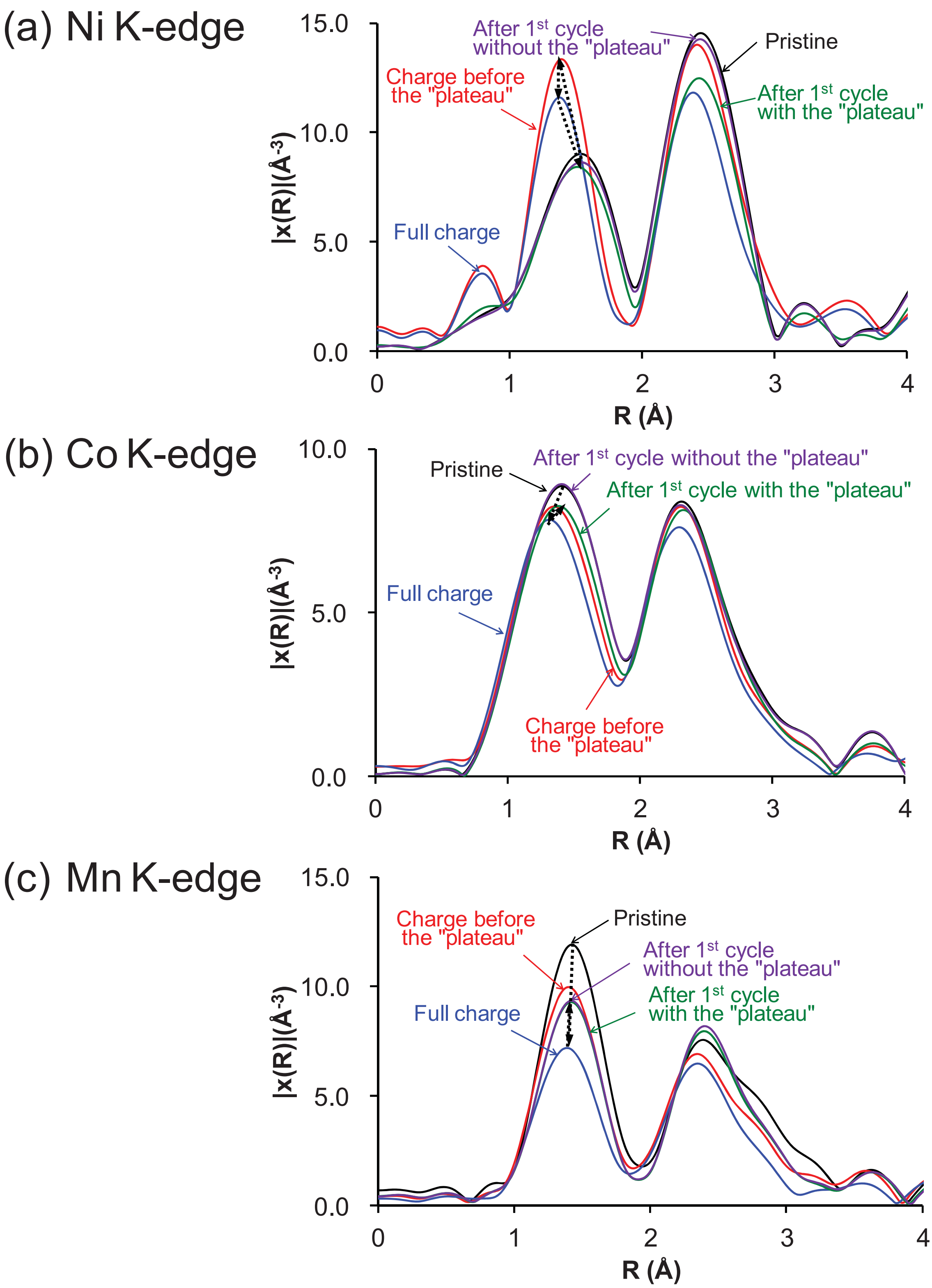

Fig. IV. 11: Fourier transforms of k^3-weighted EXAFS spectra of $Li_{1.20}Mn_{0.54}Co_{0.13}Ni_{0.13}O_2$ at the Ni K-edge (a), Co K-edge (b) and Mn K-edge (c) for the pristine material, the material obtained in charge just before the “plateau”, the material obtained at the end of the charge up to 4.8 V vs. Li^+/Li, the material obtained after the 1st cycle with the “plateau” and the material obtained after the 1st cycle without the “plateau”.

Metal – first oxygen neighbor distances and metal – first metal neighbor distances obtained from the refinement of k^3-weighted Fourier transforms of EXAFS spectra are given in **Fig. IV. 12, Fig. IV. 13 and Fig. IV. 14**, the absolute error on each distance is ± 0.01. Parameters for these refinements during the 1st cycle are shown in the end of this chapter as appendix, in Table A. IV. 1, Table A. IV. 2 and Table A. IV. 3. During the 1st cycle changes observed in the Ni-O distances with or without the "plateau" are compared in **Fig. IV. 12a** to those of Ni^{II}-O and Ni^{III}-O distances in $LiNi^{II}_{1/3}Co_{1/3}Mn_{1/3}O_2$ and $LiNi^{III}_{0.80}Co_{0.15}Al_{0.05}O_2$ respectively. The Ni-O distance decreases during the charge before the "plateau" to values smaller than that observed for $LiNi^{III}_{0.80}Co_{0.15}Al_{0.05}O_2$. It is in good agreement with a decreasing ionic radius for Ni ions and their oxidation to Ni^{IV} upon Li deintercalation. Then, in discharge after a charge just before the "plateau", the Ni-O distance increases and recovers its initial value, *i.e.* that observed for the pristine material. On the other hand, the Ni-O distance remains stable during the "plateau", supporting that Ni ions are not oxidized during the "plateau". In discharge after a charge after the "plateau" (up to 4.8 V vs. Li$^+$/Li), the Ni-O distance increases and reaches that observed for the pristine material. These redox reactions involving Ni ions during the 1st cycle agree with the analysis previously done considering the shift of XANES spectra. The Ni-M distance changes similarly, in parallel, to the Ni-O distance as shown in **Fig. IV. 12b**, decreasing during the charge before the "plateau", being stable during the "plateau" and increasing in discharge.

In the 2nd cycle, the Ni-O and Ni-M distances change continuously and reversibly as classically observed for normal layered oxides as shown in **Fig. IV. 12a-b**.

Changes in Co-O distance during the 1st cycle are shown in **Fig. IV. 13a** and compared with that of Co^{III}-O in $LiNi_{1/3}Co^{III}_{1/3}Mn_{1/3}O_2$. As shown in **Fig. IV. 13** changes in Co-O follow exactly the same tendencies as changes in Ni-O during the first and second cycles, but in a smaller extent as Co ions are oxidized from Co^{3+} to Co^{4+} whereas Ni ions are oxidized from Ni^{2+} to Ni^{4+}. Changes observed during the second cycle are expected and observed for normal (non overlithiated) layered oxides.

As mentioned above, changes in the oxidation state of Mn ions during the 1st cycle was not clear from the analysis of XANES spectra at the Mn K-edge, and therefore a complementary analysis of the Mn-O distances is required to support further our conclusions. The Mn-O distances determined during the 1st cycle are compared in **Fig. IV. 14a** with Mn^{IV}-O ones in $LiNi_{1/3}Co_{1/3}Mn^{IV}_{1/3}O_2$ and Li_2MnO_3 and with Mn$^{"3.5+"}$-O ones in $LiMn^{III,IV}_2O_4$. The Mn-O distance decreases continuously from the beginning of the charge to high voltage and then reversibly increases in discharge, recovering its initial value. The total variation of the Mn-O distance over the potential window is small (0.01 Å) which remains within the accuracy of the analysis. As shown in **Fig. IV. 14a**, similar changes occur during the 2nd cycle, but again smaller than those observed for Ni and Co ions. As these small changes in the Mn-O distance were observed in $LiNi_{1/3}Co_{1/3}Mn_{1/3}O_2$ for which Mn is maintained at the Mn^{4+} tetravalent state all along the charge and discharge processes **[25]**, they could suggest modification in the local environment around Mn. Indeed, in a layered structure made of edge sharing octahedra the size of a given octahedra is strongly related to (or constrained by) the size of the neighboring ones. In oxidation when cobalt and nickel ions are oxidized there is a general lattice contraction (the a_{hex}. parameter decreases) **[24]** leading to a small decrease in the Mn-O distances. The partial oxidation at the end of the charge plays in the same way. The opposite effects occur in discharge. Then, in discharge as the Mn-O recovers its initial value, but not a bigger one. One has to notice that the Mn-M distance, in the reduced state, is slightly larger than in the pristine material. This effect was not observed for Ni-M and Co-M distances

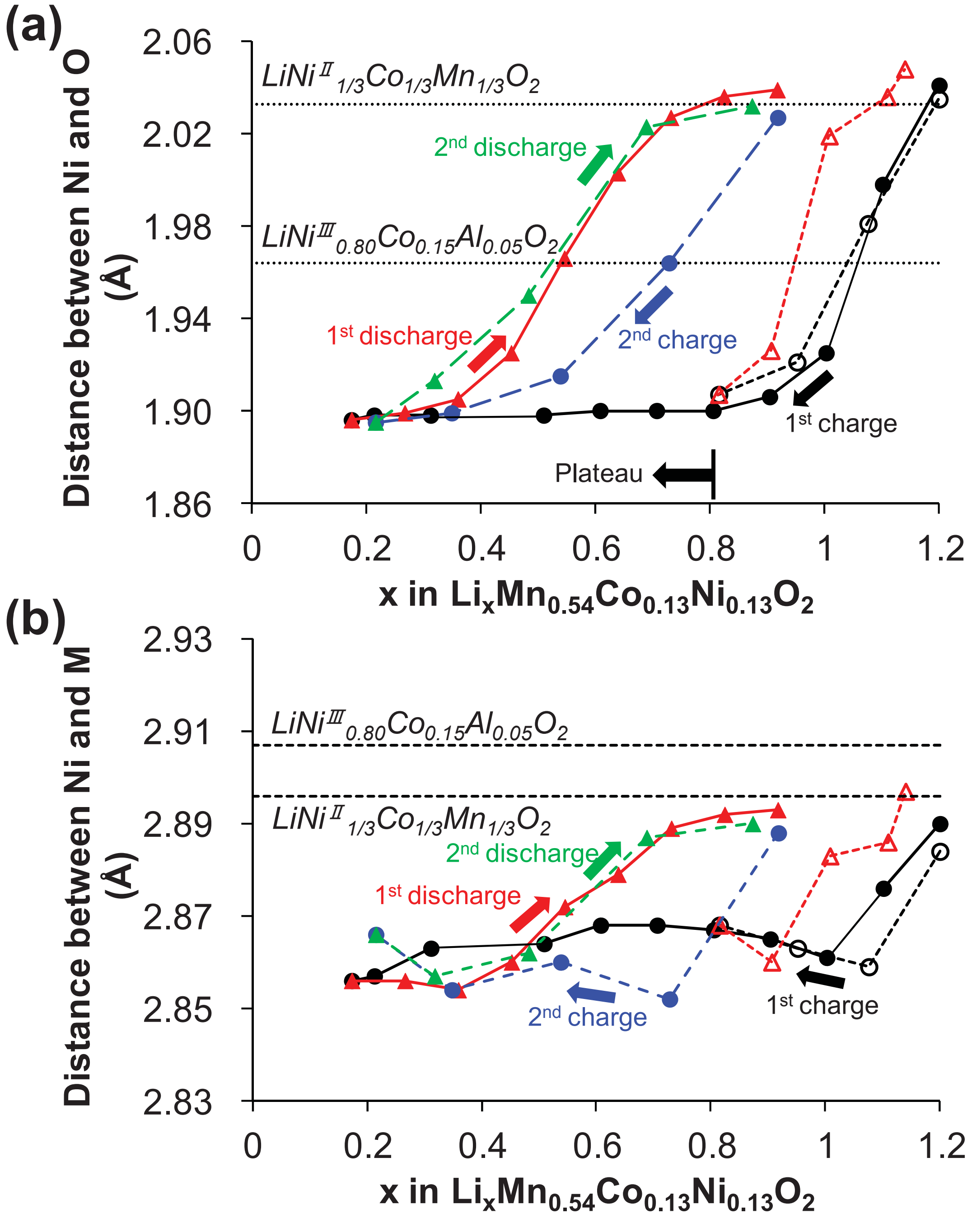

Fig. IV. 12: Distances determined between Ni and its first oxygen neighbors (a) and between Ni and its first metal neighbors (b) from the analysis of the EXAFS spectra recorded *in operando* during the 1st cycle with (solid lines) and without (short dotted lines) the "plateau". Ni-O and Ni-M distances determined from the analysis of the EXAFS spectra during the 2nd cycle of Li//$Li_{1.20}Mn_{0.54}Co_{0.13}Ni_{0.13}O_2$ (long dotted lines in a-b). $LiNi_{1/3}Co_{1/3}Mn_{1/3}O_2$ and $LiNi_{0.80}Co_{0.15}Al_{0.05}O_2$ are given as reference for Ni^{II}-O(M) and Ni^{III}-O(M) respectively.

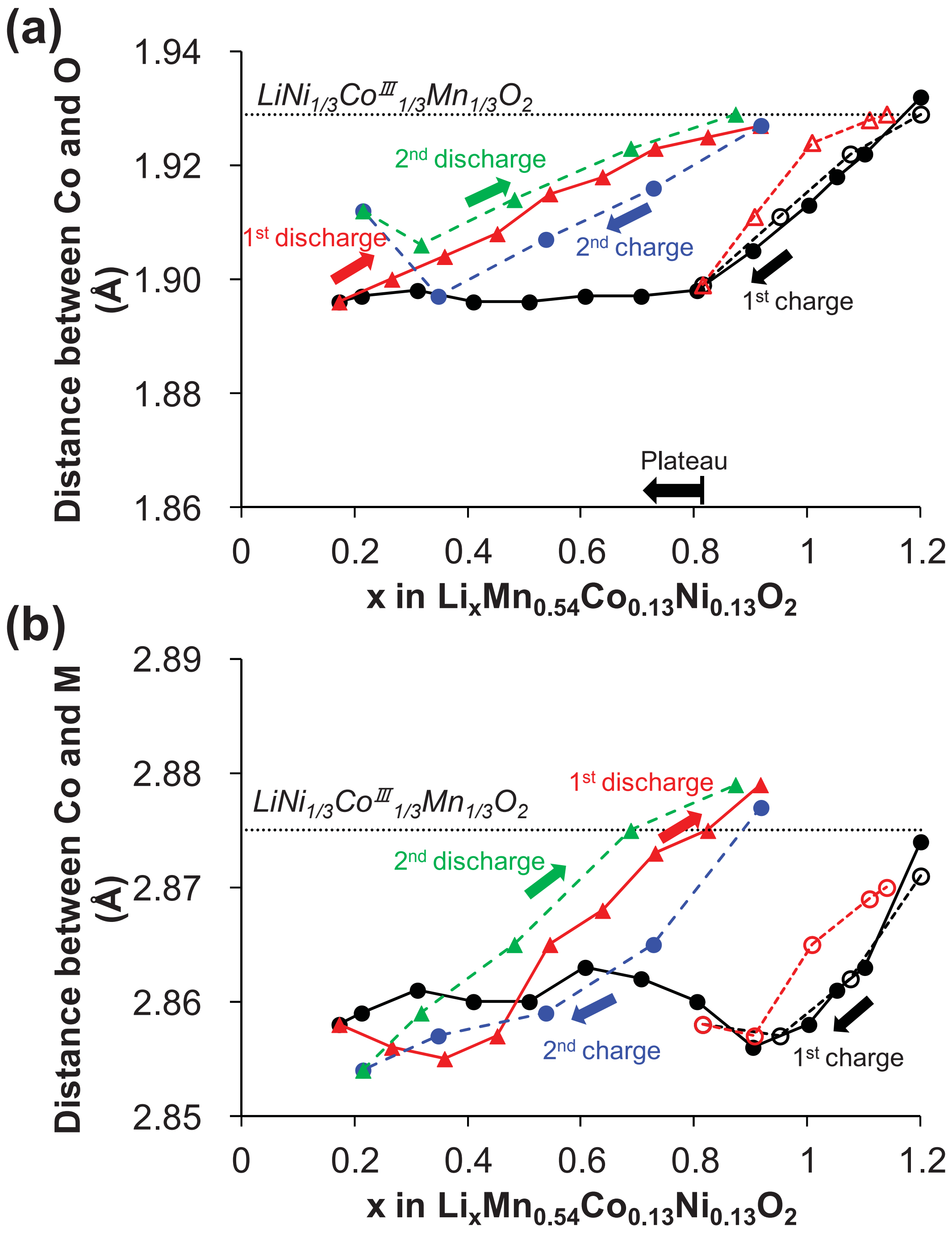

Fig. IV. 13: Distances determined between Co and its first oxygen neighbors (a) and between Co and its first metal neighbors (b) from the analysis of the EXAFS spectra recorded *in operando* during the 1st cycle with (solid lines) and without (short dotted lines) the “plateau”. Co-O and Co-M distances determined from the analysis of the EXAFS spectra during the 2nd cycle of Li//$Li_{1.20}Mn_{0.54}Co_{0.13}Ni_{0.13}O_2$ (long dotted lines in a-b). $LiNi_{1/3}Co_{1/3}Mn_{1/3}O_2$ is given as reference for Co^{III}-O(M).

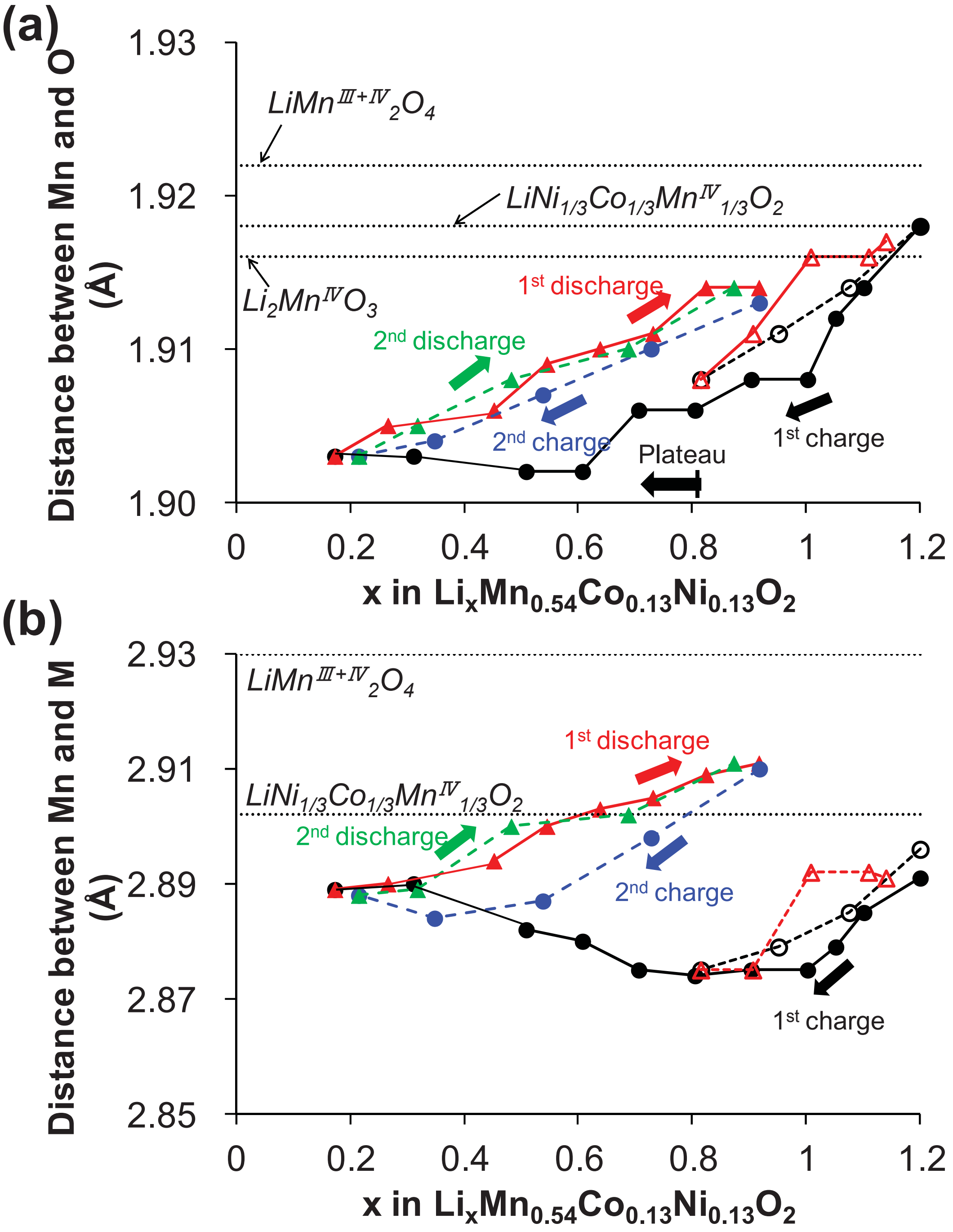

Fig. IV. 14: Distances determined between Mn and its first oxygen neighbors (a) and between Mn and its first metal neighbors (b) from the analysis of the EXAFS spectra recorded *in operando* during the 1st cycle with (solid lines) and without (short dotted lines) the "plateau". Mn-O and Mn-M distances determined from the analysis of the EXAFS spectra during the 2nd cycle of Li//$Li_{1.20}Mn_{0.54}Co_{0.13}Ni_{0.13}O_2$ (long dotted lines in a-b). $LiNi_{1/3}Co_{1/3}Mn_{1/3}O_2$ as well as Li_2MnO_3, and $LiMn_2O_4$ are given as reference for Mn^{IV}-O(M) and $Mn^{III,IV}$-O(M) respectively.

IV. 3. 4 - Discussion

Electrochemical experiments have revealed that during the 1st charge 1.03 mol Li were deintercalated from the layered structure. 0.39 mol Li deintercalated are compensated by the oxidation of Ni^{2+} and Co^{3+} to Ni^{4+} and Co^{4+} respectively. These oxidations were confirmed by shifts to higher energy of XANES spectra recorded at the Ni and Co K-edges and by changes observed in the Ni-O and Co-O distances and revealed from the analysis of the EXAFS spectra recorded at the Ni and Co K-edges. It was proposed that the next 0.64 mol Li deintercalated were compensated through oxidation of oxygen ions before their release as oxygen gas **[9]**. In fact, changes in the shape of XANES spectra recorded at the Co and Mn K-edges during the "plateau" in the 1st charge indicate that modification of the local structure around Co and Mn ions occurs due to irreversible extraction of Li ions locating in the slabs as second neighbors of Co and Mn, but not due to their oxidation. In discharge, 0.75 mol Li ions was inserted: 0.39 mol Li ions inserted are compensated by the reduction of Ni and Co from Ni^{4+} and Co^{4+} to Ni^{2+} and Co^{3+} as confirmed by the shift to lower energy of XANES spectra recorded at Ni and Co K-edges. The next 0.36 mol Li are expected to be inserted with reduction of Mn from Mn^{4+} to $Mn^{3.3+}$. However the reduction of Mn ions could not be observed from the XANES spectra recorded at the Mn K-edge and the Mn-O distances determined from the analysis of EXAFS spectra during the discharge. Although it can not be completely excluded its contribution is significantly smaller than $0.33e^-$ for 0.54 Mn^{4+}. Therefore the redox reaction occurring during the 1st cycle of $Li_{1.20}Mn_{0.54}Co_{0.13}Ni_{0.13}O_2$ could not be explained considering only the oxygen loss model whatever the model (densification or oxygen vacancies). Therefore, as discussed in reference **[24]**, we proposed that participation of oxygen in charge and in discharge is such as oxygen ions are oxidized during the "plateau" during the 1st charge, but for most of them reversibly without oxygen loss and with a participation in the next discharge through its reduction **[21, 24]**.

IV. 4 - Conclusions

Study of redox reaction of $Li_{1.20}Mn_{0.54}Co_{0.13}Ni_{0.13}O_2$ during the charge and discharge was characterized through *Operando* XAS measurements. Changes in the oxidation state of each transition metal ion were followed according to the shift of XANES spectra recorded at the Ni, Co and Mn K-edges and to modifications in the metal-oxygen distances. Ni and Co are oxidized in the 1st charge before the "plateau" and they are maintained at the Ni^{4+} and Co^{4+} oxidation states during the "plateau". Mn is stable as Mn^{4+} during the 1st charge. It reveals that oxygen ions are oxidized on the "plateau" with Li deintercalation. In discharge, Ni and Co are reduced and recover their initial states as those observed in the pristine material, whereas Mn is not reduced in a large extent as it could have been expected from the results of the electrochemical tests. Therefore, these results support again as those reported in chapter III that the oxygen loss model is not sufficient to explain the reactions occurring upon cycling of $Li_{1.20}Mn_{0.54}Co_{0.13}Ni_{0.13}O_2$. These results support thus the involvement of oxygen in the reversible redox reactions, in addition to those of Ni and Co.

IV. 5 - References

[1] Mizushima, K.; Jones, P. C.; Wiseman, P. J. and Goodenough, J. B., *Mater. Res. Bull.*,**1980**, 15, 783

[2] Ellis, B. L.; Lee, K. T.; Nazar, L. F. ; *Chem. Mater.,* **2010**, 22, 691

[3] Maccario, M.; Croguennec, L.; Le Cras, F.; and Delmas, C.; *J Power Sources*, **2008**, 183, 411

[4] Lu, Z.; MacNeil, D.D.; Dahn, J. R., *Electrochemical and solid state letters,* **2001**, 4, A191

[5] Park, Y. J.; Hong, Y. S.; Wu, X.; Ryu, K. S.; Chang, S. H., *J. Power Sources*, **2004**, 129, 288

[6] Wu, Y.; Manthiram, A., *Electrochem. Solid-State Lett.* **2006**, 9, A221.

[7] Lu, Z.; Beaulieu, L.Y.; Donaberger, R.A.; Thomas, C.L.; and Dahn, J.R., *J. Electrochem. Soc.*, **2002**, 149, A778-791

[8] Jiang, M.; Key, B.; Meng, Y.S.; and Grey, C.P., *Chem. Mater.*, **2009**, 21, 2733-2745

[9] Armstrong, R.; Holzapfel, M.; Novak, P.; Johnson, C. S.; Kang, S. -H.; Thackeray, M. M.; Bruce, P. G., *J. Am. Chem. Soc*, **2006**, 128, 8694

[10] Leriche, J. B.; Hamelet, S.; Shu, J.; Morcrette, M.; Masquelier, C.; Ouvrard, G.; Zerrouki, M.; Soudan, P.; Belin, S.; Elkaïm, E.; and Baudelet, F.; *J. Electrochem. Soc.*, **2010**, 157 5 A606-A610

[11] Koga, H.; Croguennec, L.; Mannessiez, P.; Ménétrier, M.; Weill, F.; Bourgeois, L.; Duttine, M.; Suard, E.; and Delmas, C., *J. Phys. Chem.* C, **2012**, 116, 13497-13506

[12] Fonda, E.; Rochet, A.; Ribbens, M.; Belin, S.; Briois. V., *J. Synchrotron Rad.*, **2012**, 19, 417–424

[13] Ravel, B.; Newville, M.; *J. Synchrotron Rad.*, **2005**, 12, 537

[14] Kim, Ni_M. G.; Sung, N. E.; Shin, H. J.; Shin, N. S.; Ryu, K. S.; Yo, C. H., *Electrochemica Acta,* **2004**, 50, 501-504

[15] Balasubramanian, M.; Sun, X.; Yang, X.Q.; McBreen, J., *J. Power Sources,* **2001**, 92, 1-8

[16] Mansour, A. N.; Yang, X. Q.; Sun, X.; McBreen, J.; Croguennec, L.; and Delmas, C., *J. Electrochem. Soc.*, **2000**, 147, 2104-2109

[17] Yoon, W.-S.; Chung, K. Y.; McBreen, J.; Fischer, D. A.; Yang, X.-Q., *J. Power Sources,* **2007**, 174,1015-1020

[18] Kim, J.-M.; Chung, H.-T., *Electrochimica Acta,* **2004**, 49, 3573-3580

[19] Chan, H.-W. ; Duh, J.-G.; Lee, J.-F., *Electrochemistry Commun.*, **2006**, B, 1731-1736

[20] Kim, G. -Y.; Yi, S. -B.; Park Y. J.; Kim, H. -G., *Material research bulletin*, **2008**, 43, 3542-3552

[21] Ito, A.; Sato, Y.; Sanada, T.; Hatano, M.; Horie, H.; Ohsawa, Y., *J. Power Sources*, **2011**, 196, 6828-6834

[22] Simonin, L.; Colin, J.-F.; RanierV.; Canevet, E.; Martin, J. -F.; Bourbon, C.; Baehtz, C.; Strobel, P.; Daniel L. and Patoux, S., *J. Mater. Chem.*, **2012**, 22, 11316

[23] Balasubramanian, M.; McBreen, J.; Davidson, I. J.; Whitfield, P. S. and Kargina, *I., J. Electrochem. Soc*., **2002**, 149 (2), A176-A184

[24] Koga, H.; Croguennec, L.; Ménétrier, M.; Mannessiez, P.; Weill, F. and Delmas, C., accepted to *J. Power Sources*, **2013**

[25] Tsai, Y. W.; Hwang, B. J.; Ceder, G.; Sheu, H. S.; Liu, D. G.; and Lee, J. F., *Chem. Mater.*, **2005**, 17, 3191-3199

IV.6 Appendix

Table IV. A. 1: Ni K-edge EXAFS parameters in the material during the 1st cycle with "plateau".

x	Ni-O distance (Å)	σ^2 (10^{-3} Å^2)	Ni-M distance (Å)	σ^2 (10^{-3} Å^2)	ΔE (eV)	CN	K-range	R-range	R-factor
1.20	2.04	5.14	2.89	4.27	-6.1	6	2-10	1-3.5	0.0265
1.10	2.00	3.35	2.88	4.51	-6.8	6	2-10	1-3.5	0.0061
1.00	1.93	6.03	2.87	4.08	-9.2	6	2-10	1-3.5	0.0129
0.90	1.91	4.10	2.87	3.97	-8.6	6	2-10	1-3.5	0.0158
0.80	1.90	3.61	2.87	4.09	-8.1	6	2-10	1-3.5	0.0189
0.71	1.90	3.59	2.87	4.22	-7.5	6	2-10	1-3.5	0.0177
0.61	1.90	3.35	2.87	4.13	-8.5	6	2-10	1-3.5	0.0166
0.51	1.90	3.27	2.87	4.19	-8.0	6	2-10	1-3.5	0.0169
0.41	1.90	3.33	2.87	4.21	-8.6	6	2-10	1-3.5	0.0156
0.31	1.90	3.32	2.87	4.34	-9.0	6	2-10	1-3.5	0.0153
0.21	1.90	3.36	2.86	4.33	-8.0	6	2-10	1-3.5	0.0145
0.17	1.90	3.51	2.86	4.39	-9.6	6	2-10	1-3.5	0.0142
0.27	1.90	3.71	2.86	4.52	-9.3	6	2-10	1-3.5	0.0149
0.36	1.91	4.29	2.86	4.50	-10.4	6	2-10	1-3.5	0.0107
0.45	1.93	5.96	2.87	4.88	-10.0	6	2-10	1-3.5	0.0127
0.55	1.97	8.73	2.88	5.58	-7.6	6	2-10	1-3.5	0.0112
0.64	2.01	9.37	2.88	6.07	-6.8	6	2-10	1-3.5	0.0142
0.73	2.03	7.83	2.90	6.06	-5.8	6	2-10	1-3.5	0.0102
0.82	2.04	7.31	2.90	6.26	-5.4	6	2-10	1-3.5	0.0153
0.92	2.04	6.90	2.90	6.21	-5.8	6	2-10	1-3.5	0.0124

Table IV. A. 2: Co K-edge EXAFS parameters in the material during the 1st cycle with "plateau".

x	Co-O distance (Å)	σ² (10⁻³ Å²)	Co-M distance (Å)	σ² (10⁻³ Å²)	ΔE (eV)	CN	K-range	R-range	R-factor
1.20	1.93	1.44	2.87	3.66	-4.4	6	2-9	1-3.5	0.0124
1.10	1.92	1.54	2.86	3.57	-4.4	6	2-9	1-3.5	0.0125
1.00	1.91	1.66	2.86	3.56	-4.2	6	2-9	1-3.5	0.0124
0.90	1.90	2.20	2.86	3.68	-4.8	6	2-9	1-3.5	0.0131
0.80	1.90	2.83	2.86	3.90	-4.7	6	2-9	1-3.5	0.0130
0.71	1.89	3.90	2.86	4.09	-5.9	6	2-9	1-3.5	0.0096
0.61	1.89	3.20	2.86	4.20	-6.0	6	2-9	1-3.5	0.0109
0.51	1.89	3.43	2.86	4.42	-7.2	6	2-9	1-3.5	0.0109
0.41	1.89	2.96	2.86	4.09	-6.2	6	2-9	1-3.5	0.0100
0.31	1.89	3.11	2.86	4.25	-6.9	6	2-9	1-3.5	0.0099
0.21	1.89	3.12	2.86	4.31	-8.0	6	2-9	1-3.5	0.0099
0.17	1.89	3.09	2.86	4.51	-9.6	6	2-9	1-3.5	0.0096
0.27	1.90	3.01	2.86	4.46	-7.0	6	2-9	1-3.5	0.0106
0.36	1.90	2.29	2.86	4.40	-5.3	6	2-9	1-3.5	0.0116
0.45	1.91	2.29	2.86	3.94	-5.3	6	2-9	1-3.5	0.0114
0.55	1.91	2.17	2.87	5.58	-5.0	6	2-9	1-3.5	0.0105
0.64	1.92	2.13	2.87	3.98	-4.8	6	2-9	1-3.5	0.0096
0.73	1.92	2.20	2.87	3.91	-4.4	6	2-9	1-3.5	0.0103
0.82	1.92	1.86	2.87	3.83	-4.2	6	2-9	1-3.5	0.0103
0.92	1.93	1.99	2.88	3.87	-4.6	6	2-9	1-3.5	0.0093

Table IV. A. 3: Mn K-edge EXAFS parameters in the material during the 1st cycle with "plateau".

x	Mn-O distance (Å)	σ² (10⁻³ Å²)	Mn-M distance (Å)	σ² (10⁻³ Å²)	ΔE (eV)	CN	K-range	R-range	R-factor
1.20	1.92	1.41	2.89	3.90	-4.5	6	2-10	1-3.3	0.0357
1.10	1.91	1.95	2.88	5.92	-4.6	6	2-10	1-3.3	0.0336
1.00	1.91	2.31	2.88	6.13	-4.5	6	2-10	1-3.3	0.0330
0.90	1.91	2.87	2.87	6.58	-4.9	6	2-10	1-3.3	0.0329
0.80	1.91	3.51	2.87	6.97	-5.8	6	2-10	1-3.3	0.0329
0.71	1.90	3.95	2.87	7.38	-5.5	6	2-10	1-3.3	0.0294
0.61	1.90	4.31	2.88	7.62	-6.1	6	2-10	1-3.3	0.0277
0.51	1.90	4.86	2.88	7.78	-6.6	6	2-10	1-3.3	0.0261
0.41	1.90	5.24	2.88	7.79	-7.1	6	2-10	1-3.3	0.0250
0.31	1.90	5.63	2.88	7.62	-7.2	6	2-10	1-3.3	0.0232
0.21	1.90	5.72	2.89	7.37	-7.7	6	2-10	1-3.3	0.0232
0.17	1.90	5.78	2.89	7.23	-7.6	6	2-10	1-3.3	0.0220
0.27	1.90	5.46	2.89	7.04	-7.7	6	2-10	1-3.3	0.0214
0.36	1.90	5.27	2.89	6.97	-7.1	6	2-10	1-3.3	0.0192
0.45	1.91	5.05	2.89	6.79	-5.5	6	2-10	1-3.3	0.0160
0.55	1.91	4.93	2.90	6.48	-5.7	6	2-10	1-3.3	0.0169
0.64	1.91	4.85	2.90	6.23	-4.9	6	2-10	1-3.3	0.0149
0.73	1.91	4.84	2.91	6.19	-4.7	6	2-10	1-3.3	0.0148
0.82	1.91	4.60	2.91	6.08	-4.7	6	2-10	1-3.3	0.0153
0.92	1.91	4.43	2.91	6.13	-5.0	6	2-10	1-3.3	0.0162

Chapter V

The charge and discharge mechanism of $Li_{1.20}Mn_{0.54}Co_{0.13}Ni_{0.13}O_2$ - Study of materials prepared chemically -

Reversible oxygen participation to the redox processes revealed for $Li_{1.20}Mn_{0.54}Co_{0.13}Ni_{0.13}O_2$

H. Koga, L. Croguennec, M. Ménétrier, K. Douhil, S. Belin, L. Bourgeois, E. Suard, F. Weill and C. Delmas

J. Electrochem. Soc., 160 (2013) A786-A792

Chapter V – The charge and discharge mechanism of $Li_{1.20}Mn_{0.54}Co_{0.13}Ni_{0.13}O_2$
- Study of materials prepared chemically -

V. 1 - Introduction

Lithium-ion batteries with high energy density are key component for portable devices, more recently they are developed to be used as large batteries for hybrid vehicles and electric vehicles. $LiCoO_2$ has been used as a positive electrode in Lithium-ion batteries for portable devices due to its high energy density, cyclability over long range cycling and its ease of preparation **[1]**. Nevertheless, $LiCoO_2$ does not fit to the requirements of large batteries developed for transportation due to its high cost and safety issues in the charged state of the battery. New positive electrode materials have thus been proposed as attractive alternatives to $LiCoO_2$: $(1\text{-}x)LiMO_2.xLi_2MnO_3$ (M = Ni, Co, Mn) was reported as one of those delivering the largest capacity as compared to other layered oxides **[2-4]**. An irreversible *plateau* is observed at ~4.5 V vs. Li^+/Li during the 1st charge of these lithium and manganese-rich materials **[2-4]**, on the contrary to what is observed for conventional layered oxides: it is considered to be at the origin of the large overcapacity obtained for these materials **[5]**. Oxygen “gas” would be lost from the material as a result of oxygen oxidation as it was previously observed by mass spectrometry and estimated from the weight loss of the electrodes after the charge **[6-7]**. Different mechanisms were proposed to accommodate together, lithium deintercalation, charge compensation with an oxygen loss and stabilization of the host structure with a reduced O/M ratio **[6, 8]**: *(1)* Oxygen ions diffuse from the inside to the outside of the particles and are released as oxygen gas on the surface of the particles. In that case a structure with oxygen vacancies is formed. *(2)* Oxygen ions are released only at the surface of the particles with a migration of the transition metal ions from the outside to the inside of the particles in the sites left vacant by the extra lithium ions. In that case shrinkage and densification of the host structure occur. Several studies were performed to confirm (or not) these hypotheses, but the details of the charge and discharge mechanism still remains not clear. As we discussed in details in reference **[8]** for $Li_{1+x}(Ni_{0.425}Mn_{0.425}Co_{0.15})_{1-x}$ ($x \leq 0.12$), from solid state chemist’s considerations and considering especially the instability of Mn^{4+} and Ni^{4+} in MO_5 environment, hypothesis *(1)* is not valid as it would induce a large amount of oxygen vacancies and thus of MO_5 environment for the transition metal ions. Hypothesis *(2)* with transition metal migration can also not explain their large discharge capacity because the theoretical discharge capacity estimated taking account of a decrease of available Li sites due to densification is much less than experimental capacity **[9]**. We thus proposed that oxygen participates to the reactions involved upon cycling of $Li_{1.20}Mn_{0.54}Co_{0.13}Ni_{0.13}O_2$ involving a phase separation **[9]**. At the surface oxygen ions are oxidized and then released as oxygen gas during the "plateau" observed in the 1st charge, leading to densification through the migration of transition metal ions from the surface to the bulk. Densification with migration of transition metal ions is expected to be much more difficult in the bulk than at the surface. Oxygen is also oxidized in the bulk, but without oxygen release, and is then reduced in the next discharge. In fact, the dominance of these two different reactions would continuously change between surface and bulk. As shown in reference **[9]**, depending on the composition (in manganese especially) and thus on the electronic structure of these lithium and manganese-rich layered oxides, oxygen can participate or not to the redox processes reversibly. Indeed for $Li_{1.12}Ni_{0.374}Mn_{0.374}Co_{0.132}O_2$ a densification mechanism was proposed without reversible participation of oxygen whereas for $Li_{1.20}Mn_{0.54}Co_{0.13}Ni_{0.13}O_2$, richer in manganese, reversible participation of oxygen was considered **[8]**.

We have studied in details the structure and charge-discharge mechanism of $Li_{1.20}Mn_{0.54}Co_{0.13}Ni_{0.13}O_2$ **[9-10]**, also sometimes written as 0.4 $LiNi_{1/3}Mn_{1/3}Co_{1/3}O_2$ – 0.4 Li_2MnO_3. $Li_{1.20}Mn_{0.54}Co_{0.13}Ni_{0.13}O_2$ is a solid solution with a local monoclinic symmetry (*C2/m* as Li_2MnO_3) and ordered domains limited to a few layers along the c-axis, no segregation between domains of $LiNi_{1/3}Mn_{1/3}Co_{1/3}O_2$ and Li_2MnO_3 exists in this material as we recently showed by electron microscopy **[10]**. The analytical results definitely revealed that the mechanism observed during the 1st cycle of $Li_{1.20}Mn_{0.54}Co_{0.13}Ni_{0.13}O_2$ in a lithium battery cannot be explained considering only hypothesis *(2)* mentioned above, *i.e.* the densification model. We thus proposed based on our experimental data that oxygen participates to the redox processes **[9]**. In order to support further this hypothesis, we prepared chemically materials with similar chemical compositions, oxidation states for transition metal ions, structural and electrochemical properties as those obtained electrochemically. The absence of carbon and polyvinylidene fluoride (PVdF) as additives in the electrode allows for instance characterizations such as density measurements and neutron diffraction analyses, essential to conclude.

V. 2 - Experimental

$Li_{1.20}Mn_{0.54}Co_{0.13}Ni_{0.13}O_2$ was prepared using the sol-gel method with a final thermal treatment at high temperature (1000°C for 5 h), as described in details in reference **[10]**. Lithium was deintercalated chemically from $Li_{1.20}Mn_{0.54}Co_{0.13}Ni_{0.13}O_2$, which was preliminary dried at 120°C overnight, by dropping an 0.3M NO_2BF_4 acetonitrile solution in excess into a suspension of the powder $Li_{1.20}Mn_{0.54}Co_{0.13}Ni_{0.13}O_2$ in acetonitrile. The obtained mixture was maintained under stirring for 1 day. Chemical lithium reinsertion was then performed by adding an 0.3M LiI acetonitrile solution in excess into a suspension in acetonitrile of the material previously chemically deintercalated, stirring was maintained for 3 days. The powders obtained after chemical lithium deintercalation and reinsertion were washed thoroughly with acetonitrile. All these chemical lithium deintercalation and reinsertion were carried out in an argon filled glove box.

Li, Ni, Mn and Co contents present in the material were determined using inductively coupled plasma spectroscopy (ICP) after the complete dissolution of the powder into an acidic solution. The morphology of the powders was observed by scanning electron microscopy (SEM) using a Hitachi S4500 field emission microscope with an accelerating voltage of 5.0 kV. The materials were coated with a thin layer of platinum in order to prevent any charge accumulation on their surface. The powders were characterized by X-ray diffraction (XRD) using a Siemens D5000 diffractometer equipped with a detector using energy discrimination and Cu Kα radiation, in the 15 – 80 ° ($2\theta_{Cu}$) range, with steps of 0.02 ° ($2\theta_{Cu}$) and a constant counting time of 15s. Neutron diffraction was performed using the D2B beam line at ILL (Institut Laue-Langevin) in Grenoble (France). The diffraction pattern was collected in transmission mode at room temperature with a wavelength of 1.593610 Å in the [0-160]° angular range using an 0.05° (2θ) step with an accumulation time of 10 hours. The sample was contained in an 8 mm diameter vanadium tube. Due to the geometry of the neutron diffractometer, it was necessary to correct the absorption in order to take into account a decrease of the experimental diffracted intensity compared to the expected one, through the μR factor (R the radius of the vanadium cylinder and μ the linear absorption factor). μR was found to be equal to 0.9. The samples were maintained in specific sample-holders prepared in glove box to prevent any contact with ambient atmosphere and thus avoid their evolution during the acquisition. The profile matching and the Rietveld refinement of the X-ray and neutron diffraction patterns were performed using the Fullprof software **[11]**. Raman scattering measurements were performed with a Horiba Jobin Yvon Labram HR-800 micro-spectrometer. Spectra were recorded using a 514.5 nm excitation wavelength of an Ar^+ laser, with a power adjusted to ca. 100 µW in order to avoid any degradation of the sample. No specific sample preparation was required. The average oxidation state of transition metal ions was determined by iodometric titration. The sample was dissolved at 60 °C overnight in an aqueous solution of HCl and KI, and then this solution was titrated with $Na_2S_2O_3$. Magnetic measurements were performed under a magnetic field of 500 Oe as a function of temperature (between 4 and 300K) using a Super-conducting Quantum Interference Device (SQUID) (quantum design MPMS-5S). X-ray absorption spectroscopy (XAS) experiments were performed using the SAMBA beam line in transmission mode at Soleil in Gif-sur-Yvette (France). Thanks to the large camshaft of the Si111 Quick-EXAFS monochromator, the Mn, Co and Ni edges were recorded simultaneously two by two: first the Mn and Co K edges, then the Co and Ni K edges, 30 s to 3 min. later changing the alignment parameters of this monochromator via a script. XANES data were analyzed using Athena software. Oxides (layered, spinel or rocksalt-types), well controlled in structure and composition, were used as references for the different oxidation states possible for Mn, Co and Ni. The volume density of the materials after drying for one night under vacuum was measured using an Ultrapycnometer 1000 (Quantachrome Instruments) with helium gas.

The electrochemical properties of the prepared materials were tested using CR2325 coin cells with lithium metal as counter and negative electrode. The positive electrodes consisted of 80 wt% of active material, 10 wt% of a carbon black / graphite (1:1) mixture and 10 wt% of polyvinylidene fluoride (PVdF) binder and were cast on an aluminum foil. They were then pressed at 40 MPa after drying at 80°C overnight. The cells were assembled in an argon filled glove box with the electrolyte 1M $LiPF_6$ dissolved in a mixture of propylene carbonate (PC), ethylene carbonate (EC), and dimethylcarbonate (DMC) 1:1:3 by volume. The electrochemical measurements were performed between 2.5 and 4.8 V *vs.* Li^+/Li, the cycling rate being defined such as the C rate corresponds to a theoretical exchange of one electron in 1 hr during charge. Before their characterization the samples were recovered in glove box, washed with DMC in large excess and dried under vacuum.

V. 3 - Results and discussion

V. 3. 1 - Comparison of the materials obtained from chemical and electrochemical reactions

NO_2BF_4 was chosen as the appropriate oxidizer to (almost) fully deintercalate our material $Li_{1.20}Mn_{0.54}Co_{0.13}Ni_{0.13}O_2$ as the redox couple NO_2^+/NO_2 is reported to be at 5.1 V vs. Li^+/Li **[12]**, which is well above the irreversible *plateau* observed at 4.5 V vs. Li^+/Li during the first charge **[9-10]**. The chemical lithium deintercalation from conventional layered oxides $LiMO_2$ (M: Co, Ni, Mn) with NO_2BF_4 occurs according to the following global equation (1):

$$LiMO_2 + NO_2BF_4 \rightarrow MO_2 + NO_2 + LiBF_4 \qquad (1)$$

Chemical lithium reinsertion using LiI was then performed in the material previously deintercalated, with a voltage for the redox couple I^0/I close to 3V vs. Li^+/Li **[13-14]**. The chemical lithium reinsertion in MO_2 is for instance expected to occur according to equation (2):

$$MO_2 + LiI \rightarrow LiMO_2 + 1/2I_2 \qquad (2)$$

Table V. 1 gives the comparison of the chemical compositions determined by ICP, fixing the total ratio of transition metal ions to 0.8, for the pristine material $Li_{1.20}Mn_{0.54}Co_{0.13}Ni_{0.13}O_2$, the material recovered from the battery after a first charge up to 4.8 V vs. Li^+/Li, the material obtained after chemical lithium deintercalation using NO_2BF_4, the material recovered from the battery after the 1st cycle (charged up to 4.8 V vs. Li^+/Li and discharged down to 2.5 V vs. Li^+/Li) and the material obtained after chemical lithium reinsertion using LiI. After chemical lithium deintercalation with NO_2BF_4 0.09 mol Li^+ ions remain in the host structure. The amount of Li^+ ions deintercalated chemically is larger than that deintercalated electrochemically at the end of the first charge of the battery up to 4.8 V vs. Li^+/Li at a rate of C/20 (~1.10 versus ~1.00), as expected from the higher potential imposed by the redox couple NO_2^+/NO_2 (5.1 V vs. Li^+/Li). These chemical analyses show also that 0.94 mol Li^+ was reinserted chemically using LiI to the material previously deintercalated to form $Li_{1.03}Mn_{0.54}Co_{0.13}Ni_{0.13}O_2$. For comparison, the material recovered from the battery after a first electrochemical cycle at C/20 is, despite slightly smaller lithium content, close in composition with $Li_{0.96}Mn_{0.54}Co_{0.13}Ni_{0.13}O_2$. As expected no change in Mn, Co and Ni contents was observed.

Table V. 1: Chemical compositions determined by ICP for the pristine material, the material recovered from the battery after a first charge up to 4.8 V vs. Li^+/Li, the material obtained after chemical lithium deintercalation, the material recovered from the battery after the 1st cycle and the material obtained after chemical lithium deintercalation and reinsertion.

Sample	Composition			
	Li	Mn	Co	Ni
The pristine material	1.19	0.54	0.13	0.13
The material after the first charge up to 4.8V vs. Li^+/Li	0.18	0.54	0.14	0.13
The material after chemical Li deintercalation	0.09	0.54	0.13	0.13
The material after the 1st cycle	0.96	0.53	0.14	0.13
The material after chemical Li deintercalation and reinsertion	1.03	0.54	0.13	0.13

Fig. V. 1 gives a comparison of the SEM micrographs obtained for the pristine material $Li_{1.20}Mn_{0.54}Co_{0.13}Ni_{0.13}O_2$, the material recovered after a 1st cycle in a lithium battery (*i.e.* with carbon and PVdF as additives) and the material obtained chemically after lithium deintercalation and reinsertion. The shape of the particles is maintained in both cases. No obvious damage is observed at the surface of the particles, as well as no obvious formation of degradation products is detected at the surface and in the grain boundaries of the aggregates. It is interesting to mention that our XPS analyses (not reported here) have confirmed for these materials that the mechanism involved upon cycling is not associated with a drastic formation of solid electrolyte interphases (SEI) **[15]**.

(a) Pristine material

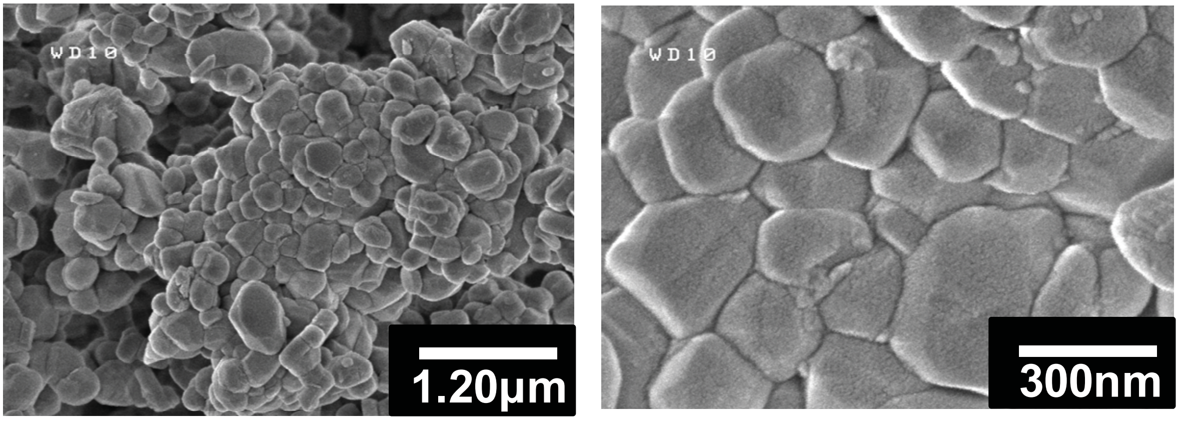
WD10
1.20µm
WD10
300nm

(b) The material after the 1^{st} cycle

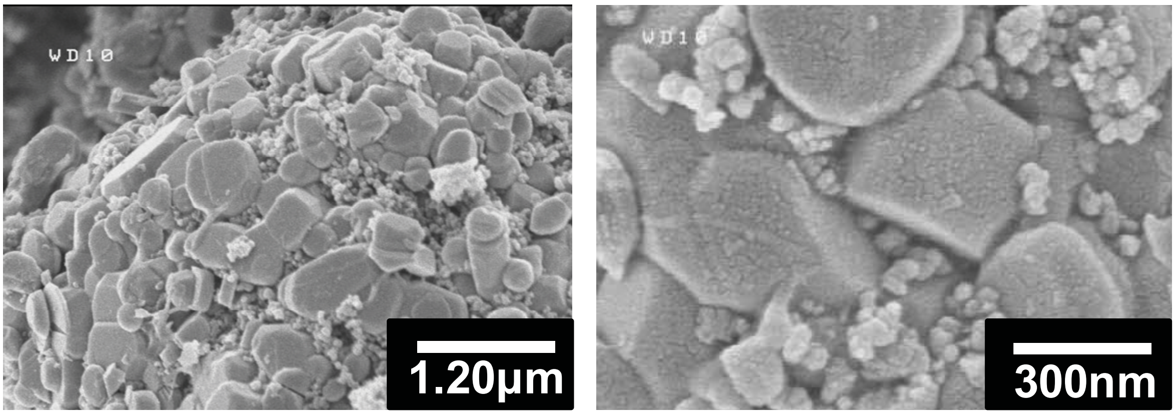
WD10
1.20µm
WD10
300nm

(c) The material after chemical Li deintercalation and reinsertion

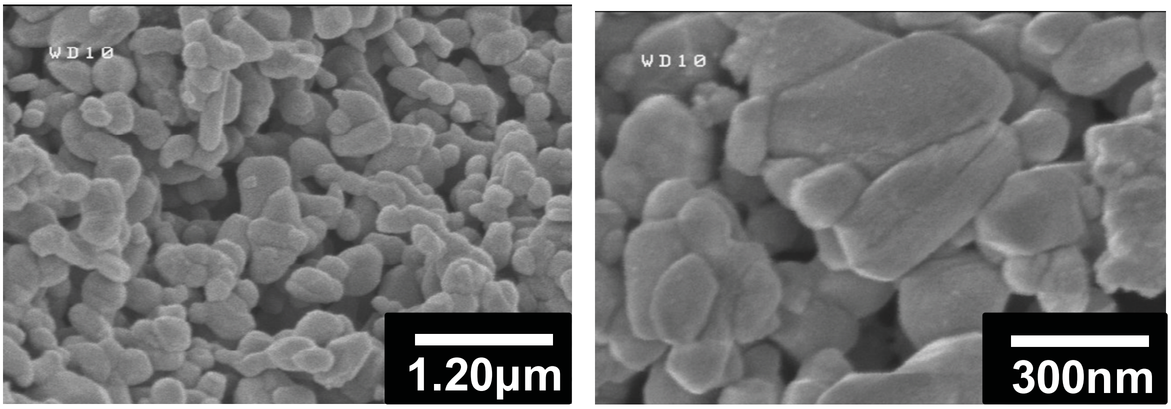
WD10
1.20µm
WD10
300nm

Fig. V. 1: SEM images of the pristine material (a), the material recovered from the battery after the 1^{st} cycle with carbon and PVdF (b) and the material obtained after chemical Li deintercalation and reinsertion (c).

The XRD patterns obtained for the five samples are given in **Fig. V. 2**: the materials recovered from batteries after a first full charge and after a first cycle are compared to the pristine material in **Fig. V. 2a** and the chemically deintercalated and reintercalated materials are compared to the pristine material in **Fig. V. 2b**. All the peaks except the extra peaks due to cation ordering in the transition metal layers (enlarged in the angular range [20 – 24°(2θ)] and those due to carbon additives in the electrode (noted by * in **Fig. V. 2a**) can be indexed in α-$NaFeO_2$-type unit cells described in the space group *R-3m*. The peaks present in the angular range [20 – 24°(2θ)] and corresponding to the cation ordering in the transition metal layers show a broadening and a decrease in their intensity after chemical lithium deintercalation from $Li_{1.20}Mn_{0.54}Co_{0.13}Ni_{0.13}O_2$ and they are not recovered after chemical lithium reinsertion (**Fig. V. 2b**). These observations are in good agreement with those made from the corresponding electrochemical experiments as shown in **Fig. 2a**. As shown in the angular range [43.5 – 45.5°(2θ)] the *(104)* peak is in fact separated into two lines, as it is especially obvious for the materials obtained after electrochemical lithium deintercalation and lithium reintercalation. This phase separation is maintained upon cycling as we reported recently in reference **[9]**, *phase 1* in the bulk where oxygen could participate to the redox reaction and *phase2* at the surface where oxygen loss occurs with transition metal migration. Note that there is not strictly two phases but a continuous modification from the surface to the bulk. For the materials obtained after chemical lithium deintercalation and lithium reinsertion, the separation of the *(104)* peak is not obvious even if a broadening is observed. Phase separation previously found for electrochemical obtained materials is not observed in this case, but broadening of the lines suggests the same behavior. The comparison of the cell parameters determined for the five samples from the refinement of their XRD data by the Le Bail method is given in **Table V. 2**. Note that for all these samples (obtained electrochemically or chemically) none of the phases observed shows a $c_{hex.}/a_{hex.}$ ratio of 4.90 as expected for a long range spinel structure. These results suggest thus again that even if migration of transition metal ions from the slabs to the interslab spaces occurs, it is probably limited. In order to get more insight in possible changes of the local structure of these materials their characterization using Raman spectroscopy was performed.

(a) Electrochemical experiments

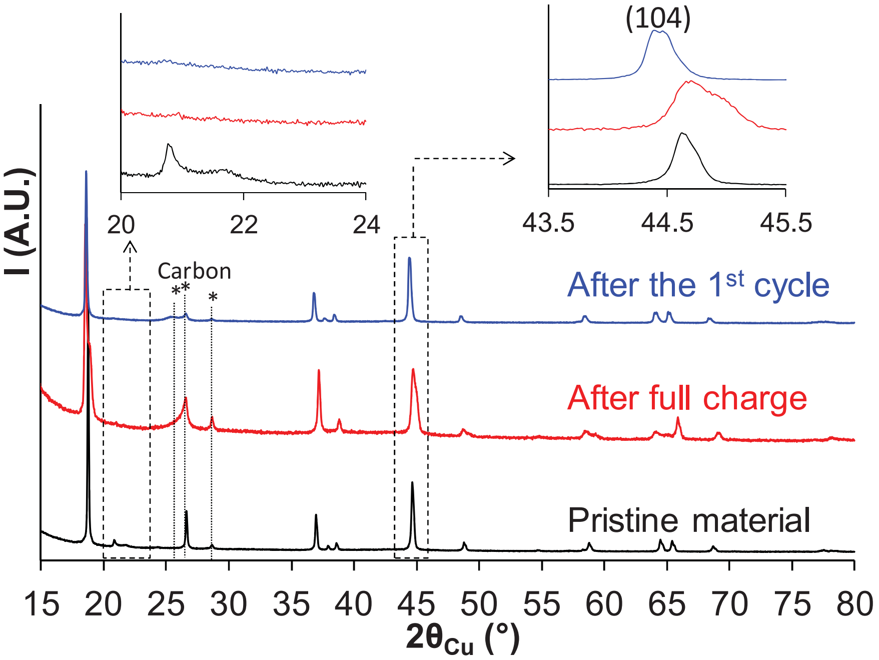

(b) Chemical experiments

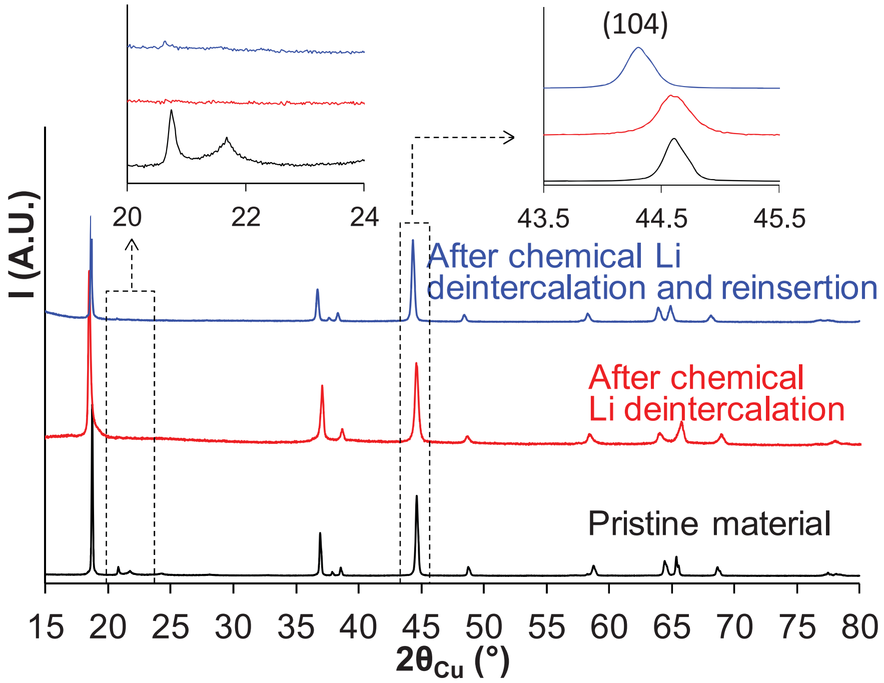

Fig. V. 2: Comparison of the X-ray diffraction patterns recorded in the angular range 15-80° 2θ_{Cu} for the pristine material, the material recovered from the battery after the full charge up to 4.8 V vs. Li^+/Li and the material recovered from the battery after the 1st cycle (a) and in parallel, comparison of the X-ray diffraction patterns recorded for the pristine material, the material obtained after chemical Li deintercalation and the material obtained after chemical Li deintercalation and reinsertion (b). Enlargements are given in the 20-24° and 43.5-45.5° angular ranges.

Table V. 2: Cell parameters, determined by the Le Bail refinement of the X-ray diffraction data, for the pristine material, the material recovered from the battery after a first charge up to 4.8 V vs. Li^+/Li, the material obtained after chemical lithium deintercalation, the material recovered from the battery after the 1st cycle and the material obtained after chemical lithium deintercalation and reinsertion

Sample		a_{hex} (Å)	c_{hex} (Å)	c_{hex}/a_{hex}	V (Å^3)
The pristine material		2.8511(2)	14.235(2)	4.99	100.21(2)
The material after the first charge up to 4.8V vs. Li^+/Li *	Phase 1 (Bulk)	2.8341(3)	14.406(3)	5.08	100.21(8)
	Phase 2 (External)	2.8342(2)	14.376(4)	5.07	98.52(2)
The material after chemical Li deintercalation		2.8417(1)	14.396(5)	5.07	100.68(5)
The material after the 1st cycle *	Phase 1 (Bulk)	2.8629(2)	14.344(2)	5.01	101.82(2)
	Phase 2 (External)	2.8568(7)	14.29(3)	5.00	101.01(5)
The material after chemical Li deintercalation and reinsertion		2.8750(3)	14.364(3)	5.00	102.82(2)

* Mixture of *two phases* identified as in reference **[9]**: *Phase 1* with the larger $c_{hex.}$ and *Phase 2* with the smaller $c_{hex.}$

Raman spectra of the same five materials (pristine, electrochemical and chemical) are compared in **Fig. V. 3a**. The spectrum of the pristine material was discussed in details in our previous paper **[10]**. Our study revealed first that the Raman spectrum of "$Li_{1.20}Mn_{0.54}Co_{0.13}Ni_{0.13}O_2$" is not a simple combination of those of Li_2MnO_3 and $LiNi_{1/3}Mn_{1/3}Co_{1/3}O_2$, showing that it is not made of domains of these two compositions and structures but that it is an actual solid solution. The number of bands supports the presence of environments with similar local symmetry as in Li_2MnO_3 (*C2/m* space group). The comparison of the materials obtained electrochemically in batteries or by chemical reaction in solution shows that the spectra of the two materials deintercalated in Li are very similar in the shape and position of the bands, but very different from that of the pristine material: peaks appear at ~473 and ~530 cm^{-1} whereas others decrease in intensity at ~493 and ~604 cm^{-1}. Then, the materials reintercalated in Li are characterized by spectra close again to that of the pristine material. It thus reveals first, that the materials obtained electrochemically in batteries and by chemical reaction in solution are very similar whatever their state of charge or discharge and second, that the local symmetry remains the same in the two materials after their deintercalation and reintercalation. Indeed, in discharge the peaks observed at ~473 and ~530 cm^{-1} disappear, whereas on the contrary those at ~493 and ~604 cm^{-1} increase again in intensity. Singh et al. reported very recently an *in situ* Raman study of layered solid solution Li_2MnO_3 – $LiMO_2$ (M = Ni, Co, Mn) and observed changes in their Raman spectra very similar to those we observed in charge and in discharge **[16]**: they interestingly tried to attribute each peak, for instance to Nickel oxidation as well as cation migration or Li deintercalation. Here our purpose was more to compare the materials obtained using chemical and electrochemical reactions, first between them and then, with the pristine material. Our main conclusion here is that the materials obtained after an electrochemical cycle up to high voltage with the *plateau* or after chemical lithium deintercalation and reintercalation remain very similar to the pristine material (**Fig. V. 3b**) with local symmetry that remains similar to that in Li_2MnO_3, *i.e.* with a cation ordering in a very local scale in the slabs.

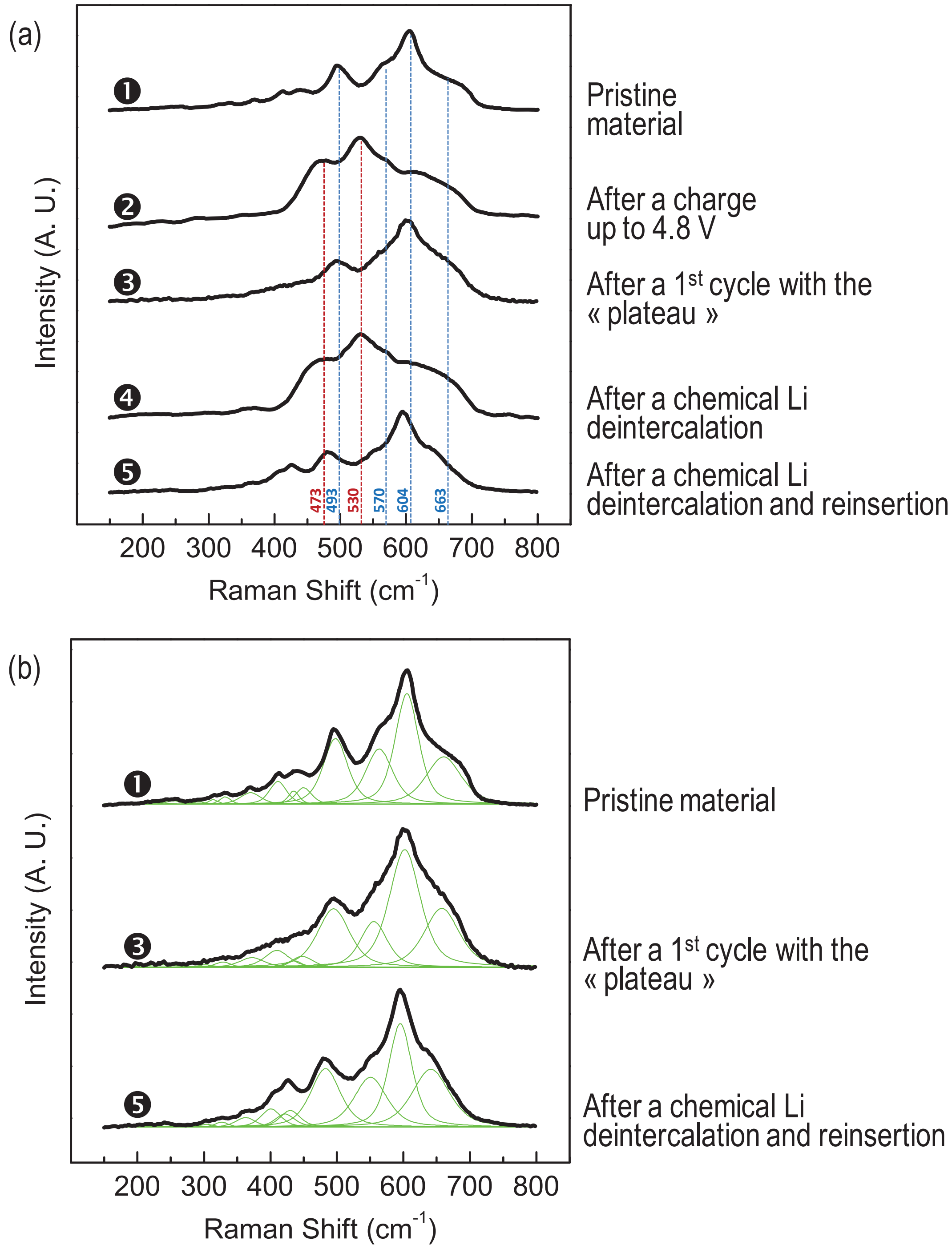

Fig. V. 3: Comparison of the Raman spectra obtained for the pristine material, the material recovered from the battery after the full charge up to 4.8 V vs. Li^+/Li, the material recovered from the battery after the 1st cycle, the material obtained after chemical Li deintercalation and the material obtained after chemical Li deintercalation and reinsertion (a). The spectra of the pristine material, the material recovered from the battery after a 1st cycle and the materials obtained chemically after Li deintercalation and reinsertion were decomposed using Pseudo-Voigt bands (here in green) to allow their easier comparison (b).

Fig. V. 4a shows the discharge and charge curves obtained for Lithium batteries using the material recovered after chemical Li deintercalation as positive electrode in a lithium cell. The initial open circuit voltage of the battery is about 4.4 V vs. Li^+/Li as expected for highly oxidized transition metal ions. At first the lithium cell was discharged (Li insertion) down to 2.5 V vs. Li^+/Li before being charged again up to 4.8 V vs. Li^+/Li. The shape of the first discharge curve is different from those obtained during the next cycles. Other electrochemical tests were performed using as positive electrode the material recovered after chemical Li deintercalation and reinsertion, as shown in **Fig. V. 4b**. The cells were charged (Li deintercalation) up to 4.8 V vs. Li^+/Li, before being discharged down to 2.5 V vs. Li^+/Li and then cycled between 2.5 and 4.6 V. The voltage of the first charge is higher than that observed for the next charges in both cases (**Fig. V. 4a** and **Fig. V. 4b**), it would be induced by the formation of a “parasitic layer” at the surface of the particles during the chemical reactions. The charge and discharge curves obtained for the pristine material $Li_{1.20}Mn_{0.54}Co_{0.13}Ni_{0.13}O_2$ are compared in **Fig. V. 5** to those obtained for the material recovered after a chemical lithium deintercalation and reintercalation. In the 1st charge, the pristine material shows the long *plateau* that is not recovered during the next discharge and charge. Note that as expected the cycling curves obtained for the material recovered after chemical lithium reinsertion do not show this *plateau*. Indeed, the redox potential of NO_2BF_4 being about 5.1 V vs. Li^+/Li, *i.e.* at higher voltage than that of the *plateau*, its use as oxidizing agent leads to the formation of a highly deintercalated material during the chemical Li deintercalation. The charge-discharge curves obtained for the material after chemical Li reinsertion are in fact similar to the 2nd cycle curves obtained for the pristine material.

From these results, the materials prepared by chemical Li (de)intercalation with NO_2BF_4 and LiI revealed very similar chemical composition, structure and electrochemical performance to the material recovered after the 1st electrochemical cycle. The material obtained after chemical Li deintercalation and reinsertion was thus characterized in details, especially regarding the oxidation state of transition metal ions, in order to confirm the participation of oxygen ions in the charge and discharge reaction. The mechanism occurring upon cycling in these materials was then deeply discussed.

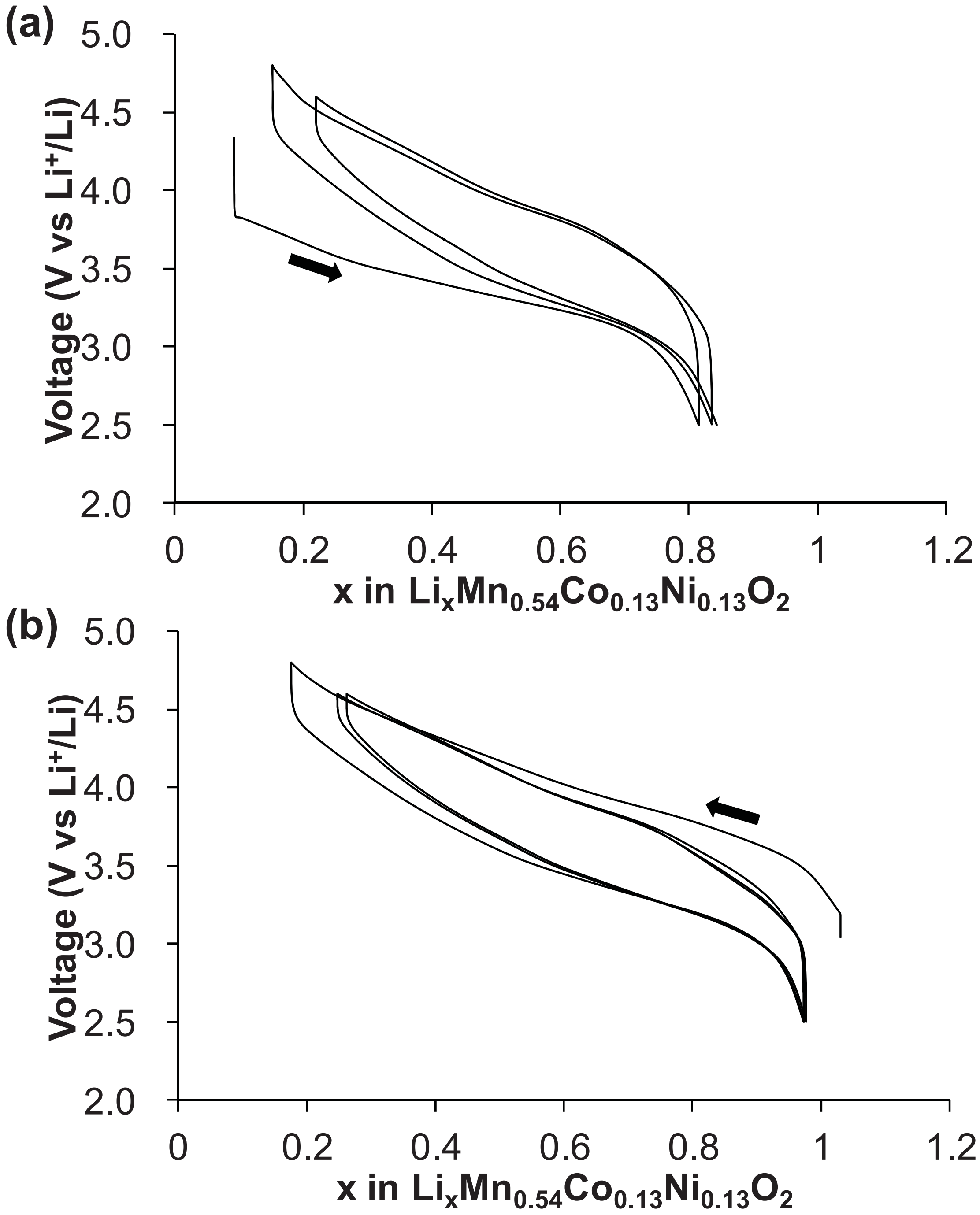

Fig. V. 4: Charge and discharge curves obtained for lithium batteries using as positive electrodes: (a) the material obtained after chemical Li deintercalation and (b) the material obtained after chemical Li deintercalation and reinsertion. The first cycle was performed between 2.5 and 4.8 V vs. Li^+/Li, whereas the next cycles were charged only up to 4.6 V vs. Li^+/Li.

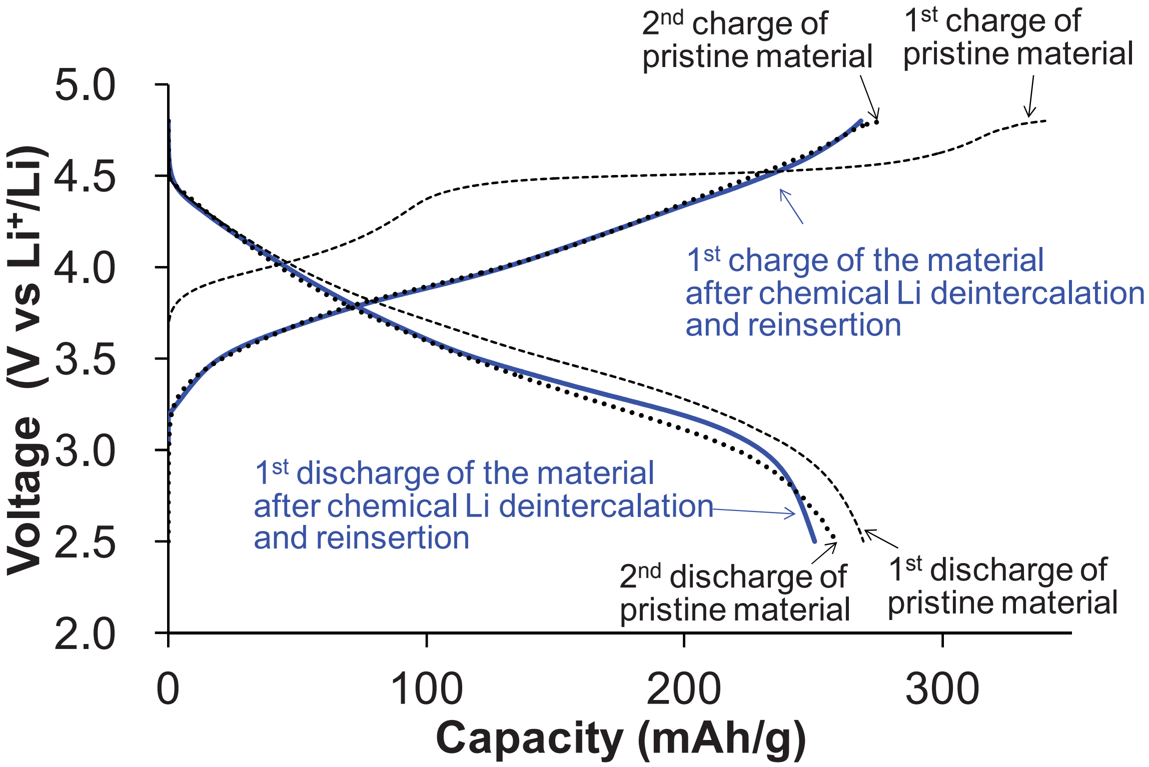

Fig. V. 5: Comparison of the charge and discharge curves obtained during the 1st and 2nd cycles of lithium batteries using the pristine material as positive electrode (dotted black lines) with those obtained during the 1st cycle of lithium batteries using the material recovered after chemical Li deintercalation and reinsertion as positive electrode (continuous blue lines).

V. 3. 2 - Characterization of the material recovered after chemical Li deintercalation and reinsertion

The average oxidation state of the transition metal ions in the material prepared chemically was determined combining redox titration, magnetic measurements and XAS measurements in order to confirm the discrepancy between experimental and estimated participation of oxygen – through oxygen loss – to compensate for Lithium deintercalation on the *plateau*. This discrepancy would be the result of oxygen participation in the charge and discharge reaction. **Table V. 3** compares the average oxidation state of transition metal ions in the pristine material and in the material recovered after chemical Lithium deintercalation and reinsertion. The experimental values obtained for the pristine material is close to that expected considering the formula $Li_{1.20}Mn_{0.54}Co_{0.13}Ni_{0.13}O_2$ and the presence of Mn, Co and Ni at the tetravalent, trivalent and divalent oxidation states, respectively. The average oxidation state of transition metal ions in the material recovered after chemical Li deintercalation and reinsertion was estimated to be 3.45 from redox titrations while the theoretical average oxidation state of transition metal ions was estimated to be 2.81 taking into account oxygen loss during the 1st charge and then reduction of Mn for charge compensation during the next discharge. Taking into account the average oxidation state of 3.45 for the transition metal ions the chemical composition is estimated to be $Li_{1.03}Mn_{0.54}Co_{0.13}Ni_{0.13}O_{1.90}$ with an oxidation state of 3.91 for Mn, indicating small involvement of Mn ions in the charge and discharge reaction. It also strongly indicates that oxygen ions participate in the redox reaction.

Table V. 3: Average oxidation state of the transition metal ions in the pristine material and in the material recovered after chemical Li deintercalation and reinsertion.

Sample	Average oxidation state of transition metal ions	
	Experimental value	Theoretical value
Pristine material	3.56	3.50 *1
After chemical Li deintercalation and reinsertion	3.45	2.81 *2

*1 Calculated from the chemical formula $Li_{1.20}Mn_{0.54}Co_{0.13}Ni_{0.13}O_2$

*2 Calculated considering an oxygen loss during the charge on the “plateau”, and then the reduction of Ni and Co, but also of Mn, to compensate for Lithium intercalation in $Li_{1.03}Mn_{0.54}Co_{0.13}Ni_{0.13}O_{1.645}$ during the discharge

Magnetic measurements were performed to compare the pristine material and the material formed after chemical Li deintercalation and reinsertion. The H/M ratio (H the applied field of 500 Oe and M the magnetization) was measured in the [5-300K] temperature range. As the number of mol of transition metal ions per gram was estimated from the results of ICP analyses, all the magnetic measurements are reported here relatively to the number of mol of transition metal ions. Indeed, as the chemical composition in oxygen is questioned in these materials, it could be very critical to report the magnetic measurements per mol of material. As shown in **Fig. V. 6** the thermal evolution of the H/M ratio is significantly different for the two materials. The Curie constants reported in **Table V. 4** were estimated considering the data in the linear domain in the temperature range [150 K – 300 K]. The experimental Curie constant determined for the pristine material is in good agreement with the theoretical value (1.34 *vs.* 1.43) whereas that determined for the material recovered after chemical Li deintercalation and reinsertion is again significantly different from that expected considering oxygen loss (1.68 *vs.* 2.08). From this result the chemical formula estimated for the material is $Li_{1.03}Mn_{0.54}Co_{0.13}Ni_{0.13}O_{1.84}$ with an oxidation state of 3.7 for Mn and not, $Li_{1.03}Mn_{0.54}Co_{0.13}Ni_{0.13}O_{1.645}$ with an oxidation state of 3 for Mn.

Table V. 4: Curie constants estimated from thermal evolution of the H/M ratio for the pristine material and the material recovered after chemical Li deintercalation and reinsertion. They are compared to the theoretical Curie constants determined considering oxygen loss for the material recovered after chemical Li deintercalation and insertion.

Sample	Curie constant	
	Experimental value	Theoretical value
The pristine material	1.34	1.43 [*1]
The material after chemical Li deintercalation and reinsertion	1.65	2.08 [*2]

[*1] based on the electronic configurations d^3 ($t_{2g}^3e_g^0$) for Mn^{4+}, d^6 (LS $t_{2g}^6e_g^0$) for Co^{3+} and d^8 ($t_{2g}^6e_g^2$) for Ni^{2+} in $Li_{1.20}Mn^{4+}_{0.54}Co^{3+}_{0.13}Ni^{2+}_{0.13}O_2$

[*2] based on the electronic configurations d^3 ($t_{2g}^3e_g^0$) for Mn^{4+}, d^4 (HS $t_{2g}^3e_g^1$) for Mn^{3+}, d^6 (LS $t_{2g}^6e_g^0$) for Co^{3+} and d^8 ($t_{2g}^6e_g^2$) for Ni^{2+} in $Li_{1.03}(Mn^{4+}_{0.08})(Mn^{3+}_{0.46})Co^{3+}_{0.13}Ni^{2+}_{0.13}O_{1.645}$, supposing that all transition metal ions are in octahedral environment.

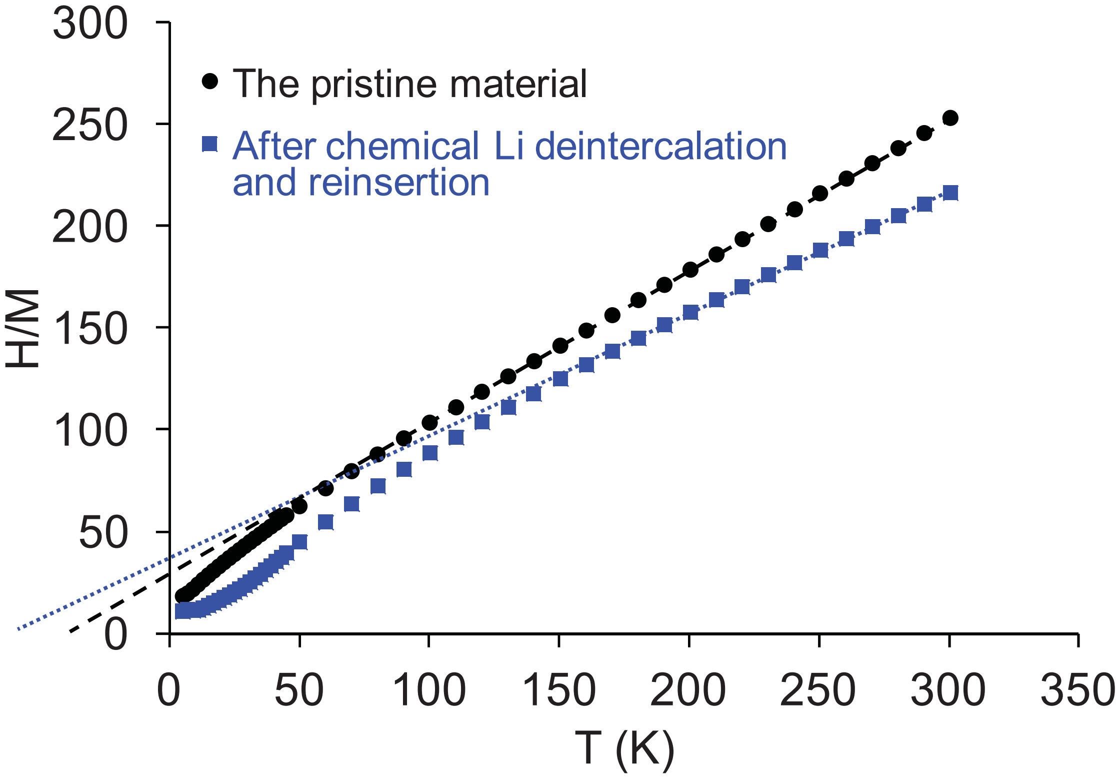

Fig. V. 6: Thermal evolution of the H/M ratio for the pristine material and the material recovered after chemical Li deintercalation and reinsertion. Curie constants were estimated considering the data between 150 K and 300 K.

Volume density measurements were performed in order to get more insight into the structure of the material: Is oxygen actually lost from the material? Volume density of pristine material was shown to be 4.18 g/cm^3 which is very close to the theoretical value of 4.24 g/cm^3. The material obtained after chemical Li deintercalation and reintercalation (*i.e.* without any additive) was shown to be characterized by a volume density of 3.88 g/cm^3. The measure was performed several times on different samples of powders and found to be reproducible within the accuracy of ± 0.01 g/cm^3. If all the lithium ions deintercalated on the *plateau* were compensated by oxygen loss, with oxygen vacancies due to oxygen migration or with a densification of the oxygen lattice due to transition metal migration, the volume densities would be of 3.79 g/cm^3 or 4.60 g/cm^3 respectively. A volume density of 4.03 g/cm^3 would be observed considering no oxygen loss. The comparison of these volume densities with the experimental one (3.88 g/cm^3) strongly suggests that if oxygen is lost, it is significantly less than expected.

In order to support this hypothesis neutron diffraction was performed as it is sensitive to oxygen stoichiometry. The experimental data recorded for the material chemically deintercalated and reintercalated were refined by the Rietveld method considering a single phase with: *(i)* the formula $(Li_{1.00-x-y}Ni_y)_{3b}(Li_{0.03+x}Mn_{0.54}Co_{0.13}Ni_{0.13-y})_{3a}(O_{2-z})_{6c}$ described in the *R-3m* space group, *(ii)* a possible distribution of Li between the interslab space and the slab (x), *(iii)* a possible migration of Ni from the slab to the interslab space (y) and *(iv)* a possible oxygen loss (z). This single phase is in fact an average phase taking into account the "two phases" formed from the beginning of the *plateau* that are very close in cell parameters in the discharge state of the battery **[9]**. The atomic displacement parameters (*Biso*) were fixed to those determined for the pristine material **[10]**. The comparison of the experimental and calculated neutron diffraction patterns is given in **Fig. V. 7**, a good minimization of the difference was obtained with $x = 0.04$, $y = 0.04$ and $z = 0.14$ and thus an average composition of $Li_{1.03}Mn_{0.54}Co_{0.13}Ni_{0.13}O_{1.86}$ for the sample. This result reveals that no drastic migration of Ni ions occurs into the interslab space and also that less oxygen is lost from the material than the amount expected considering compensation of the lithium deintercalated on the *plateau* by oxygen loss ($z = 0.14$ instead of 0.36 whatever the model (densification or oxygen vacancies)). The oxygen stoichiometry thus determined is in very good agreement with those deduced from redox titration as well as magnetic measurement, combined for both of them with chemical analyses.

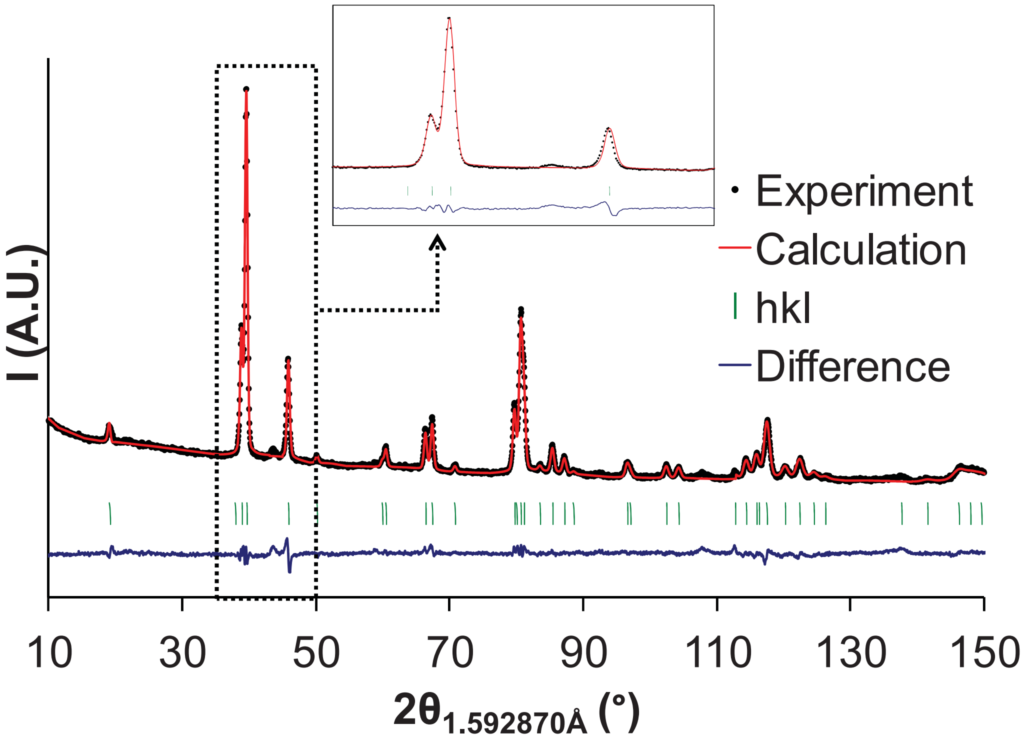

Fig. V. 7: Comparison of the experimental and calculated neutron diffraction patterns for the material obtained after chemical Li deintercalation and reinsertion in $Li_{1.20}Mn_{0.54}Co_{0.13}Ni_{0.13}O_2$. The experimental data were refined using the Rietveld method and considering a description of the unit cell in the *R-3m* space group

The comparison of the XANES spectra obtained at the Ni, Co and Mn K-edge for the pristine material, the material recovered from the battery after the 1st cycle with the *plateau* and the material obtained after chemical Li reinsertion are compared in **Fig. V. 8** with those of reference samples ($LiNi^{II}_{1/3}Mn^{IV}_{1/3}Co^{III}_{1/3}O_2$, $LiNi^{III}_{0.80}Co^{III}_{0.15}Al_{0.05}O_2$, $Co^{II,III}_3O_4$, $Li_2Mn^{IV}O_3$, and $LiMn^{III,IV}_2O_4$). The spectrum recorded at the Ni K-edge for the material recovered after chemical Li deintercalation and reinsertion is very similar to that of the material recovered from the battery after the 1st cycle with the *plateau*, and both are also very similar to that of the prisine material (**Fig.V. 8a**). The oxidation state of Ni ions in all these materials is expected to be close to Ni^{2+} as their spectra (and especially their (pre-)edges) are similar to that of the reference $LiNi^{2+}_{1/3}Mn_{1/3}Co_{1/3}O_2$. The spectra obtained at the Co K-edge for the material formed after chemical Li deintercalation and for that recovered after a first cycle reveal a shape similar between them, but significantly different from that of the pristine material (**Fig. V. 8b**). Nevertheless the position of the edge remains very similar for the three materials and close to that observed for the reference $LiNi_{1/3}Mn_{1/3}Co^{3+}_{1/3}O_2$. The oxidation state of Co in all these materials is thus expected to be about Co^{3+}. Finally the spectra recorded at the Mn K-edge for the materials recovered after chemical and electrochemical Li reinsertion are very similar in shape and in position. They are different from that of the pristine material (in shape and in position), with a small shift of less than 1 eV to lower energy. The oxidation state of Mn is expected to be $Mn^{3.4+}$ from ICP results reported in **Table V. 1** and considering the loss of 0.36 mol oxygen during Li deintercalation on the *plateau*, but from the comparison with the spectra of $Li_2Mn^{IV}O_3$ and $LiMn^{III,IV}_2O_4$ the actual oxidation state appears to be very close to Mn^{4+}, even if slightly smaller. This discrepancy between the oxidation state determined experimentally for Mn versus that theoretically expected considering the mechanism of oxygen loss has already been pointed out by other research groups, suggesting the possibility for other uncommon redox processes to occur in addition to normal redox of transition metal ions **[17]**. The changes observed in the shape of the spectra recorded at the Mn and Co K-edges versus that of the pristine material (and not observed at the Ni K-edge) are probably explained by the cation ordering present in the transition metal slabs. Indeed, the Li^+ ions present in excess in the slabs occupy the same sub site (α) that the Ni^{2+} ions, whereas the Co^{3+} and Mn^{4+} ions occupy the same sub site (β) as precisely described in **[10]**. Li deintercalation from the slabs (which is mostly irreversible as reported by **[15]**) modifies the direct environment of Mn and Co that are initially surrounded by 3Li and 3M (M = Mn, Co), whereas that of Ni (as initially surrounded by 6M) is not significantly modified. This result is in good agreement with the results of the redox titration and magnetic measurements.

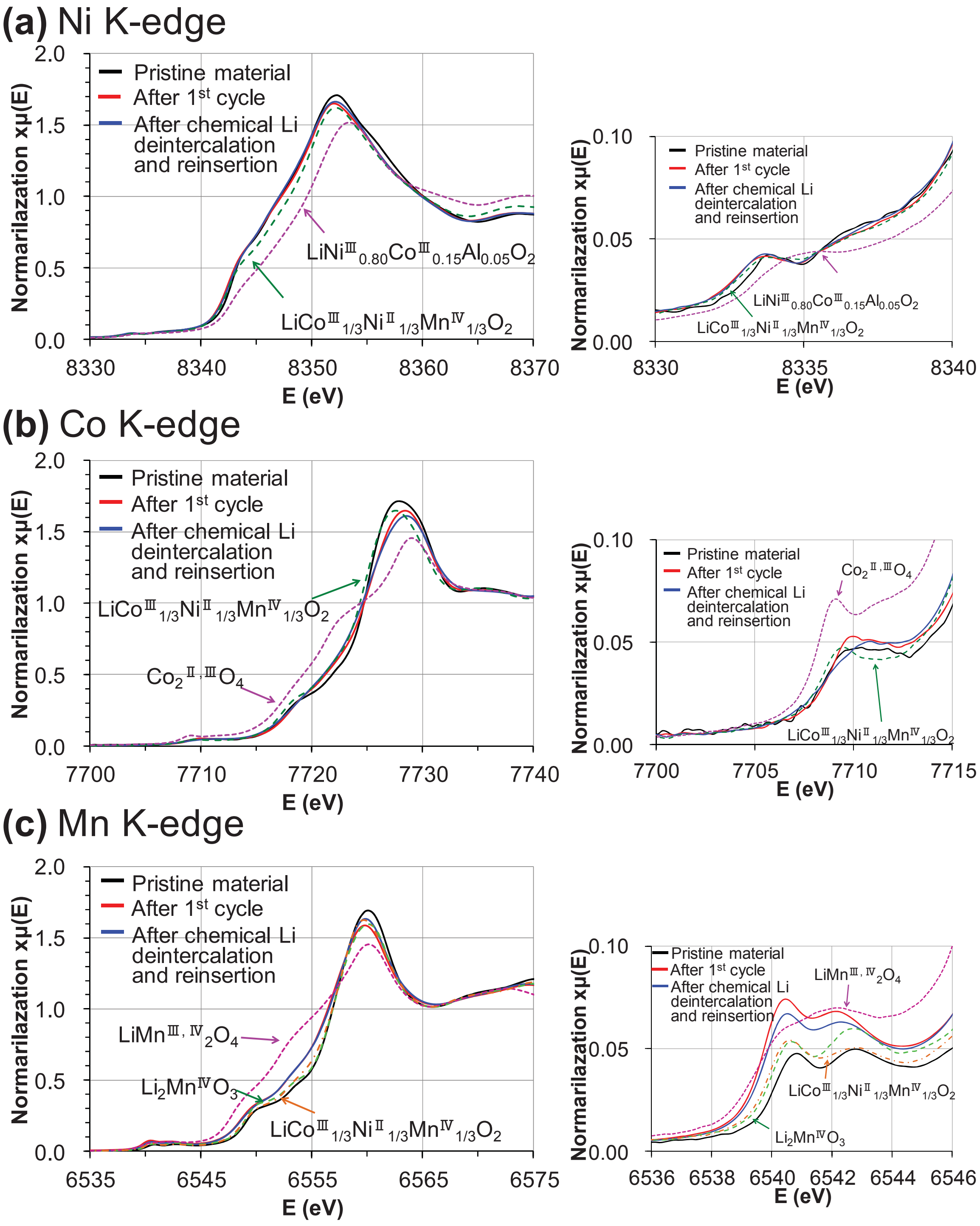

Figure V. 8: Comparison of the XANES spectra at the Ni K-edge (a), Co K-edge (b) and Mn K-edge (c) for the pristine material (Black line), the material recovered from the battery after the 1st cycle (Red line) and the material obtained after chemical Li deintercalation and reinsertion (Blue line). XANES spectra recorded for fully characterized samples of $LiCo^{III}_{1/3}Ni^{II}_{1/3}Mn^{IV}_{1/3}O_2$, $LiNi^{III}_{0.80}Co^{III}_{0.15}Al_{0.05}O_2$, $Co^{II,III}_3O_4$, $Li_2Mn^{IV}O_3$ and $LiMn^{III,IV}_2O_4$ are given as references.

V. 3. 3 - Discussion

Supposing that Li deintercalation on the *plateau* is fully compensated by oxygen loss, the chemical composition of the material recovered after chemical Li deintercalation and reinsertion was expected to be $Li_{1.03}Mn_{0.54}Co_{0.13}Ni_{0.13}O_{1.64}$ with an average oxidation state for the transition metal ions of 2.81. The reduction of manganese from Mn^{4+} to Mn^{3+} was considered, with those of Ni^{4+} to Ni^{2+} and Co^{4+} to Co^{3+}, to balance Li intercalation during the first discharge. The actual average oxidation state was determined to be 3.45 by redox titration, much higher than the theoretical value, suggesting thus that manganese is almost not oxidized. From the results of redox titration and ICP analysis the chemical composition determined for that material is actually $Li_{1.03}Mn_{0.54}Co_{0.13}Ni_{0.13}O_{1.90}$. This result is also supported by magnetic measurement and neutron diffraction analysis, the first leads to a composition of $Li_{1.03}Mn_{0.54}Co_{0.13}Ni_{0.13}O_{1.84}$ and the second to $Li_{1.03}Mn_{0.54}Co_{0.13}Ni_{0.13}O_{1.86}$. The composition thus determined (*i.e.* $Li_{1.03}Mn_{0.54}Co_{0.13}Ni_{0.13}O_{1.87\pm0.03}$), combining redox titration, magnetic measurement, neutron diffraction and chemical analyses, is also in very good agreement with the results obtained by XAS and density measurements. Indeed, XAS revealed that Mn participates significantly less than expected to the redox processes and density measurement that more oxygen remains in the material after Li reinsertion than expected, it shows that a part of oxygen participates reversibly to the redox processes. These results support the interpretations we did previously **[9]**, *i.e.* the occurrence of two types of reactions to compensate for deintercalation of the extra Li on the *plateau*. Within the bulk the oxidation of oxygen occurs without oxygen loss and is reversible during the next discharge, whereas on the surface oxidation and loss of oxygen occurs leading to densification and to the participation of manganese (reduction) to the redox processes during the next discharge. These two reactions are associated to the ‘‘two phases’’ observed on the voltage *plateau* **[10]**.

V. 4 - Conclusions

The materials prepared from the Li and Mn-rich layered oxide $Li_{1.20}Mn_{0.54}Co_{0.13}Ni_{0.13}O_2$, by chemical Li deintercalation with NO_2BF_4 and reinsertion with LiI, were fully characterized in order to clarify the mechanism occurring upon cycling. From the beginning of the *plateau* oxygen participates to compensate for lithium deintercalation. Ni, Co and O are the cations and anion involved in the redox processes during the first charge, and especially O at high voltage. The oxygen anions present at the surface are unstable in their oxidized state. They are thus lost from the lattice, leading to a destabilization of the transition metal ions in the last atomic layers and to their migration from the surface to the bulk with a densification of the lattice. Then, Mn is, in addition to Ni and Co, involved in the redox processes occurring at the surface during the first discharge and next cycles. Within the bulk Ni, Co and O participate reversibly to the redox processes. This difference in reactions (stabilities) between the surface and the bulk explains the formation of these two phases, but also the lower participation of Mn to the redox processes and the smaller loss of oxygen than those expected considering only oxygen loss model.

V. 5 - References

[1] Mizushima, K.; Jones, P. C.; Wiseman, P. J. and Goodenough, J. B., *Mater. Res. Bull.*, **1980**, 15, 783

[2] Lu, Z.; MacNeil, D. D and Dahn, J. R., *Electrochem. Solid State lett.,* **2001**, 4(11) A191.

[3] Park, Y. J.; Hong, Y. S.; Wu, X.; Ryu, K. S and Chang, S. H., *J. Power Sources* **2004**, 129 288.

[4] Lu, Z.; Beaulieu, L. Y.; Donaberger, R.A.; Thomas, C. L. and Dahn, J. R., *J. Electrochem. Soc.*, **2002**, 149, A778-791

[5] Lu, Z. and Dahn, J. R., *J. Electrochem. Soc.*, **2002**, 149, 7, A815-A822

[6] Armstrong, R.; Holzapfel, M.; Novak, P.; Johnson, C .S.; Kang, S. -H.; Thackeray, M. M.; Bruce, P. G., *J. Am. Chem. Soc.*, **2006**, 128, 8694

[7] Hong, Y. -S.; Park, Y. J.; Ryu, K. S.; Change S. H. and Kim, M. G., *J. Mater. Chem.*, **2004**, 14, 1424-1429

[8] Tran, N.; Croguennec, L.; Menetrier, M.; Weil, F.; Biensan, P.; Jordy, C and Delmas, C., *Chem. Mater*, **2008**, 20, 4815-4825

[9] Koga, H. ; Croguennec, L. ; Ménétrier, M.; Mannessiez, P. ; Weill, F.; Delmas, C., *accepted in J. Power. Sources, 2013.*

[10] Koga, H. ; Croguennec, L. ; Mannessiez, Ph. ; Ménétrier, M.; Weill, F.; Bourgeois, L. ; Duttine, M. ; Suard, E. ; Delmas, C., *J. Phys. Chem.* **2012**, 116(25), 13497

[11] Rodriguez-Carvajal, J. Laboratoire Léon Brillouin., http://www-llb.cea.fr/fullweb/powder.htm, **2004**

[12] Wizansky, A.R.; Rauch, P. E. and Disalvo, F. J., *J. Solid state Chem.*, **1989**, 81, 203

[13] Popov, A. I. and Geske, D. H., *J. Am. Chem. Soc.*, **1958**, 80, 1340

[14] Tarascon, J. M., Guyomard, D., *J. Electrochem. Soc.,* **1991**, 138, 2864

[15] Jiang, M.; Key, B.; Meng, Y.S and Grey, C.P., *Chem. Mater.,* **2009**, 21, 2733-2745

[16] Singh, G.; West, W. C.; Soler, J. R.; Katiyar, S., *J. Power. Sources*, **2012**, 218, 34-38

[17] Ito, A.; Shoda, K.; Sato, Y., Hatano, M.; Horie, H.; Ohsawa, Y., **2011**, 196, 4785-4790

Chapter VI

The charge and discharge mechanism of $Li_{1.20}Mn_{0.54}Co_{0.13}Ni_{0.13}O_2$ - Local structural change observed with HAADF STEM -

C. Genevois, H. Koga, L. Croguennec, M. Ménétrier,
C. Delmas and F. Weill
To be published

Chapter VI – The charge and discharge mechanism of $Li_{1.20}Mn_{0.54}Co_{0.13}Ni_{0.13}O_2$ - Local structural change observed with HAADF STEM-

I. 1 - Introduction

From our previous results we have proposed that phase separation that occurs during the 1st charge of $Li_{1.20}Mn_{0.54}Co_{0.13}Ni_{0.13}O_2$ is associated at the surface, to transition metal migration from the surface to the bulk with oxygen loss at the surface (densification) and within the bulk, to the participation of oxygen to the redox processes in charge and in discharge without remarkable structural changes **[1]**.

Aberration-corrected high-angle annular dark-field scanning transmission electron microscopy (HAADF-STEM) and nano electron diffraction were performed to characterize the material recovered after the 1st cycle of $Li_{1.20}Mn_{0.54}Co_{0.13}Ni_{0.13}O_2$ with and without the "plateau", to confirm the structural changes occurring during the 1st cycle and especially during the "plateau". HAADF-STEM will allow making difference between atoms with small and large Z electron numbers and thus determining possible difference in stacking of transition metal layers but also in possible migration between the transition metal layers (slabs) and the lithium layers (interslabs). Nano electron diffraction will allow screening the structural changes within a particle from the near surface to the bulk. For comparison, a material with similar chemical composition, structural and electrochemical properties to that recovered from the batteries was prepared by chemical Li reinsertion after chemical Li deintercalation. That material prepared chemically is very attractive for analyses as no additives (carbon and binder) are included in the sample. This study was done in close collaboration with Cécile Genevois from IRMA-Rouen who did all the microscopy experiments reported here.

VI. 2 - Experimental

$Li_{1.20}Mn_{0.54}Co_{0.13}Ni_{0.13}O_2$ was prepared using the sol-gel method, as described in details in reference **[2]**. The positive electrodes consisted of 80 wt% of active material, 10 wt% of a carbon black / graphite (1:1) mixture and 10 wt% of polyvinylidene fluoride (PVdF) binder cast on an aluminum foil. They were then pressed at 40 MPa after drying at 80°C during overnight. Coin cells were assembled in an argon filled glove box with Li metal as counter electrode and 1M $LiPF_6$ dissolved in a mixture of propylene carbonate (PC), ethylene carbonate (EC), and dimethylcarbonate (DMC) 1:1:3 by volume, as electrolyte. A first sample was recovered from the battery after a charge before the "plateau" and a discharge.

Another sample was also recovered from the battery, but after a 1st charge up to 4.8 V vs. Li^+/Li (i.e. after the "plateau") and a discharge, as shown in **Fig. VI. 1**.

Li was deintercalated chemically from $Li_{1.20}Mn_{0.54}Co_{0.13}Ni_{0.13}O_2$, which was preliminary dried at 120°C overnight, by dropping an 0.3M NO_2BF_4 acetonitrile solution into a suspension of the powder $Li_{1.20}Mn_{0.54}Co_{0.13}Ni_{0.13}O_2$ in acetonitrile. The obtained mixture was maintained under stirring for 1 day. Chemical Li reinsertion was performed by adding an 0.3M LiI acetonitrile solution to the material previously chemically deintercalated in suspension in acetonitrile, stirring was maintained for 3 days. The powder obtained after chemical Li deintercalation and reinsertion was washed thoroughly with acetonitrile. All these chemical Li deintercalation and reinsertion were carried out in an argon filled glove box.

Prior to the observation in electron microscopy, a suspension was obtained by grinding the material in hexane, a droplet of this suspension being deposited on a Formvar carbon film supported on a copper grid. Electron diffraction experiments were carried out on many crystallites and very reproducible results were observed. The particles studied were chosen as isolated as possible. HAADF-STEM images and nano electron diffraction patterns were obtained using a JEM ARM200F microscope. Note that HAADF-STEM images were obtained only near the surface of the particles due to limitations in resolution by thickness.

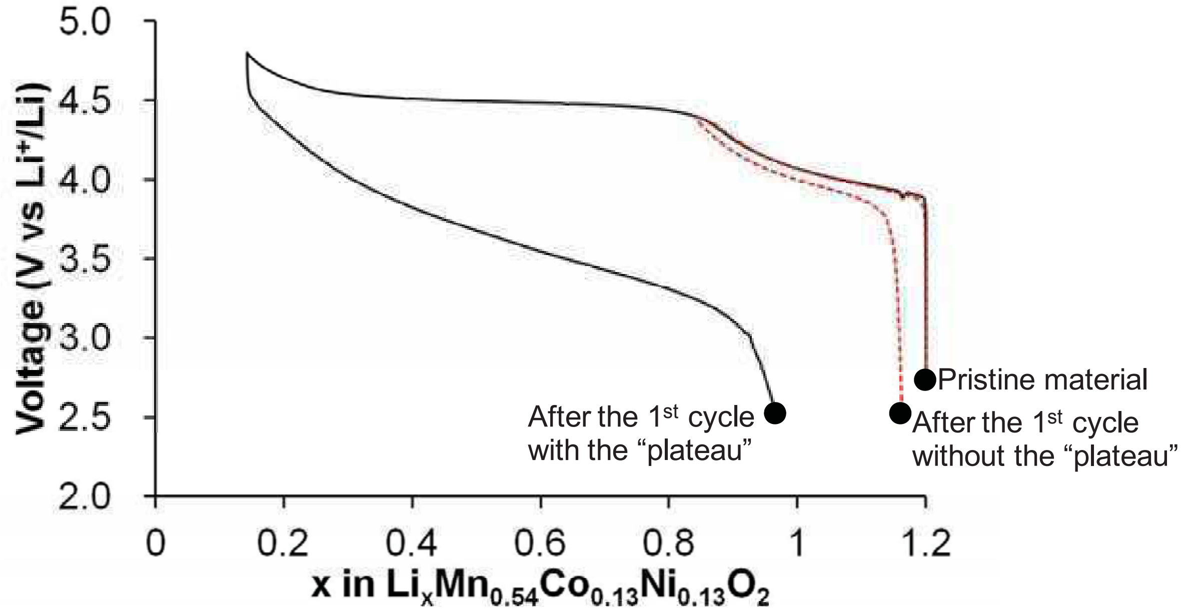

Fig. VI. 1: Charge and discharge curves of $Li//Li_{1.20}Mn_{0.54}Co_{0.13}Ni_{0.13}O_2$ cells.

VI. 3 - Results and discussion

VI. 3. 1 - Pristine material

Fig. VI. 2 presents a typical HAADF-STEM image of the material and the corresponding electron diffraction pattern. On the electron diffraction pattern, three rows of intense reflections are visible. They can be indexed in the *R-3m* space group used to describe the structure of the O3-type layered materials. Diffuse lines, parallel to c*, are visible between the rows of the mains reflections. They are the signature of a two dimensional ordering in the transition metal layer **[3]**. Nevertheless, note that in our case, the intensity along the diffuse lines is not homogeneous and obviously reflections can be distinguished.

On the image, the lamellar character of the structure is clearly visible with lines with bright dots separated with lines with only dark dots. As a matter of fact, the contrast in this type of images is in first approximation proportional to Z **[4-5]**. As expected, the slab with mainly transition metal atoms appears with bright dots whereas the interslab space with mainly lithium atoms appears as black. In the slab the ordering between the cations is also observed since the contrast of the image (sequence of two bright dots - one dark dot) corresponds to the order (TM-TM- $Li_{2/3}Ni_{1/3}$) with TM = (Co^{3+}, Mn^{4+}).

Note that very locally, for instance in the slab indicated by an arrow on **Fig. VI. 2**, a uniform contrast is observed indicating at least the presence of defaults in the ordering of the cations or even the absence of ordering in this particular slab. The ratio of these disordered slabs versus the ordered ones is obviously very different from what we could expect (1:1) if one consider, as Boulineau et al. recently did in $Li_{1.20}Mn_{0.61}Ni_{0.18}Mg_{0.01}O_2$ **[6]**, the material is made of separated domains of Li_2MnO_3 on one hand and $LiNi_{1/3}Mn_{1/3}Co_{1/3}O_2$ on the other hand. On the contrary, our observations are far away from a 1:1 ratio and are another confirmation that $Li_{1.20}Mn_{0.54}Co_{0.13}Ni_{0.13}O_2$ is a solid solution **[2]**. As mentioned earlier, in our composition the ratio large cations / small cations is 1/2 allowing an extended cation ordering, according to the superstructure $\sqrt{3}a_{hex.}x\sqrt{3}a_{hex.}$, within the slabs built in a triangular lattice. For comparison, it is interesting to mention that in $Li_{1.20}Mn_{0.61}Ni_{0.18}Mg_{0.01}O_2$ the ratio is 1/1.56 making thus impossible by itself to form an extended cation ordering within the slabs.

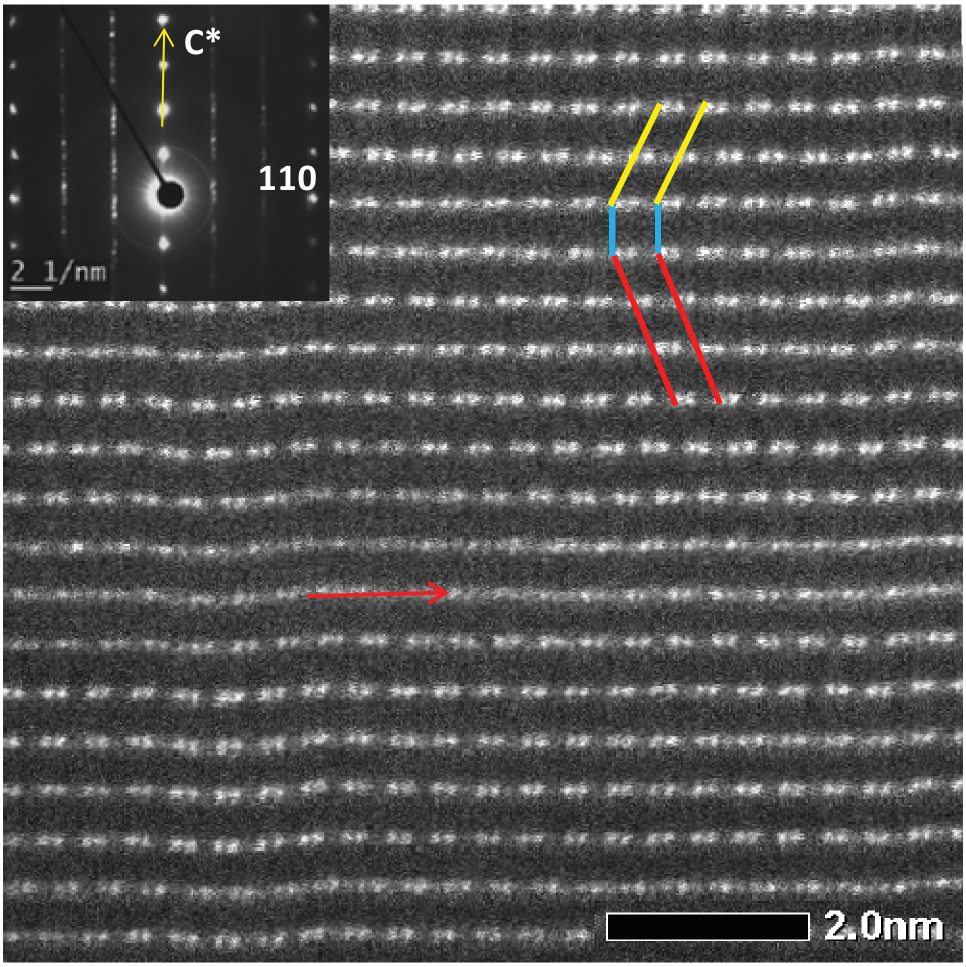

Fig. VI. 2: HAADF-STEM image and the corresponding electron diffraction pattern of pristine material $Li_{1.20}Mn_{0.54}Co_{0.13}Ni_{0.13}O_2$. The colored lines highlight the different types of stacking for the ordered transition metal layers.

More interesting is to look carefully at the stacking of the slabs. Obviously three different stackings, materialized by lines on **Fig. VI. 2,** can be observed. The stacking pointed out by the yellow line corresponds exactly to the ideal stacking along the $[2\text{-}10]_{R\text{-}3m}$ projection of the ordered slabs observed in the model compound Li_2MnO_3, which can also be written as $Li(Li_{1/3}Mn_{2/3})O_2$. In this stacking the sequence (TM-TM- $Li_{2/3}Ni_{1/3}$) is shifted from one slab to the next one (**Fig. VI. 3a**). The experimental image can be directly compared to the projection of the structure. In this ideal stacking, the actual crystalline symmetry is decreased to monoclinic (space group *C2/m*). In the corresponding electron diffraction pattern given in **Fig. VI. 3d**, the additional reflections lie exactly on the diffuse line observed on the electron diffraction pattern of **Fig. VI. 2**. The order (TM-TM- $Li_{2/3}Ni_{1/3}$) in the transition metal layers can be also observed along other directions, rotated of 60° and 120° from $[2\text{-}10]_{R\text{-}3m}$, as shown in **Fig. IV. 3g**. In the second stacking experimentally observed and indicated by the blue line on **Fig. VI. 2**, there is no more shift between the (TM-TM- $Li_{2/3}Ni_{1/3}$) sequences from one slab to the other. This situation corresponds to the projection of the model compound along the $[120]_{R\text{-}3m}$ direction (**Fig. VI. 3b**). The third stacking corresponds to a projection along the direction $[1\text{-}10]_{R\text{-}3m}$ (**Fig. VI. 3c**), with the ordered layers stacked in opposite direction to the first stacking as indicated by the red line on **Fig. VI. 2**. As previously described, the decrease of symmetry also creates additional reflections as shown in **Fig. VI. 3e** and **in Fig. VI. 3f**, which also lie on the diffuse lines in the experimental pattern given in **Fig. VI. 2**. Note that if one considers only the main reflections of the electron diffraction pattern corresponding to the non ordered *R-3m* structure of both projections, i.e. [2-10], [120] and [1-10] projections given in **Fig. VI. 3e** and in **Fig. VI. 3f** respectively, the electron diffraction patterns can be exactly superimposed since the rotation between each of three projections is 60°. Only, the location of the additional reflections can distinguish the three projections. These domains can be considered as twins since their stacking tends to recreate the ternary axis of the non ordered material. The image in a red rectangle given in **Fig. VI. 4a** is presented the theoretical image obtained by the stacking along c of the three types of domains as well as the corresponding electron diffraction pattern, the thickness of each of them being three slabs. Obviously the theoretical image is similar to the experimental one (outside of a red rectangle in **Fig. VI. 4a**). The additional reflections in the experimental diffraction pattern are less defined than the corresponding ones in the theoretical pattern as shown in **Fig. VI. 4b-c**. This is due to the fact that the stacking of the two domains is actually less ordered than that used to calculate the theoretical pattern. Furthermore the average experimental thickness of each domain is about 6 to 7 slabs, and not of 3 slabs.

To get an idea of the homogeneity of the crystallites of the sample, nano diffraction experiments have been performed. **Fig. VI. 5** presents a set of typical nano diffraction patterns obtained on a single nano crystal. About the whole volume of the particle is explored using the nanobeam. All the diffraction patterns are similar. The only difference is in the relative intensity along the diffuse lines. This observation means that locally the relative thickness of the domains varies and that in the volume explored by the nano beam one domain is predominant. Note nevertheless, that in none of the domains explored, the electron diffraction pattern indicates the exclusive presence of only one type of domain. The same observations have been made on all the crystallites explored by this technique.

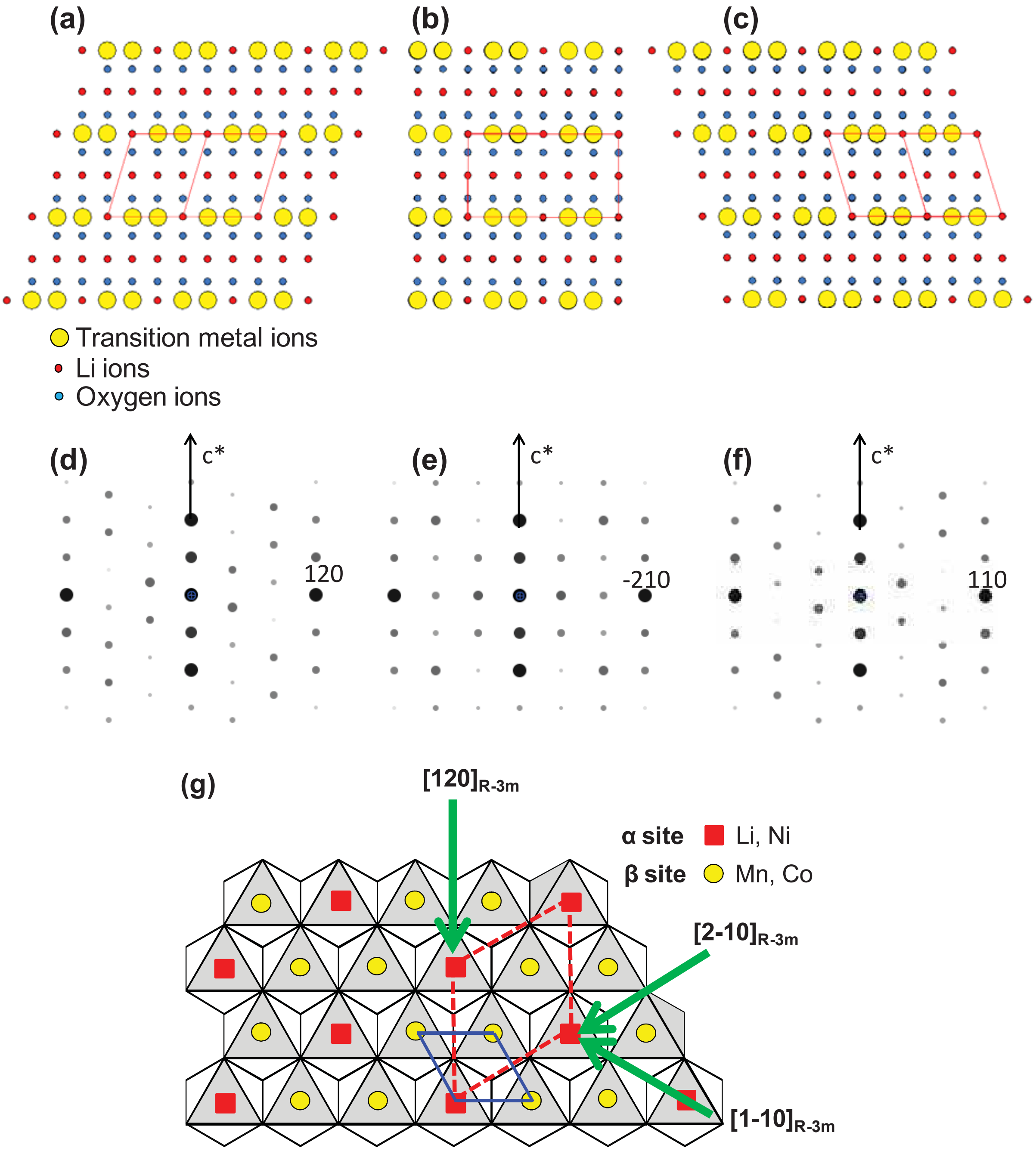
(a)
(b)
(c)
Transition metal ions
Li ions
Oxygen ions
(d)
c*
120
(e)
c*
-210
(f)
c*
110
(g)
[120]R-3m
α site
Li, Ni
β site
Mn, Co
[2-10]R-3m
[1-10]R-3m

Fig. VI. 3: Stacking of metal and oxygen ions along $[2\text{-}10]_{R\text{-}3m}$ *(a)*, $[120]_{R\text{-}3m}$ *(b)*, and $[1\text{-}10]_{R\text{-}3m}$ *(c)*, the corresponding electron diffraction patterns calculated (*(d), (e)* and *(f)*, respectively) and representation of an ordered transition metal layer with the three directions of projection indicated by green arrows (g).

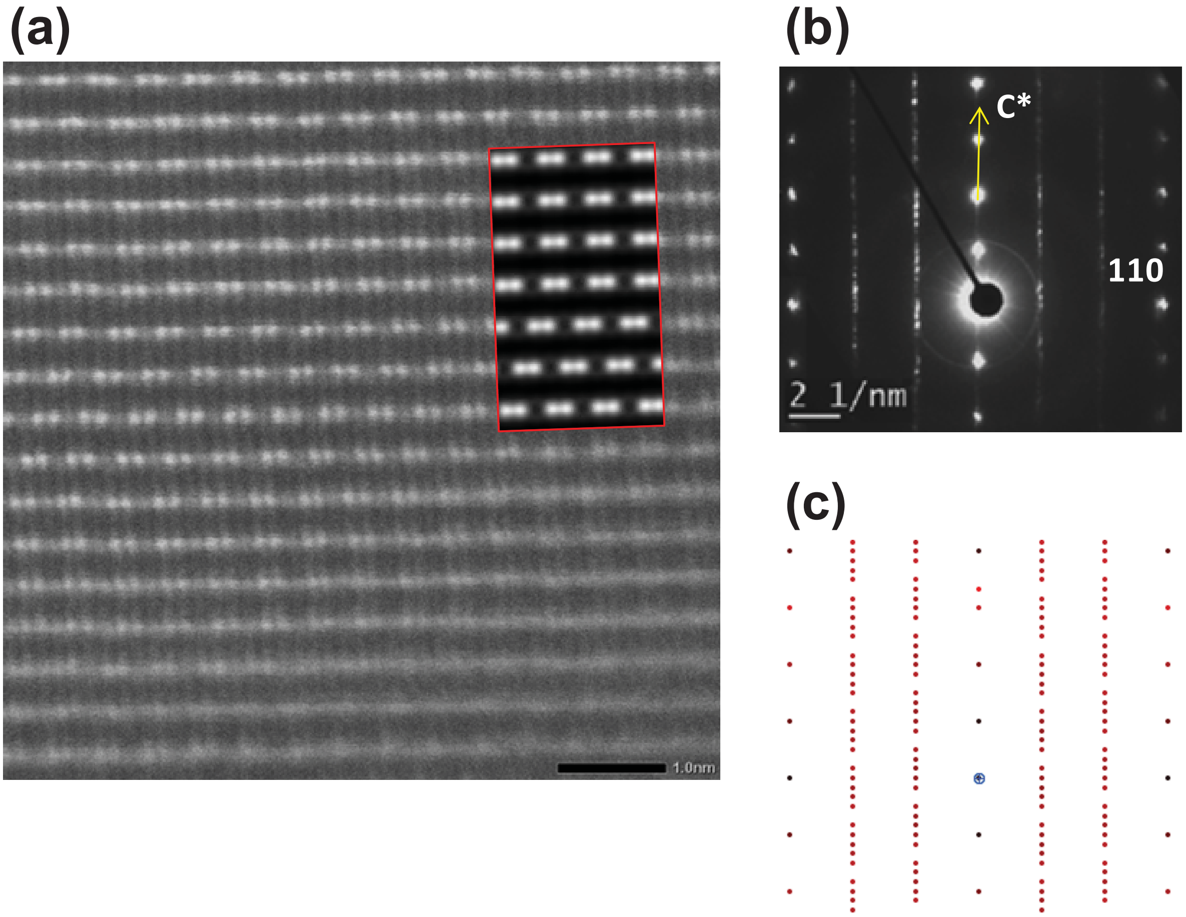

Fig. VI. 4: Comparison of an experimental STEM image obtained for the pristine material $Li_{1.20}Mn_{0.54}Co_{0.13}Ni_{0.13}O_2$ with the simulated image given in a red rectangle (a) and comparison of the corresponding experimental electron diffraction pattern (b) with the simulated one (c).

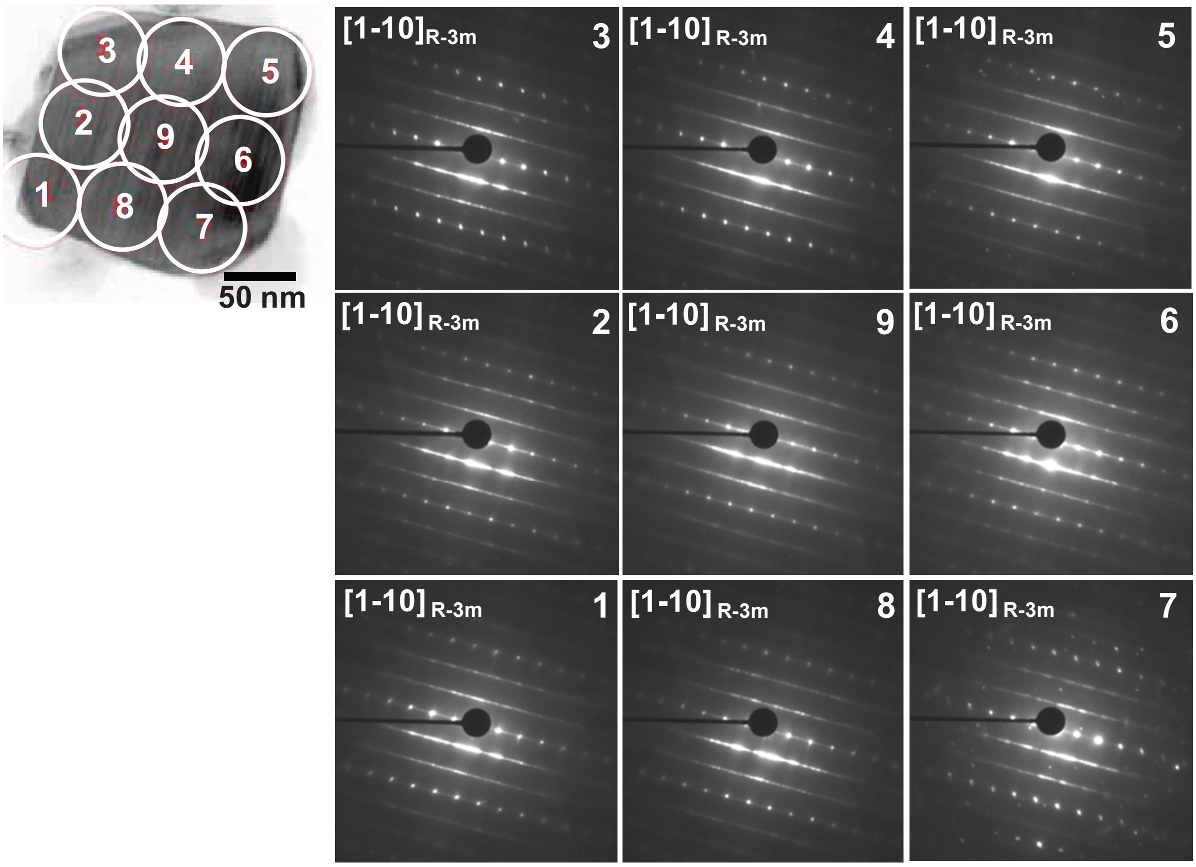
3
4
5
2
9
6
1
8
7
50 nm
[1-10]R-3m 3
[1-10] R-3m 4
[1-10] R-3m 5
[1-10] R-3m 2
[1-10] R-3m 9
[1-10] R-3m 6
[1-10] R-3m 1
[1-10] R-3m 8
[1-10] R-3m 7

Fig. VI. 5: Nano electron diffraction patterns in a particle of pristine material $Li_{1.20}Mn_{0.54}Co_{0.13}Ni_{0.13}O_{2}$.

VI. 3. 2 - Upon Lithium deintercalation and reintercalation

VI. 3. 2. 1 - Comparison of the materials obtained electrochemically after the 1st cycle, with or without the "plateau"

Representative HAADF-STEM images of the material recovered after the 1st cycle without the "plateau" are given in **Fig. VI. 6**. These images could be obtained in thin parts of the particle studied and are very similar to that shown in **Fig. VI. 2** for the pristine material. The ordering observed in the transition metal layers (TM-TM-$Li_{2/3}Ni_{1/3}$) is not affected, as well as the extent of the 2D lamellar character. No obvious presence of TM ions is observed in the Li sites. **Fig. VI. 7** presents the corresponding electron diffraction pattern. Surprisingly weak additional spots appear between the diffusion lines as indicated by the arrows. They could be assigned to spinel-like defects with the presence of transition metal ions in the lithium sites **[7]**. This result would thus suggest that in some parts of the crystal transition metal ions would migrate from transition metal layers to Li layers, at low voltage before the "plateau". Nevertheless, the intensity of these extra spots is very small versus the global intensity of the pattern showing that these defects are not extended, in good agreement with the non observation of bright spots in the Li layers (**Fig. VI. 6a-b**).

Fig. VI. 8 shows representative HAADF-STEM images with different scales for the material recovered after the 1st cycle of the battery with the "plateau". These images could be obtained in thin parts of the particle. The ordering (TM-TM- $Li_{2/3}Ni_{1/3}$) in the transition metal layers is still largely maintained as shown in **Fig. VI. 8a**, but some dark dots from the sequence bright dot – bright dot –dark dot are also clearly less visible (they are whitened). In addition, bright dots appear also in some Li layers as indicated by arrows in **Fig. VI. 8b**. It suggests first, that upon cycling at high voltage on the "plateau" transition metal ions have migrated to vacancies formed in the slabs by Li deintercalation and then, that some others have also migrated from the slabs to the interslabs **[8]**. These images are in rather good agreement with (at least) a partial densification of the host structure of the material. **Fig. VI. 9** presents the corresponding electron diffraction pattern, extra spots are again observed between the "diffusion lines": they suggest the presence of spinel-like defects appearing due to migration of transition metal ions from the slabs to the interslab spaces.

Further experiments are required, performed in exactly the same conditions, in order to compare carefully the relative intensity of the spinel-type extra spots versus those of the layered structure, in both compounds – *i.e.* in the material recovered after the 1st cycle without the "plateau" and in that recovered after the 1st cycle with the "plateau". Indeed, first observations suggest as expected that the migration of transition metal ions is more extended when the battery is charged at higher voltage after the "plateau", but it is not so obvious. The statement that can be made, for sure, is that the spinel-type defects are still far from being dominant (extended) on the contrary to the observations made by Boulineau *et al.* for $Li_{1.20}Mn_{0.61}Ni_{0.18}Mg_{0.01}O_2$ **[6]**. As shown in **Fig. 10b-d** in their paper, spinel extended domains are clearly observed in a large amount of crystallites, next to layered domains: the spots associated to the spinel structure are much more intense than in our case.

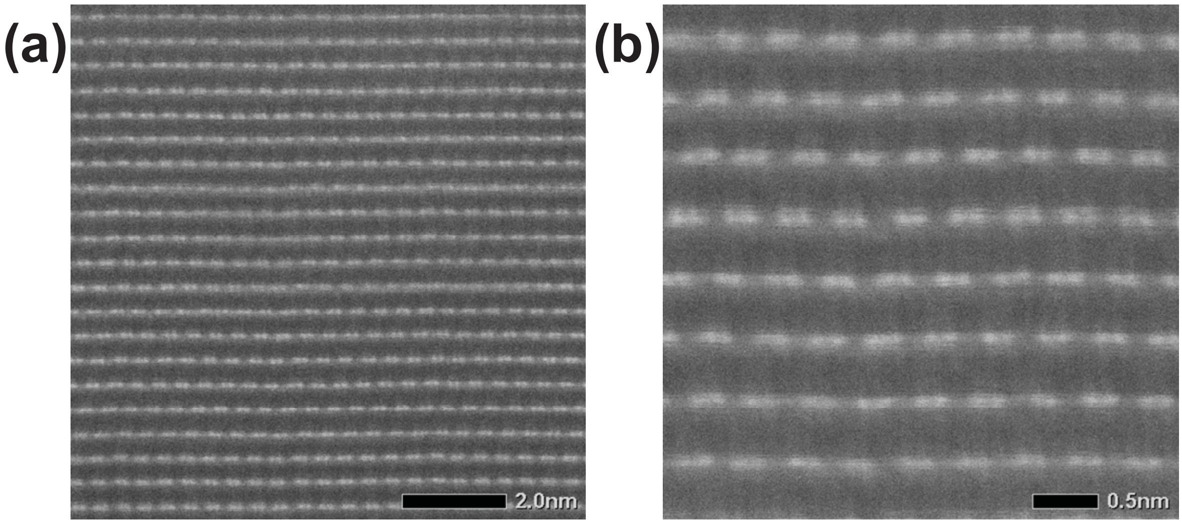

Fig. VI. 6: HAADF-STEM image of the material recovered after the 1st cycle of the battery without the “plateau” with different scales, large scale (a) and small scale (b) in different places in a particle.

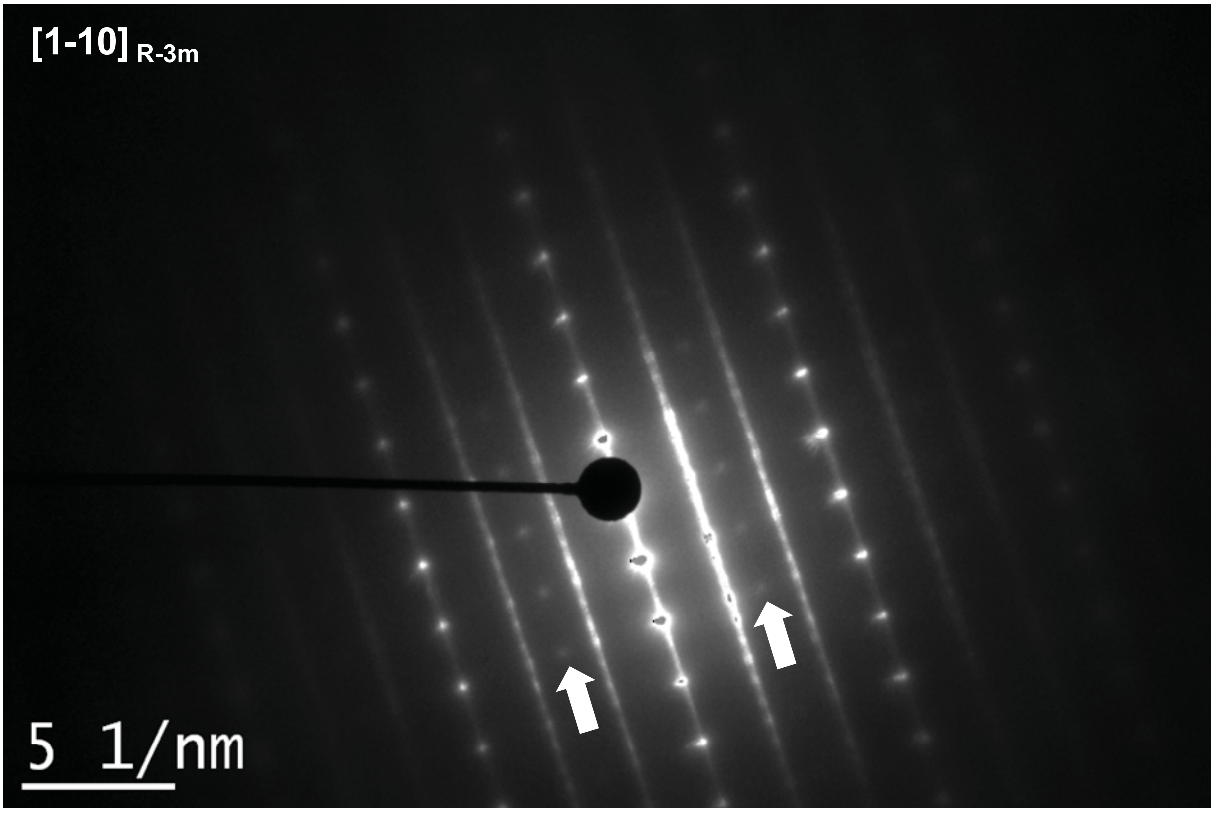

Fig. VI. 7: SAED pattern of the material recovered after the 1st cycle of the battery without the “plateau”.

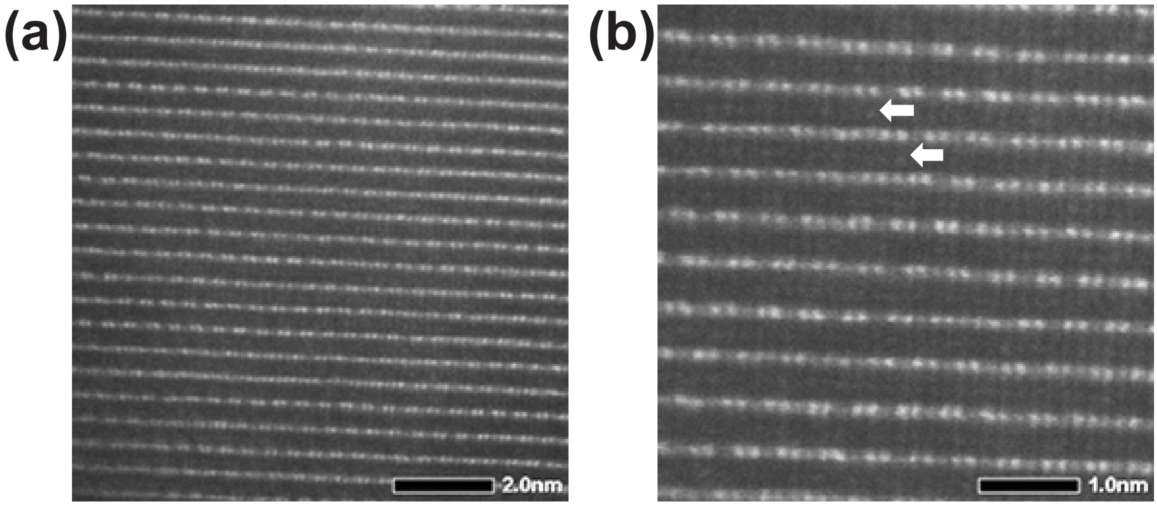

Fig. VI. 8: HAADF-STEM images of the material recovered after the 1st cycle of the battery with the "plateau" with different scales, large scale (a) and small scale (b) in different places in a particle. White arrows indicate the presence of transition metal ions into the Li layers.

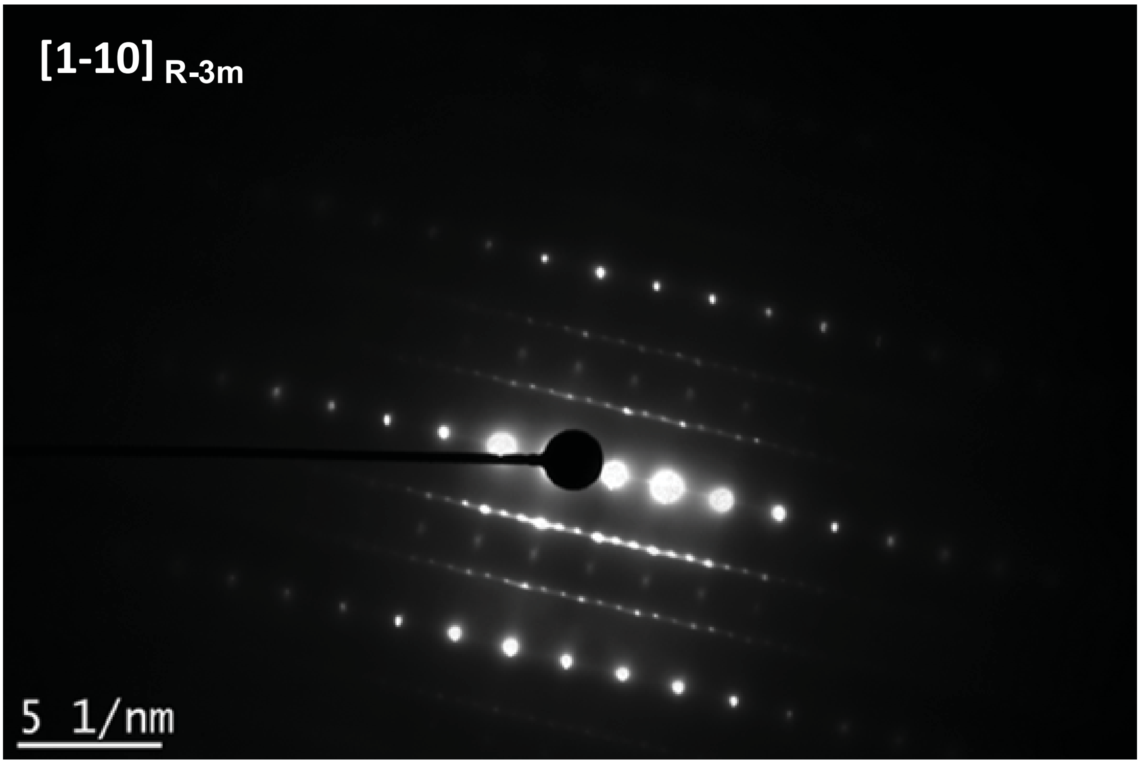

Fig. VI: 9: SAED pattern of the material recovered after the 1st cycle of the battery with the "plateau".

VI. 3. 2. 2 - After chemical Lithium deintercalation and reinsertion

The material prepared chemically was largely analyzed using HAADF-STEM and nano electron diffraction to study the detailed structural changes of $Li_{1.20}Mn_{0.54}Co_{0.13}Ni_{0.13}O_2$ during the 1st cycle.

Fig. VI. 10 shows representative HAADF images of the crystallites observed for the material prepared chemically. The ordering (TM-TM- $Li_{2/3}Ni_{1/3}$) in the transition metal layers is maintained in some parts of the crystals as shown in **Fig. VI. 10a**, but as shown in **Fig. VI. 10b** in other parts some transition metals have migrated into the vacancies formed by Li deintercalation from the slabs and from the slabs to the interslab spaces in the Li sites. Transition metals migrated in the TM layers appear to be rather ordered in some interslabs as shown in **Fig. VI. 10b**, but detail of this order is still not clear. It indicates that in some parts, densification, at least partial, occurs whereas in other parts, the pristine structure is maintained. This results support the heterogeneous reaction occurring during the 1st cycle with the formation of “two” phases.

Analysis using nano electron diffraction was performed for the material prepared using chemical reactions. A screening of the particle was done from the surface to the bulk as shown in **Fig. VI. 11a** to confirm the difference in structures between the surface and the bulk. For patterns 1 and 2, the additional spots present between the diffusion lines reveal the formation of spinel-type defects near the surface, whereas their absence show that the initial structure is maintained within the bulk. These results reveal again the formation of heterogeneous particles during the 1st cycle. These observations are in good agreement with the results of other analyses suggesting: *(i)* oxidation of oxygen at the surface leading to oxygen loss and migration of transition metal ions from the surface to the bulk (densification) and *(ii)* reversible oxidation of oxygen in the bulk without significant structural changes.

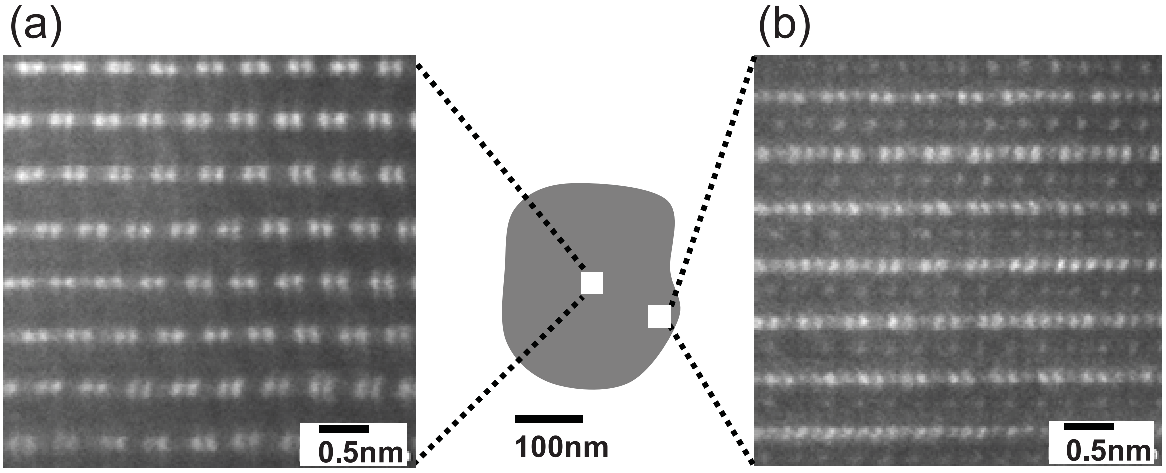
(a)
(b)
0.5nm
100nm
0.5nm

Fig. VI. 10: HAADF-STEM images of the material obtained after chemical Li reinsertion in a material previously chemically deintercalated, in the bulk (a) and at the surface (b) of a particle.

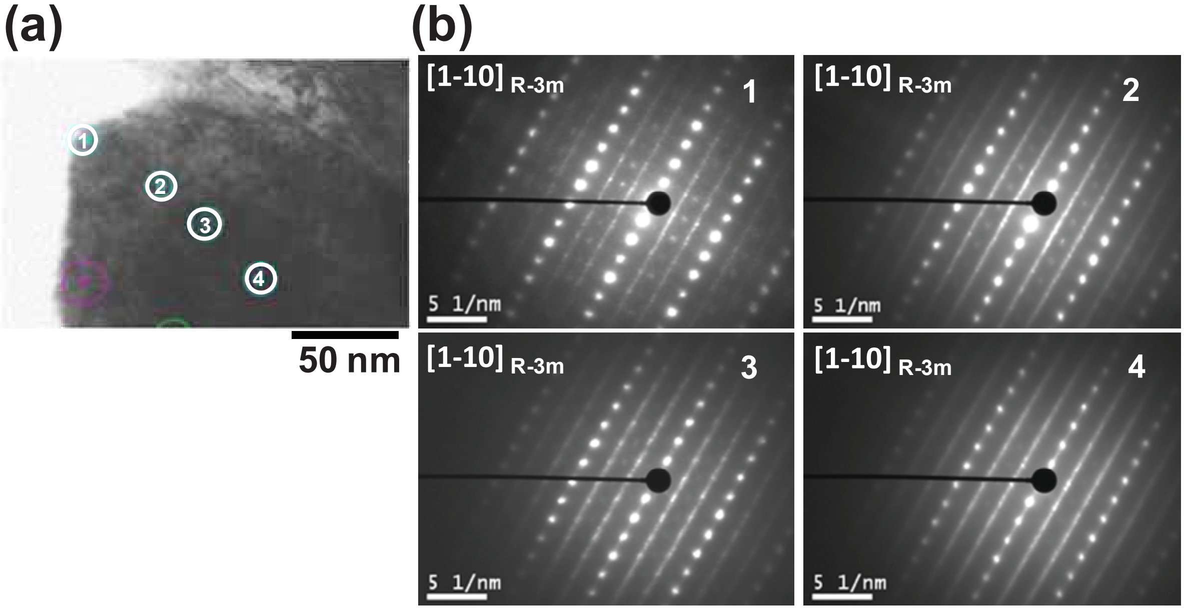
(a)
①
②
③
④
50 nm
(b)
[1-10] R-3m
1
5 1/nm
[1-10] R-3m
2
5 1/nm
[1-10] R-3m
3
5 1/nm
[1-10] R-3m
4
5 1/nm

Fig. VI. 11: Zones of the crystal analyzed by nano electron diffraction given in (a) and corresponding nano electron diffraction patterns (b) for the material prepared chemically from $Li_{1.20}Mn_{0.54}Co_{0.13}Ni_{0.13}O_{2.}$

VI. 4 - Conclusions

HAADF-STEM and nano electron diffraction were performed to characterize the materials recovered from the batteries after the 1st cycle, with and without the “plateau”, and the material prepared by chemical Li reinsertion after chemical Li deintercalation. The pristine material is characterized by the stacking of extended ordered transition metal layers (with TM-TM-$Li_{2/3}Ni_{1/3}$ succession as expected for $\sqrt{3}.a_{hex.}$ x $\sqrt{3}.a_{hex.}$ superstructure) along the c-axis and by changes in the orientation of the stacking every few TM layers. In the cycled materials, it appears that screening the particles from the surface to the bulk the concentration of spinel-type defects decreases to reach no spinel-type defects within the bulk of the particles. These spinel-type defects are the results of transition metal ions migration from the transition metal layers to the Li layers. In addition to these defects, at the surface of the particles we observed also migration of transition metals into the vacancies formed by Li deintercalation in the transition metal layers during the “plateau” in the 1st charge. This observation fully supports the occurrence of the densification process at the surface of the particles, implying irreversible oxygen loss and migration of transition metal from the surface to the “bulk”. The last essential information obtained also from these experiments is that no significant structural modifications occur in the bulk of the particle, in good agreement with the reversible oxidation of oxygen ions (without oxygen loss) in the core of particles.

VI. 5 - References

[1] Koga, H.; Croguennec, L.; Ménétrier, M.; Mannessiez, P.; Weill, F. and Delmas, C., accepted to *J. Power Sources*, **2013**

[2] Koga, H.; Croguennec, L.; Mannessiez, P.; Ménétrier, M.; Weill, F.; Bourgeois, L.; Duttine, M.; Suard, E.; and Delmas, C., *J. Phys. Chem.*, **2012**, 116, 13497-13506

[3] Boulineau, A.; Croguennec L.; Delmas C. and Weill F., *Chem. Mater*., **2009**, 21, 4216.

[4] Guilmard, M.; Pouillerie, C.; Croguennec, L.; Delmas, C., *Solid State Ionics,* **2003**, 160, 39-50.

[5] Guilmard, M.; Croguennec, L.; Delmas, C. *Chem. Mater,*. **2003**, 15, 4484-4493.

[6] Boulineau A.; Simonin L.; Colin J.- F.; Canevet E.; Daniel L.; Patoux S., *Chem. Mater.*, **2012**, 24 (18) 3558-3566

[7] Boulineau, A.; Croguennec, L.; Delmas, C; Weill, F., *Solid State Ionics,* **2010**, 180, 1652-1659

[8] Ito, A.; Shoda, K.; Sato, Y.; Hatano, M.; Horie, H.; Ohsawa, Y., *J. Power. Sources*, **2011**, 196, 4785-4790

Conclusion

Conclusion

The Lithium-rich layered oxides belonging to the (1-x)$LiMO_2$.xLi_2MnO_3 system (M = Ni, Co, Mn) delivering high capacity are considered as promising positive electrode materials for Li-ion batteries in place of conventional $LiCoO_2$ positive electrode. These materials have been studied intensively since Dahn reported in 2002 that they delivered large capacity after being charged over 4.5 V vs. Li^+/Li. It was assumed that oxygen loss reaction would occur during the first charge on a “plateau” observed at 4.45 V vs. Li^+/Li and this unusual mechanism is expected to be at the origin of the large capacity observed for these materials. Two mechanisms were proposed to explain the oxygen loss. The first one considers oxygen ions migration from the inside to the surface of the particles where they are released as oxygen gas: in that hypothesis a structure with oxygen vacancies is formed. The second one considers oxygen loss at the surface of the particles with transition metal migration from the outside to the inside through vacancies formed by deintercalation of Li ions from the transition metal layers: in that case a densification of the host structure occurs. In literature there are still controversies concerning the nature of the mechanism involved on the “plateau”, but also concerning the structure of the pristine material: Is there formation of a complete solid solution between $LiMO_2$ (M = Ni, Co, Mn) and Li_2MnO_3 or of local domains of both types? A general study was carried out in order to get more insight into the understanding of these materials. Our studies were mainly focused on $Li_{1.20}Mn_{0.54}Ni_{0.13}Co_{0.13}O_2$ with high capacity which belongs to the Li_2MnO_3-$LiNi_{1/3}Mn_{1/3}Co_{1/3}O_2$ system with the 0.4 : 0.4 ratio.

$Li_{1.2}Mn_{0.54}Co_{0.13}Ni_{0.13}O_2$ was synthesized at 1000°C through sol-gel method. Neutron diffraction data analysis leads to the following cation distribution $(Li_{0.98}Ni^{II}_{0.02})(Li_{0.22}Mn^{IV}_{0.54}Ni^{II}_{0.11}Co^{III}_{0.13})O_2$: 0.02 mol Ni ions are stabilized in the Li layers because of their similar ionic radius with Li. Electron diffraction analysis has revealed the formation of a $\sqrt{3}a_{hex.} \times \sqrt{3}a_{hex.}$ superstructure with the ordering of the Li(Ni) ions within the transition metal layers. The results of XRD, neutron diffraction and HAADF-STEM have shown that the ordering along the $c_{hex.}$ axis is not extended, it is in fact limited to a few layers. Nevertheless, $Li_{1.20}Mn_{0.54}Co_{0.13}Ni_{0.13}O_2$ was shown to be a solid solution and not made of separated domains of Li_2MnO_3 and $LiNi_{1/3}Mn_{1/3}Co_{1/3}O_2$. This composition is such that the ratio (Li^+, Ni^{2+}; large cations) / (Co^{3+}, Mn^{4+}; small cations) is equal to 1/2, which is ideal to form an extended ordering in the slabs, whereas the ordering along the c_{hex} axis is probably limited due to the presence of two cations in the two sub sites, Li^+ and Ni^{2+} on one side and Mn^{4+} and Co^{3+} on the other side.

From the charge and discharge curves of $Li_{1.20}Mn_{0.54}Co_{0.13}Ni_{0.13}O_2$, 1.08 mol Li ions were deintercalated during the 1st charge from $Li_{1.20}Mn_{0.54}Co_{0.13}Ni_{0.13}O_2$ and 0.90 mol Li ions were reinserted during the discharge. Supposing that oxygen loss occurs during the 1st charge with formation of oxygen vacancies within the lattice, almost all MO_6 environments would be changed to MO_5 whereas it is known that Mn^{4+} and Ni^{4+} ions are not stable into MO_5 environments. This hypothesis was thus not considered as possible. On the contrary, densification of the lattice after the oxygen loss allows a stabilization of all the transition metal ions in octahedral sites, but with a decrease of the Li sites available: only 0.78 mol Li can be inserted during the 1st discharge. The experimental value being 0.90 mol Li, experience cannot be explained by densification only. The mechanism involved in these Li and Mn-rich layered oxides had thus to be studied further.

The XRD patterns of materials recovered after the first charge in the irreversible “plateau”, the next discharge and subsequent cycles show the existence of “two phases”. In fact, this only a crude description of a more complex behavior that suggests the existence of a structural evolution. This separation of phases is observed whatever the cycling conditions (temperature and rate) but also the powder particle size: the ratio between the two phases evolves depending on the specific surface area, the temperature and the cycling rate. These “two phases” were associated to: *(i)* one phase localized within the bulk of the particles, for which oxygen is oxidized on the “plateau” without oxygen loss and then reversibly reduced in discharge, and *(ii)* another phase present on the external part of the particles, for which oxygen is oxidized and lost from the surface leading then to cation migration from the surface to the inside and densification of the oxygen lattice. In fact, one can assume that the densification occurs also in the bulk with a very small extent, while it is prevailing on the external part of the particles. Mn would thus participate less than expected (considering the oxygen loss models) to the redox processes involved upon cycling and the loss of oxygen would be smaller.

XAS analyses have shown that as expected Ni and Co are involved reversibly in the redox processes, from Ni^{2+} to Ni^{4+} for Ni and from Co^{3+} to Co^{4+} for Co. Surprisingly, Mn was less involved than expected. During the first two cycles, Mn is no significantly reduced during discharge. This result supports again that oxygen participates to the redox processes to compensate for Lithium (de)intercalation.

In order to confirm these redox processes, i.e. the oxidation state of Mn and the occurrence of oxygen contribution, materials were prepared from $Li_{1.20}Mn_{0.54}Co_{0.13}Ni_{0.13}O_2$ (without any additives) by chemical Li deintercalation with NO_2BF_4 and chemical Li reinsertion with LiI. The material prepared chemically was shown to be very similar in composition, structure and properties to the material recovered from the battery after the 1st electrochemical cycle.

Redox titrations and magnetic measurements, combined with chemical analyses, have shown that the average oxidation of Mn is around 3.7 to 3.9 whereas 3.3 is expected if the structural modification during the first charge result only of formation of oxygen vacancies. Similarly the amount of oxygen lost is 0.16 instead of 0.36 in the previous hypothesis.

Combination of HAADF-STEM and nano-electron diffraction has revealed that the surface of the particles is different from the bulk. Within the bulk the structure remains very similar to that determined for the pristine material, with an extended ordering within the slabs and an ordering limited to a few layers along the $c_{hex.}$ axis. At the surface, a densification of the slabs is observed with the disappearance of the cation ordering, as well as a partial cation migration from the slabs to the interslab spaces. A spinel-like phase is thus formed. These observations are in good agreement with the formation of the "two phases" observed by XRD from the beginning of the "plateau" in the first charge, but also with no significant modification of the structure within the bulk, whereas a densification is observed on the external part of the particles.

As the result of all these experiments, we propose that oxygen participate to the mechanism involved upon cycling, as a reversible redox couple within the bulk and as oxygen lost at the surface to compensate for lithium deintercalation during the "plateau".

List of figures

List of figure

Introduction

Fig. 1: Unit cell of $LiCoO_2$.

Fig. 2: Structural schematic view of $LiCoO_2$.

Fig. 3: Arrangement of metal ions in transition metal layers of $LiNi_{1/3}Mn_{1/3}Co_{1/3}O_2$.

Fig. 4: Structural schematic views of $LiMn_2O_4$.

Fig. 5: Structural schematic view of Li_2MnO_3.

Fig. 6: Arrangement of metal ions in transition metal layers of Li_2MnO_3.

Fig. 7: Charge and discharge curves of Li_2RuO_3.

Fig. 8: Charge and discharge curves of Li_2NiO_3.

Chapter I

Fig. I. 1: (a) Electron diffraction pattern of $Li_{1.20}Mn_{0.54}Co_{0.13}Ni_{0.13}O_2$ and (b) representation of an ordered transition metal layer.

Fig. I. 2: The 1st cycle curves obtained at a rate of C/20 for different Li// $Li_xMn_{0.54}Co_{0.13}Ni_{0.13}O_2$ cells.

Fig. I. 3: (a) X-ray diffraction patterns of $Li_{1.20}Mn_{0.54}Co_{0.13}Ni_{0.13}O_2$ recovered during the 1st cycle at different states of charge and discharge. A typical electrochemical curve is given on the right part of the figure in order to indicate the lithium composition of the material studied. (b) Detailed XRD data in the 18 - 19.5° ($2\theta_{Cu}$) angular range, (c) in the 20-24° ($2\theta_{Cu}$) angular range, and (d) in the 44 - 45.5° ($2\theta_{Cu}$) angular range.

Fig. I. 4: (a) Comparison of the 1st, 2nd, 10th, 50th and 100th charge-discharge curves obtained for Li//$Li_{1.20}Mn_{0.54}Co_{0.13}Ni_{0.13}O_2$ cells with $Li_{1.2}Mn_{0.54}Co_{0.13}Ni_{0.13}O_2$ prepared at 1000°C. (b) Corresponding differential curves dQ/dV = f(V).

Fig. I. 5: X-ray diffraction patterns of $Li_{1.20}Mn_{0.54}Co_{0.13}Ni_{0.13}O_2$ synthesized at 1000°C and recovered from the batteries after the 1st, 10th, 50th and 100th cycle (a); detailed XRD data in the 18–19.5° ($2\theta_{Cu}$) range (b) and in the 43-46° ($2\theta_{Cu}$) range (c).

Fig. I. 6: (a) XANES spectra recorded at the Mn K-edge, in operando, during the 1st discharge of Li//$Li_{1.20}Mn_{0.54}Co_{0.13}Ni_{0.13}O_2$ cells, (b) the corresponding M-O distances determined from EXAFS spectra obtained at the Mn K-edge.

Fig. I. 7: Comparison of the charge and discharge curves obtained during the the 1st and 2nd cycles of lithium batteries using the pristine material $Li_{1.20}Mn_{0.54}Co_{0.13}Ni_{0.13}O_2$ as positive electrode (dotted black lines) with those obtained during the 1st cycle of lithium batteries using the material recovered after chemical Li deintercalation and reinsertion as positive electrode (continuous blue lines).

Fig. I. 8: STEM image of $Li_{1.20}Mn_{0.54}Co_{0.13}Ni_{0.13}O_2$.

Fig. I. 9: HAADF-STEM images of the material obtained after chemical Li reinsertion in a material previously chemically deintercalated, in the bulk (left) and at the surface (right) of a particle.

Chapter II

Fig. II. 1: TG-DTA curves obtained for “$Li_{1.20}Mn_{0.54}Co_{0.13}Ni_{0.13}O_2$”: (a) Comparison of the results obtained for 2 samples thermal-treated at 120°C for 10 h in air before the TGA-DTA experiment (temperature range 25 - 1200°C, heating rate 200 °C/h) and (b) “$Li_{1.20}Mn_{0.54}Co_{0.13}Ni_{0.13}O_2$” thermal-treated at 500°C for 5 h in air before the TGA-DTA experiment (the preheating to 800°C was done at 800°C/h and then the heating rate was 100°C/h in the temperature range 800 - 1200°C).

Fig. II. 2: In-situ XRD patterns obtained during the heat treatment between 25°C and 1000°C of the sample thermal-treated at 500°C for 5 h before the measurement. Heating conditions:

Heating rate 4°C /min, temperature maintained at 1000° C for 10 h, cooling rate 10°C /min. (a) in the 15 – 80°, (b) 20 – 23°, (c) 23 – 28°, (d) 40 – 45°, (e) 50 – 53° 2θ angular ranges. Refer to the experimental part for more details on the *in situ* XRD experiment during the thermal treatment.

Fig. II. 3. XRD patterns of the pristine material thermal-treated at 500°C for 5 h before the measurement, upon a continuous thermal treatment at 800°C, 940°C and 1000°C (heating rate 4°C /min), after 10 h at 1000°C and finally after cooling. The $a_{cub.}$ cell parameter of the spinel-type phase (*Fd-3m*) formed upon heating is given for information for each XRD. Its decrease suggests an increasing average oxidation state for the transition metal ions.

Fig. II. 4: X-ray diffraction patterns of "$Li_{1.20}Mn_{0.54}Co_{0.13}Ni_{0.13}O_2$" synthesized at 800°C, 900°C and 1000°C in the 10 – 80° ($2\theta_{Cu}$) range; an enlargement of the XRD patterns is given in the 20 – 30° 2θ angular range.

Fig. II. 5: Thermal evolution of the H / M ratio of "$Li_{1.20}Mn_{0.54}Co_{0.13}Ni_{0.13}O_2$" synthesized at 800°C, 900°C and 1000°C. H : the applied field (H = 500 Oe) and M : the measured magnetization. A Curie-Weiss type behavior is observed above 150K.

Fig. II. 6: Raman spectra of the materials synthesized at 800°C, 900°C and 1000°C.

Fig. II. 7: ^{7}Li MAS NMR spectra for the three "$Li_{1.20}Mn_{0.54}Co_{0.13}Ni_{0.13}O_2$" compounds (Synchronized Hahn echo, 39 MHz, spinning 30 kHz). The main isotropic contributions are shown by arrows, the other signals being spinning sidebands.

Fig. II. 8: Comparison for the 1000°C "$Li_{1.20}Mn_{0.54}Co_{0.13}Ni_{0.13}O_2$" sample between the experimental XRD pattern and that calculated by the Rietveld method: in the 10 – 80° ($2\theta_{Cu}$) range (a), in the 36 – 39° (b), in the 43 - 46° (c) and in the 64 - 66° (d). These enlargements are given in order to highlight the good agreement between the two patterns and thus the good minimization of the difference.

Fig. II. 9: Hysteresis loops (magnetization *vs.* magnetic field at 5K) obtained for "$Li_{1.20}Mn_{0.54}Co_{0.13}Ni_{0.13}O_2$" synthesized at 800°C, 900°C and 1000°C.

Fig. II. 10: Electron diffraction patterns of $Li_{1.20}Mn_{0.54}Co_{0.13}Ni_{0.13}O_2$: (a) [001] and (b) [1-10]. The circled reflections correspond to the cationic ordering in the transition metal layers. The diffusion lines pointed by the arrows indicate it is only a 2D ordering. The red arrows indicate

elongated spots observed along the diffusion lines.

Fig. II. 11: Comparison of the experimental and calculated neutron diffraction data for the material “$Li_{1.20}Mn_{0.54}Co_{0.13}Ni_{0.13}O_2$” synthesized at 1000°C, the calculated patterns being obtained considering a description of the unit cell either in the *R-3m* space group (a) or in the *C2/m* space group (b).

Fig. II. 12: Raman spectrum of “$Li_{1.20}Mn_{0.54}Co_{0.13}Ni_{0.13}O_2$” obtained at 1000°C and its comparison with those of Li_2MnO_3, $LiNi_{1/3}Mn_{1/3}Co_{1/3}O_2$ and $LiCoO_2$. The spectra were fitted using pseudo-Voigt bands (here in green) in order to allow their easier comparison.

Fig. II. 13: The 1st to 10th cycling curves obtained for different $Li//Li_xMn_{0.54}Co_{0.13}Ni_{0.13}O_2$ cells, “$Li_{1.20}Mn_{0.54}Co_{0.13}Ni_{0.13}O_2$” being synthesized at 1000°C, 900°C and 800°C (a-c). Changes in reversible capacity observed for the different $Li//Li_xMn_{0.54}Co_{0.13}Ni_{0.13}O_2$ cells (d). Voltage range is 2.5 – 4.8 V vs. Li^+/Li in the 1st cycle and 2.5 – 4.6V vs. Li^+/Li in the 1st cycle after the 2nd cycle.

Chapter III

Fig. III. 1: *(a)* X-ray diffraction patterns of $Li_{1.20}Mn_{0.54}Co_{0.13}Ni_{0.13}O_2$ synthesized at 800°C, 900°C and 1000°C in the 10 – 80° ($2\theta_{Cu}$) range. *(b)* Detailed XRD data in the 20 – 30° angular range.

Fig. III. 2: SEM images of $Li_{1.20}Mn_{0.54}Co_{0.13}Ni_{0.13}O_2$ synthesized at *(a)* 800°C, *(b)* 900°C and *(c)* 1000°C.

Fig. III. 3: The 1st cycle curves obtained at a rate of C/20 for different $Li//Li_xMn_{0.54}Co_{0.13}Ni_{0.13}O_2$ cells, $Li_{1.20}Mn_{0.54}Co_{0.13}Ni_{0.13}O_2$ being synthesized at 800°C, 900°C and 1000°C.

Fig. III. 4: *(a)* X-ray diffraction patterns of $Li_{1.20}Mn_{0.54}Co_{0.13}Ni_{0.13}O_2$ recovered during the 1st cycle at different states of charge and discharge of the lithium battery. A typical electrochemical curve is given on the right part of the figure in order to indicate the lithium composition of the material studied. *(b)* Detailed XRD data in the 18 - 19.5° ($2\theta_{Cu}$) angular range, *(c)* in the 20 - 24° ($2\theta_{Cu}$) angular range, and *(d)* in the 44 - 45.5° ($2\theta_{Cu}$) angular range.

Fig. III. 5: Changes in lattice parameters, a_{hex} *(a)* and c_{hex} *(b),* versus lithium composition (x in $Li_xMn_{0.54}Co_{0.13}Ni_{0.13}O_2$) during the 1st charge and discharge. Due to the presence of these two phases in the material formed upon cycling, x defines the average composition in lithium for the mixture but not that of each phase.

Fig. III. 6: *(a)* Results of the refinement by the Le Bail method of the X-ray diffraction pattern obtained for $Li_{1.20}Mn_{0.54}Co_{0.13}Ni_{0.13}O_2$ recovered from the battery after a 1st cycle at C/20 rate and at room temperature; detailed XRD data in the 18 – 19.2° ($2\theta_{Cu}$) range *(b)* and in the 44 - 45° ($2\theta_{Cu}$) range *(c)*.

Fig. III. 7: Changes in the X-ray diffraction patterns of $Li_xMn_{0.54}Co_{0.13}Ni_{0.13}O_2$ synthesized at 800°C, 900°C and 1000°C and recovered from the batteries at different states of charge and discharge during the 1st cycle: *(a)* in the initial state, *(b)* on the *plateau*, *(c)* at the end of the *plateau* and *(d)* at the end of the 1st cycle. The angular range is limited to 18 – 19.5° ($2\theta_{Cu}$) in order to focus especially on the *(003)* diffraction lines.

Fig. III. 8: *(a)* Comparison of the 1st, 2nd, 10th, 50th and 100th charge-discharge curves obtained for Li // $Li_{1.20}Mn_{0.54}Co_{0.13}Ni_{0.13}O_2$ cells with $Li_{1.20}Mn_{0.54}Co_{0.13}Ni_{0.13}O_2$ prepared at 1000°C. *(b)* Corresponding differential curves dQ/dV = f(V).

Fig. III: 9. X-ray diffraction patterns of $Li_{1.20}Mn_{0.54}Co_{0.13}Ni_{0.13}O_2$ synthesized at 1000°C and recovered from the batteries after the 1st, 10th, 50th and 100th cycle *(a)*; detailed XRD data in the 18 – 19.5° ($2\theta_{Cu}$) range *(b)* and in the 43 - 46° ($2\theta_{Cu}$) range *(c)*.

Fig. III. 10: Comparison of the first charge and discharge curves obtained for Li // $Li_{1.20}Mn_{0.54}Co_{0.13}Ni_{0.13}O_2$ cells in different conditions of cycling: charge with cycling rates of C/20 or C/100, discharge with cycling rate of C/20, cycling temperature of 25°C or 55°C.

Fig. III. 11: Comparison of the X-ray diffraction patterns obtained for the material $Li_{1.20}Mn_{0.54}Co_{0.13}Ni_{0.13}O_2$ recovered from lithium cells charged in different conditions. All the discharges were performed at a C/20 rate.

Chapter IV

Fig. IV. 1: Energy range accessible by edge jumping with the Si(111) Quick-XAS monochromator.

Fig. IV. 2: Charge and discharge curves obtained for Li//$Li_{1.20}Mn_{0.54}Co_{0.13}Ni_{0.13}O_2$ lithium cells: *(a)* 1st cycle obtained using a coin cell and *(b)* 1st cycle obtained with (in black) or without (in blue) the "plateau" during the 1st charge, as well as 2nd cycle (in red), these three last cycles being obtained using the cell developed for *Operando* Synchrotron studies [10].

Fig. IV. 3: Normalized XANES spectra at the Ni K-edge for $Li_{1.20}Mn_{0.54}Co_{0.13}Ni_{0.13}O_2$ during the 1st charge before the "plateau" (a), the 1st charge during the "plateau" up to 4.8 V vs. Li^+/Li (b) and the 1st discharge after the "plateau" (c).

Fig. IV. 4: Normalized XANES spectra at the Ni K-edge for $Li_{1.20}Mn_{0.54}Co_{0.13}Ni_{0.13}O_2$ during the 1st discharge before the "plateau" (a), the 2nd charge after a 1st cycle in the potential window 2.5 - 4.8 V (b) and the 2nd discharge after a 1st cycle in the potential window 2.5 - 4.8 V (c).

Fig. IV. 5: Normalized XANES spectra at the Co K-edge for $Li_{1.20}Mn_{0.54}Co_{0.13}Ni_{0.13}O_2$ during the 1st charge before the "plateau" (a), the 1st charge during the "plateau" up to 4.8 V vs. Li^+/Li (b) and the 1st discharge after the "plateau" (c).

Fig. IV. 6: Normalized XANES spectra at the Co K-edge for $Li_{1.20}Mn_{0.54}Co_{0.13}Ni_{0.13}O_2$ during the 1st discharge before the "plateau" (a), the 2nd charge after a 1st cycle in the potential window 2.5 - 4.8 V (b) and the 2nd discharge after a 1st cycle in the potential window 2.5 - 4.8 V (c).

Fig. IV. 7: Normalized XANES spectra at the Mn K-edge for $Li_{1.20}Mn_{0.54}Co_{0.13}Ni_{0.13}O_2$ during the 1st charge before the "plateau" (a), the 1st charge during the "plateau" up to 4.8 V vs. Li^+/Li (b) and the 1st discharge after the "plateau" (c).

Fig. IV. 8: Normalized XANES spectra at the Mn K-edge for $Li_{1.20}Mn_{0.54}Co_{0.13}Ni_{0.13}O_2$ during the 1st discharge before the "plateau" (a), the 2nd charge after a 1st cycle in the potential window 2.5 - 4.8 V (b) and the 2nd discharge after a 1st cycle in the potential window 2.5 - 4.8 V (c).

Fig. IV. 9: Pre-edge of normalized XANES spectra at the Mn K-edge of $Li_{1.20}Mn_{0.54}Co_{0.13}Ni_{0.13}O_2$ during the 1st charge before the "plateau" (a), the 1st charge up to 4.8 V vs. Li^+/Li (b), the 1st discharge after the "plateau" (c), and the 1st discharge before the "plateau" (d).

Fig. IV. 10: Normalized XANES spectra of $Li_{1.20}Mn_{0.54}Co_{0.13}Ni_{0.13}O_2$ at the Ni K-edge (a), Co

K-edge (b) and Mn K-edge (c) for the pristine material, the pristine material within the cell developed for Operando studies, the material recovered *ex-situ* after the 1st cycle of a Lithium cell, the material after the 1st cycle within the *in operando* cell and the material recovered *ex-situ* from a Lithium cell after 10 cycles.

Fig. IV. 11: Fourier transforms of k^3-weighted EXAFS spectra of $Li_{1.20}Mn_{0.54}Co_{0.13}Ni_{0.13}O_2$ at the Ni K-edge (a), Co K-edge (b) and Mn K-edge (c) for the pristine material, the material obtained in charge just before the “plateau”, the material obtained at the end of the charge up to 4.8 V vs. Li^+/Li, the material obtained after the 1st cycle with the “plateau” and the material obtained after the 1st cycle without the “plateau”.

Fig. IV. 12: Distances determined between Ni and its first oxygen neighbors (a) and between Ni and its first metal neighbors (b) from the analysis of the EXAFS spectra recorded *in operando* during the 1st cycle with (solid lines) and without (short dotted lines) the “plateau”. Ni-O and Ni-M distances determined from the analysis of the EXAFS spectra during the 2nd cycle of $Li//Li_{1.20}Mn_{0.54}Co_{0.13}Ni_{0.13}O_2$ (long dotted line in a-b). $LiNi_{1/3}Co_{1/3}Mn_{1/3}O_2$ and $LiNi_{0.80}Co_{0.15}Al_{0.05}O_2$ are given as reference for Ni^{II}-O(M) and Ni^{III}-O(M) respectively.

Fig. IV. 13: Distances determined between Co and its first oxygen neighbors (a) and between Co and its first metal neighbors (b) from the analysis of the EXAFS spectra recorded *in operando* during the 1st cycle with (solid lines) and without (short dotted lines) the “plateau”. Co-O and Co-M distances determined from the analysis of the EXAFS spectra during the 2nd cycle of $Li//Li_{1.20}Mn_{0.54}Co_{0.13}Ni_{0.13}O_2$ (long dotted line in a-b). $LiNi_{1/3}Co_{1/3}Mn_{1/3}O_2$ is given as reference for Co^{III}-O(M).

Fig. IV. 14: Distances determined between Mn and its first oxygen neighbors (a) and between Mn and its first metal neighbors (b) from the analysis of the EXAFS spectra recorded *in operando* during the 1st cycle with (solid lines) and without (short dotted lines) the “plateau”. Mn-O and Mn-M distances determined from the analysis of the EXAFS spectra during the 2nd cycle of $Li//Li_{1.20}Mn_{0.54}Co_{0.13}Ni_{0.13}O_2$ (long dotted lines in a-b). $LiNi_{1/3}Co_{1/3}Mn_{1/3}O_2$ as well as Li_2MnO_3, and $LiMn_2O_4$ are given as reference for Mn^{IV}-O(M) and $Mn^{III,IV}$-O(M) respectively.

Chapter V

Fig. V. 1: SEM images of the pristine material (a), the material recovered from the battery after the 1st cycle with carbon and PVdF (b) and the material obtained after chemical Li deintercalation and reinsertion (c).

Fig. V. 2: Comparison of the X-ray diffraction patterns recorded in the angular range 15-80° $2\theta_{Cu}$ for the pristine material, the material recovered from the battery after the full charge up to 4.8 V vs. Li^+/Li and the material recovered from the battery after the 1st cycle (a) and in parallel, comparison of the X-ray diffraction patterns recorded for the pristine material, the material obtained after chemical Li deintercalation and the material obtained after chemical Li deintercalation and reinsertion (b). Enlargements are given in the 20-24° and 43.5-45.5° angular ranges.

Fig. V. 3: Comparison of the Raman spectra obtained for the pristine material, the material recovered from the battery after the full charge up to 4.8 V vs. Li^+/Li, the material recovered from the battery after the 1st cycle, the material obtained after chemical Li deintercalation and the material obtained after chemical Li deintercalation and reinsertion (a). The spectra of the pristine material, the material recovered from the battery after a 1st cycle and the materials obtained chemically after Li deintercalation and reinsertion were decomposed using Pseudo-Voigt bands (here in green) to allow their easier comparison (b).

Fig. V. 4: Charge and discharge curves obtained for lithium batteries using as positive electrodes: (a) the material obtained after chemical Li deintercalation and (b) the material obtained after chemical Li deintercalation and reinsertion. The first cycle was performed between 2.5 and 4.8 V vs. Li^+/Li, whereas the next cycles were charged only up to 4.6 V vs. Li^+/Li.

Fig. V. 5: Comparison of the charge and discharge curves obtained during the 1st and 2nd cycles of lithium batteries using the pristine material as positive electrode (dotted black lines) with those obtained during the 1st cycle of lithium batteries using the material recovered after chemical Li deintercalation and reinsertion as positive electrode (continuous blue lines).

Fig. V. 6: Thermal evolution of the H/M ratio for the pristine material and the material recovered after chemical Li deintercalation and reinsertion. Curie constants were estimated considering the data between 150 K and 300 K.

Fig. V. 7: Comparison of the experimental and calculated neutron diffraction patterns for the material obtained after chemical Li deintercalation and reinsertion in $Li_{1.20}Mn_{0.54}Co_{0.13}Ni_{0.13}O_2$. The experimental data were refined using the Rietveld method and considering a description of the unit cell in the *R-3m* space group

Figure V. 8: Comparison of the XANES spectra at the Ni K-edge (a), Co K-edge (b) and Mn K-edge (c) for the pristine material (Black line), the material recovered from the battery after the 1st cycle (Red line) and the material obtained after chemical Li deintercalation and reinsertion (Blue line). XANES spectra recorded for fully characterized samples of $LiCo^{III}_{1/3}Ni^{II}_{1/3}Mn^{IV}_{1/3}O_2$, $LiNi^{III}_{0.80}Co^{III}_{0.15}Al_{0.05}O_2$, $Co^{II,III}_3O_4$, $Li_2Mn^{IV}O_3$ and $LiMn^{III,IV}_2O_4$ are given as references.

Chapter VI

Fig. VI. 1. Charge and discharge curves of $Li//Li_{1.20}Mn_{0.54}Co_{0.13}Ni_{0.13}O_2$ cells.

Fig. VI. 2: HAADF-STEM image and electron diffraction pattern of pristine material $Li_{1.20}Mn_{0.54}Co_{0.13}Ni_{0.13}O_2$. The colored lines highlight the different types of stacking for the ordered transition metal layers.

Fig. VI. 3: Stacking of metal and oxygen ions along $[2\text{-}10]_{R\text{-}3m}$ *(a)*, $[120]_{R\text{-}3m}$ *(b)*, and $[1\text{-}10]_{R\text{-}3m}$ *(c)*, the corresponding electron diffraction patterns calculated (*(d), (e)* and *(f)*, respectively) and representation of an ordered transition metal layer with the three directions of projection indicated by green arrows (g).

Fig. VI. 4: Comparison of an experimental STEM image obtained for the pristine material $Li_{1.20}Mn_{0.54}Co_{0.13}Ni_{0.13}O_2$ with the simulated image given in a red rectangle (a) and comparison of the corresponding experimental electron diffraction pattern (b) with the simulated one (c)

Fig. VI. 5: Nano electron diffraction patterns in a particle of pristine material $Li_{1.20}Mn_{0.54}Co_{0.13}Ni_{0.13}O_2$.

Fig. VI. 6: HAADF-STEM image of the material recovered after the 1st cycle of the battery without the “plateau” with different scales, large scale (a) and small scale (b) in different places in a particle.

Fig. VI. 7: SAED pattern of the material recovered after the 1st cycle of the battery without the “plateau”.

Fig. VI. 8: HAADF-STEM images of the material recovered after the 1st cycle of the battery with the “plateau” with different scales, large scale (a) and small scale (b) in different places in a particle. White arrows indicate the presence of transition metal ions into the Li layers.

Fig. VI. 9: SAED pattern of the material recovered after the 1st cycle of the battery with the “plateau”.

Fig. VI. 10: HAADF-STEM images of the material obtained after chemical Li reinsertion in a material previously chemically deintercalated, in the bulk (a) and at the surface (b) of a particle.

Fig. VI. 11: Zones of the crystal analyzed by nano electron diffraction given in (a) and corresponding nano electron diffraction patterns (b) for the material prepared chemically from $Li_{1.20}Mn_{0.54}Co_{0.13}Ni_{0.13}O_2$.

List of tables

List of tables

Chapter II

Table II. 1: Chemical composition, average oxidation state of transition metal ions and Curie constant determined for the three samples “$Li_{1.20}Mn_{0.54}Co_{0.13}Ni_{0.13}O_2$” synthesized at 800°C, 900°C and 1000°C.

Table II. 2: Structural parameters obtained from the refinement by the Rietveld method of the X-ray diffraction data recorded for “$Li_{1.20}Mn_{0.54}Co_{0.13}Ni_{0.13}O_2$” synthesized at 800°C, 900°C and 1000°C.

Table II. 3: Structural parameters obtained from the refinement by the Rietveld method of the neutron diffraction data recorded for the pristine material “$Li_{1.20}Mn_{0.54}Co_{0.13}Ni_{0.13}O_2$” synthesized at 1000°C considering a unit cell described in the *R-3m* space group.

Table II. 4: Structural parameters obtained from the refinement by the Rietveld method of the neutron diffraction data recorded for the pristine material “$Li_{1.20}Mn_{0.54}Co_{0.13}Ni_{0.13}O_2$” synthesized at 1000°C considering a unit cell described in the *C2/m* space group.

Chapter III

Table III. 1: Changes in lattice parameters during the 1st charge and discharge.

Chapter IV

Table IV. A. 1: Ni K-edge EXAFS parameters in the material during the 1st cycle with “plateau”.

Table IV. A. 2: Co K-edge EXAFS parameters in the material during the 1st cycle with “plateau”.

Table IV. A. 3: Mn K-edge EXAFS parameters in the material during the 1st cycle with “plateau”.

Chapter V

Table V. 1: Chemical compositions determined by ICP for the pristine material, the material recovered from the battery after a first charge up to 4.8 V vs. Li^+/Li, the material obtained after chemical lithium deintercalation, the material recovered from the battery after the 1st cycle and the material obtained after chemical lithium deintercalation and reinsertion.

Table V. 2: Cell parameters, determined by the Le Bail refinement of the X-ray diffraction data, for the pristine material, the material recovered from the battery after a first charge up to 4.8 V vs. Li^+/Li, the material obtained after chemical lithium deintercalation, the material recovered from the battery after the 1st cycle and the material obtained after chemical lithium deintercalation and reinsertion

Table V. 3: Average oxidation state of the transition metal ions in the pristine material and in the material recovered after chemical Li deintercalation and reinsertion.

Table V. 4: Curie constants estimated from thermal evolution of the H/M ratio for the pristine material and the material recovered after chemical Li deintercalation and reinsertion. They are compared to the theoretical curie constants determined considering oxygen loss for the material recovered after chemical Li deintercalation and insertion.